



DIPARTIMENTO DI INGEGNERIA CIVILE

***Dottorato di Ricerca in Ingegneria delle Strutture e del
Recupero Edilizio ed Urbano***

IX Ciclo N.S. (2007-2010)

**ANALISI TEORICO-SPERIMENTALE
DI COLLEGAMENTI DISSIPATIVI A PARZIALE
RIPRISTINO DI RESISTENZA IN STRUTTURE
INTELAIATE IN ACCIAIO**

Massimo Latour

Il Tutor
Prof. Gianvittorio Rizzano

Il Coordinatore
Prof. Ciro Faella

Il Co-Tutor
Prof. Ing. Vincenzo Piluso

RINGRAZIAMENTI

Concludere questa tesi significa per prima cosa giungere al termine di questi tre anni sicuramente belli, anche se non sempre sereni, di esperienza di dottorato. Il rammarico con cui si lascia alle spalle quanto vissuto fin qui, per continuare la propria vita lavorativa verso nuovi obiettivi, è enorme.

Il ringraziamento più grande voglio rivolgerlo alle persone con cui mi sono ritrovato ogni giorno a condividere tutto (dal laboratorio ai pranzi frugali). Un particolare ricordo va a Riccardo e Fabio, colleghi del gruppo di ricerca, con cui ho trascorso gran parte di questo periodo e senza i quali non avrei mai conseguito questo obiettivo. Mi rende felice e per questo mi fa piacere menzionare Saverio e Francesco, compagni di stanza, ma prima di tutto amici. E' doveroso ringraziare, con grande stima e riconoscenza, il Prof. Gianvittorio Rizzano e il Prof. Vincenzo Piluso, che hanno rappresentato per me un punto di riferimento, ma anche un meraviglioso esempio di come si possa essere persone prima ancora che valenti accademici.

In questo momento non posso non pensare a mia madre e mio padre che, ormai, non sopportano più di vedermi curvo su libri di cui non riescono a comprendere nemmeno il significato del titolo. Infine Manuela, presenza costante cui devo molto di quanto sono riuscito a costruire in questi ultimi tre anni e senza la quale forse non ce l'avrei fatta ad essere qui a mettere questo punto.

Knowledge without follow-through is worse than no knowledge

(Charles Bukowski)

CONTENTS

1. INTRODUCTION

1.1 SCOPE OF THE STUDY	1
------------------------	---

2. SEISMIC BEHAVIOR OF MOMENT RESISTING FRAMES

2.1 THE STRUCTURAL TYPOLOGY	5
2.1.1 MRFS SPATIAL DISTRIBUTION	10
2.1.2 THE CONNECTION TYPOLOGIES	15
2.1.3 DUCTILITY CLASS	21
2.1.4 STIFFNESS AND STRENGTH OF JOINTS	28
2.2 FRAMES AND JOINTS CLASSIFICATION	34
2.3 THE COMPONENT METHOD	42
2.4 THE ROLE OF CONNECTIONS ON THE OVERALL STRUCTURAL BEHAVIOR	53
2.5 REFERENCES	67

3. CYCLIC BEHAVIOR OF BEAM-TO-COLUMN JOINTS: EXPERIMENTAL CAMPAIGN

3.1 INTRODUCTION	73
3.2 DESCRIPTION OF THE TEST SETUP	78
3.3 DESIGN OF THE SPECIMENS	93
3.3.1 DESIGN OF SPECIMEN EEP-CYC 01	93
3.3.2 DESIGN OF SPECIMEN EEP-CYC 02	107
3.3.3 DESIGN OF SPECIMEN EEP-DB-CYC 03	112
3.3.4 DESIGN OF SPECIMEN TS-CYC 04	118
3.4 DESCRIPTION OF THE EXPERIMENTAL TESTS	121
3.4.1 DESCRIPTION OF TEST EEP-CYC 01	121
3.4.2 DESCRIPTION OF TEST EEP-CYC 02	127
3.4.3 DESCRIPTION OF TEST EEP-DB-CYC 03	136
3.4.4 DESCRIPTION OF TEST TS-CYC 04	141
3.4.5 GEOMETRICAL AND MECHANICAL PROPERTIES OF THE SPECIMENS	148
3.4.6 COMPARISON AMONG THE TESTS	153
3.6 REFERENCES	157

4. CYCLIC BEHAVIOR OF BEAM-TO-COLUMN JOINTS: MECHANICAL MODELING

4.1 INTRODUCTION	163
------------------	-----

4.2 CYCLIC MODELING OF THE JOINT COMPONENTS: LITERATURE REVIEW	166
4.2.1 MODELING OF THE PANEL ZONE IN SHEAR	166
4.2.1.1 FIELDING AND HUANG MONOTONIC MODEL (1971)	169
4.2.1.2 KRAWINKLER MONOTONIC MODEL (1971)	174
4.2.1.3 WANG MONOTONIC MODEL (1985)	178
4.2.1.4 FIELDING AND WANG MODIFIED MONOTONIC MODEL (1996)	181
4.2.1.5 KIM & ENGELHARDT MONOTONIC MODEL (2002)	183
4.2.1.6 KIM & ENGELHARDT CYCLIC MODEL (2002)	190
4.2.2 MODELING OF COLUMN WEB PANELS UNDER TENSION AND COMPRESSION	201
4.2.3 MODELING OF THE T-STUB IN TENSION	212
4.3 ASSEMBLY AND ACCURACY OF THE MODEL	218
4.4 REFERENCES	239

5. APPLICATION OF DISSIPATIVE DEVICES TO BEAM-TO-COLUMN JOINTS

5.1 ENERGETIC APPROACHES: MAIN FEATURES	243
5.1.1 PASSIVE ENERGY DISSIPATING SYSTEM	255
5.1.2 BASIC RESPONSE OF STRUCTURES EQUIPPED WITH HYSTERETIC DAMPERS	258

5.1.3 METALLIC AND FRICTION DAMPERS	267
5.1.3.1 METALLIC FLEXURAL DISSIPATING DEVICES	273
5.1.3.2 METALLIC SHEAR DISSIPATING DEVICES	278
5.1.3.3 FRICTION DISSIPATING DEVICES	280
5.2 DEVELOPMENT OF DISSIPATIVE T-STUBS	283
5.2.1 MECHANICAL MODELING	286
5.2.1.1 RECTANGULAR T-STUBS – PILUSO ET AL. MODEL (1997)	286
5.2.1.2 DISSIPATIVE T-STUBS – PROPOSED MODEL	310
5.2.2 EXPERIMENTAL BEHAVIOR UNDER CYCLIC LOADS	329
5.2.2.1 MONOTONIC TESTS - T-STUBS ON RIGID SUPPORT	336
5.2.2.2 MONOTONIC TESTS - COUPLED T-STUBS	343
5.2.2.3 CYCLIC TESTS – T-STUBS ON RIGID SUPPORT	348
5.2.2.4 CYCLIC TESTS – COUPLED T-STUBS	354
5.3 APPLICATION OF DISSIPATIVE T-STUBS TO DOUBLE SPLIT TEE JOINTS	358
5.3.1 THE ROLE OF MOMENT-SHEAR INTERACTION	366
5.3.1.1 EFFECT OF MOMENT-SHEAR INTERACTION ON THE VALUE OF THE PLASTIC MOMENT	366
5.3.1.2 OPTIMUM SHAPE OF DISSIPATIVE T-STUBS	381
5.3.2 EXPERIMENTAL TESTS ON DISSIPATIVE T-STUB JOINTS	391
5.3.2.1 DESIGN OF TESTED SPECIMENS	392
5.3.2.2 DESCRIPTION OF TEST TSJ-XS-CYC 06	399

5.3.2.3 DESCRIPTION OF TEST TSJ-XS-CYC 07	406
5.3.2.4 COMPARISON BETWEEN DISSIPATIVE AND CLASSICAL JOINTS	412
5.4 REFERENCES	415

LIST OF FIGURES

<i>Fig. 2.1 – Steel Moment Resisting Frames in U.S.A.</i>	5
<i>Fig. 2.2 - Structural Typologies of CBF and EBF</i>	7
<i>Fig. 2.3 - Buildings Erected applying the “Column Tree” Technique</i>	8
<i>Fig. 2.4 – Classification of Moment Resisting Frames</i>	9
<i>Fig. 2.5 – Spatial Distribution of Space Frames</i>	10
<i>Fig. 2.6 – Spatial Distribution of Perimeter Frames</i>	11
<i>Fig. 2.7 – Spatial Distribution of Perimeter Frames with only few rigid bays</i>	12
<i>Fig. 2.8 – Spatial Distribution of Planar Frames</i>	13
<i>Fig. 2.9 – Spatial Distribution of Hybrid Systems</i>	14
<i>Fig. 2.10 – Rivets and High Strength Bolts</i>	16
<i>Fig. 2.11 - Examples of riveted structures</i>	17
<i>Fig. 2.12 – On the left: FCAW welding technique; On the right: SMAW welding technique</i>	18
<i>Fig. 2.13 – Failure of beam-to-column fillet welded connection (Kobe Earthquake)</i>	20
<i>Fig. 2.14 – Structural Joints Configuration (CEN, 2005)</i>	28
<i>Fig. 2.15 – Distinction between Connection and Panel zone</i>	30
<i>Fig. 2.16 – Pinned, Continuous and Semi-continuous joints</i>	31
<i>Fig. 2.17 – Modeling of a welded joint with the component method</i>	46
<i>Fig. 2.18 – Simplified model adopted by (Piluso et al., 1994)</i>	59
<i>Fig. 2.19 – Influence of non-dimensional stiffness on the period of vibration</i>	61
<i>Fig. 2.20 – Influence of non-dimensional stiffness on stability coefficient</i>	62
<i>Fig. 2.21 – Results of the parametric analysis (Aribert & Grecea, 2000)</i>	64
<i>Fig. 2.22 – Proposal of behavioral factor for semi-continuous MRFs</i>	65
<i>Fig. 3.1 – Constraining devices used in the experimental campaign</i>	79

<i>Fig. 3.2 – MTS Hydraulic testing machine</i>	81
<i>Fig. 3.3 – Universal testing machine SCHENCK Hydropuls S56</i>	82
<i>Fig. 3.4 – Scheme and picture of an LVDT</i>	83
<i>Fig. 3.5 – Scheme and picture of an LVDT</i>	84
<i>Fig. 3.6 – Scheme and picture of an inclinometer</i>	85
<i>Fig. 3.7 – Scheme of a Strain Gauge</i>	85
<i>Fig. 3.8 – Actions in a frame due to seismic loads</i>	86
<i>Fig. 3.9 – Scheme reproduced in laboratory</i>	86
<i>Fig. 3.10 – AISC loading history for beam-to-column joints</i>	87
<i>Fig. 3.11 – Position of the instruments</i>	89
<i>Fig. 3.12 – Setup of the measurement devices</i>	90
<i>Fig. 3.13 – Experimental Setup</i>	92
<i>Fig. 3.14 – Definition of the equivalent shear acting in the panel zone</i>	94
<i>Fig. 3.15 – Rendering and Geometry of joint EEP – CYC 01</i>	99
<i>Fig. 3.16 – Simplified model considered in the design of end-plate (CEN, 2005)</i>	100
<i>Fig. 3.17 – Influence of coefficient α on the collapse mechanism</i>	103
<i>Fig. 3.18 – Geometry and rendering of specimen EEP-CYC 02</i>	112
<i>Fig. 3.19 – Definition of RBS parameters</i>	113
<i>Fig. 3.20 – Typical scheme of beam with RBS</i>	114
<i>Fig. 3.21 – Scheme of the actions transferred by the RBS to the column</i>	117
<i>Fig. 3.22 – Rendering and Geometry of test TS-CYC 04</i>	120
<i>Fig. 3.23 – Test EEP-CYC 01</i>	121
<i>Fig. 3.24 – Measurement devices EEP-CYC 01</i>	121
<i>Fig. 3.25 – Measurement devices EEP-CYC 01</i>	122
<i>Fig. 3.26 – Failure of EEP-CYC 01 specimen due to brittle collapse of beam flange to end-plate welds</i>	123
<i>Fig. 3.27 – EEP-CYC 01 Moment-Rotation curve</i>	124

<i>Fig. 3.28 – Hysteretic response of end plate equivalent T-stubs</i>	125
<i>Fig. 3.29 – Cyclic response of column web in shear</i>	126
<i>Fig. 3.30 – Cyclic response of column web under alternate tension and compression</i>	126
<i>Fig. 3.31 – Energy dissipation of specimen EEP-CY 01</i>	127
<i>Fig. 3.32 – Test EEP-CYC 02</i>	128
<i>Fig. 3.33 – Measurement devices EEP-CYC 02</i>	129
<i>Fig. 3.34 – EEP-CYC 02 Moment-Rotation Curve</i>	130
<i>Fig. 3.35 – Component Hysteretic curves for specimen EEP-CYC 02</i>	132
<i>Fig. 3.36 – Formation of the crack in the end-plate</i>	133
<i>Fig. 3.37 – Failure of the end-plate</i>	134
<i>Fig. 3.38 – Energy dissipation of specimen EEP-CYC 02</i>	135
<i>Fig. 3.39 – Setup of test EEP-DB-CYC 03</i>	136
<i>Fig. 3.40 – Measurement instruments used to monitor the joint components</i>	137
<i>Fig. 3.41 – Straining Gauge used to monitor deformations of the Dog-Bone</i>	137
<i>Fig. 3.42 – Energy Dissipation of specimen EEP-DB-CYC 03</i>	138
<i>Fig. 3.43 – Flange and web buckling</i>	139
<i>Fig. 3.44 – Flange and web buckling</i>	140
<i>Fig. 3.45 – Test TS-CYC 04</i>	141
<i>Fig. 3.46 – Measurement devices</i>	142
<i>Fig. 3.47 – TS-CYC 04 Moment-Rotation Curve</i>	143
<i>Fig. 3.48 – Formation of the plastic hinges in correspondence of bolts and plate-web tie</i>	144
<i>Fig. 3.49 – Plasticization of the Tee elements</i>	145
<i>Fig. 3.50 – Development of the plastic hinges and failure of the Tee elements</i>	146
<i>Fig. 3.51 – Components hysteretic curves for specimen TS-CYC 04</i>	147
<i>Fig. 3.52 – Energy Dissipation of TS-CYC 04 joint</i>	148

<i>Fig. 3.53 – Experimental results of a coupon tensile test</i>	149
<i>Fig. 3.54 – Comparison between the actual and the engineering stress-strain relationship</i>	150
<i>Fig. 3.55 – Notation for the definition of the geometrical properties</i>	151
<i>Fig. 3.56 - Energy dissipation capacities of the tested joints</i>	154
<i>Fig. 3.57 – Comparison among the cyclic curves of the testes specimens</i>	155
<i>Fig. 4.1 – Mechanical model for bolted connections</i>	164
<i>Fig. 4.2 – Modeling of an internal welded joint</i>	168
<i>Fig. 4.3 – (Mulas, 2004) FEM model</i>	169
<i>Fig. 4.4 – Bilinear model of Fielding and Huang</i>	170
<i>Fig. 4.5 – Post-elastic model of Fielding and Huang (1971)</i>	172
<i>Fig. 4.6 – Translational equilibrium (Fielding model)</i>	172
<i>Fig. 4.7 – Application of Fielding & Huang model</i>	173
<i>Fig. 4.8 – Tri-linear model of Krawinkler</i>	174
<i>Fig. 4.9 – Post-elastic model (Krawinkler,1971)</i>	175
<i>Fig. 4.10 – Krawinkler model in case of HEB 200 column and IPE 270 beam</i>	177
<i>Fig. 4.11 – Shear panel model (Wang, 1985)</i>	178
<i>Fig. 4.12 – Wang post-elastic model</i>	179
<i>Fig. 4.13 – Wang model</i>	180
<i>Fig. 4.14 – Comparison between Fielding and Wang models (Left) and Improved Fielding and Wang models (Right)</i>	182
<i>Fig. 4.15 – Quadri-linear model of Kim & Engelhardt</i>	183
<i>Fig. 4.16 – Comparison among literature models in case of HEB 200-IPE 270 coupling</i>	188
<i>Fig. 4.17 – Comparison among literature models for FEM analysis $t_{cf}=27$ mm</i>	189
<i>Fig. 4.18 – Comparison among literature models for FEM analysis $t_{cf}=36$ mm</i>	190

<i>Fig. 4.19 – Comparison among literature models for FEM analysis $t_{cf}=45$ mm</i>	190
<i>Fig. 4.20 – Kinematic Hardening model</i>	191
<i>Fig. 4.21 – Application of Kinematic Hardening model to Krawinkler specimen-A1</i>	192
<i>Fig. 4.22 – Cyclic steady state curve</i>	193
<i>Fig. 4.23 – Shear Panel cyclic curve</i>	194
<i>Fig. 4.24 – Dafalias-Popov model for Hysteresis Curve</i>	196
<i>Fig. 4.25 – Procedure for the translation of the bound line</i>	197
<i>Fig. 4.26 – Comparison with Krawinkler test A1</i>	199
<i>Fig. 4.27 – Comparison with Krawinkler test A2</i>	200
<i>Fig. 4.28 – Column web subjected to compression</i>	201
<i>Fig. 4.29 – Column web subjected to tension</i>	202
<i>Fig. 4.30 – Transitory phase</i>	203
<i>Fig. 4.31 – Stabilized response</i>	204
<i>Fig. 4.32 – Stabilized response after softening</i>	205
<i>Fig. 4.33 – Hardening factor</i>	206
<i>Fig. 4.34 – Softening factor</i>	207
<i>Fig. 4.35 – Relaxation factor</i>	208
<i>Fig. 4.36 – Cyclic curve at the i-th cycle for panels in tension and compression</i>	210
<i>Fig. 4.37 – Hysteresis curve in Cofie model</i>	211
<i>Fig. 4.38 – Theoretical-experimental comparisons</i>	212
<i>Fig. 4.39 – Piluso et al. model</i>	215
<i>Fig. 4.40 – Geometry of EEP-CYC 01 specimen</i>	220
<i>Fig. 4.41 – Geometry of EEP-CYC 02 specimen</i>	221
<i>Fig. 4.42 – Geometry of TS-CYC 04 specimen</i>	222
<i>Fig. 4.43 – Geometry of FPC/B specimen (Bernuzzi et al., 1996)</i>	223

<i>Fig. 4.44 – Geometry of J-1.3 specimen (Nogueiro et al., 2006)</i>	224
<i>Fig. 4.46 – Theoretical-Experimental comparison for specimen EEP-CYC 01</i>	226
<i>Fig. 4.47 – Theoretical-Experimental comparison for specimen J-1.3</i>	226
<i>Fig. 4.48 – Comparison of the energy dissipated for specimen EEP-CYC 01</i>	227
<i>Fig. 4.49 – Comparison of the energy dissipated for specimen J-1.3</i>	227
<i>Fig. 4.50 – Theoretical-Experimental comparison for specimen FW</i>	229
<i>Fig. 4.51 – Comparison of the energy dissipated for specimen FW</i>	230
<i>Fig. 4.52 – Theoretical-Experimental comparison for specimen EEP-CYC 02</i>	231
<i>Fig. 4.53 – Theoretical-Experimental comparison for specimen TS-CYC 04</i>	231
<i>Fig. 4.54 – Theoretical-Experimental comparison for specimen FPC/B</i>	232
<i>Fig. 4.55 – Comparison of the energy dissipated for specimen EEP-CYC 02</i>	233
<i>Fig. 4.56 – Comparison of the energy dissipated for specimen TS-CYC 04</i>	233
<i>Fig. 4.57 – Comparison of the energy dissipated for specimen FPC/B</i>	234
<i>Fig. 4.58 – Model performance - Peak Moment for Authors' Tests</i>	236
<i>Fig. 4.59 – Model performance - Unloading Stiffness for Authors' Tests</i>	237
<i>Fig. 4.60 – Model performance - Peak Moment for Literature Tests</i>	237
<i>Fig. 4.61 – Model performance - Unloading Stiffness for Literature Tests</i>	238
<i>Fig. 5.1 – Time variation of the energy dissipate by viscous damping of an elastic (top) and inelastic system (bottom)</i>	246
<i>Fig. 5.2 – Rain flow analogy</i>	247
<i>Fig. 5.3 – Seismic Control Systems</i>	250
<i>Fig. 5.4 – Control Schemes</i>	251
<i>Fig. 5.5 – Tuned Mass Damper - Tuned Sloshing Damper – Tuned Liquid Damper</i>	254
<i>Fig. 5.6 – Response of damped system subjected to harmonic forces</i>	259
<i>Fig. 5.7 – Deformation response factor for damped system (harmonic force)</i>	261
<i>Fig. 5.8 – Single-degree-of-freedom system incorporating hysteretic damper</i>	262
<i>Fig. 5.9 – Steady-state response amplitude of single-degree-of-freedom with</i>	

<i>hysteretic damper under harmonic base excitation, $kd/k = 0.55$</i>	265
<i>Fig. 5.10 – Typical response of metals subjected to monotonic and cyclic loads</i>	268
<i>Fig. 5.11 – Atomic arrangements corresponding to: a) edge dislocation; b) screw dislocation</i>	270
<i>Fig. 5.12 – Cyclic response of ADAS devices</i>	273
<i>Fig. 5.13 – Curvatures developed for different plate geometry</i>	274
<i>Fig. 5.14 – Application of ADAS device to a three stories steel MRFs</i>	275
<i>Fig. 5.15 – Geometry and Response of T-ADAS devices</i>	276
<i>Fig. 5.16 – Geometry and Response of Honeycomb devices</i>	277
<i>Fig. 5.17 – Distribution of Shear Panels in MRFs (Nakashima, 1995)</i>	278
<i>Fig. 5.18 – Shear Damper proposed by (Cahis et al., 1997)</i>	279
<i>Fig. 5.19 – Shear Damper proposed by (Tsai) (Tsai & Wang, 1998)</i>	280
<i>Fig. 5.20 – T-stub Identification in case of Extended end plate Connections</i>	286
<i>Fig. 5.21 – Failure modes of bolted T-stubs</i>	287
<i>Fig. 5.22 – Adopted Notation</i>	288
<i>Fig. 5.23 – Influence of parameter β on the collapse mechanism</i>	291
<i>Fig. 5.24 – Yield lines for T-stubs with only one bolt row</i>	292
<i>Fig. 5.25 – Yield lines in case of group of bolts</i>	293
<i>Fig. 5.26 – Collapse mechanisms according to Piluso et al. model</i>	294
<i>Fig. 5.27 – Material Uni-axial behavior</i>	296
<i>Fig. 5.28 – Quadrilinear force-displacement curve</i>	299
<i>Fig. 5.29 – Definition of geometry, curvature and bending moment diagrams</i>	311
<i>Fig. 5.30 – Simplified model for stiffness prediction</i>	313
<i>Fig. 5.31 – Moment on the cantilever</i>	315
<i>Fig. 5.32 – Diagram of Curvatures in the fictitious scheme</i>	316
<i>Fig. 5.33 – Correlation between ζ factor and the ratio s/B</i>	320
<i>Fig. 5.34 – Derivation of effective width</i>	323

<i>Fig. 5.35 – Ratio between effective and maximum plate width</i>	326
<i>Fig. 5.36 – Typologies of Tested Specimens</i>	330
<i>Fig. 5.37 – Finite Element Model</i>	332
<i>Fig. 5.38 – Experimental test on hourglass T-stub on rigid Support</i>	336
<i>Fig. 5.39 – Experimental test on rectangular T-stub on rigid Support</i>	337
<i>Fig. 5.40 – TS01-M vs TS01-XS-M: monotonic tests comparison</i>	338
<i>Fig. 5.41 – TS02-M vs TS02-XS-M: monotonic tests comparison</i>	338
<i>Fig. 5.42 – Deformed shape of T-stub on rigid support and Coupled T-stubs</i>	339
<i>Fig. 5.43 – Typical failure of rectangular T-stubs on rigid support under monotonic loads</i>	340
<i>Fig. 5.44 – Typical failure of hourglass T-stubs on rigid support under monotonic loads</i>	341
<i>Fig. 5.45 – Rectangular T-stub – Model Comparison</i>	342
<i>Fig. 5.46 – Hourglass T-stub – Model Comparison</i>	342
<i>Fig. 5.47 – TSD series</i>	344
<i>Fig. 5.48 – TSD-XS series</i>	345
<i>Fig. 5.49 – TSD test result and models comparison</i>	346
<i>Fig. 5.50 – TSD-XS test results and model comparison</i>	346
<i>Fig. 5.51 – Typical failure of TSD specimens</i>	347
<i>Fig. 5.52 – Typical failure of TSD-XS specimens</i>	347
<i>Fig. 5.53 – TS01-C and TS01-XS-C test results</i>	348
<i>Fig. 5.54 – TS02-C15 and TS02-XS-C15 test results</i>	349
<i>Fig. 5.55 – Propagation of the heat along the flanges – Hourglass T-stub</i>	350
<i>Fig. 5.56 – Propagation of the heat along the flanges – Rectangular T-stub</i>	350
<i>Fig. 5.57 – Definition of the conventional collapse</i>	351
<i>Fig. 5.58 – TS and TS-XS low-cycle fatigue curves</i>	354
<i>Fig. 5.59 – TSD and TSD-XS series – Cyclic Tests</i>	356
<i>Fig. 5.60 – TSD and TSD-XS – low cycle fatigue curves</i>	356

<i>Fig. 5.61 – Comparison among low cycle fatigue curves</i>	357
<i>Fig. 5.62 – Different joint hysteretic behaviors</i>	361
<i>Fig. 5.63 (Huang & Foutch, 2009) results</i>	363
<i>Fig. 5.64 – Distribution on internal stresses in the yielding condition under bending moment and shear</i>	369
<i>Fig. 5.65 – Representation of M-V Interaction Domain</i>	370
<i>Fig. 5.66 – Distribution of internal forces on an X-shaped T-stub</i>	372
<i>Fig. 5.67 – Influence of hourglass geometry on the position of the section of minimum resistance</i>	377
<i>Fig. 5.68 – Reduction of resistance due to moment-shear interaction for different values of m/t</i>	380
<i>Fig. 5.69 – Average of the ratio between optimum shape and exponential law (Devices with same resistance and same m/t ratio)</i>	386
<i>Fig. 5.70 – s/B optimum vs m/t</i>	387
<i>Fig. 5.71 –Optimum shape vs Exponential Shape</i>	390
<i>Fig. 5.72 –Specimen TSJ-XS-CYC-06</i>	397
<i>Fig. 5.73 –Specimen TSJ-CYC-07</i>	398
<i>Fig. 5.74 –Test TSJ-XS-CYC 06</i>	399
<i>Fig. 5.75 –Measurement devices (TSJ-XS-CYC 06)</i>	400
<i>Fig. 5.76 –TSJ-XS-CYC 06 Moment-Rotation Curve</i>	400
<i>Fig. 5.77 –Plasticization of the tee elements</i>	401
<i>Fig. 5.78 –Thermal state of the specimen during first cycles</i>	403
<i>Fig. 5.79 –Joints after failure. On the left: TS-CYC-04- On the right: TS-XS-CYC-06</i>	404
<i>Fig. 5.80 –Rotation of the plate due to the force acting on the T-stub</i>	405
<i>Fig. 5.81 – Dissipated Energy – TSJ-XS-CYC 06</i>	406
<i>Fig. 5.82 –Test TSJ-XS-CYC 07</i>	407
<i>Fig. 5.83 –Measurement devices (TSJ-XS-CYC 07)</i>	408

<i>Fig. 5.84 –Cyclic Response of Joint TSJ-XS-CYC 07</i>	409
<i>Fig. 5.85 –Crack Formation and propagation (TSJ-XS-CYC 07)</i>	410
<i>Fig. 5.86 – Position of the section of mimum resistance (TSJ-XS-CYC 07)</i>	411
<i>Fig. 5.87 – Energy dissipated by joint TSJ-XS-CYC 07</i>	412
<i>Fig. 5.88 – Comparison between joints TS-CYC 04 and TSJ-XS-CYC 07</i>	413
<i>Fig. 5.89 – Cyclic envelopes of all tested joints</i>	414
<i>Fig. 5.90 – Energy dissipated by joints</i>	415

CHAPTER 1 – INTRODUCTION

1.1 Scope of the study

Before seismic events of Northridge (Los Angeles, 17 January 1994) and Hyogoken-Nanbu (Kobe, 17 January 1995) MRFs were supposed to be the most reliable seismic resistant systems due to the high number of dissipative zones that are able to develop. Before these earthquakes, especially in United States, MRFs were realized, generally, by adopting fully welded connections, which, at the time, were retained to perform better compared to other joint typologies. In addition, the economic advantages deriving from the adoption of field fully welded connections, strongly influenced choices of building owners' and, as a result, led to the adoption of this joint typology in almost all pre-Northridge steel MRFs. After Northridge earthquake, even though the loss of life was limited, the unexpected amount of damages occurred in structures adopting as seismic resistant system welded Moment Resisting Frames put into question the role played by welded connections on the whole structural behavior.

Therefore, after the seismic events, two strategies were identified to improve behavior of fully welded connections. The first one is related to the improvement of the welding technique, usually strengthening the critical area subjected to fracture. The second one is based on the possibility of concentrating the energy dissipation in the beam, reducing the bending resistant area of beams by properly cutting the flanges in a zone close to

beam-to-column connection. This weakening approach is commonly called RBS. A new design approach, which has been the subject of many studies in last decades, has gained growing interest in last years. In fact, Eurocode 8 has opened the door to the idea of dissipating the seismic input energy in the connecting elements of beam-to-column joints. It has been recognized that semi-rigid partial strength connections can lead to dissipation and ductility capacity compatible with the seismic demand, provided that they are properly designed by means of an appropriate choice of the joint component where the dissipation has to occur.

In this work, the attention is focused on this last approach. The first part of the work is descriptive and deals with the historical development and, in general, with the seismic behavior of Moment Resisting Frames. In the same chapter general concepts concerning the component method, as introduced by last version of Eurocode 3, are given. Finally, the influence of the joint behaviour on main characteristics of partial strength and/or semi-rigid MRFs is evaluated by properly accounting for existing literature. Third chapter deals with an experimental analysis on the cyclic behaviour of classical partial strength beam-to-column joints. The main scope of the experimental campaign is to show how to control the dissipative behaviour of joints by properly designing the weakest joint component and by over-strengthening the other connecting elements. Therefore, a design procedure is pointed out and the comparison among the results obtained by cyclic tests is presented in terms of energy dissipation capacity. In addition, by monitoring during the experimental tests both the whole joint and the single joint components it is shown that the energy dissipated by the joint is equal to the sum of the energy dissipated by the joint components. This result assures that the first phase of the component approach, i.e. the component identification, has been properly carried out and

that interaction between components under cyclic loads is negligible. Chapter 4 represents the continuation of the work carried out in previous chapter. In fact, on the base of the obtained results, the goal is to provide a mechanical cyclic model for the prediction of the overall joint behaviour, starting from existing literature models. Hence, a state-of-the-art review is first presented and then, model employed to set up a computer program devoted to the prediction of the cyclic behaviour of steel beam-to-column joints is shown. In particular, cyclic model adopts Kim & Engelhardt model for shear panel, Cofie & Krawinkler model for Panels in Tension and Compression and Piluso et al. model for the prediction of the T-stub behavior. Finally, in chapter 5, an innovative approach to improve the seismic behavior of bolted beam-to-column joints, which are affected by strength and stiffness degradation, is presented. The development of a dissipative device representing the application of ADAS concept to T-stubs, is detailed. First, a mechanical and finite element model able to predict the whole force displacement curve of the so-called hourglass T-stubs are set up. Next, an experimental analysis aiming to compare the hysteretic behaviour and the dissipative capacities of rectangular and dissipative T-stubs is carried out. Finally, as a consequence of the study of the joint component, a further experimental analysis concerning the application of such devices to partial strength beam-to-column joints is presented and the results, in terms of moment-rotation curve and energy dissipation capacity, are discussed and compared to those obtained by the cyclic testing of classical joints.

CHAPTER 2 – SEISMIC BEHAVIOR OF MOMENT RESISTING FRAMES

2.1 The structural typology

For different reasons Moment Resisting Frames (MRF) have become very popular in last century and many buildings have been built applying this technique. Architects and building owners usually appreciate layouts obtained using this structural typology, in fact such a system provides large open spaces without the obstruction usually due to the presence of braces or walls. Steel MRFs have been used worldwide especially for applications in low-rise industrial buildings and multi-storey low, medium and high-rise buildings (Fig. 2.1).



Fig. 2.1 – Steel Moment Resisting Frames in U.S.A.

MRFs are structures that withstand seismic actions by the bending of girders, columns and connections. Their main source of stiffness and lateral strength is given by the flexural resistance of members and connections, and the seismic energy dissipation capacity and ductility is provided by the formation of a high number of dissipative zones which can be located in beams, columns or joints depending on the applied design philosophy. Classically, framed structures are designed to possess strong columns, weak beams and full strength rigid connections, so that the earthquake input energy is dissipated through the plastic engagement of the end of beams and of the end of columns of the first storey.

For the above mentioned architectural characteristics, often MRFs are preferred to other structural systems, such as concentrically (CBF) and eccentrically (EBF) braced frames, where pendular frames are combined with stiff and strong braced frames (Giuncu & Mazzolani, 2000; Mazzolani & Piluso, 1996). With these approaches pendular frames are required to carry vertical loads and the energy dissipation capacity is entrusted to the bracing system. In case of CBF, the energy dissipation capacity is provided by the plasticization of diagonals in tension while, in case of EBF the hysteretic dissipation is relied on the plasticization of predetermined regions of the beams, individuated by the bracing system, which are subjected to high bending and/or shear (Fig. 2.2).

Notwithstanding the undoubted advantages which are possible to obtain by using Moment Resisting Frames, this structural typology possesses some weak points. First of all, the low lateral stiffness can significantly affect the response of the structure both at the ULS and at the SLS. In fact, the susceptibility to second order effects and the fulfillment of the serviceability limit states in terms

of maximum lateral drifts, can become governing parameters of the design process, leading to member size greater than the minimum needed for the satisfaction of the strength requirements. So that, especially for high-rise buildings, MRFs can become uneconomical with respect to other systems.

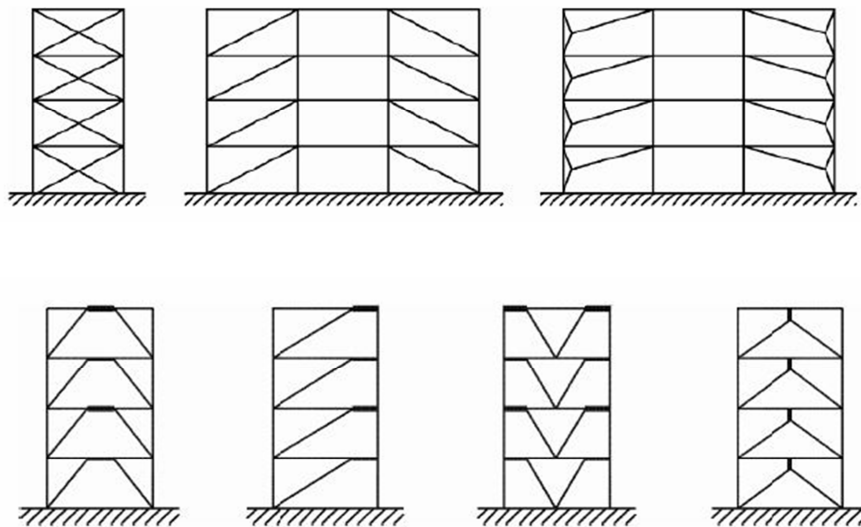


Fig. 2.2 - Structural Typologies of CBF and EBF

Other problems can be individuated in the difficulties which are possible to encounter in providing adequate stiffness and resistance to joints when these have to be rigid and designed to be over-resistant with respect to the connected beam. In fact, providing adequate stiffness and strength to joints can, in some cases, become onerous (Mazzolani & Piluso, 1996; Bruneau et al., 1998). In addition, when welded joints are adopted it is of fundamental importance to avoid as much as possible the use of field welds, which have been demonstrated, by evaluating the damages on steel structures caused by

Northridge and Kobe earthquakes, to be unreliable due to the limited deformation capacity and to the presence of welding defects (SAC, 2000a; SAC, 2000b). Therefore, when welding details are adopted it would be better to rely on shop welds (Astaneh-Asl, 1986).

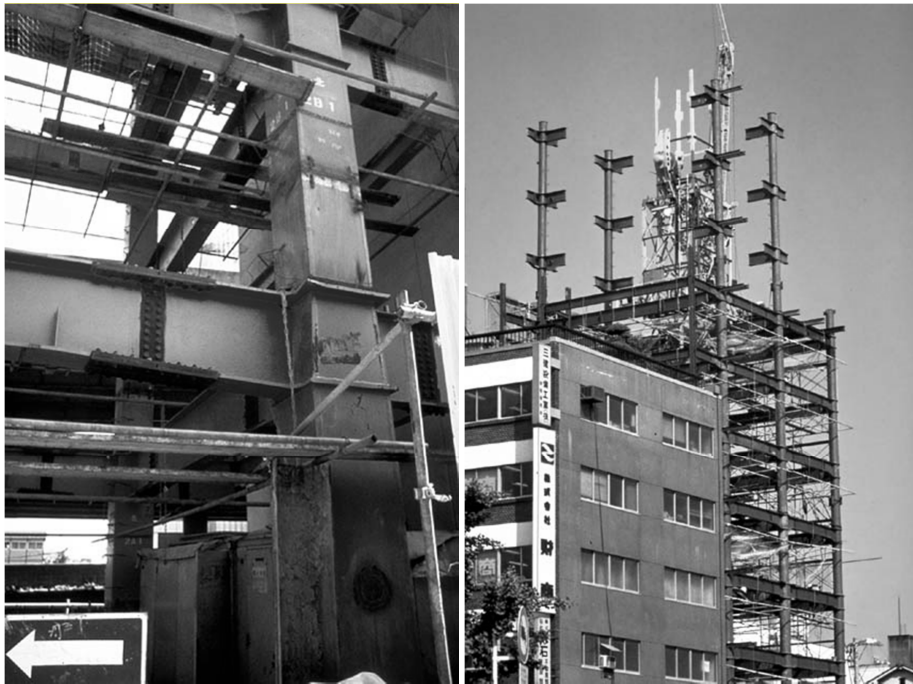


Fig. 2.3 - Buildings Erected applying the “Column Tree” Technique

A constructional procedure, which proposes to combine shop welded and field bolted connections is the so-called “column-tree” technique (Astaneh-Asl, 1987; Mazzolani & Piluso, 1996). In this practice, columns are welded with short girder stubs in the shop, successively erected in the field and finally connected by bolting the middle segment of the beam (Fig. 2.3). Usually, the

bolted part of the connection is designed to be full strength. As a consequence, its contribution to the frame stiffness and resistance is negligible and therefore, it does not play a major role on the overall structural behavior. Furthermore, the “column tree” technique assures high reliability and economy. In fact, in general, shop welds are less expensive and guarantee higher performances than field welds, which require inspections and good weather conditions to be executed.

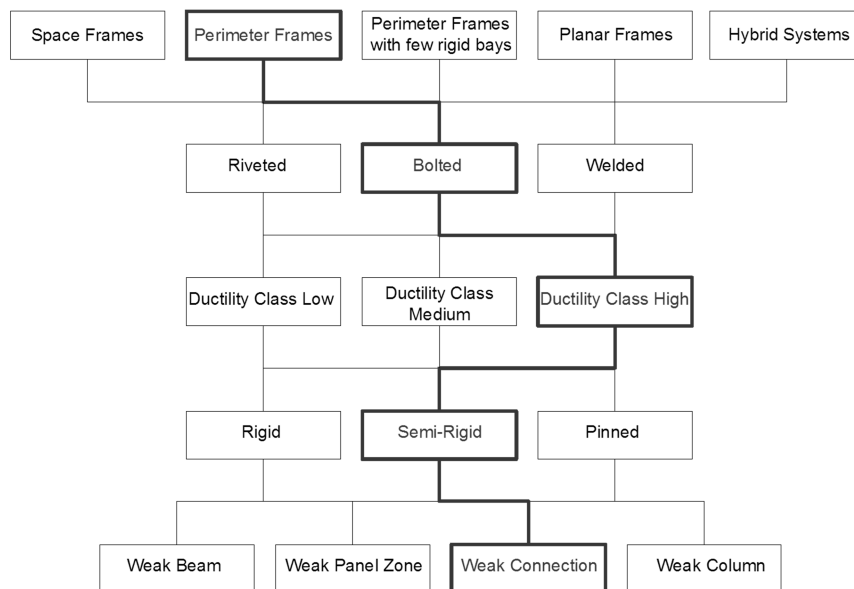


Fig. 2.4 – Classification of Moment Resisting Frames

A classification of MRFs, according to (Astaneh-Asl, 1995), can be arranged with reference to the following characteristics (Fig. 2.4):

- the spatial distribution of the frames within the whole building (e.g. perimeter frames, few rigid bays, etc.);
- the type of connections provided to connect girders and columns (riveted, bolted or welded);
- ductility class of the frame system (Low, Medium, High);
- stiffness of the connections (Pinned, Semi-Rigid, Rigid);
- relative resistance of the structural members, i.e. beams and columns, panel zone and elements composing the connection.

2.1.1 MRFs Spatial Distribution

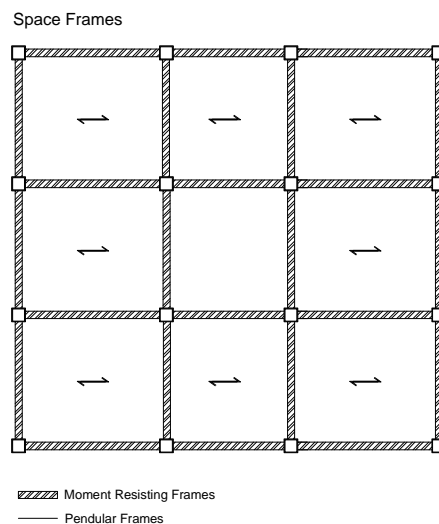


Fig. 2.5 – Spatial Distribution of Space Frames

MRFs can be categorized according to their spatial distribution in: ***Space Frames, Perimeter Frames, Perimeter Frames with only Few Rigid Bays, Planar Frames and Hybrid Systems.***

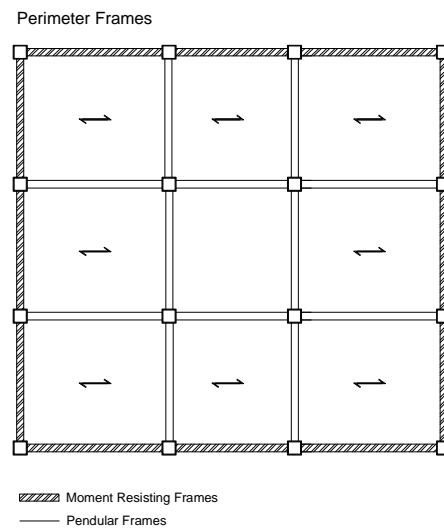


Fig. 2.6 – Spatial Distribution of Perimeter Frames

In case of ***Space Frames***, MRFs are uniformly spread in the structure and all the columns, girders and connections are required to carry both the vertical and lateral loads (Fig. 2.5).

Such a kind of typology traditionally necessitates the adoption of expensive rigid full strength joints and as a consequence can result in structures which are not cost/effective.

It is probably for this reason, that the adoption of **Perimeter Moment Resisting Frames** has gained increasing attention by U.S. designers in the last decade (Fig. 2.6). In fact, in this approach, only the exterior frames are part of the earthquake resistant system, while the interior beams and columns compose a pendular organism which has to carry only the gravity loads.

Thus, interior beams and columns can be designed to have pinned connections and only the perimeter frames, which resist the horizontal loads, have to be designed with rigid joints. In this manner, the number of expensive connections is reduced and a more economical design is achieved.

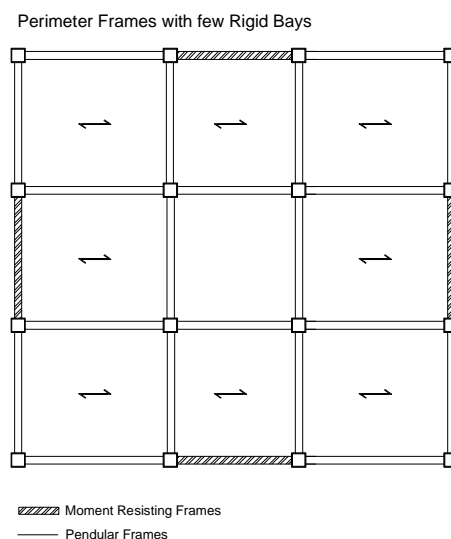


Fig. 2.7 – Spatial Distribution of Perimeter Frames with only few rigid bays

The extension of the concept of perimeter moment resisting frame is the **Perimeter Moment Resisting Frame with only few Rigid Bays** (Fig. 2.7). In this

structural typology only few bays of the exterior frames are called to withstand the seismic action, while the other parts of the structure have to carry only the vertical loads. Even though reducing the number of moment resisting connections provides indisputable advantages, the variation of the structural scheme from the space frame to the perimeter frame with only few rigid bays reduces not only the cost, but also the structural redundancy.

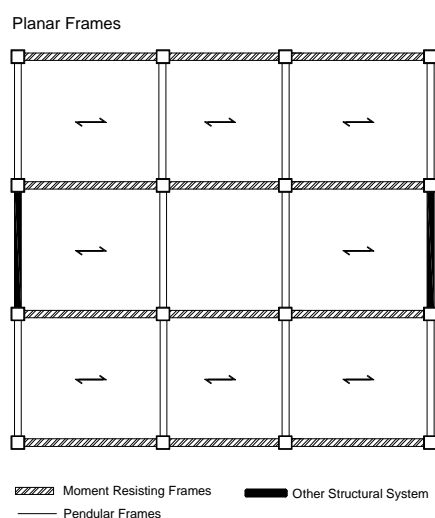


Fig. 2.8 – Spatial Distribution of Planar Frames

This aspect has been object of discussion in the past, and in particular in the aftermath of Northridge earthquake (Song & Wen, 2000). In fact, a large percentage of structure that was affected by structural damages, especially by the fracture of welds in correspondence of girder-to-column joints, was realized with perimeter frames and only few rigid bays. The reasons of such an unsatisfactory behavior have to be searched in the reduction of the number of

dissipative zones which consequently increases the ductility demand in the dissipative zones, i.e. the plastic hinges.

In case of **Planar frames**, moment resisting structures are used to resist to lateral forces only in one of the main directions of the building whilst, out of the plane of MRFs other seismic resistant organisms are used to adsorb the seismic action. These structural typologies are frequently used when, for architectural reasons, it is not possible to dispose braced frames on all the facades of the building (Fig. 2.8).

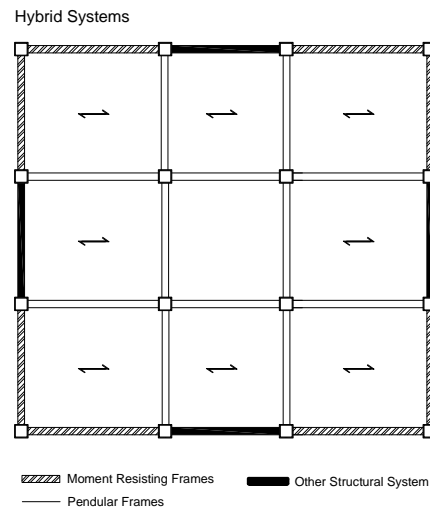


Fig. 2.9 – Spatial Distribution of Hybrid Systems

Hybrid systems are defined by the coupling of MRFs with other structural elements, such as reinforced concrete core or walls, infill panels or steel walls (Fig. 2.9). In the first case the support to vertical loads is mainly provided by MRFs and the resistance to the lateral loads is given in part by the core or the

walls and in part by the frames. The response of dual systems depends on the relative stiffness of the seismic resisting elements. If the shear resistance provided by the frame is greater than the 50% of the total shear resistance the system is called “frame-equivalent dual system” conversely, if the greater contribute to the resistance for lateral loads is given by the reinforced concrete elements it is called “wall/core-equivalent dual system”.

When MRFs are coupled with infill panels, the infills which usually are designed as secondary elements and thus separated from the steel frames, are rigidly connected to the beams and the columns, stiffening the structure with respect to the lateral loads. It is obvious that in this case the designer has to take particular care of the connection between the infill and the structure, avoiding the slippage of the two parts. Finally, MRFs can be coupled to Steel shear walls. These are usually designed to dissipate the seismic input energy by means of cyclic inelastic deformations. Compared to RC walls, steel walls are definitely much lighter, providing advantages to the load-carrying system and to the foundations, quick to erect, if field bolted/shop welded connections are adopted, with low architectural impact and more cost/effective since are faster to construct.

2.1.2 The Connection Typologies

MRFs can be classified according to the detail applied to fasten the girder to the column in **riveted, welded and bolted**. In ordinary practice, before the 20's, steel structures were built exclusively assembling girders and columns by means of **riveted joints** (Fig. 2.10).



Fig. 2.10 – Rivets and High Strength Bolts

The rivet is a mechanical fastener that consists, before the installation, of a shaft with a head only on one end. Typically, rivets are positioned in pre-drilled holes and the termination of the shaft without the head is mechanically deformed to about 1.5 times the original diameter. As a consequence, a connection which can sustain both shear and tension loads is obtained. The installation of rivets, in past was made manually by means of a hammer and more recently by means of pneumatic machines. Noteworthy examples of totally riveted structures are built worldwide as, for instance, the “Eiffel Tower” in Paris or the bridge “Dom Luis I” in Oporto (Fig. 2.11).

Between the 1920s and 1950s the introduction of **High Strength Bolts** represented a significant innovation. High strength bolts allowed to fasten plates through high contact pressures, leading to the development of the so-called slip resistant joints. In this type of connections the force transfer is achieved by means of the friction exploited between two clamped surfaces. The adoption of High Strength bolts allowed significant time-savings associated with the ease of installation due to threads and washers. Besides, the adoption of this system favorite the realization of smaller connections,

reducing simultaneously deformability of frames under lateral loads caused by bolt-holes gaps.



Fig. 2.11 - Examples of riveted structures

At the same time, during the 20's, the use of welding was becoming popular in the mechanical industry due to the introduction of advanced techniques, such as the automatic welding, in which the weld was made by means of the continuous fusion of an electrode wire, or the shielded metal arc welding. Up to the 50's welds have been applied only in the fabrication process of electric motors or mechanical equipment. Starting from the 60's, with the refinement of the welding procedures and the reduction of the cost of the welding process, such a technique has also been applied to steel structures, allowing to join

girders and columns only by the melting of the two parts and by adding a filler material (SAC, 2000c).

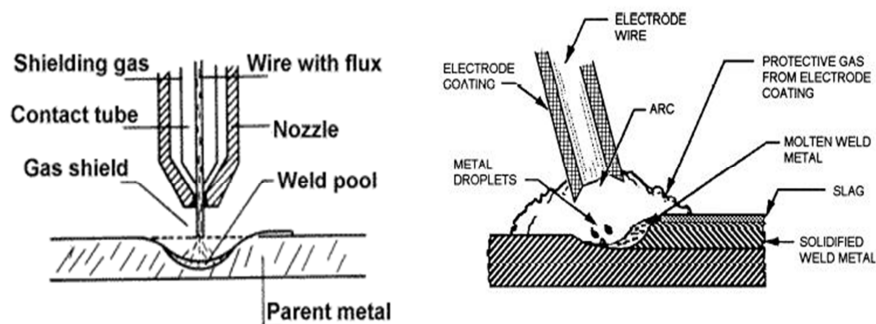


Fig. 2.12 – On the left: FCAW welding technique; On the right: SMAW welding technique

Firstly, welds have been used to absorb exclusively shear actions, connecting only the web of beams to the columns, but successively welded details have also been applied to connect flanges, allowing to easily obtain “fully-restrained joints” and, as a consequence to reduce moments and deflections of girders as well as to enhance the lateral stiffness of frames. The reasons of the widespread use of welded joints in steel structures built in United States and Japan during the period from 1960 to 1990 have to be mainly searched in the relative cost of welded and bolted connections. Besides, the possibility of joining members avoiding the use of rivets, bolts, plates and structural sections was positively considered by engineers of the time. In the 1970, typical connection adopted in U.S. Welded Special Moment resisting Frames (WSMF) was realized by bolting the beam web to a shear tab and welding the flanges. According to reports of the “Steel Committee of California” referred to years

1979, 1983 and 1986 this joint typology was the less expensive (Table 2.1), with a cost of approximately one half compared to fully bolted connection (SAC, 2000c).

Table 2.1. *Relative Costs of Moment Connections (Source: Steel Committee of California)*

Beam Flange Connection	Beam Web Connection	Relative Cost		
		1979	1983	1986
Full Penetration Field weld	Bolted to shear tab	1.00	1.00	1.00
Full Penetration Field weld	Fillet welded to shear tab	1.07	1.07	1.07
Full Penetration Field weld	Full penetration weld to column	1.25	1.18	1.25
Bolted flange plate (Shop welded to column)	Bolted to shear tab	2.00	1.75	2.00

Notwithstanding the significant advantages provided by the adoption of welded connections, in last years, after the earthquakes of Northridge and Kobe, the adoption of welded details in MRFs has been subject of discussions and strongly reconsidered. In fact, in both the seismic events, several Perimeter and Space Moment Resisting Steel Frames experienced damages due to the unexpected failure of welded connections. Different reasons have been individuated to explain the unsatisfactory behavior of Northridge and Kobe welded joints, above all the welding techniques of that time have been harshly criticized.

During the 1970s, in U.S.A., the self-shielded flux-core process (FCAW-SS) was recognized to be faster and less expensive compared to the shielded metal arc welding (SMAW) which had been used up to that time. Indeed,

several cost analysis of the time showed that the total cost of FCAW-SS was at least one third compared to SMAW. As a consequence, in the period from 1960 to 1990, the greatest part of full penetration field welded connections of MRFs was made applying self-shielded flux core technique (Fig. 2.12).



Fig. 2.13 – Failure of beam-to-column fillet welded connection (Kobe Earthquake)

Despite economic aspects post-Northridge inspections pointed out that a great part of the welded connections realized applying FCAW-SS, especially of the 80's, had been made melting the electrode E70T-4 whose notch toughness was not certified by the producers. Indeed, post-Northridge studies have demonstrated that the unfortunately famous detail realized applying FCAW-SS and E70T-4 electrode, now known with the name of “Pre-Northridge

connection”, exhibited during the seismic event a low-ductile behavior which led to the numerous cases of failure (SAC, 2000c).

After the seismic events of Northridge the role of welded joints has been reevaluated and the costly but reliable bolted connections have been reconsidered as an effective alternative to the low ductile and brittle “Pre-Northridge” field welded girder-to-column joints (Fig. 2.13).

2.1.3 Ductility Class



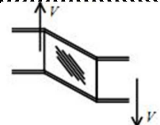
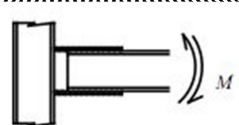
As mentioned before, aiming to obtain a cost/effective structural design, in modern practice, structures are required to be designed so that under severe ground motions, a certain amount of plasticization is allowed. In case of MRFs, international codes provide that the earthquake input energy has to be dissipated through the plastic engagement of some specific zones, i.e. the plastic hinges, located, on the base of the adopted design approach, at beam ends, in connections, in panel zones or in column ends. In the framework of capacity design, dissipative zones have to be designed to possess adequate stiffness, strength and rotational capacity with reference to the internal actions due to the lateral forces provided by the code. Conversely, the other structural elements, namely non-dissipative zones, have to be designed to remain in elastic range for the actions corresponding to the attainment of the full plasticization of the dissipative zones.


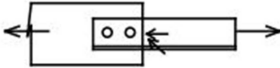
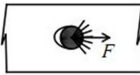
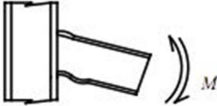
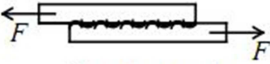

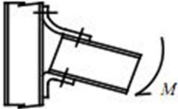
As far as classical design approach of MRFs is considered, dissipative zones have to be located at the beam ends whilst the other structural parts, i.e. the connections, the panel zones and the columns have to be designed to possess adequate overstrength compared to the maximum actions transferred

by the fully developed plastic hinges. In particular, connections and panel zones are required to possess a flexural strength greater than the maximum bending resistance of the fully yielded and strain-hardened beam ends and columns design have to be carried out satisfying the so-called strong column-weak beam requirements.

Dealing with the definition of dissipative and non-dissipative mechanisms, it is useful to note that inelasticity in steel structures can arise from different mechanisms, such as the yielding of steel due to the bending of beams or connections, the shear plasticization of panel zones and the friction due to the slippage of plates. Conversely, some examples of non-dissipative mechanisms are local buckling of members and/or of plates, yielding of low ductile materials, such as the steel of high strength bolts, and the plastic engagement of welds, which have been discovered to possess, in light of recent seismic events, low dissipation capacities. Aiming to obtain ductile structures, non-dissipative mechanisms have to be absolutely avoided and the brittle elements have to be over-strengthened with respect to the maximum actions associated with the development of the inelastic mechanisms (Table 2.2).

Table 2.2. Dissipative and non-dissipative mechanisms in steel structures

Dissipative mechanisms	Non-Dissipative mechanisms
	
Steel Yielding	Bolts in Tension
	

Dissipative mechanisms	Non-Dissipative mechanisms
Yielding of Panel Zones	
	
Plastic Hinge at Beam Ends	Plasticization in small regions Requires high Ductility Demand
	
Bearing of Bolts	Local Buckling of members
	
Slippage of plates	Failure of welds
	
Inelastic Behavior of the connecting elements	

From the above considerations, it is evident that structural local and global ductility play a role of paramount importance in current design approach. In fact, the plasticization of the dissipative zones elongates the period of vibration of the structure and increases the amount of hysteretic damping, resulting in a reduction of the seismic forces developed (Astaneh-Asl, 1995). In general, with the term local and global ductility it is intended the capacity of a structural element or of a structural system to withstand deformation in inelastic range

without significant loss of resistance. In case of MRFs, global ductility assumes the meaning of ratio between the ultimate top sway displacement, accounting for second order effects, and the top sway displacement evaluated in correspondence of the elastic limit. Moreover, the definition of local ductility of MRFs is concerned with the rotational capacity of the plastic hinges, i.e. of beam ends and/or of joints (Mazzolani & Piluso, 1996).

As a result of the importance in current approach of the ductility supply, international codes provide a classification of structures with reference to their capacity of resisting deformations in plastic field. In Eurocode 8 (CEN, 2005c) and AISC 2005 (AISC, 2005), MRFs can be designed to be less or more ductile, according to the three following categories:

- **EC8:** Ductility Class Low (DCL), **AISC 2005:** Ordinary Moment Frames (OMF);
- **EC8:** Ductility Class Medium (DCM), **AISC 2005:** Intermediate Moment Frames (IMF);
- **EC8:** Ductility Class High (DCH), **AISC 2005:** Special Moment Frames (SMF);

In both European and U.S. codes, provided that some requirements on strength and ductility supply are satisfied, yielding is allowed to occur either in beam, panel zone or connections. The formation of plastic hinges in columns is prohibited, made exception for base plates, column ends at the top of multi-storey frames, and in case of single storey MRFs.

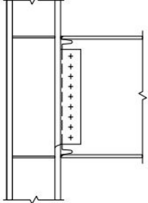

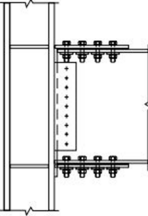
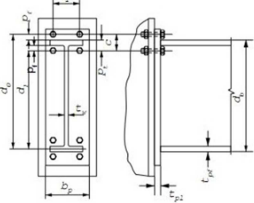
EC8, in general, favorites a design of MRFs which provides the development of plastic hinges at beam ends rather than in other zones. Dissipation in beam-to-

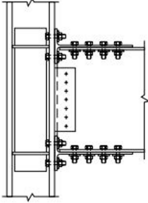
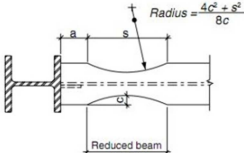
column joints is allowed but strongly limited in everyday practice. In fact, when the weak connection-strong column-strong beam design philosophy is adopted, the ductility supply and strength of connections have to be certified by experimental evidence, providing cyclic tests of joints.

AISC 2005 also favors design of MRFs which provide the formation of plastic hinges at beam ends, but still offers the possibility to dissipate an amount of seismic input energy by the inelasticity of joints. In particular, AISC 2005 requires that both in case of full-strength and partial strength joints a “conformance demonstration” of the cyclic behavior of beam-to-column connections adopted in the Seismic Load Resisting System (SLRS) is provided by the designer. As a result, connections have to be pre-qualified in order to satisfy code requirements in terms of plastic rotation supply and flexural/shear strength, compatibly with the ductility class of the designed MRF. Therefore, designers have two alternatives: the adoption of prequalified joints or the qualification of specific details. In the former case, joints whose cyclic characteristic have already been qualified, such as the prequalified connections contained in document FEMA 350, are used. In the latter case, joint dissipative characteristics have to be demonstrated to be adequate by means of the qualification procedures contained in AISC 2005.

In reason of the desired global ductility supply, both Eurocode 8 and AISC 2005 provide some requirements regarding inelastic capacities of the dissipative zones. The idea is that, in case of DCH/SMF, the structural system is designed to behave in ductile manner when subjected to a severe seismic event. Thus, brittle mechanisms and buckling are avoided and dissipation is reached by means of inelastic behavior of plastic hinges (Table 2.3).

Table 2.3. Examples of pre-qualified Joint - Source: (SAC, 2000a)

Joint typology	Maximum Ductility Class	
	AISC 2005	European Classification
<p>Welded Unreinforced Flanges – Bolted Web Connections</p> 	OMF	DCL
<p>Welded Unreinforced Flanges – Welded Web Connections</p> 	SMF	DCH
<p>Bolted Flange Plate Connections</p> 	SMF	DCH
<p>Bolted End Plate Connections</p> 	SMF	DCH

Joint typology	Maximum Ductility Class	
	AISC 2005	European Classification
Double Split Tee Connections 	SMF	DCH
Reduced Beam Section Connections 	SMF	DCH

In particular, in AISC 2005 and EC8, connections are required to sustain an interstorey drift angle of 40 mrad and of 35 mrad respectively. In case of DCL/OMF, MRFs are expected to exhibit a low dissipative behavior and connections are not required to possess specific plastic rotation supply (Table 2.4).

Table 2.4. Required Ductility of Connections – EC8 vs AISC 2005

Eurocode 8		AISC 2005	
Ductility Class	Rotational Capacity [mrad]	Ductility Class	Rotational Capacity [mrad]
Ductility Class High	35	Special Moment Frame	40
Ductility Class Medium	25	Intermediate Moment Frame	20
Ductility Class Low	-	Ordinary Moment Frame	-

In case of DCM/IMF the behavior is expected to be intermediate between high and low dissipative and, according to EC8 and AISC 2005, connections are required to sustain rotations of 25 and 20 *mrad*.

2.1.4 Stiffness and Strength of Joints

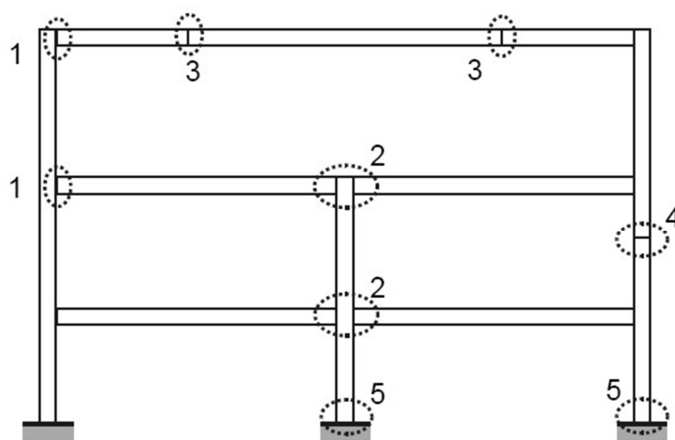


Fig. 2.14 – Structural Joints Configuration (CEN, 2005)

Structural joints are typically classified according to their geometry, stiffness and resistance. With reference to the geometric characteristics, (CEN, 2005b) individuate the following categories (Fig. 2.14):

1. single sided Beam-to-Column Joints;
2. double sided Beam-to-Column Joints;
3. beam splices;
4. column splices;
5. base plate joints.

Usually the words “joint” and “connection” are used likewise to individuate the region of intersection between the beam and the column. In general, with the term “connection” is usually intended the zone where the mechanical devices (bolts, plates, welds etc.), used to join the beam to the column, are located.

With the term “panel zone” is indicated the region of the column web contained within the flanges of the connected beam (Fig. 2.15). The region which includes beam-to-column connections and panel zone is called in technical literature with the word “joint” (Mazzolani & Piluso, 1996; Nethercot & Zandonini, 1990; Kirby et al., 1990; Faella et al., 2000).

Structural response of MRFs strongly depends on the behaviour of its connections. In fact, stiffness and strength of joints deeply affect dynamic properties of frames and their post-elastic behaviour. Furthermore, also the internal actions arising in the structure, both due to Serviceability and Ultimate loads, depend on the elastic and post-elastic stiffness of the connecting elements.

It is well known in technical literature that the actual flexural behaviour of a joint can be considered as intermediate between the two extreme conditions of infinitely rigid or infinitely deformable.

When the elements composing the connection, i.e. the plates, the bolts and the panel zone, are sufficiently stiff and no relative rotation between the beam and the column occurs, in design practice, the joint is usually modelled as a clamp. Conversely, when the beam is free to rotate with respect to the connected elements, the joint is usually considered as a pin. In all the other cases, i.e. when the connecting elements are neither adequately rigid to allow to model

the connection as a clamp nor so deformable to consider the beam free to rotate, the beam-to-column joint is defined semi-rigid. In general, all beam-to-column connections are semi-rigid and should be modelled properly, considering their actual relationship between the bending moment and the rotation (Fig. 2.16).

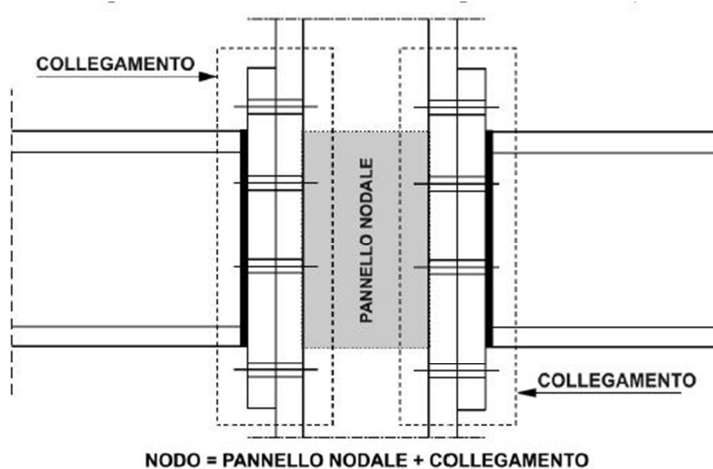


Fig. 2.15 – Distinction between Connection and Panel zone

Moreover, a joint can be classified as full-strength, pinned or partial strength on the base of the relative resistance of the joint and of the connected beam. If the flexural strength of the joint is greater than the bending resistance of the beam, the connection is defined “full-strength”. Conversely, if the joint is completely incapable to withstand bending, connection is usually called “pinned”, meaning that it is only capable to transfer shear actions. In all the other cases, i.e. when the joint flexural resistance is minor than the bending strength of beam, connection is defined “partial strength”. From the standpoint

of the location of dissipative zones, different behaviors are obviously expected if full strength or partial strength connections are adopted.

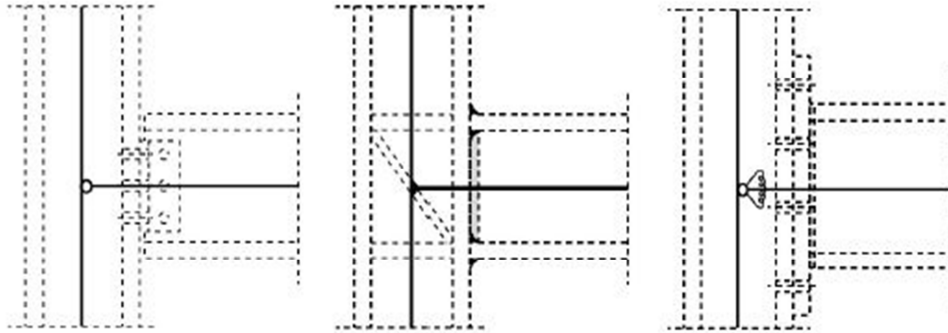


Fig. 2.16 – Pinned, Continuous and Semi-continuous joints

Basically, three cases can be individuated depending on the relative resistance of beams and joints:

- plastic resistance of the beam lower than the ultimate bending resistance of the connection;
- plastic resistance of the beam greater than the ultimate bending resistance of the connection;
- plastic resistance of the beam and ultimate bending resistance of the connection balanced.

In the first case, the beam-connection overall behavior can be effectively represented with an elastic-plastic model. A plastic hinge will probably develop on the beam, while the connection will contribute only by means of its elastic stiffness. In the second case, the opposite situation will develop.

Dissipative zone is located in the connection and the overall structural behavior at ULS is influenced by joints inelastic behavior. In this case, an accurate representation of the connections moment-rotation curve is needed. In the third case, joint and beam bending strength is balanced and, as a consequence, both the elements will be engaged in plastic range under a severe seismic event, so as to the dissipation of the earthquake input energy will be relied on the inelastic behavior either of the beam and of the connection.

Within this framework, it is easy to understand that the design of connections plays a role of fundamental importance in the seismic design of MRFs. In fact, design of joints can be lead aiming to obtain different values of stiffness, strength and rotational capacity on the base of the desired overall structural behavior. As an example, if the design is aimed to obtain a weak beam-strong column – strong joint structural behavior, joints will be designed to be full strength and rigid. So that, thick plates, reinforcing ribs, doubler and continuity plates will be probably adopted to exclude from the dissipative mechanisms panel zones and connecting elements. Conversely, if the design is aimed to obtain a weak connection-strong beam-strong column behavior, joints will be designed to be partial strength and the rotational capacity of the connecting elements will have to be carefully evaluated.

It is clear from the above considerations that detailing of joint plays a role of fundamental importance within MRFs overall structural behaviour. In fact, joints ultimate behaviour can be completely modified by strengthening some elements rather than others, governing the failure mode by means of simple modifications of the joint detail.

In conclusion, as will be shown later, on the base of the classification of joints according to strength and stiffness, the following typologies of MRFs can be individuated:

- frames with full-strength rigid connections;
- frames with full-strength semi-rigid connections;
- frames with partial-strength rigid connections;
- frames with partial-strength semi-rigid connections.

2.2 Frames and Joints Classification

Classification of joints and frames are strictly related. As discussed earlier, the overall structural response of MRFs is strongly influenced by joints strength, stiffness and rotational capacity. In fact, the distribution of the internal actions, the structural ductility, the susceptibility to second order effects and the location of the plastic zones are all parameters which are influenced by the existing relationship between the bending moment and the joint rotation.

Last version of Eurocode 3 (CEN, 2005a) classifies MRFs according to the following two characteristics:

- the susceptibility to second order effects;
- the presence of a bracing system.

On the base of the first feature MRFs are divided in sway and non-sway. A frame is defined non-sway if its lateral displacements are small enough to retain that the internal actions due to the deformability of the frame are negligible. Conversely, a frame is called sway if the deformed geometry leads to a substantial increase of the internal actions or modify significantly the structural behavior. According to (CEN, 2005a) a frame can be considered to be non-sway if the following relationship are satisfied:

- $\alpha_{cr} = \frac{F_{cr}}{F_{Ed}} > 10$ for elastic analysis;
- $\alpha_{cr} = \frac{F_{cr}}{F_{Ed}} > 15$ for plastic analysis;

where α_{cr} is the factor by which the design loading would have to be increased to cause elastic instability in a global mode, F_{cr} is the elastic critical buckling load for global instability mode based on initial elastic stiffnesses and F_{Ed} is the design loading on the structure. In all the other cases frames have to be classified as sway.

Moreover, frames are divided in braced or unbraced. In the first case MRFs are stiffened by specific elements which reduce the lateral displacement of at least the 80%, in the second case frames are defined unbraced. A further classification of MRFs, depending on the joints characteristics, is provided by (CEN, 2005b), where frames are categorized in:

- **simple:** joints do not transmit bending moment to the column;
- **continuous:** the behavior of the joint may be assumed rigid;
- **semi-continuous:** the behavior of the joint has to be taken into account by adopting proper models.

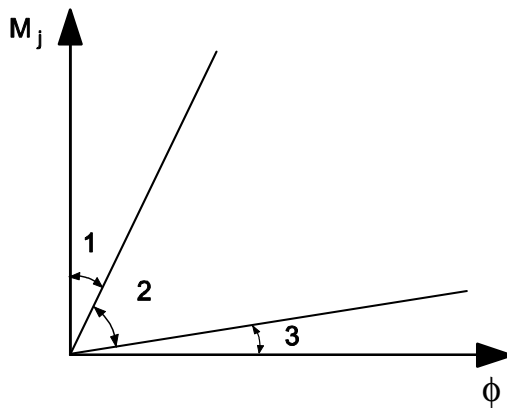
In the first case, joints are able to transfer to the columns only shear and beams are free to rotate, as a consequence the obtained structural system is pendular and joints can be faithfully modeled by means of hinges. In the second case, joints behavior is rigid and their resistance is greater than the flexural strength of the connected beam, so that connections can be structurally represented by means of clamps. In the case of semi-continuous frames, joints are intermediate between the extreme situation of pinned and rigid-full strength, so that their structural behavior has to be properly accounted for by means of accurate models representing the actual moment-rotation curve.

Aiming to individuate quantitatively the boundaries between rigid, semi-rigid and pinned behavior, (CEN, 2005b) introduces the following two parameters:

- $S_b = \frac{EI_b}{L_b}$
- $S_c = \frac{EI_c}{L_c}$

where S_b is the bending stiffness of the beam, S_c is the bending stiffness of the column, E is the steel elastic modulus, I_b and I_c are the beam and column inertia modulus, L_b and L_c are the beam and column lengths. Eurocode boundaries are determined by defining “rigid” a joint whose stiffness do not reduce by more than the 5% the Euler buckling load of the structure with full rigid attachments. On the base of the so-called “5% criterion” the following classifications derive:

BEAM-TO-COLUMN JOINTS



Zone 1: rigid, if $S_{j,ini} \geq k_b E I_b / L_b$

where

(BRACED FRAMES)

$k_b = 8$ for frames where the bracing system reduces the horizontal displacement by at least 80 %

(UNBRACED FRAMES)

$k_b = 25$ for other frames, provided that in every storey $K_b/K_c \geq 0,1$ *)

Zone 2: semi-rigid

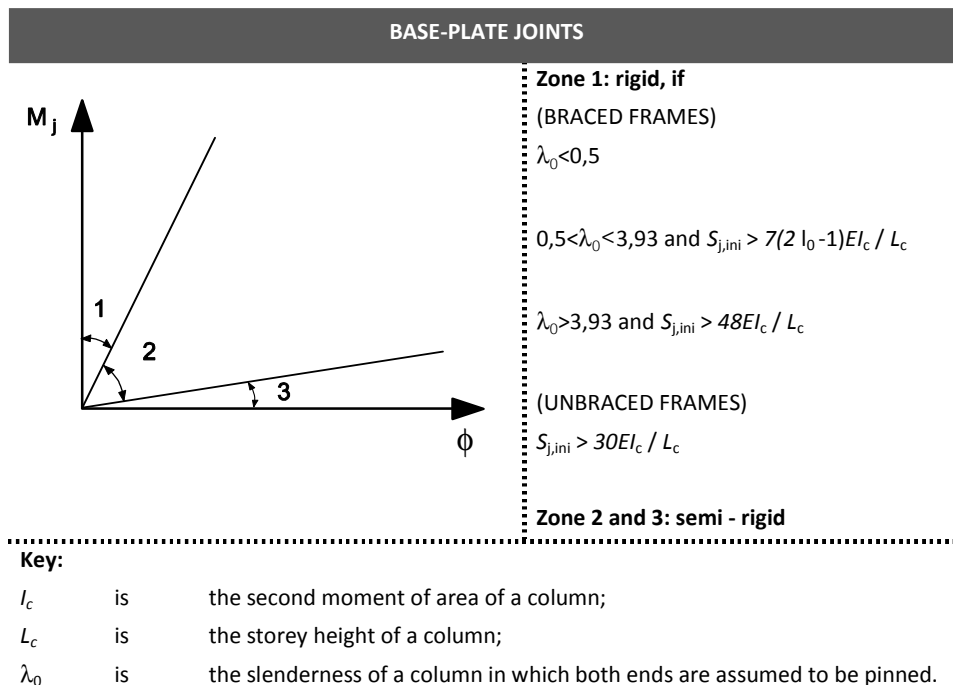
All joints in zone 2 should be classified as semi-rigid. Joints in zones 1 or 3 may optionally also be treated as semi-rigid.

Zone 3: nominally pinned, if $S_{j,ini} \leq 0,5 E I_b / L_b$

*) For frames where $K_b/K_c < 0,1$ the joints should be classified as semi-rigid.

Key:

K_b	is	the mean value of I_b/L_b for all the beams at the top of that storey;
K_c	is	the mean value of I_c/L_c for all the columns in that storey;
I_b	is	the second moment of area of a beam;
I_c	is	the second moment of area of a column;
L_b	is	the span of a beam (centre-to-centre of columns);
L_c	is	the storey height of a column.



Furthermore, as previously underlined, (CEN, 2005b; Jaspert, 2002) provides a classification of joints on the base of the resistance, individuating full strength, partial strength and nominally pinned joints. Such a classification is obtained comparing joint and connected beam/column flexural resistance:

- full strength joints: $M_{b,pl,Rd} < M_{j,Rd}$;
- partial strength joints: $0,25M_{b,pl,Rd} < M_{j,Rd} < M_{b,pl,Rd}$;
- nominally pinned joints: $M_{j,Rd} < 0,25M_{b,pl,Rd}$.

where $M_{j,Rd}$ and $M_{b,pl,Rd}$ are the joint and beam plastic moment resistance respectively.

Dealing with rotational capacity, a further classification of connections has been proposed by (Jaspart, 2002). The author suggests to categorize connections in:

- ductile;
- semi-ductile;
- brittle;
- pinned.

Joints are defined ductile if their plastic rotation supply is adequate to allow a sufficient redistribution of the internal actions. As a result, ductile connections are suitable for plastic frame analysis. Conversely, connections are defined brittle if their post-elastic capacity is so limited to retain that no redistribution of the internal actions is allowed. Semi-ductile joints behave in an intermediate way between ductile and brittle. Moreover, as mentioned before, nominally pinned connections are designed to transfer only shear to the columns, but a check of the connection rotational capacity has to be provided. In fact, pinned joints should be designed to possess sufficient rotation capacity to sustain the imposed rotations.

The quantification of the boundaries between the three individuated behaviors can derive only by a preliminary comparison between the required and available ductility. In addition, up to now, few studies have been devoted to the valuation of the ductility supply of joints. Indeed, the lack of experimental studies on this topic is negatively reflected on (CEN, 2005b) where few

indications for the assessment of the rotation capacity of welded and bolted joints are given.

As far as the method of analysis is elastic, elastic-plastic or rigid-plastic, joints modeling and classification are different. If an elastic analysis of the frame is performed, internal actions and deflections are only influenced by connections rotational stiffness and, as a consequence, the joints have to be classified as pinned, semi-rigid or rigid (Table 2.5).

Table 2.5. Joint Classification

Method of global analysis	Classification of joint		
	Nominally pinned	Rigid	Semi-rigid
Elastic	Nominally pinned	Rigid	Semi-rigid
Rigid-Plastic	Nominally pinned	Full-strength	Partial-strength
Elastic-Plastic	Nominally pinned	Rigid and full-strength	Semi-rigid and full-strength Rigid and partial-strength
Type of joint model	Simple	Continuous	Semi-continuous

If a rigid-plastic analysis is lead, the only parameter which plays a role on the overall response is the connection bending resistance and, as a result, joints can be classified as full-strength, partial strength or pinned. When an elastic-plastic analysis is considered both initial stiffness and flexural resistance have to be accounted for and a classification according to both parameters is needed. In conclusion, on the base of stiffness and strength the following categories can be individuated:

- full-strength rigid connections;
- full-strength semi-rigid connections;
- partial-strength rigid connections;
- partial-strength semi-rigid connections;
- pinned connections.

2.3 The Component Method

Since 1994 the Commission of the European Communities has introduced in Eurocode 3, within its Annex J, the so-called component method. Such a method provides the general rules to obtain a mechanical model able to predict initial stiffness and plastic resistance of joints. Its validity has been verified in last fifteen years with particular reference to steel joints, but in recent times it has been indicated as a general tool for the prediction of the characteristic of any kind of joint, even made of materials different from steel. Indeed, the application of the component method has been recently extended to joints of composite structures and base plate joints. In addition, some preliminary attempts to apply component method also to timber and precast structures have been made. Substantially, it is in mind of the European scientific community to develop a unified approach for the study of structural connections whatever the material and the joint configuration.

The component method is mainly based on the following steps:

- identification of the source of strength and stiffness of the joint;
- mechanical modeling of the components;
- assembly of the components;
- classification.

In the first step a set of basic components, characterizing the strength and stiffness of the connection is individuated and the joint, intended as a whole, is decomposed in different components characterizing its moment-rotation behavior. Then, each component is modelled and its mechanical properties

are determined, i.e. stiffness, strength and deformation capacity. This procedure of characterization is made essentially by means of experimental tests, finite element modelling, numerical simulations and analytical modelling. In the third step, all the components are combined to provide a prediction of the whole joint moment-rotation relationship. Finally, as above shown, joints are properly classified in terms of resistance, stiffness and rotational capacity. The main goal of the classification procedure is to simplify, if possible, the joint modelling within the structural analysis, for example by representing in case of fully “rigid” or “deformable” connections the joints with a clamp or a hinge (Bijlaard, 2004).

Within the framework of (CEN, 2005b), up to now, the application of the component method to structural connections is still limited to a narrow range of cases. In fact, only connections between H- or I- sections hot-rolled or shop-welded profiles are available. In particular, the following joint typologies are concerned:

- welded joints;
- bolted end-plate connections;
- bolted flange cleated joints;
- base plate connections;
- minor axis joints where the beam is connected to the web of a H- or I-section;
- steel-concrete composite joints;
- joints with beam haunches.

The prediction of stiffness and strength of such a types of connections is obtained by the assemblage of different joint components properly modelled.

For each joint component, (CEN, 2005b) provides the rules to calculate the plastic resistance and the initial stiffness. The following components are considered in (CEN, 2005b):

- column web panel in shear;
- column web in transverse compression;
- column web in transverse tension;
- column flange in bending;
- end-plate in bending;
- flange cleat in bending;
- beam or column flange and web in compression;
- beam web in tension;
- plate in tension or compression;
- bolts in tension;
- bolts in shear;
- bolts in bearing;
- concrete in compression including grout;
- base plate in bending under compression;
- base plate in bending under tension;
- anchor bolts in tension;
- anchor bolts in shear;
- anchor bolts in bearing;
- welds;
- haunched beam.

Dealing with a major axis welded beam-to-column connection, following the steps previously highlighted, an example of application of the component method codified in (CEN, 2005b), can be provided.

First of all the main sources of deformability and strength of the connection have to be individuated. Such sources can be chosen from the components modelled by (CEN, 2005b):

- column web panel in shear (*cws*);
- column web in transverse tension (*cwt*);
- column web in transverse compression (*cwc*);
- column flange in bending (*cfb*);
- beam flange and web in compression (*bffc*);
- welds (*w*).

As it is possible to realize from Fig. 2.17, some components are either source of stiffness and strength and, therefore, are represented by an elastic-plastic model. Conversely, other components provide only a limitation to the joint flexural resistance and, as a consequence, can be modelled by a simple rigid-plastic model. In fact, in case of welded connections, panel zone in shear and panels in tension and compression govern the joint response both in terms of stiffness and strength, whilst the column flange in bending, the welds and the beam flange and web in compression provide only a limitation to the bending resistance, not contributing to the overall response in terms of stiffness.

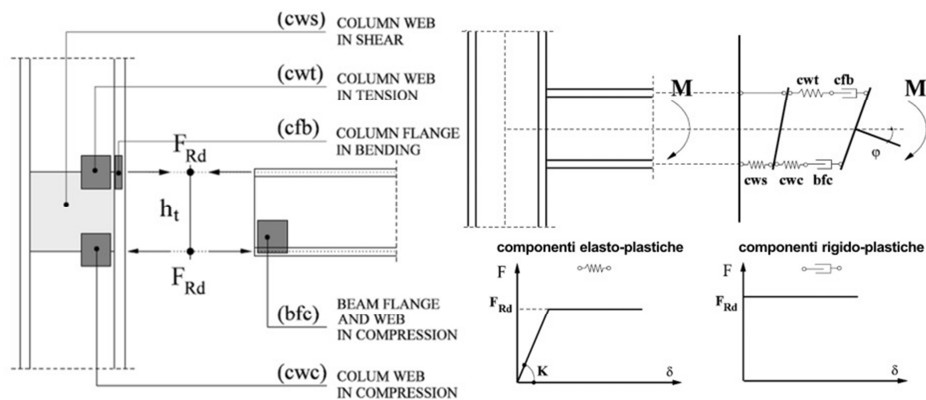
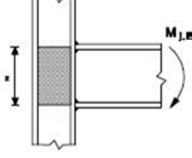
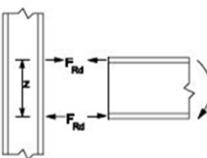
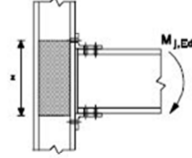
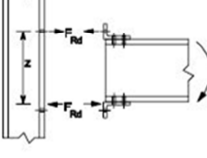
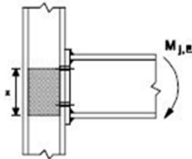
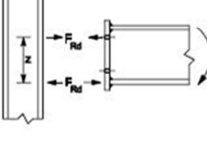
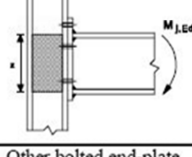
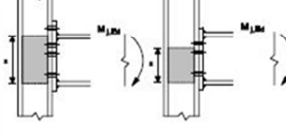


Fig. 2.17 – Modeling of a welded joint with the component method

Through the formulations given in (CEN, 2005b) is then possible to define the values of strength and stiffness of each joint component. Finally, by means of the assemblage procedure, the whole joint stiffness and resistance are determined.

Table 2.6. Definition of the lever arm

Type of connection	Centre of compression	Lever arm	Force distributions
a) Welded connection 	In line with the mid-thickness of the compression flange	$z = h - t_{fb}$ h is the depth of the connected beam t_{fb} is the thickness of the beam flange	
b) Bolted connection with angle flange cleats 	In line with the mid-thickness of the leg of the angle cleat on the compression flange	Distance from the centre of compression to the bolt-row in tension	
c) Bolted end-plate connection with only one bolt-row active in tension 	In line with the mid-thickness of the compression flange	Distance from the centre of compression to the bolt-row in tension	
d) Bolted extended end-plate connection with only two bolt-rows active in tension 	In line with the mid-thickness of the compression flange	Conservatively z may be taken as the distance from the centre of compression to a point midway between these two bolt-rows	
e) Other bolted end-plate connections with two or more bolt-rows in tension 	In line with the mid-thickness of the compression flange	An approximate value may be obtained by taking the distance from the centre of compression to a point midway between the farthest two bolt-rows in tension	A more accurate value may be determined by taking the lever arm z as equal to z_{eq} obtained using the method given in 6.3.3.1.

As the mechanical model depicted in Fig. 2.17 is concerned, in hypothesis of pure bending and centre of compression located in correspondence of the mid-thickness of the beam compression flange, the joint resistance is governed by the resistance of the weakest component:

$$F_{Rd} = \min\{F_{cws,Rd}; F_{cwt,Rd}; F_{cwc,Rd}; F_{cfb,Rd}; F_{bfwc,Rd}\} \quad (2.1)$$

where F_{Rd} is the component minimum resistance and the terms in curly brackets are respectively the resistances of the column web in shear (*cws*), column web in tension (*cwt*), column web in compression (*cwc*), column flange in bending (*cfb*), beam flange and web in compression (*bfwc*).

In general, the height of the lever arm depends on the joint typology (Table 2.6). In case of welded connections the lever arm corresponds to the beam depth minus the thickness of the beam flange. As a consequence, the joint flexural resistance can be determined as follows:

$$M_{j,Rd} = F_{Rd}Z \quad (2.2)$$

where $M_{j,Rd}$ is the joint flexural resistance, and z is the lever arm. As well as strength, stiffness can be determined starting from the flexibilities of the basic components, obtaining:

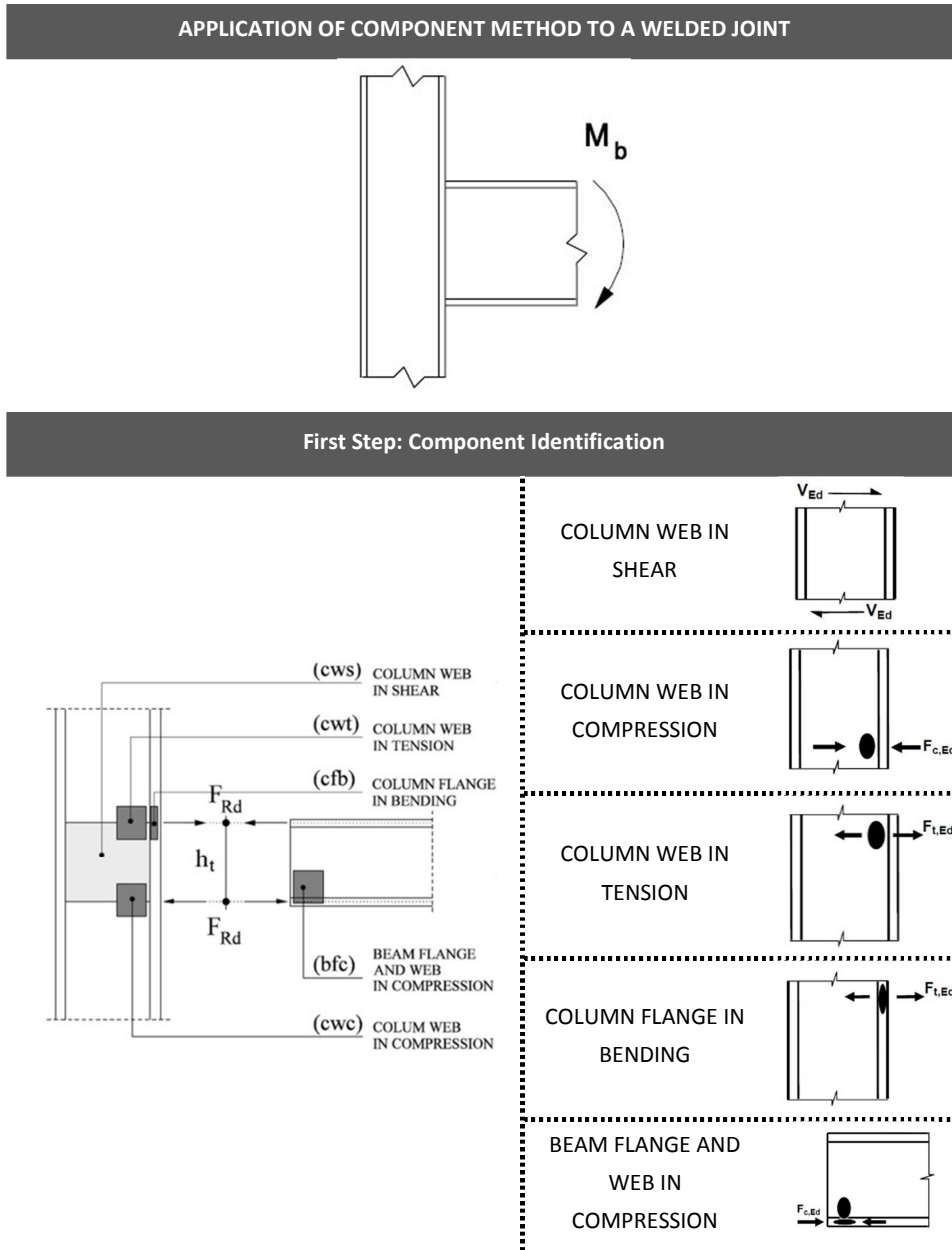
$$S_{j,ini} = \frac{EZ^2}{\sum_i \frac{1}{k_i}} \quad (2.3)$$

where $S_{j,ini}$ is the elastic stiffness, E is the steel Young modulus and k_i is the stiffness of the i -th basic component contributing to the bending stiffness.

As joint stiffness and resistance have been determined, a classification of the connection can be pointed out on the base of the type of structural analysis. If structural analysis is elastic, joint will be classified as rigid, semi-rigid or pinned; if the considered analysis is rigid-plastic the classification to provide is full-strength, partial strength or pinned; finally, in case of elastic-plastic analysis the cases of rigid-full strength, semi-rigid partial strength, semi-rigid full strength, rigid partial strength and pinned have to be considered.

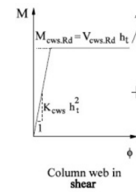
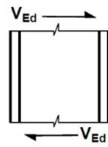
All the steps provided to apply the component method to a welded joint are summarized in Table 2.7.

Table 2.7. Application of Component method to a welded connection

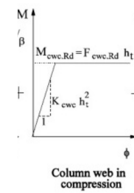
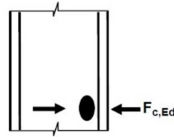


Second Step: Component Mechanical Modeling

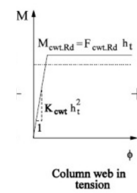
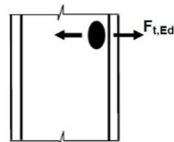
COLUMN WEB IN
SHEAR



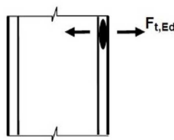
COLUMN WEB IN
COMPRESSION



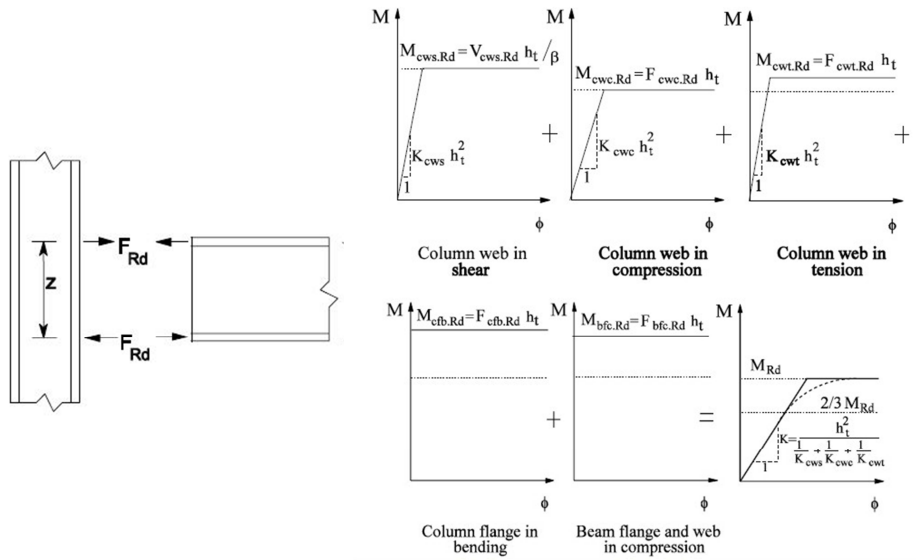
COLUMN WEB IN
TENSION



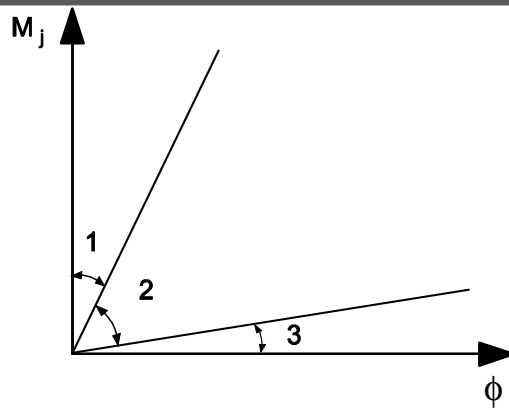
COLUMN FLANGE IN
BENDING



Third Step: Component Assemblage



Final Step: Joint Classification



2.4 The Role of Connections on the Overall Structural Behavior

As already underlined, modern design of seismic resistant buildings requires the individuation of some zones, the so-called dissipative zones, which have to provide, through their plastic engagement, the dissipation of the earthquake input energy. According to most recent codes, dissipative zones can be located either at beam ends, panel zones or in the connecting elements.

It is well known in technical literature that, traditionally, MRFs are designed aiming to promote the development of dissipative zones at beam ends rather than in other elements. To this scope, non-dissipative zones, i.e. connections, panel zones and columns, have to be designed to remain in elastic range for the actions corresponding to the full development of the plastic zones.

In general, dealing with the overstrength that joints have to possess to obtain a full strength design, two effects have to be accounted for: the first one related to the random material variability and the second one associated with the overstrength exhibited by the beam or column due to the strain-hardening (Bennett & Najem-Clarke, 1987; Tucker & Bennett, 1990; Gervasio et al., 2002). This last effect depends mainly on the width-to-thickness ratio of the connected beam/column flange and web. In (Mazzolani & Piluso, 1996), such effect has been modeled by properly calibrating the main parameters involved in the definition of the overstrength factor due to the strain hardening, i.e. the width-to-thickness ratios of the plates composing the beam/column and the bending moment gradient. To this end the following expression has been derived:

$$M_{max} = (s - \rho)M_p \quad (2.4)$$

where M_{max} is the beam/column maximum moment accounting for the strain-hardening effect, M_p is the beam/column plastic moment accounting for the moment-shear interaction effects, ρ is the ratio between the axial load and the squash load ($\rho < 1$; $\rho = 0$ in the case of pure bending) and s is the degree of overstrength given by the following relationship:

$$s = \frac{1}{0.695 + 1.632 \lambda_f^2 + 0.062 \lambda_w^2 - 0.602 \frac{b_f}{L^*}} \leq \frac{f_u}{f_y} \quad (2.5)$$

where the slenderness parameters relative to the plates composing the member section are defined as:

$$\lambda_f = \frac{b_f}{2t_f} \sqrt{\frac{f_y}{E}} \quad \lambda_w = \frac{d_{w,e}}{t_w} \sqrt{\frac{f_y}{E}} \quad (2.6)$$

where b_f and t_f are the flange width and thickness, t_w is the web thickness, $d_{w,e}$ is the compressed part of the web, f_y is the yield stress, f_u is the ultimate stress, E is the steel modulus of elasticity and L^* is the distance between the plastic hinge and the point of zero moment.

Within this framework, in order to obtain full strength joints, the approach suggested by Eurocode 8 is to design the connecting parts of all joints typologies, made exception for full penetration welded connections whose

resistance is assumed to be sufficient, requiring that the following relationship is satisfied:

$$R_d = 1.1\gamma_{ov}R_{fy} \quad (2.7)$$

where R_d is the resistance of the connection as defined in Eurocode 3, R_{fy} is the plastic resistance of the connected dissipative member based on the design yield stress of the material, γ_{ov} is the overstrength factor depending on the ratio between the actual and nominal value of the steel yield strength. In particular, γ_{ov} can be taken equal to 1.00 if the actual strength of the dissipative elements is determined on the base of specific experimental tests, such condition is usually verified when the assessment of an existing building is considered or when steels are taken from specific stocks. In the other situations, even though the overstrength factor should be specified by the national annex, Eurocode 8 recommends the value $\gamma_{ov}=1.25$.

Concerning Eq.(2.7), proposed by Eurocode 8, it is clear that the two coefficients multiplying the plastic resistance of the connected member are introduced to account for the two above said effects: the random variability and the beam or column overstrength. If reference is made to the coefficient related to the strain-hardening, the value 1.1, prescribed by Eurocode 8, is not able to cover all the range of real cases as already demonstrated by (Mazzolani & Piluso, 1996) both for beams ($\rho=0$) and for columns (under ULS usually $0.1 < \rho < 0.2$). In addition, with reference to beam-to-column joints, a full probabilistic analysis carried out in (Piluso & Rizzano, 2003; Latour & Rizzano, 2010) has demonstrated that the factor accounting for the random material variability in case of steel S235 and bolt class 8.8/10.9 varies in the range 1.11-

1.26 being, therefore, in general lower than the coefficient proposed by EC8 equal to 1.25.

Furthermore, in order to provide MRFs with weak beams and strong columns, (CEN, 2005c) suggests the adoption of members hierarchy criterion. This requirement imposes that at each beam-to-column joint the following inequality has to be satisfied:

$$\sum M_{Rc} \geq 1.3 \sum M_{Rb} \quad (2.8)$$

where the term on the left side is the sum of the plastic moments of the columns and the term on the right is the sum of the plastic moments of connected beams. It is worth note that the fulfilment of such design requirement does not guarantee the development of a global type mechanism, but only prevents the formation of the so-called weak-storey collapse mechanism. Indeed, in order to design MRFs failing according to a global mechanism, more accurate design methods should be used. Failure mode control of MRFs has been studied in past by different authors and several design methods have been proposed. As an example, a procedure of design which has been demonstrated to be effective is the one proposed by (Mazzolani & Piluso, 1996) based on the upper bound theorem of the plastic collapse. Through this method, beams are preliminary dimensioned to resist gravity loads and then columns are designed so that the kinematically admissible multiplier of the horizontal forces corresponding to the attainment of a global collapse mechanism is lower than the one corresponding to the other kinematically admissible mechanisms, such as the soft-storey mechanisms.

Up to now, design philosophy of weak beam-strong column-strong connection has been widely used in seismic design, currently it is well accepted by designer and, in truth, very reasonable. The success of this design philosophy is mainly related to the importance that second order effects may have on the global ductility. In fact, it is well known that a frame developing hinges in beam is more stable than a frame developing plastic zones in columns. Furthermore, it is widely recognized that normal actions strongly affect the development of a stable plasticization, so that yielding of elements subjected to low axial loads, i.e. the beams, is usually desirable compared to yielding of column ends, which typically have to withstand, especially at low storeys, high vertical loads.

On the other hand, it is easy to demonstrate that in some cases the design of frames according to classical approach can be expensive and not cost/effective. This might be the case of structures with few storeys and/or with long spans, where the design of beams is mainly governed by vertical loads rather than lateral loads and the fulfilment of the hierarchy criterion can be very costly to implement. It is for this reason that modern design codes allow, in case of single-storey buildings, the implementation of weak column-strong beam approach, provided that the axial loads on columns are limited (Schenider et al., 1991; Schiff et al., 1988). As an alternative to the weak column-strong beam approach, by means of the application of partial-strength joints, the new design philosophy of the strong column-weak connection has been recently introduced (Nader & Astanteh-Asl, 1991; Nader & Astanteh-Asl, 1996; Awkar & Lui, 1999; Elghazouli, 1998; Faella et al., 2000; Della Corte et al., 2002; Huh & Haldar, 2002; Lee & Foutch, 2002; Hamburger et al., 2004). In this way, even though the beam is strong due to dead loads, as for example in case of low rise and/or long spans buildings, by the use of partial strength joints only a part of the bending moment is transferred to the column and a

more cost/effective design is achieved. In conclusion, partial strength connections can be, in some cases, effectively applied to prevent the oversizing of columns (Faella et al., 1998; Tahir et al., 2006).

The growing interest of the scientific community to solutions adopting partial strength joints is reflected in last version of Eurocode 8. In fact the code has opened the door to the use of partial strength joints in MRFs allowing the dissipation of the seismic input energy by the inelastic behavior of connecting elements and with some limitations of panel zones. Even though the use of partial strength joints is not prohibited by EC8, the real application of this technique for dissipative purposes is strongly limited in practice. In fact, according to the code, the actual dissipative capacities of joints have to be demonstrated by experimental evidence. It is obvious that such requirement is out of the possibilities of designers, and therefore makes the implementation of partial strength joints in steel structures still far from the common practice. Hence, new experimental and modeling efforts of the scientific community are necessary so as to provide proper design criteria for MRFs under seismic loads and accurate models for the prediction of monotonic and cyclic response of joints. Up to now, the seismic behavior of semi-rigid steel frames with partial strength joints has been studied by different authors and some proposal of behavioral factor have been outlined (Aribert & Grecea, 2000; Astaneh-Asl & Nader, 1994; Grecea et al., 2004). In spite of the works here cited, there is still a lack of knowledge with reference to the rules for detailing MRFs and dissipative joints. Furthermore, last version of EC3-1-8 provides a mechanical model for the prediction of the joint behavior only under monotonic loads whilst the prediction of the post-elastic behavior under cyclic loadings still deserves further investigations.

In the following, the results of some past studies concerning the behavior of partial strength semi-rigid MRFs are described so as to make out the main parameters which influence the overall structural response of frames adopting semi-continuous joints. To this scope, in (Rizzano, 1995; Rizzano, 2006) a parametric study dealing with the influence of the joint elastic and post-elastic behavior has been carried out.

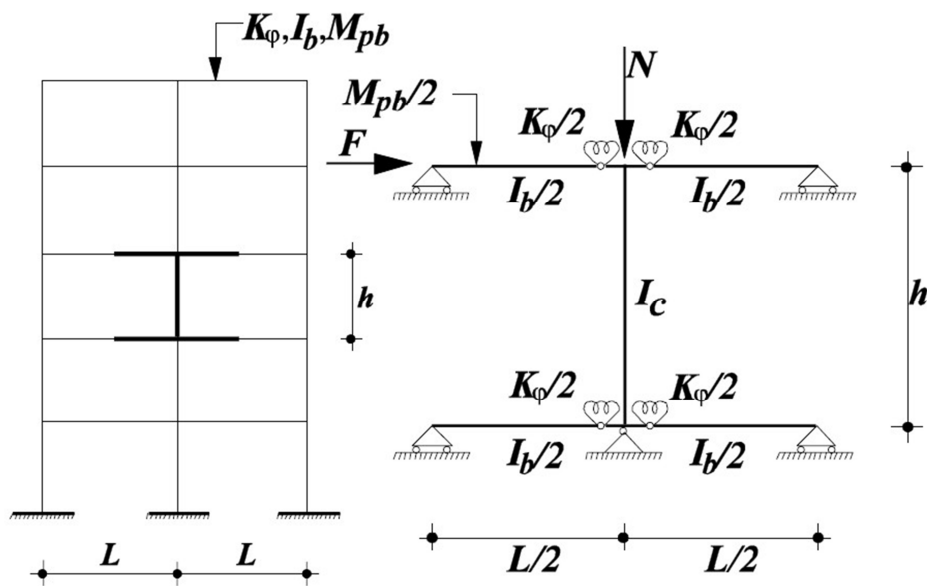


Fig. 2.18 – Simplified model adopted by (Piluso et al., 1994)

In these works, the analysis of the structural sub-assembly depicted in Fig. 2.18 has been considered. The basic hypothesis of the elementary model are the following:

- the point of contra-flexure is located in correspondence of the beam mid-span, which is a condition usually acceptable if seismic loads are considered;
- the beams belong to two stories, so that their mechanical properties are halved;
- the behavior of beam-to-column joints is accounted for by means of an elastic-plastic moment-rotation spring.

As a consequence, the performance of the simplified model is governed by the following three non-dimensional parameters:

$$\zeta = \frac{EI_b/L_b}{EI_c/h} \quad \bar{K} = \frac{K_\varphi L_b}{EI_b} \quad \bar{m} = \frac{M_{j,Rd}}{M_{b,Rd}} \quad (2.9)$$

where ζ is the ratio between the flexural stiffness of beams and column, \bar{K} is a stiffness parameter defined as the ratio between joint and beam rotational stiffness, \bar{m} is a resistance parameter defining the ratio between joint and beam plastic resistance, I_b and I_c are the beam and column inertia modulus and L_b and h are the beam and column length.

On the base of the introduced factors, in (Rizzano, 1995) the response of the sub-model has been studied. In particular, the influence of the joint rotational stiffness on the period of vibration and on the sensitivity to second order effects have been evaluated. The significance of joint stiffness on the period of vibration has been evaluated by studying the translational stiffness matrix of the sub-model, obtaining the following expression:

$$\frac{T_k}{T_\infty} = \sqrt{\frac{\bar{K}(1 + \zeta) + 6}{\bar{K}(1 + \zeta)}} \quad (2.10)$$

where T_k and T_∞ are the period of vibration of the model with semi-rigid and rigid joints respectively (Fig. 2.19).

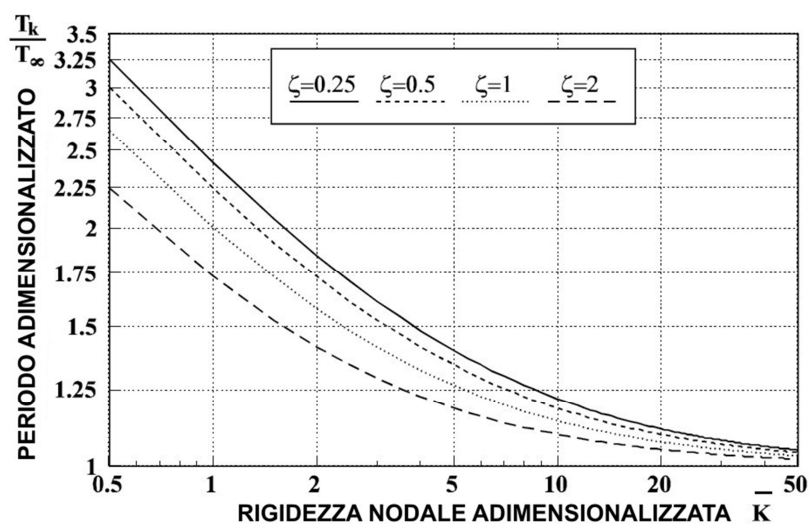


Fig. 2.19 – Influence of non-dimensional stiffness on the period of vibration

Furthermore, the influence of the joints rotational stiffness on the sensitivity to second order effects has been analyzed by means of the stability coefficient:

$$\gamma = \frac{N}{K_0 h} \quad (2.11)$$

where N is the axial force in the column and K_0 is the lateral stiffness of the sub-assembly. The analysis of the model has led to the following expression:

$$\frac{\gamma_k}{\gamma_\infty} = \frac{\bar{K}(1 + \zeta) + 6}{\bar{K}(1 + \zeta)} \quad (2.12)$$

where γ_k and γ_∞ are the stability coefficients in cases of structure with semi-rigid and rigid joints (Fig. 2.20).

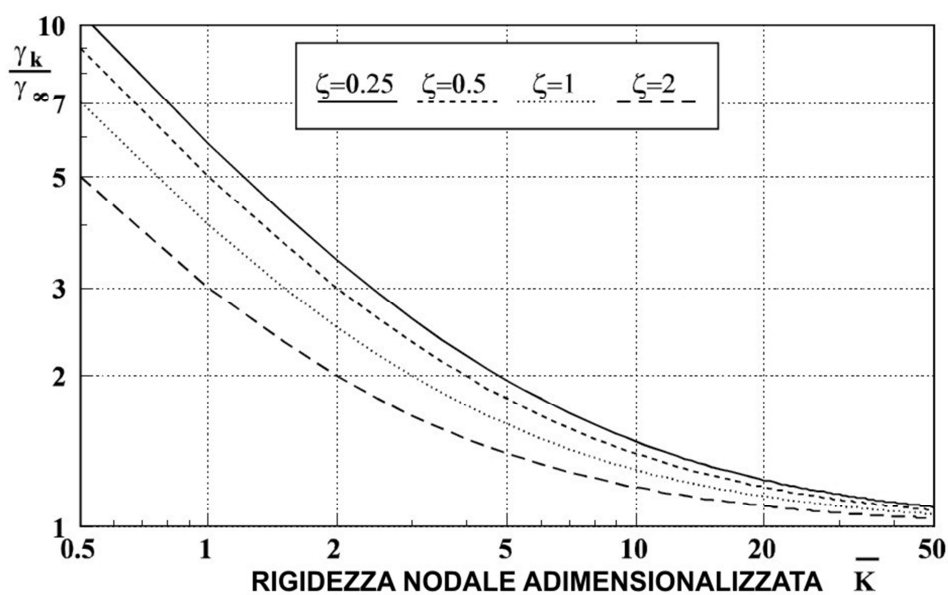


Fig. 2.20 – Influence of non-dimensional stiffness on stability coefficient

As expected, it is worth note from equations (2.11) and (2.12) that joint deformability produces two opposite effects. In fact, the increase of joint

deformability increases the period of vibration and, consequently, provides a beneficial effect due to the lower forces attracted by the structure, but on the other hand amplifies also the susceptibility to second order effects increasing the stability coefficient. Moreover, in (Rizzano, 1995) the influence of joints on the frame global ductility has been evaluated. Regarding full strength joints, the global ductility is mainly governed by the plastic rotation capacity of the beams, conversely, in case of partial strength joints global ductility is limited by the joints plastic rotation supply:

$$\mu_k^{FS} = 1 + \frac{3R_b}{1(1 + \zeta)} \quad (2.13)$$

$$\mu_k^{PS} = 1 + \frac{6R_c}{\bar{K}(1 + \zeta) + 6} \quad (2.14)$$

where R_b represents the rotation capacity of the beam and R_c is the connection rotation supply defined as:

$$R_c = \frac{\vartheta_{jp}}{\vartheta_{jy}} \quad (2.15)$$

where ϑ_{jp} is the ultimate plastic rotation of the joint and ϑ_{jy} is the rotation corresponding to first yielding. Moreover, in (Rizzano, 1995) the simplified model has also been used to propose a formulation of the behavioral factor for frames adopting semi-rigid partial strength joints. The authors, starting from the formulation of the q-factor proposed by (Krawinkler & Nassar, 1992) and by

accounting for second order effects through the expression given by (Cosenza et al., 1988) have found:

$$q_k^{PS} = \frac{[c(\mu_k^{PS} - 1) + 1]^{1/c}}{[1 - \psi_1(\mu_k^{PS} - 1)^{\psi_2}\gamma_k]} (1 - \gamma_k) \quad (2.16)$$

where $\psi_1 = 0.62$ and $\psi_2 = 1.45$ provides the average value of the coefficient accounting for second order effects (Cosenza et al., 1988). The parameter c according to (Krawinkler & Nassar, 1992) is equal to:

$$c = \frac{T}{1 + T} + \frac{0.42}{T} \quad (2.17)$$

M_g	Criterion	K_{avg}			$0.8K_{avg}$			$0.6K_{avg}$		
		q	α_{Nj}	θ_j	q	α_{Nj}	θ_j	q	α_{Nj}	θ_j
1.0	$\phi_{0.015}$	1.5	0.50	0.044	1.6	0.60	0.046	1.8	0.80	0.054
	$\phi_{0.030}$	2.3	1.00	0.054	2.8	1.20	0.066	2.7	1.20	0.071
	$\phi_{0.045}$	3.4	1.60	0.069	3.5	1.60	0.073	3.2	1.60	0.079
0.8	$\phi_{0.015}$	1.5	0.50	0.043	1.7	0.50	0.047	1.9	0.70	0.052
	$\phi_{0.030}$	2.8	1.00	0.068	2.9	1.00	0.070	2.8	1.10	0.074
	$\phi_{0.045}$	3.5	1.40	0.069	3.8	1.50	0.072	3.5	1.60	0.078
0.6	$\phi_{0.015}$	1.9	0.50	0.042	2.3	0.50	0.049	2.3	0.60	0.056
	$\phi_{0.030}$	3.2	1.00	0.065	3.5	1.00	0.070	3.2	1.10	0.075
	$\phi_{0.045}$	4.2	1.40	0.075	4.6	1.50	0.079	4.0	1.70	0.082

Fig. 2.21 – Results of the parametric analysis (Aribert & Grecea, 2000)

Another attempt to provide an estimate of the q-factor has been carried out by (Aribert & Grecea, 2000). In their work, the authors propose a numerical study devoted to the definition of the behavioral factor for frames characterized by the following parameters:

- partial strength coefficient ($0.6M_b$, $0.8M_b$ and M_b);
- joints elastic rotational stiffness ($0.6S_{int}$, $0.8S_{int}$, S_{int});
- joints rotational capacity (0.015, 0.030, 0.045).

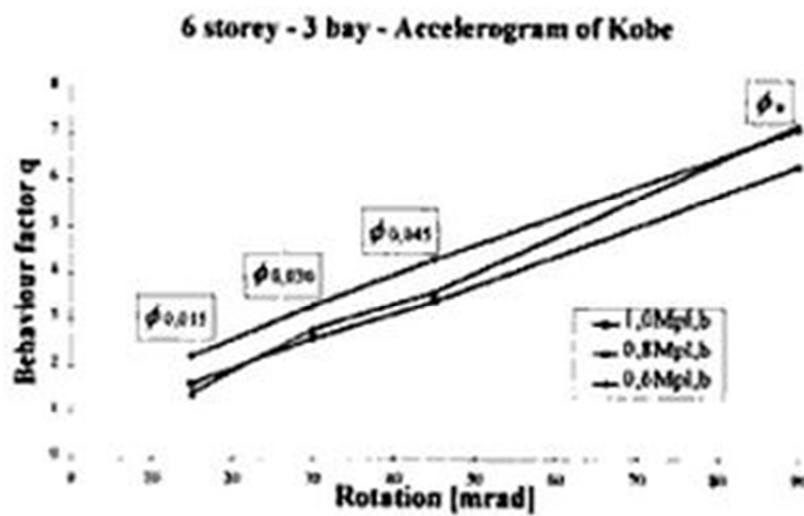


Fig. 2.22 – Proposal of behavioral factor for semi-continuous MRFs

By performing a series of time-history analysis on frames subjected to the accelerograms of Kobe (1995) and Bucharest (1977), accounting for the elastic-plastic behavior of steel and for second order effects the authors have defined the q -factor as equal to the ratio between the theoretical base shear force and the actual inelastic base shear force:

$$q = \frac{V_{el}^{th}}{V_{inel}} \quad (2.18)$$

as a result, the authors have found that the q -factor of partial strength semi-rigid frames is not significantly affected by the initial stiffness, while joints resistance and rotational capacity strongly influence the ultimate behavior Fig. 2.21. In conclusion, an expression of the q -factor for the accelerograms of Bucharest (1977) and Kobe (1995) has been proposed and is here reported in Fig. 2.22.

2.5 References

AISC, 2005. *Seismic Provisions for Structural Steel Buildings*. Chicago, Illinois.

Aribert, J. & Grecea, D., 2000. Numerical investigation of the q-factor for steel frames with semi-rigid and partial-strength joints. In *Proceedings of the 3d International Conference STESSA 2000*. Montreal, 2000.

Astaneh-Asl, A., 1986. *Field Moment Connection*. Berkeley, University of California: Department of Civil and Environmental Engineering.

Astaneh-Asl, A., 1987. *Experimental Investigation of Tee Framing Connection*. AISC.

Astaneh-Asl, A., 1995. Seismic Design of Bolted Steel Moment-Resisting Frames. July.

Astaneh-Asl, A. & Nader, N., 1994. Proposed code provision for seismic design of steel semi-rigid and rigid frames. In *Proceedings of the 5th U.S. National Conference of Earthquake Engineering (EERI)*. Chicago, 1994.

Awkar, J. & Lui, E., 1999. Seismic Analysis and Response of Multistorey Seimirigid Frames. *Journal of Structural Engineering - ASCE*, 21, pp.1865-72.

Bennett, R. & Najem-Clarke, F., 1987. Reliability of Bolted Steel Tension Members. *Journal of Structural Engineering - ASCE*, 113 (8), pp.1865-72.

Bijlaard, F., 2004. Joints in steel structures based on eurocode 3. In *Steel & Composite Structures (ICSCS'04)*. Yuseong, Korea, 2004. Techno-Press. (TUD).

Bruneau, M., Uang, C. & Whittaker, A., 1998. *Ductile Design of Steel Structures*. U.S.A.: McGraw-Hill.

CEN, 2005a. *Eurocode 3: Design of steel structures - Part 1-1: General rules and rules for buildings*.

CEN, 2005b. *Eurocode 3: Design of steel structures - Part 1-8: Design of joints*.

CEN, 2005c. *Eurocode 8: Design of structures for earthquake resistance - Part 1: General rules, seismic actions and rules for buildings*.

Cosenza, E., De Luca, A., Faella, C. & Piluso, V., 1988. A rational formulation for the q-factor in steel structures. In *Proceedings of the IX WCEE*. Tokyo-Kyoto, 1988.

Della Corte, G., De Matteis, G., Landolfo, R. & Mazzolani, F., 2002. Seismic Analysis of MR steel frames based on refined hysteretic models of connections. *Journal of Constructional Steel Research*, 58, pp.1331-45.

Elghazouli, A., 1998. Seismic Design of Steel Frames with Partial Strength Connections. In *Proceedings of the 6th SECED Conference on Seismic Design Practice*. Oxford, UK, 1998.

Faella, C., Montuori, R., Piluso, V. & Rizzano, G., 1998. Failure mode control: economy of semi-rigid frames. In *Proceedings of the XI European Conference on Earthquake Engineering*. Paris, 1998.

Faella, C., Piluso, V. & Rizzano, G., 2000. *Structural Steel Semi-Rigid Connections*. Boca Raton: CRC Press.

Gervasio, H., Simoes Da Silva, L. & Borges, L., 2002. Reliability Assessment of the post-limit Stiffness and Ductility of Steel Joints. In *Proceedings of the Third European Conference on Steel Structures*. Coimbra, 2002.

Giuncu, V. & Mazzolani, F., 2000. *Seismic Resistant Steel Structures*. New York: CISM Courses and Lectures No 420.

Grecea, D., Dinu, F. & Dubina, D., 2004. Performance Criteria for MR Steel Frames in Seismic Zones. *Journal of Constructional Steel Research*, 60, pp.739-49.

Hamburger, R., Fouthc, D. & Cornell, C., 2004. Performance basis of guidelines for evaluation, upgrade and design of moment-resisting steel frames. In *Proceedings of 12 World Conference on Earthquake Engineering*. Vancouver, Canada, 2004.

Huh, J. & Haldar, A., 2002. Seismic Reliability of non-linear frames with PR connections using systematic RSM. *Probabilistic Engineering Mechanics*, 17, pp.177-90.

Jaspart, J.P., 2002. Design of Structural Joints in Building Frames. *Progress in Structural Engineering and Materials*, Vol.4(18-34).

Kirby, P., Zandonini, R. & Davison, J., 1990. On the determination of moment rotation characteristics of beam-to-column joints. In *RILEM Workshop: Needs in Testing Metals*. Napoli, 1990.

Krawinkler, H. & Nassar, A., 1992. Seismic design based on ductility and cumulative damage demands and capacities. In *Nonlinear Seismic Analysis and Design of Reinforced Concrete Buildings*. London: Elsevier.

Latour, M. & Rizzano, G., 2010. Full Strength Design of Steel Column Base Joints: Influence of Material Variability. In *European Conference on Earthquake Engineering*. Ohrid, 2010.

Lee, K. & Foutch, D., 2002. Performance Evaluation of new steel frame buildings for seismic loads. *Earthquake Engineering and Structural Dynamics*, 31, pp.653-70.

Mazzolani, F. & Piluso, V., 1996. *Theory and Design of Seismic Resistant Steel Frames*. London: E & FN Spon, an Imprint of Chapman & Hall.

Nader, M. & Astanteh-Asl, A., 1991. Dynamic Behavior of Flexible, Semi-Rigid and Rigid Steel Frames. *Journal of Constructional Steel Research - ASCE*, 18, pp.179-92.

Nader, M. & Astanteh-Asl, A., 1996. Shaking Table Tests of Rigid, Semi-Rigid and Flexible Steel Frames. *Journal of Constructional Steel Research - ASCE*, 122 (6), pp.589-96.

Nethercot, D. & Zandonini, R., 1990. *Methods of prediction of joint behaviour: beam-to-column connections*. Elsevier Applied Science Publishers.

Piluso, V. & Rizzano, G., 2003. Reliability of full-strength end-plate connections: design criteria and Monte Carlo simulation. In *Proceedings of the ASSCCA '03 Advances in Structures*. Sidney, Australia, 2003.

Rizzano, G., 1995. *Modellazione nodale e comportamento sismico dei telai in acciaio a nodi semirigidi*. PhD thesis ed. Napoli: Università degli Studi di Napoli.

Rizzano, G., 2006. Seismic Design of Steel Frames with Partial Strength Joints. *Journal of Earthquake Engineering*, 10(5), pp.725-47.

SAC, 2000a. *Recommended Seismic Design Criteria for New Steel Moment Resisting Frame Buildings*. California: FEMA.

SAC, 2000b. *State of the Art Report on Systems Performance of Steel Moment Frames Subject to Earthquake Ground Shaking*. California, U.S.A.: FEMA.

SAC, 2000c. *State of the Art Report on Past Performance of Steel Moment-Frame Buildings in Earthquakes*. California: FEMA.

Schenider, S., Roeder, C. & Carpenter, J., 1991. *Seismic performance of weak-column strong-beam steel moment resisting frames*. Finale Report on Research Sponsored by the National Science Foundation Grant BCS-8819952. Washington: University of Washington.

Schiff, S., Hall, W. & Foutch, D., 1988. *Seismic design studies of low-rise steel frames*. Urbana-Champaign: Department of Civil Engineering University of Illinois.

Song, S. & Wen, Y., 2000. *Structural Redundancy of Dual and Steel Moment Frame Systems Under Seismic Excitation*. Urbana-Champaign: Department of Civile and Environmental Engineering University of Illinois.

Tahir, M. et al., 2006. *Economic Aspects of the Use of Partial and Full Strength Joints on Multi-Storey Unbraced Steel Frames*. Faculty of Civile Engineering.

Tucker, G. & Bennett, R., 1990. Reliability Analysis of Partially Restrained Steel Connections. *Journal of Structural Engineering - ASCE*, 116 (4), pp.1090-101.

CHAPTER 3 – CYCLIC BEHAVIOR OF BEAM-TO-COLUMN JOINTS: EXPERIMENTAL CAMPAIGN

3.1 Introduction

As already remarked, after the seismic events of Kobe and Northridge, two strategies have been identified to improve the seismic behavior of steel MRFs subjected to seismic loads. A first approach has been based on the idea of improving the seismic behavior of the so-called Pre-Northridge welded connections (SAC, 2000b; SAC, 2000a; SAC, 2000c). Aiming to this goal, the existing welding techniques have been enhanced so as to obtain adequate over-resistances of the welds in the critical zone with respect to the fully yielded and strain-hardened beam end. A second approach has been based on the idea of shifting the dissipative zones, i.e. the plastic hinges, away from the face of the column and as a consequence far away from the welds, reducing the flexural resistance of the beam by properly cutting the flanges in a zone close to the beam-to-column connection. This weakening approach is commonly called Reduced Beam Section (RBS) or Dog Bone (Richard et al., 1995; Chen et al., 1996; Chen et al., 1997; Carter & Iwankiw, 1998; Joh & Chen, 1999; Moore et al., 1999; SAC, 2000a).

A new design approach, which has been the subject of many studies in last decades, has gained growing interest in last years. In fact, Eurocode 8 (CEN, 2005c) has opened the door to the idea of dissipating the seismic input energy

in the connecting elements of beam-to-column joints. It has been recognized that semi-rigid partial strength connections can lead to dissipation and ductility capacity compatible with the seismic demand, provided that they are properly designed by means of an appropriate choice of the joint component where the dissipation has to occur. It is well known that the study of semi-rigid steel joints can be carried out by means of the so-called component approach (Jaspart, 1991; Rizzano, 1995; Mazzolani & Piluso, 1996; Jaspart, 2002; Faella et al., 2000; Bijlaard, 2004; Rizzano, 2006) which has been codified by Eurocode 3 (CEN, 2005b). With reference to beam-to-column joints, the component approach allows the prediction of the moment-rotation response, provided that all the sources of strength and deformation, i.e. the joint components, are properly identified.

The component approach provides an answer to the important topic of the prediction of joint rotational response parameters, such as stiffness and flexural strength, leading off from the geometrical properties of connecting elements and the mechanical properties of materials. Even though the component approach, in its codified version (CEN, 2005b), is mainly devoted to the prediction of strength and stiffness, it is important to underline that it could be successfully applied also for the prediction of the cyclic response of beam-to-column joints, provided that cyclic modelling of joint components with a proper definition of degradation laws of stiffness and strength parameters is available. This goal can be achieved with the support of experimental tests devoted to the cyclic response of the single joint components or the cyclic response of beam-to-column joints as a whole. Many experimental programs regarding the study of beam-to-column joints as a whole have been carried out in last decades. Conversely, quite a little experimental programs have been carried out concerning the cyclic behaviour of the single joint components

(Faella et al., 1998a; Faella et al., 1998b; Faella et al., 2000; Swanson & Leon, 2000; Clemente et al., 2004; Dubina et al., 2008; Piluso & Rizzano, 2008);. Notwithstanding significant research efforts are still needed to develop complete mechanical models, based on the component approach, able to lead to the prediction of the cyclic rotational response of beam-to-column joints starting from the knowledge of their geometrical properties and of material properties.

It doesn't appear useless to remember that Eurocode provides information to evaluate the monotonic behaviour of beam-to-column connections, but it doesn't give any indication concerning the modelling of the cyclic behaviour of the joint components. In addition, according to Eurocode 8 (CEN, 2005c), the development of experimental tests is required in the case of partial strength joints aiming to demonstrate the attainment of the code required plastic rotation supply.

One of the main goals is the investigation of the actual possibility of extending the component approach to the prediction of the cyclic response of beam-to-column joints. To this scope an experimental program has been carried out at the Material and Structure Laboratory of Salerno University by testing bolted beam-to-column connections, characterized by different structural details, subjected to cyclic loads under displacement control. The attention has been focused on the measure of the deformation of the single joint components. It will be demonstrated that the overall energy dissipation provided by the joint can be obtained as the sum of those provided by the single joint components, provided that they are properly identified and monitored. This is the first need towards the extension of the component approach to the prediction of the joint rotational response under cyclic loads. In addition, the presentation of the

design criteria adopted for the tested specimens will show how bolted beam-to-column connections can be designed controlling the failure mode, the flexural resistance and the plastic rotation supply. It will be pointed out how the ultimate behaviour can be completely modified by strengthening some components rather than others, governing the failure mode by means of simple modifications of the joint detail.

Finally, the development of a mechanical model based on the component approach for predicting the cyclic response of bolted connections will be presented in next chapter.

In addition, in this chapter, all the aspects regarding the setup of an experimental campaign, started at the University of Salerno in 2007 dealing with the cyclic behaviour of beam-to-column joints is presented. In particular, the attention is focused on the main aspects regarding the employed testing machines, the testing setup and the criteria adopted for the design of the specimens.

The aim of the work presented in this section is the investigation of the behaviour of joint components within the overall rotational response of beam-to-column joints subjected to cyclic loads. In particular, it is pointed out how the typology of the hysteresis loops is mainly governed by the weakest joint component. To this scope, the tested specimens have been designed aiming to obtain the same flexural strength, but different locations of the weakest joint component, leading to different values of rotational stiffness and plastic rotational supply. In particular four specimens have been tested:

- **EEP-CYC 01** is a partial strength extended end-plate joint having the panel zone as weakest joint component;
- **EEP-CYC 02** is a partial strength extended end-plate joint having the end-plate in bending as weakest joint component;
- **EEP-DB-CYC 03** is a full strength extended end-plate joint designed forcing the development of plastic hinge in the beam by cutting the beam flanges following the design criteria for the reduced beam section (RBS) strategy;
- **TS-CYC 04** is a partial strength joint with a couple of T-stubs bolted to the beam flanges and to the column flanges and designed to be the main source of plastic deformation capacity.

3.2 Description of the test setup

The setup of the experimental tests has been realized at the Laboratory on materials and structures of the University of Salerno. The different devices, instruments and machines which have been employed can be categorized in:

- constraining devices;
- loading machines;
- measurement instruments.

In the first category are contained all the devices which are usually adopted to counteract the actions due to loading machines. Constraining devices are, in general, used to realize, during the experimental tests, the restraints necessary to obtain the desired structural scheme and to avoid the arise of undesired second order effects, as for instance the lateral torsional buckling of a steel member.

The main constraining system of the laboratory is, in truth, a part of the building itself. In fact, the floor of the laboratory is constituted by a one meter thick reinforced concrete slab, which is, in elevation, structurally separated from the laboratory building, but connected to the building in the foundations. Such rigid and strong slab possesses holes spaced according to a 1 m x 1 m grid. The holes, with a diameter of 80 mm, allow to fix the constraining structures by means of high strength dywidag bars.

The considered experimental campaign has required the adoption of two counteract devices: a rigid and strong vertical frame and an horizontal base sleigh. Both the devices are realized by the assemblage of fully welded steel plates and structural members. The vertical frame is used to position the

hydraulic actuators to a certain height and to react to the horizontal forces produced during the experimental tests. The base sleigh, is constituted by rigid steel plates drilled so as to fasten, by means of M30 bolts, further constraining devices (Fig. 3.1).

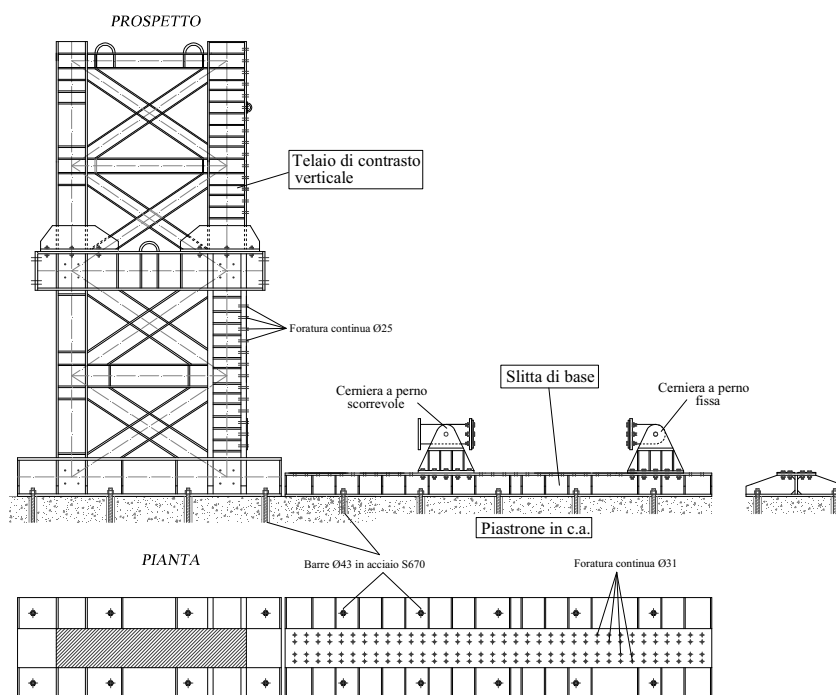


Fig. 3.1 – Constraining devices used in the experimental campaign

It is clear that the two described structural systems are conceived to be used, in general, for different types of experimental tests. As shown later, in the particular case of the considered experimental campaign on beam-to-column joints, the detail of specific supplementary constraining elements able to

simulate the restraining condition of a connection in a real structure have been necessary.

In particular, two steel hinges, designed to resist shear actions of *2000 kN* and bolted to the base sleigh have been realized. The first of the two hinges has been detailed to absorb shear and axial actions by means of a pin and of calibrated holes. The other one has been designed so as to allow the slippage in the horizontal direction and to restrain displacements in the orthogonal direction by means of a pin and slotted holes. Last constraining device is composed by an horizontal counteract frame, which has the task to avoid the development of lateral-torsional buckling phenomena of the steel members during the experimental tests.

Dealing with the loading machines, in this category are basically contained the hydraulic actuators. Such devices are constituted by an hydraulic piston able to convert electrical input in desired displacements or, as an alternative in desired loadings.

For the experimental campaign on beam-to-column joints, two different actuators have been used. The first one is called *MTS 243.60* with a maximum loading capacity of *1000 kN* in compression and of *650 kN* in tension with a piston stroke of *+/- 125 mm*. The second one is called *MTS 243.35* with loading capacity of *250 kN* in tension and compression and piston stroke of *+/- 500 mm*. Actuator *MTS 243.60* has been used to simulate, operating under loading control, the axial load in the column, whilst Actuator *MTS 243.35* has been exploited to apply, under displacement control, the desired displacement history at the end of the beam (Fig. 3.2).

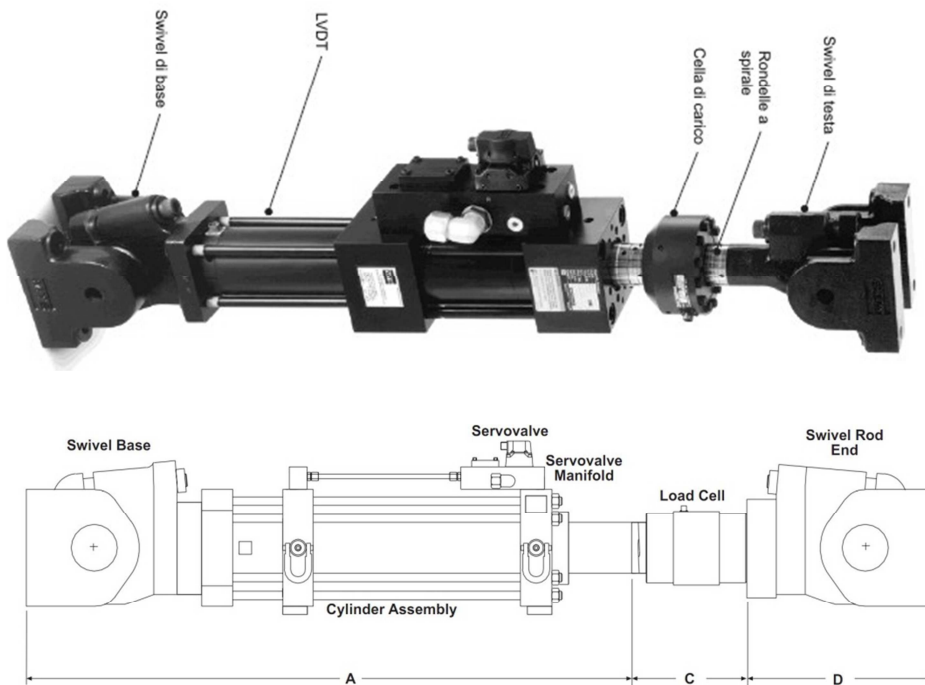


Fig. 3.2 – MTS Hydraulic testing machine

Modern actuators, even though belong to the wider family of the hydraulic rams, are different from classical jacks for the higher technological content, which makes the actuators either reliable and delicate instruments.

MTS testing machines are usually accessorized with LVDTs (Linear Variable Differential Transformer) for the continuous measurement of the piston displacement during the experimental tests, load cells in tension/compression for the continuous measurement of the load level, servovalves for the control of the oil flow necessary to develop the desired displacement/load and base/end swivels for limiting the actions withstood by the actuator.



Fig. 3.3 – Universal testing machine SCHENCK Hydropuls S56

For the experimental tests on the base materials composing steel sections and plates an universal machine *SCHENCK Hydropuls S56* has been used. This machine is constituted by an hydraulic piston with loading capacity of ± 630 kN, stroke of ± 125 mm and a self-balanced steel frame used to counteract the axial loadings. The machine works both under displacement and load control. In order to measure displacements the testing machine is equipped with an LVDT, while the tension/compression loads are controlled by means of a load cell (Fig. 3.3).

The development of an experimental campaign requires the adoption of proper instrumentation so as to acquire during the tests the desired displacements, angles and deformations. For the experimental program herein presented, aiming to monitor both displacements of beam and column and of the elements composing the connection, different instruments have been used:

- **Displacement Transducers (LVDT):** in this devices a magnetic flux coupling between two coils is altered by the movement of a ferromagnetic shaft within the flux path and subsequently converted into voltage. In this way LVDTs allow to acquire linear displacements by means of the movement of a metallic shaft. This instruments are very reliable with a measurement range of 50 mm with infinitesimal resolution. Main advantages of LDVTs are the following: the sensor is a non-contact device with very little friction resistance, output impedance is very low, there is low susceptibility to noise and interferences and its construction is solid and robust (Fig. 3.4).

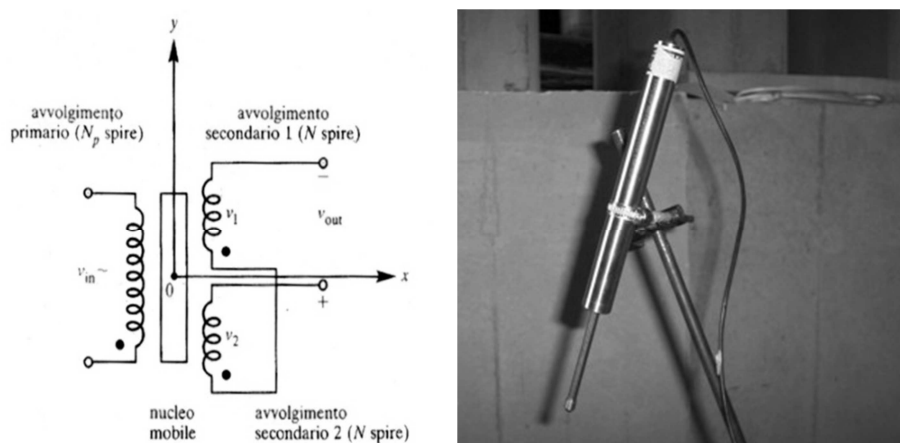


Fig. 3.4 – Scheme and picture of an LVDT

- **Wire sensors:** these devices are constituted by a steel wire reeling in a drum coupled to a potentiometer. In this way is possible to obtain the displacements of the elements fixed to the end wire clip. Models available at the Laboratory on Material and Structures of the University

of Salerno cover a measurement range of 200 mm with a resolution of $0,01\text{ mm}$. Easy to use, but with susceptibility to noise and interferences greater than LVDTs (Fig. 3.5).

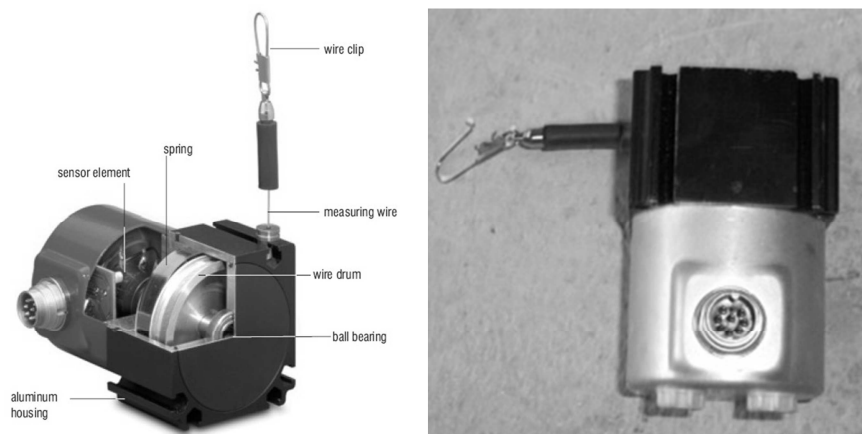


Fig. 3.5 – Scheme and picture of an LVDT

Inclinometers: are sensors constituted by a disc cavity filled with a dielectric liquid. As the sensor rotate the liquid moves covering a different area. This area change results in a change of the capacitance which is then electronically converted into an output signal that is linear with respect to the input angle. Models possessed by the laboratory of Salerno cover a measurement range of $\pm 10^\circ$ with respect to the vertical, with a precision of $0,01^\circ$. Inclinometers allow the continuous acquirement of the rotation of the element which are attached to (Fig. 3.6).

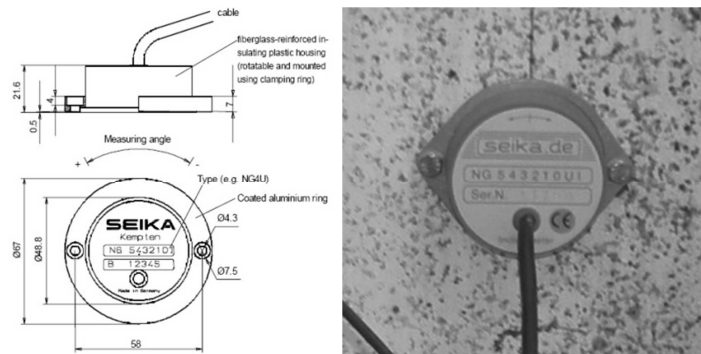


Fig. 3.6 – Scheme and picture of an inclinometer

Strain gauges: are sensors used to monitor deformations of an element. Usually Strain Gauges are constituted by a grid of thin metallic wire, rigidly fixed to a plastic support.

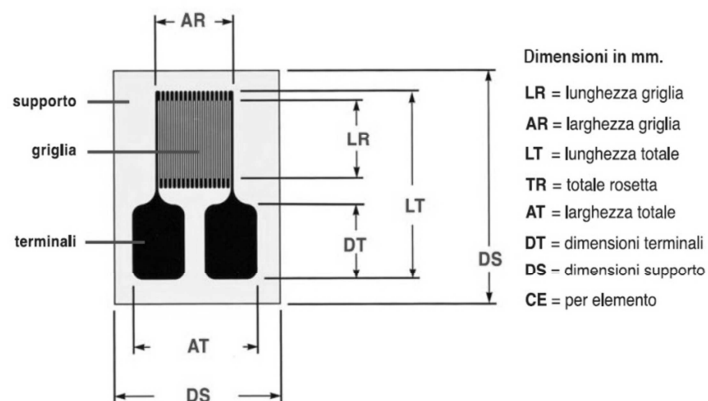


Fig. 3.7 – Scheme of a Strain Gauge

Attached to an element follow the deformation of the surface. Such deformations vary the electrical resistance of the strain gauge which is

measured and converted in strains. In the experimental tests later exposed devices covering a measurement range of $\pm 3\%$ have been used. Their reliability is strictly related to the quality of the attachment and to the roughness of the surface (Fig. 3.7).

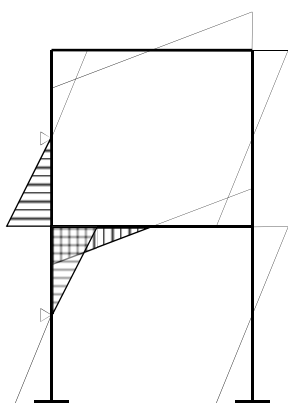


Fig. 3.8 – Actions in a

frame due to seismic loads

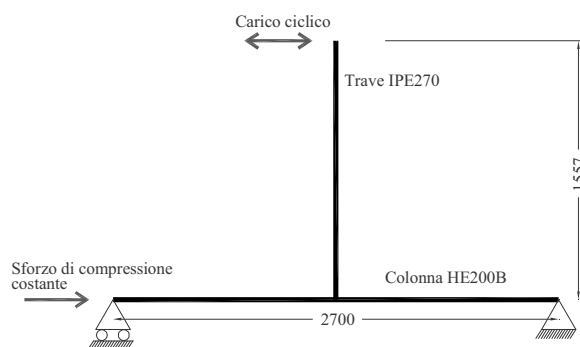


Fig. 3.9 – Scheme reproduced in laboratory

As already said the experimental tests have been executed using two hydraulic actuators. The bottom MTS actuator, having 1000 kN load capacity, has been governed under force control in order to impose a constant axial compression load equal to 650 kN which corresponds to 30% of the column squash load. The top actuator, having ± 250 kN load capacity and piston stroke equal to ± 500 mm has been connected to the top end of the beam to apply the displacement history (Fig. 3.8 - Fig. 3.9). The loading history is given in terms of drift angle in Fig.9, according to AISC provisions (2005).

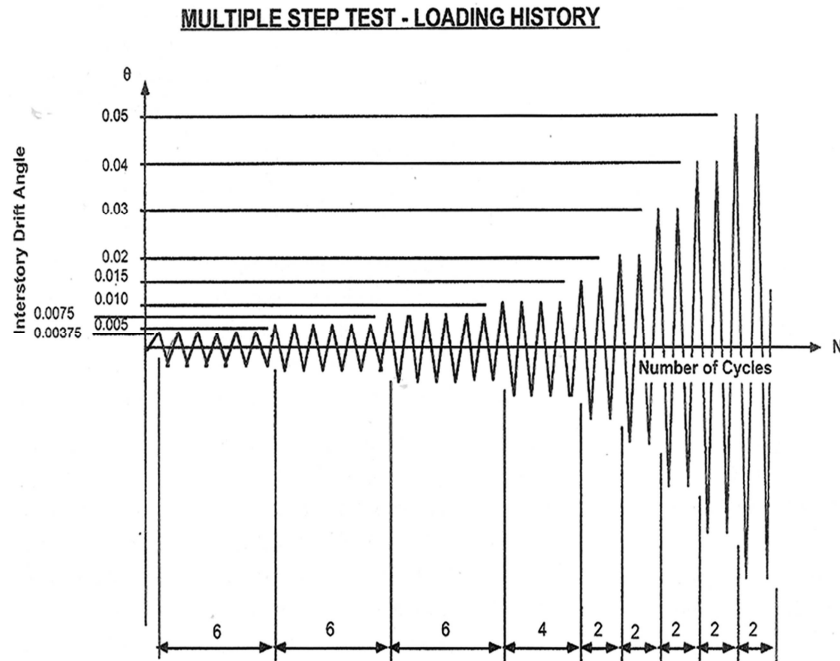


Fig. 3.10 – AISC loading history for beam-to-column joints

- 6 cycles at $\theta = 0,00375$ rad
- 6 cycles at $\theta = 0,005$ rad
- 6 cycles at $\theta = 0,0075$ rad
- 4 cycles at $\theta = 0,01$ rad
- 2 cycles at $\theta = 0,015$ rad
- 2 cycles at $\theta = 0,02$ rad
- 2 cycles at $\theta = 0,03$ rad

By the knowledge of AISC requirements, given in terms of drift angle, is possible to obtain the displacement history at the top of the beam (**Table 3.1**).

Table 3.1 – Loading History

v [mm/s]	Step	θ [rad]	# cycles	δ [mm]	t_r [s]	t_c [s]	t_{step} [s]
0,5	1	0,00375	6	5,85	11,7	47	293
	2	0,005	6	7,8	3,9	62	378
1	3	0,0075	6	11,7	3,9	47	285
	4	0,01	4	15,6	3,9	62	254
2	5	0,015	2	23,4	3,9	47	98
	6	0,02	2	31,2	3,9	62	129
	7	0,03	2	46,8	7,8	94	195
	8	0,04	2	62,4	7,8	125	257
4	9	0,05	2	78	3,9	78	160
	10	0,06	2	93,6	3,9	94	191
	11	0,07	2	109,2	3,9	109	222
6	12	0,08	2	124,8	2,6	83	169
	13	0,09	2	140,4	2,6	94	190
	14	0,1	2	156	2,6	104	211
	15	0,11	2	171,6	2,6	114	231

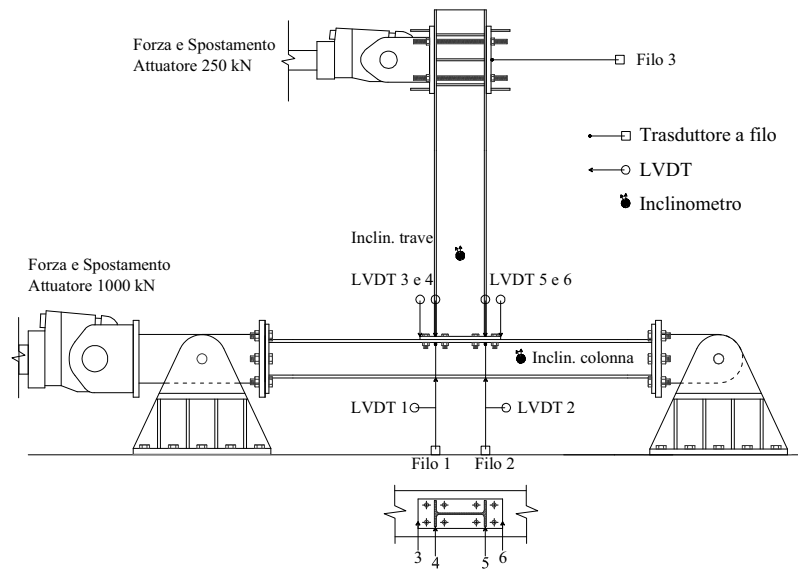


Fig. 3.11 – Position of the instruments

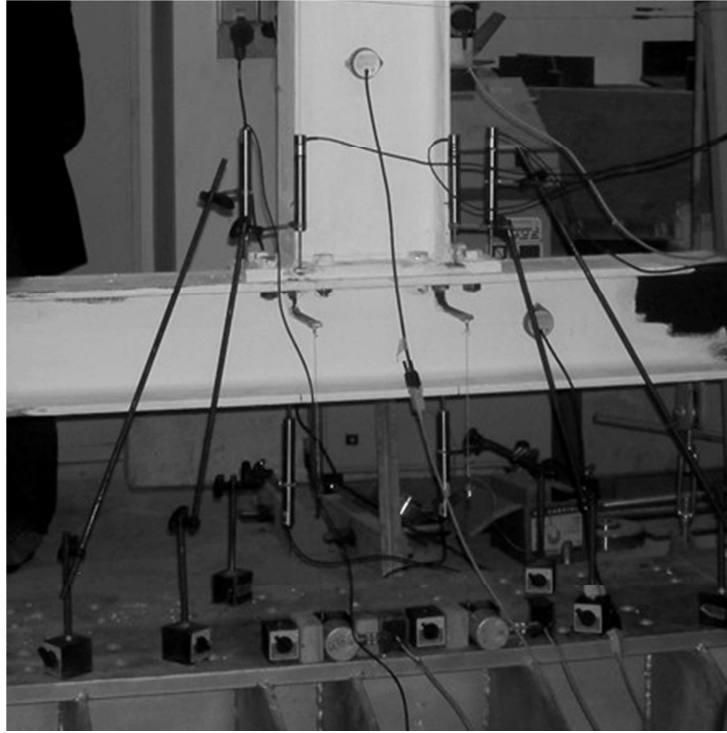


Fig. 3.12 – Setup of the measurement devices

During the tests many parameters have been monitored and acquired, in order to get the test machine history imposed by the top actuator and the displacements of the different joint components (Fig. 3.11). Aiming to the evaluation of the beam end displacements due to the beam-to-column joint rotational response only (δ_j), the displacements measured by means of transducer number 3 have been corrected by subtracting the elastic part due to the beam and to the column flexural deformability:

$$\delta_j = \delta_{Transd,3} - \frac{FL_b^3}{3EI_b} - \frac{FL_c L_b^2}{12EI_c} \left[\left(\frac{L_c}{L_c + 2a} \right)^2 + \frac{6a}{L_c + 2a} \right] \quad (3.1)$$

where a is the length of the rigid parts, due to the steel hinges.

In the following the joint rotation is computed as $\phi_j = \delta_j / L_j$, where L_j is the distance between the column axis and the top actuator (Fig.7). As previously explained, one of the goals of the experimental program is the analysis of the behaviour of each component of bolted extended end-plate connections under cyclic displacement histories. To this scope, the relative displacement recorded by LVDT 3 and 4 gives the displacement of the left T-stub and, analogously, LVDT 5 and LVDT 6 provide the displacement of right T-stub. The shear panel distortion has been computed as the ratio between the relative displacement given by transducers 1 and 2 and the height of the shear panel, equal to the distance between the axis of the beam flanges. Finally, the relative displacement between LVDT 1 and transducer 1, and between LVDT 2 and transducer 2, have provided the displacement of the left and right column panel in tension or compression, respectively.

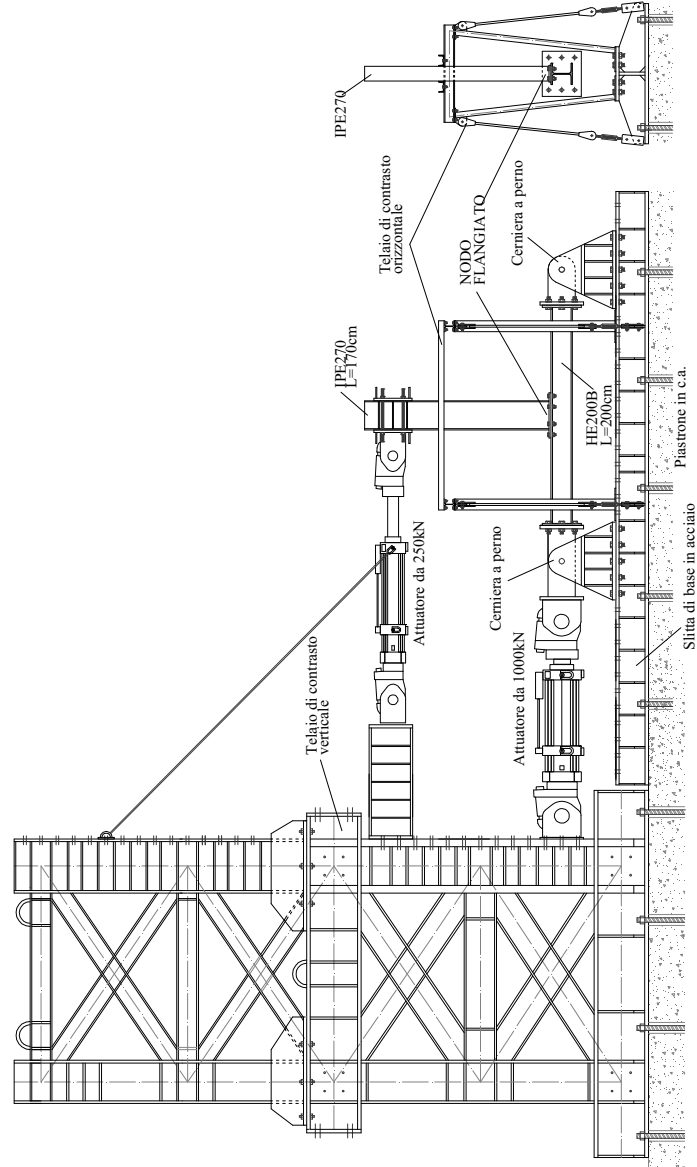


Fig. 3.13 – Experimental Setup

3.3 Design of the specimens

As previously highlighted the dissipative capacity of beam-to-column joints is strongly affected by the weakest joint component. In the following the knowledge of the basic behaviour of the single components will be exploited to govern the joint dissipation. Design of joints will be lead applying the basic concepts introduced by (CEN, 2005a; CEN, 2005b), considering model developed by (Kim & Engelhardt, 2002) for the prediction of the monotonic behaviour of the shear panel, (Faella et al., 2000; Piluso & Rizzano, 2008) model for the prediction of strength and ductility of T-stubs and the design procedure introduced by (Moore et al., 1999) for joints applying the Reduced Beam Section strategy.

All the tested specimens are constituted by an HE 200 B column made of S355 steel and an IPE 270 beam made of S275 steel.

3.3.1 Design of Specimen EEP-CYC 01

Usually beam-to-column joints whose panel zone is involved in the energy dissipation more than the other components provide a cyclic response with negligible degradation of strength and stiffness. Such behaviour is guaranteed provided that buckling of the panel zone in compression and/or shear is avoided.

The first specimen is an extended end-plate connection which has been designed aiming to limit the plastic engage of the end-plate and to maximize

the dissipation of the panel zone in shear. In order to obtain this design goal, the joint has to be designed so that the panel zone in shear is the weakest joint component where the energy dissipation is concentrated. To this scope the analytical models available in the technical literature have been considered to design the connection components.

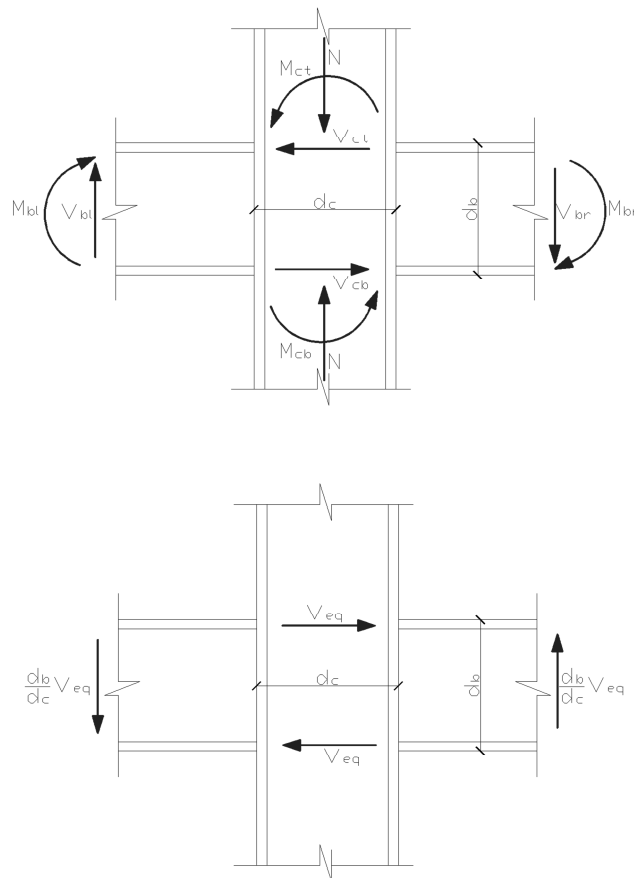


Fig. 3.14 – Definition of the equivalent shear acting in the panel zone

Aiming to obtain the design goal of specimen EEP-CYC 01, it is important to define the elastic resistance of the shear panel in order to design all the other components with sufficient over-strength aiming to engage mainly the panel zone in plastic range. All the existing mathematical models for the panel zone require the computation of the shear force acting on the panel zone.

Considering the internal actions that the joint has to withstand, the shear force acting on the panel zone is given by:

$$V_{pz} = \frac{M_{bl} + M_{br}}{(d_b - t_{bf})} - \frac{(V_{ct} + V_{cb})}{2} \quad (3.2)$$

where M_{bl} and M_{br} are the bending moments at the beam ends located at the left side and at the right side of the joint, respectively; V_{ct} and V_{cb} are the shear forces in the top and bottom column, respectively; d_b is the beam depth and t_{bf} is the thickness of the beam flanges.

By assuming that the points of zero moment in the columns are located at mid-height and accounting for the rotation equilibrium of the joint, the following relationship is obtained:

$$V_{pz} \cong \frac{M_{bl} + M_{br}}{(d_b - t_{bf})} \left(1 - \frac{(d_b - t_{bf})}{L_c} \right) = \frac{M_{bl} + M_{br}}{(d_b - t_{bf})} \beta \quad (3.3)$$

where L_c is the column length (Fig. 3.14). With reference to the tested specimens, as the external joint configuration has been adopted, it results $M_{bl} = 0$ and $M_{br} = M = FL_b$, being F the force transmitted by the actuator and L_b the beam length. In addition, the β factor is close to one as the column length is significantly greater than the beam depth. Under this point of view, it is useful to note that Eurocode 3 (CEN, 2005b) proposes a simplification using a β factor equal to one for one sided joints. For the above reasons, for simplicity the value $\beta=1$ will be used in the following.

The dissipative component of the joint, i.e. the shear panel, has been modelled by means of (Kim & Engelhardt, 2002) monotonic model.

As the ratio between the column flange thickness and the column depth increases, the influence of the column flange thickness on the panel zone yield moment cannot be neglected. Therefore, models accounting for the shear deformations only are not able to grasp the stiffening and strengthening effect due to the local bending of column flanges.

According to Kim and Engelhardt model, it is assumed that the panel zone can be modelled by means of two equivalent beams symmetric with respect to the centre of the panel zone and fixed at the centre. The boundary condition at the ends of these beams is considered to be intermediate between free and completely fixed.

The yield strength of the panel zone is given by the product of three terms:

$$M_y = K_e C_y \gamma_y \quad (3.4)$$

the elastic stiffness calculated considering both the shear stiffness of the column web panel as well as the contribution due to the flexural stiffness of the column flanges (K_e), an average shear deformation factor accounting for the distribution of shear stresses in the panel zone at yielding (C_y) and the shear deformation (γ).

In the elastic range, the shear deformation of the panel zone is computed as the sum of the contribution due to the column web panel and the contribution due to the column flanges:

$$\delta = \left(\frac{1}{k_b} + \frac{1}{k_s} \right) V_{pz} \quad (3.5)$$

where with reference to the tested specimen:

$$k_b = \frac{C_r EI_c}{\left[(d_b - t_{bf}) / 2 \right]^3} = \frac{5 \cdot 210000 \cdot 56960000}{\left[(270 - 10) / 2 \right]^3} = 27222576 \text{ N/mm} \quad (3.6)$$

$$k_s = \frac{G(A_{vc} + R_f A_{dp})}{\left[(d_b - t_{bf}) / 2 \right]} = \frac{80769 \cdot 2483}{\left[(270 - 10) / 2 \right]} = 1542688 \text{ N/mm} \quad (3.7)$$

in which C_r is a restraint factor accounting for the boundary conditions of the column flanges and calibrated by comparison between experimental test results and FEM analyses so that $C_r=5$ is suggested (Kim & Engelhardt, 2002). In addition, E and G are the elastic and the shear modulus, respectively, I_c is the moment of inertia of the column section, d_c is the column depth, A_{vc} is the

column web shear area, A_{dp} is the shear area of doubler plates if adopted in the structural detail and R_f is a factor accounting for the strain incompatibility between supplementary web plates and column web panel. The joint rotational stiffness due to the panel zone in shear is given by (Kim & Engelhardt, 2002):

$$K_e = \frac{k_b k_s}{k_b + k_s} \frac{(d_b - t_{bf})}{2} \frac{(d_b - t_{bf})}{\beta} = \frac{27222576 \cdot 1542688}{27222576 + 1542688} \frac{(270 - 10)^2}{2 \cdot 1} = 4.93 \cdot 10^{10} \text{ Nmm/rad} \quad (3.8)$$

The product $C_y \gamma_y$ in Eq.(3.4) represents the average shear deformation of the panel zone. According to Kim and Engelhardt C_y varies in the range 0.8-0.9, so that for design scopes, the mean value $C_y = 0.85$ can be adopted. The shear deformation has to be computed accounting also for the interaction between shear stress and normal stress due to the column axial force. Therefore, taking into account that for the tested specimens a constant axial force equal to 30% of the squash load has been applied, according to Von Mises yield criterion, the shear deformation at yielding is given by:

$$\gamma_y = \frac{f_y}{\sqrt{3}G} \sqrt{1 - \left(\frac{P}{P_y}\right)^2} = \frac{355}{\sqrt{3} \cdot 80769} \sqrt{1 - (0.3)^2} = 0.00242 \quad (3.9)$$

Finally, the bending moment corresponding to the yielding of panel zone in shear is computed by means of Eq.(3.4):

$$M_{y,pz} = 4.93 \cdot 10^{10} \cdot 0.85 \cdot 0.00242 = 1.01 \cdot 10^8 \text{ Nmm} = 101 \text{ kNm} \quad (3.10)$$

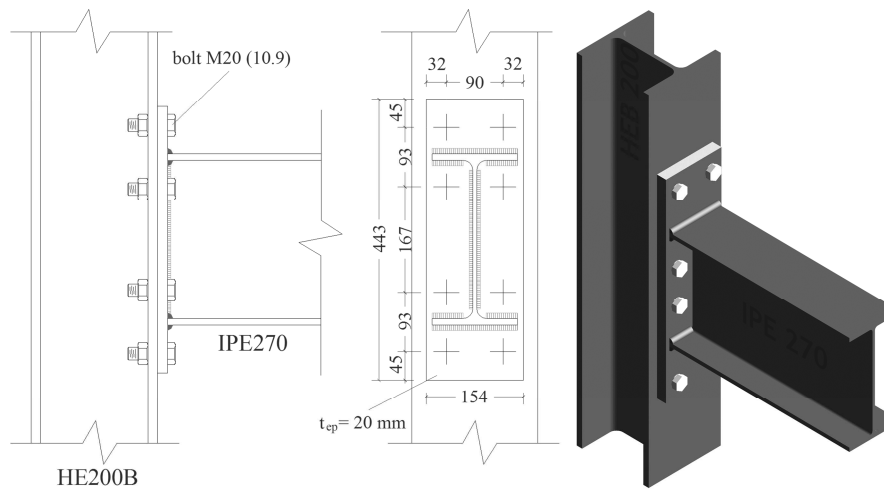


Fig. 3.15 –Rendering and Geometry of joint *EEP – CYC 01*

The plastic moment of the connected beam (IPE270) is given by:

$$M_{pb} = W_{pl} f_y = 484000 \cdot 275 = 1.33 \cdot 10^8 \text{ Nmm} = 133 \text{ kNm} \quad (3.11)$$

Therefore, according to the joint classification by strength proposed by Eurocode 3, the partial strength ratio of EEP-CYC 01 specimen is given by:

$$\eta_{ps} = \frac{M_{y,pz}}{M_{pb}} = \frac{101}{133} = 0.759 \quad (3.12)$$

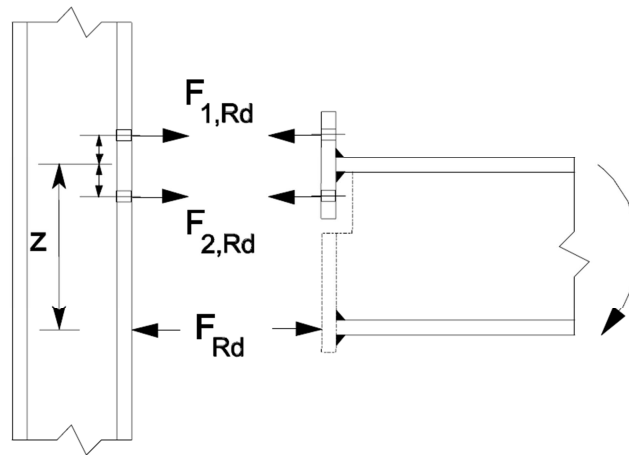


Fig. 3.16 – Simplified model considered in the design of end-plate (CEN, 2005)

The design of the end-plate requires the consideration of many parameters, such as the width of the end-plate, the number of bolt rows, the end-plate thickness and the location of the bolt rows.

Regarding the end-plate in bending, according to Eurocode 3, it is modelled by means of an equivalent T-stub. With reference to EEP-CYC 01 specimen, the structural detail of the end-plate is depicted in Fig. 3.15. It is made of S275 steel and connected with 10.9 bolts. Following the simplified approach suggested by Eurocode 3 in section 6.2.7.1 which represents a conservative simplification provided that the bolt rows are approximately equidistant from the beam flange (Fig. 3.16), the two bolt rows in tension constitute an equivalent T-stub.

It is well known that the design resistance of the equivalent T-stub is obtained as the minimum value of the design resistances corresponding to three failure

modes, namely flange yielding or type-1 mechanism, flange yielding with bolt fracture or type-2 mechanism and bolt fracture or type-3 mechanism. The design resistance for type-1 mechanism is given by:

$$F_{1,Rd} = \frac{4M_{pl,ep}}{m} \quad (3.13)$$

The design resistance for type-2 mechanism is given by:

$$F_{2,Rd} = \frac{2M_{pl,ep} + 2B_{Rd}n}{(m+n)} \quad (3.14)$$

Finally, in case of type-3 mechanism:

$$F_{3,Rd} = 2B_{Rd} \quad (3.15)$$

In the above equations [(3.13)-(3.15)], referred to a single bolt row, $M_{pl,ep}$ is the plastic moment of the end-plate, depending on its effective width b_{eff} ; m is the distance between the bolt axis and the plastic hinge located at the flange-to-web connection; n is the distance between the bolt axis and the edge where prying forces are located; B_{Rd} is the bolt design resistance. The parameter governing the failure mode is:

$$\beta_{Rd} = \frac{4M_{pl,ep}}{2B_{Rd}m} \quad (3.16)$$

The geometric parameters of the equivalent T-stub modelling the bolt rows in tension are: $m = d - 0.8\sqrt{2}a = 45 - 0.8 \cdot 10 = 37mm$, $n = 45mm$ and $b = 154mm$.

The end-plate thickness has been designed aiming to obtain two design goals. In fact, specimen EEP-CYC 01 has to be characterized by the panel zone in shear as weakest joint component, so that the end-plate in bending has to possess sufficient overstrength with respect to that component:

$$F_{ep,Rd} = 1.2 \frac{M_{y,pz}}{(d_b - t_{bf})} \quad (3.17)$$

where 20% overstrength has been imposed, being:

$$F_{ep,Rd} = \min\{F_{1,Rd}, F_{2,Rd}, F_{3,Rd}\} \quad (3.18)$$

In addition, in order to maximize the energy dissipation capacity excluding brittle failure modes, type-1 mechanism, i.e. end-plate yielding, has to be preferred. The condition assuring the development of mechanism type-1 is:

$$\beta_{Rd} \leq \frac{2\lambda}{1 + 2\lambda} \quad (3.19)$$

where $\lambda=n/m$ (Fig. 3.17).

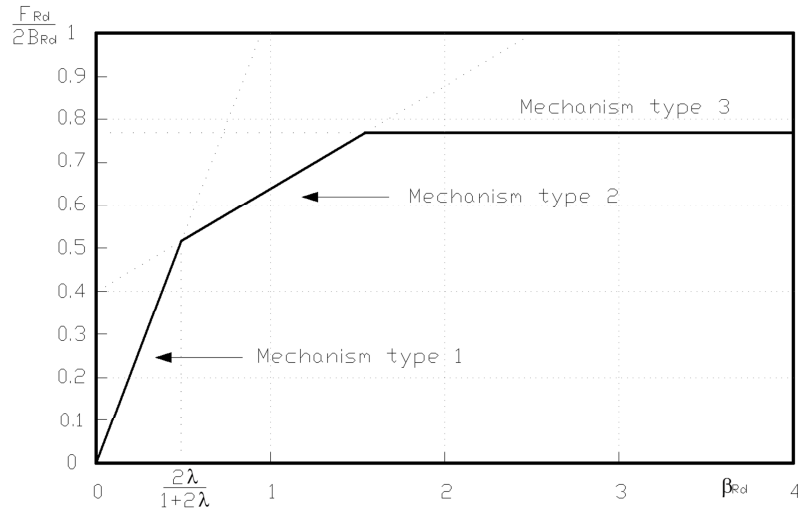


Fig. 3.17 – Influence of coefficient β_{Rd} on the collapse mechanism

From this last condition the following limitation to the thickness of the plate derives:

$$t_{ep} \leq \sqrt{\frac{4B_{Rd}nm}{b_{eff}f_y(m+2n)}} = \sqrt{\frac{4 \cdot 220500 \cdot 45 \cdot 37}{(154/2) \cdot 275(37+2 \cdot 45)}} = 23.4 \text{ mm} \quad (3.20)$$

where $B_{Rd} = k_2 f_{ub} A_s = 0.9 \cdot 1000 \cdot 245 = 220500 N$, $b_{eff} = 154/2 = 77 mm$ is the effective width of the single bolt row. Mechanism-1 is assured provided that (3.20) is satisfied. In such a case, (3.17) provides:

$$\frac{2b_{eff}t_{ep}^2}{m}f_y = 1.2 \frac{M_{y,pz}}{(d_b - t_{bf})} \quad (3.21)$$

leading to:

$$t_{ep} = \sqrt{\frac{1.2M_{y,pz}m}{(d_b - t_{bf})2b_{eff}f_y}} = \sqrt{\frac{1.2 \cdot 101000000 \cdot 37}{260 \cdot 154 \cdot 275}} = 20.18 \text{ mm} \quad (3.22)$$

Therefore, an end-plate thickness equal to 20 mm provides an adequate overstrength assuring also a type-1 mechanism.

Finally, in order to limit the plastic engagement of column web panel in transverse compression, a sufficient over-strength of this component with respect to the strength of the weakest joint component has to be assured. In addition, aiming to avoid brittle mechanisms, the occurrence of buckling phenomena regarding the column web panel in transverse compression has to be prevented. With reference to the formulation provided by Eurocode 3, the buckling resistance of an unstiffened column web panel in compression can be determined as:

$$F_{cwc} = \omega k_{wc} \rho b_{eff,cwc} t_{cwc} f_y \quad (3.23)$$

in which ω is a factor accounting for the effects of shear interaction in the column web panel, k_{wc} is a reduction factor accounting for the influence of

normal stress on the column web panel resistance, ρ provides the influence of the buckling phenomenon on the collapse strength, $b_{eff,cwc}$ is the effective width of the column web in transverse compression given by a spreading trough at 45° through the end plate and by a 1:2.5 spreading through the column. Finally, t_{cw} is the column web thickness.

The effective width of the column web panel in transverse compression for bolted end-plate connection is given by:

$$b_{eff,cwc} = t_{bf} + 2\sqrt{2}a + 5(t_{cf} + s) + s_p = 10.2 + 2 \cdot 10 + 5 \cdot (15 + 18) + 40 = 235.2 \text{ mm} \quad (3.24)$$

where s in case of rolled sections is the column flange-to-web root radius, s_p is the length obtained by a 45° spreading through the end-plate.

The reduction factor for plate buckling ρ is defined starting from the definition of the plate slenderness:

$$\bar{\lambda}_p = 0.932 \sqrt{\frac{b_{eff,cwc} d_{wc} f_y}{Et_{cw}^2}} = 0.932 \sqrt{\frac{235.2 \cdot 134 \cdot 355}{210000 \cdot 9^2}} = 0.756 \quad (3.25)$$

where d_{wc} is the column web panel height. Being the plate slenderness greater than 0.72, the reduction factor ρ accounting for the buckling phenomenon is computed according to the Winter formula:

$$\rho = \frac{(\bar{\lambda}_p - 0.2)}{\bar{\lambda}_p^2} = \frac{(0.756 - 0.2)}{0.756^2} = 0.973 \quad (3.26)$$

Besides, the ω factor, which gives the influence of the shear interaction on the resistance of the web panel in transverse compression, is function of the parameter β . As already discussed β has been assumed equal to 1, which is an assumption valid for external joints. The expression of the ω factor for $\beta=1$ is given by Eurocode 3 as a function of the ratio between column web shear area (A_{vc}) and panel area in transverse compression.

$$\omega = \sqrt{\frac{1}{1 + 1.3 \left(\frac{b_{eff,cwc} t_{cw}}{A_{vc}} \right)^2}} = \sqrt{\frac{1}{1 + 1.3 \left(\frac{235.2 \cdot 9}{2483} \right)^2}} \cong 0.717 \quad (3.27)$$

In addition, the interaction factor accounting for normal stress effects, i.e. k_{wc} , can be assumed equal to 1, provided that normal stress at the column root radius does not exceed 70% of steel ultimate stress. Thus the column web panel in transverse compression resistance is:

$$F_{cwc} = 0.717 \cdot 1 \cdot 0.973 \cdot 235.2 \cdot 9 \cdot 355 = 524252 \text{ N} \quad (3.28)$$

Therefore, the over-strength level of the panel web in transverse compression is given by the ratio:

$$\frac{F_{cwc} \cdot (d_b - t_{bf})}{M_{y,pz}} = \frac{524252 \cdot 260}{101000000} \cong 1.35 \quad (3.29)$$

Which is sufficient to prevent brittle failure modes.

3.3.2 Design of specimen EEP-CYC 02

The second beam-to-column joint included in the experimental program has been designed with the purpose of investigating the ductility and energy dissipation capacity of an extended end-plate connection where the component mainly engaged in plastic range is the end-plate in bending. In this case, the exclusion of the components related to the column web panel requires the use of stiffeners, such as doubler plates and continuity plates. Extended end-plate connections offer a great variety of geometrical configurations in the design of the structural detail due to the amount of parameters involved in the definition of stiffness, strength and ductility capacity (Faella et al., 1998a; Faella et al., 1998b; Faella et al., 2000).

Specimen EEP-CYC 02 has been designed aiming to obtain the same resistance of specimen EEP-CYC 01, but relying on the ductility supply of the end-plate, by properly designing its thickness and the bolt location.

Like the previous specimen, the first component to be designed is the weakest component, i.e. the end-plate. Successively, the other components are designed to have sufficient overstrength aiming to avoid their plastic engage.

As already done for the previous specimen, the end-plate in bending is modelled, by means of a simplified approach considering an equivalent T-stub for the bolt rows in tension (Fig. 3.16).

As already highlighted, the basic idea is to control both the joint flexural strength and the plastic rotation supply. To this scope, the width of the end-plate can be fixed while the end-plate thickness and the location of the bolts have to be properly detailed. The flexural resistance of the joint, provided that the end-plate in bending is the weakest component and it fails according to type-1 mechanism, is given by:

$$\frac{2b_{eff}t_{ep}^2}{m} f_y (d_b - t_{bf}) = M_{jR,d} = 100 \text{ kNm} \quad (3.30)$$

where b_{eff} is the effective width of the single bolt row. Eq.(3.22) is valid provided that Eq.(3.20) is satisfied.

In addition, aiming at the control of the plastic rotation supply, it can be considered that the plastic rotation supply is equal to the ratio between the plastic deformation of the T-stub modelling the bolt rows in tension and the lever arm:

$$\varphi_u = \frac{\delta_{u,ep}}{(d_b - t_{bf})} \quad (3.31)$$

According to (Piluso et al., 2001), the ultimate plastic displacement of a T-stub failing according to type-1 mechanism can be computed as:

$$\delta_{u,ep} = \frac{Cm^2}{2t_{ep}} \quad (3.32)$$

where C is a constant depending on the material properties. The value $C=0.1951$ can be assumed for S275 steel grade (Faella et al., 2000). Therefore, the plastic rotation supply can be computed as:

$$\varphi_u = \frac{Cm^2}{2t_{ep}(d_b - t_{bf})} \quad (3.33)$$

By imposing $M_j=100\text{kNm}$ (the same resistance of specimen EEP-CYC01) and $\varphi_u=0.05$ rad, Eq.(3.33) and Eq.(3.30) constitute a system where the unknowns are the bolt location m and the end-plate thickness t_{ep} whose solution provides:

$$m = \left[\frac{4M_{jR,d}\varphi^2(d_b - t_{bf})}{C^2 b_{eff} f_y} \right]^{1/3} = \left[\frac{2 \cdot 100000000 \cdot 0.05^2 \cdot 260}{0.1951^2 \cdot (154/2) \cdot 275} \right]^{1/3} = 54.4 \text{ mm} \quad (3.34)$$

and:

$$t_{ep} = \frac{Cm^2}{2\varphi_u(d_b - t_{bf})} = \frac{0.1951 \cdot 54.4^2}{2 \cdot 0.05 \cdot 260} = 22.2 \text{ mm} \quad (3.35)$$

In addition, in order to assure a type-1 mechanism, Eq.(3.20) provides the following limitation to the end-plate thickness:

$$t_{ep} \leq \sqrt{\frac{4B_{Rd}nm}{b_{eff}f_y(m+2n)}} = \sqrt{\frac{4 \cdot 220500 \cdot 40 \cdot 54.4}{(154/2) \cdot 275 \cdot (54.4 + 2 \cdot 40)}} = 25.96 \approx 26 \text{ mm} \quad (3.36)$$

On the basis of the above results, dealing with specimen EEP-CYC02, an end-plate thickness $t_{ep}=20$ mm is chosen assuming a bolt location $m=54$ mm. After the design of the weakest component of the joint, it is possible to design the components related to the column web zone. The shear panel resistance can be designed as already discussed with reference to EEP-CYC 01 specimen. In order to obtain a sufficient overstrength degree two 10 mm supplementary web plates have been adopted. By means of equations [(3.4)-(3.10)] and considering a full effectiveness of the supplementary web plates, the shear panel resistance can be computed as:

$$k_b = \frac{C_r EI_c}{[(d_b - t_{bf})/2]^3} = \frac{5 \cdot 210000 \cdot 56960000}{[(270 - 10)/2]^3} = 27222576 \text{ N/mm} \quad (3.37)$$

$$k_s = \frac{G(A_{vc} + R_f A_{dp})}{[(d_b - t_{bf})/2]} = \frac{80769 \cdot (2483 + 3700)}{[(270 - 10)/2]} = 3841498 \text{ N/mm} \quad (3.38)$$

$$\begin{aligned} K_e &= \frac{k_b k_s}{k_b + k_s} \frac{(d_b - t_{bf})}{2} \frac{(d_b - t_{bf})}{\beta} = \\ &= \frac{27222576 \cdot 3841498}{27222576 + 3841498} \frac{(270 - 10)^2}{2 \cdot 1} = 1.138 \cdot 10^{11} \text{ Nmm} \end{aligned} \quad (3.39)$$

$$M_{pz} = 1.137 \cdot 10^{11} \cdot 0.85 \cdot 0.00242 = 233.9 \cdot 10^6 \text{ Nmm} \approx 234 \text{ kNm} \quad (3.40)$$

Therefore, by adopting such supplementary web plates, the shear panel resistance is greater than the joint design resistance of a factor greater than 2, so that it is expected that the panel zone remains in elastic range up to the failure of the end-plate in bending. Moreover, the use of a couple of continuity plates with a thickness equal to the beam flange thickness assures that the column web in tension and the column web in compression also remain in elastic range. The structural detail of specimen EEP-CYC 02, as resulting from the above design criteria, is depicted in Fig. 3.18.

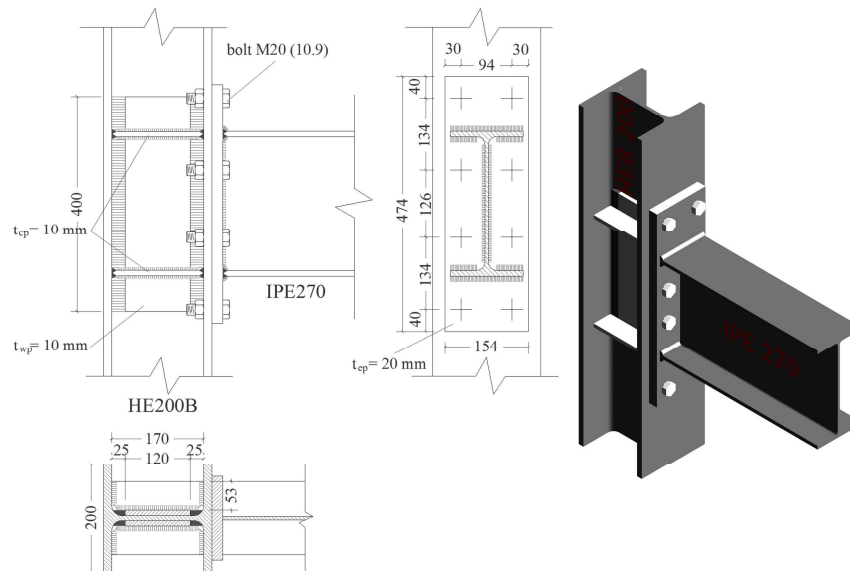


Fig. 3.18 – Geometry and rendering of specimen EEP-CYC 02

3.3.3 Design of specimen EEP-DB-CYC 03

The third specimen is a full strength extended end-plate connection, so that it is aimed to investigate the energy dissipation capacity of the connected beam. However, aiming to obtain the same flexural resistance of previous specimens, the reduced beam section (RBS) strategy, namely also “dog bone”, has been adopted. In last years, many research projects about this kind of connection have been developed. The three parameters to be designed are the distance of the reduced section zone from the face of the column flange (a), the length of the reduced section zone (b) and the flange reduction width (c) (Fig. 3.19).

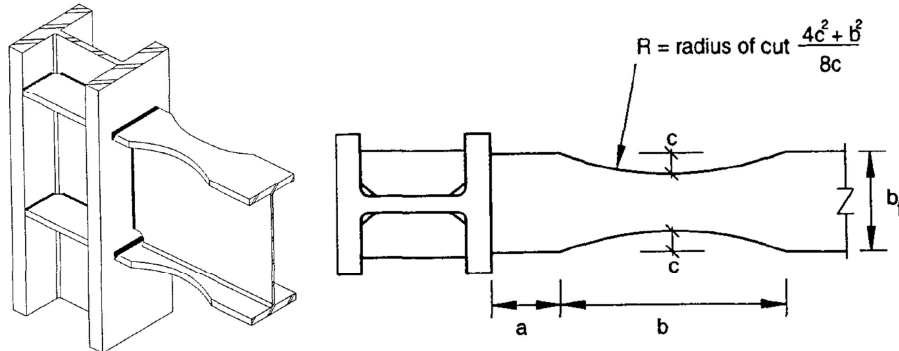


Fig. 3.19 – Definition of RBS parameters

The first two parameters should be chosen as little as possible in order to minimize the stepping up of the moment due to the distance between the plastic hinge and the column face (Fig. 3.20). At the same time the RBS centre should be not too far away to allow the complete yielding of beam flanges along the end section zone whose length should be sufficient to avoid plastic strain concentrations. A detailed discussion about the dimensioning of the amount of flange reduction (c) and of the distance between the centre of RBS zone and the face of the column flange is given in (Montuori & Piluso, 2000), where also the influence of the uniform load acting on the beam is taken into account. However, structural schemes adopted for testing beam-to-column connections are more simple than real structures, because the beam uniform load is missing. For this reason, the simple design procedure suggested in (Moore et al., 1999) can be adopted without any trouble. In particular, it is suggested to use values of the two parameters a and b according to the following ranges:

$$0.5b_f \leq a \leq 0.75b_f \quad (3.41)$$

$$0.65d_f \leq b \leq 0.85d_f \quad (3.42)$$

last parameter to be considered is the amount of flange reduction (c) which controls the maximum bending moment at the RBS and, as consequence, the maximum moment at the face of the column flange.

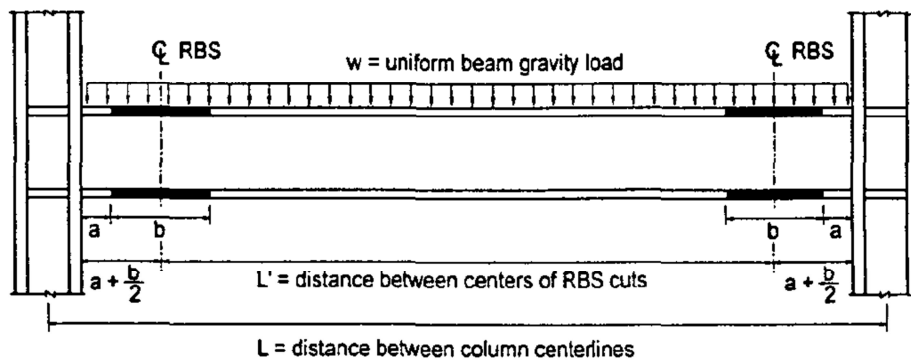


Fig. 3.20 – Typical scheme of beam with RBS

The value of c should be limited in order to obtain a moment at the column face in a range contained in the 85-100% of the beam cross section plastic moment. According to past experiences, (Engelhardt et al., 1997; Engelhardt et al., 1996) suggests to avoid the use of these kinds of connections for reductions greater than 50%. Therefore, c must not be greater than $0.25b_f$.

The design procedure usually is iterative, because the moment at the column face can be evaluated only after the choice of the three geometrical

parameters, so that the fulfilment of suggested limits can be checked. In addition, the beam-column hierarchy criterion and the absence of shear mechanisms have to be checked. With reference to IPE 270 section of tested specimens, the design parameters have been identified after few iterations:

$$a = 70\text{mm} \quad b = 180\text{mm} \quad c = 22\text{mm} \quad (3.43)$$

In particular, the amount of flange reduction (c) has been dimensioned so that the plastic moment is equal to the joint resistance of the other specimens. In fact, the plastic moment of RBS is given by:

$$\begin{aligned} M_{pl,RBS} &= W_{pl,RBS} f_y = [W_{pl,b} - 2ct_{bf}(d_b - t_{bf})] f_y = \\ &= [484000 - 2 \cdot 22 \cdot 10 \cdot (270 - 10)] \cdot 275 = 101640000 \text{Nmm} \end{aligned} \quad (3.44)$$

The design of the other elements of the connection, which have to remain in elastic range, has been carried out taking in account two effects: the strain hardening of steel, considered by a 1.15 factor and the expected yield strength herein assumed equal to $1.13f_y$, resulting from a coefficient of variation equal to 0.07. Therefore, the expected resistance of RBS at its centre line can be evaluated as:

$$\begin{aligned} M_{RBS,E} &= 1.15 W_{pl,RBS} f_{y,E} = 1.15 \cdot 369600 \cdot 1.13 \cdot 275 = \\ &= 132081180 \text{Nmm} \cong 132.1 \text{ kNm} \end{aligned} \quad (3.45)$$

Starting from the knowledge of the expected moment at the RBS centre, it is possible to evaluate the bending moment at the column face to check that it is contained in the stated limits and to design the end-plate and the shear panel in order remain in elastic range. To this scope it is necessary to evaluate the shear force acting at the RBS centreline, that is given by the ratio between the maximum moment expected at the reduced section zone given by Eq.(3.45) and the beam length up to the “dog-bone” centreline:

$$V_{RBS,E} = \frac{M_{RBS,E}}{\left(L_b - a - \frac{b}{2}\right)} = \frac{132081180}{\left(1460 - 70 - \frac{180}{2}\right)} = 101601N \cong 101.6 \text{ kN} \quad (3.46)$$

where L_b is the beam length. Neglecting the end-plate thickness, the moment acting on the column face and the plastic moment of the beam can be evaluated by means of the following expressions (Fig. 3.21):

$$M_c = M_{RBS,E} + V_{RBS,E} \left(a + \frac{b}{2}\right) = 132081180 + 101601 \left(70 + \frac{180}{2}\right) = 148337340 \text{ Nmm} \cong 148.3 \text{ kNm} \quad (3.47)$$

$$M_b = W_{pl,b} f_{y,E} = 484000 \cdot 1.13 \cdot 275 = 150403000 \text{ Nmm} \cong 150.4 \text{ kNm} \quad (3.48)$$

Therefore, being $M_c/M_b \cong 1$, the suggested limit 85%-100% is satisfied. It is easy to check that the strong column-weak beam requirement is also satisfied, being the sum of the plastic moments of columns, reduced to account for the influence of the axial load, greater than the bending moment M_c transmitted by the RBS to the column face.

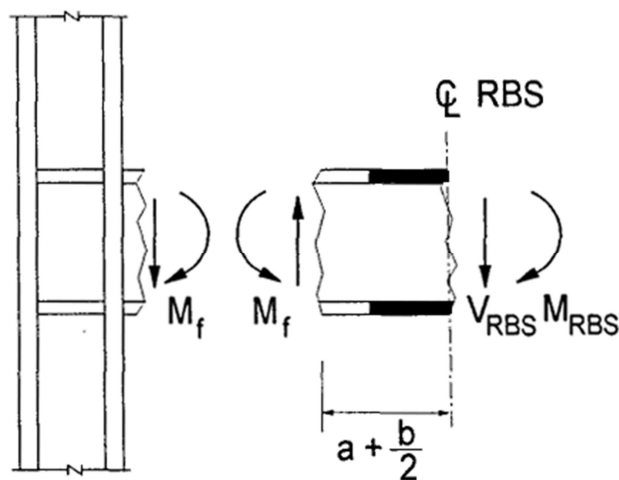


Fig. 3.21 – Scheme of the actions transferred by the RBS to the column

In addition, according to FEMA 267A (SAC, 1997), the shear panel must be designed to withstand a shear action equal to 80% of the one corresponding to the maximum bending moment acting at the column face. Adopting for the panel zone the same structural detail of EEP-CYC 02 specimen, assuming a β factor equal to one, the following overstrength is obtained.

$$\frac{V_{R,sp}}{V_{S,sp}} = \frac{V_{R,sp}}{0.8 \cdot \frac{\sum M_c}{(d_b - t_{bf})}} = \frac{900000}{\frac{0.8 \cdot 148337340}{(270 - 10)}} = 1.97 > 1 \quad (3.49)$$

Finally, the end-plate thickness can be evaluated, fixing the plate width $b=154$ mm ($b_{eff}=77$ mm), the bolt location $m=33.5$ mm and adopting M24 bolts of 10.9 class as follows:

$$t_{ep} = \sqrt{\frac{M_c m}{(d_b - t_{bf}) \cdot (2b_{eff}) f_y}} = \sqrt{\frac{148337340 \cdot 33.5}{(270 - 10) \cdot (2 \cdot 77) \cdot 275}} = 21.24 \text{ mm} \quad (3.50)$$

which gives the minimum thickness to be adopted to satisfy the resistance requirement, provided that mechanism type-1 is assured, and:

$$t_{ep} \leq \sqrt{\frac{4B_{Rd} nm}{b_{eff} f_y (m + 2n)}} = \sqrt{\frac{4 \cdot 317700 \cdot 35 \cdot 33.5}{77 \cdot 275 \cdot (33.5 + 2 \cdot 35)}} = 26.07 \text{ mm} \quad (3.51)$$

providing the condition to be satisfied to assure type-1 mechanism. On the basis of the above results, an end-plate thickness equal to 25 mm has been chosen. The geometry of specimen EEP-DB-CYC 03 is depicted in Fig.6.

3.3.4 Design of specimen TS-CYC 04

This specimen is a double tee connection. The design goal is, like in test EEP-CYC 02, to avoid the plastic engage of the components related to the column web panel, i.e. the column web in tension and column web in compression and the panel zone in shear.

The main advantage of double tee connections is due to the easy repair. In fact, if the panel zone is well designed, after a seismic event it is possible to substitute only the end T-stubs. The design of this joint can be carried out using the relationships already exploited for specimen EEP-CYC 02. Obviously, in this case the modelling by means of two separate bolted T-stub is even more realistic. Also in this case the same flexural resistance of the other joints has been imposed requiring, in addition, a plastic rotation supply of about 0.08 rad so that the following geometrical requirements have been computed:

$$m = \left[\frac{2M_{j,Rd} \varphi^2 (d_b - t_{bf})}{C^2 b f_y} \right]^{1/3} = \left[\frac{2 \cdot 100000000 \cdot 0.08^2 \cdot 260}{0.1951^2 \cdot 77 \cdot 275} \right]^{1/3} = 74.5 \text{ mm} \quad (3.52)$$

$$t_{ep} = \frac{Cm^2}{2\varphi(d_b - t_{bf})} = \frac{0.1951 \cdot 74.5^2}{2 \cdot 0.08 \cdot 260} = 26 \text{ mm} \quad (3.53)$$

$$t_{ep} \leq \sqrt{\frac{4B_{Rd}nm}{b_{eff} \cdot f_y (m + 2n)}} = \sqrt{\frac{4 \cdot 220500 \cdot 40 \cdot 74.5}{77 \cdot 275 \cdot (74.5 + 2 \cdot 40)}} = 28.3 \text{ mm} \quad (3.54)$$

A plate thickness equal to 25 mm and a bolt location with m equal to 73 mm have been chosen to respect ductility requirement. The two T-stub elements have been connected through the webs to the beam flanges by means of eight M20 bolts. The ultimate strength of such connection according to Eurocode 3, is given by:

$$F = n_b \alpha_v f_{ub} A = 8 \cdot 0.5 \cdot 1000 \cdot 245 = 980000 N \geq \frac{M_{j,Rd}}{(d_b - t_{bf})} =$$

$$= 384615 N \quad (3.55)$$

The geometry of the specimen is depicted in Fig. 3.22.

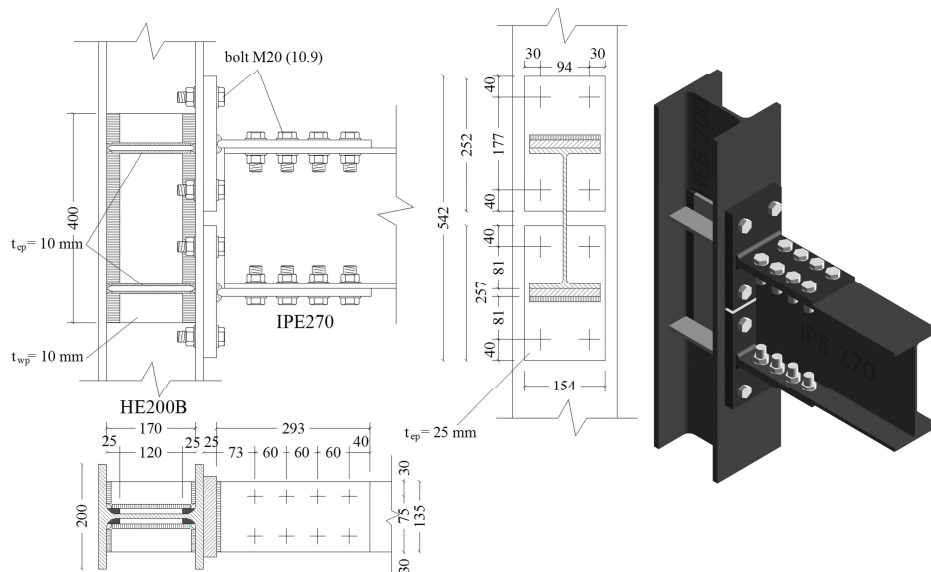


Fig. 3.22 – Rendering and Geometry of test TS-CYC 04

3.4 Description of the Experimental Tests

3.4.1 Description of test EEP-CYC 01

In the three following pictures experimental setup and measurement instruments used in test EEP-CYC 01 are shown.

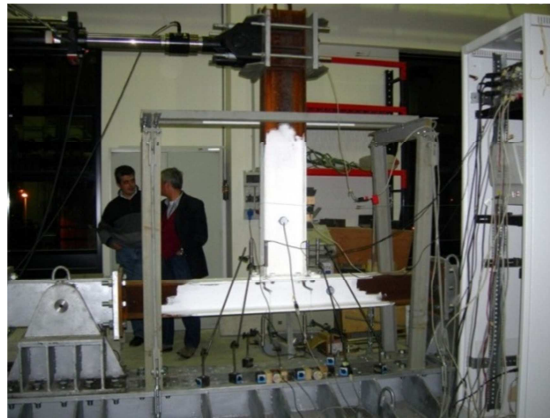


Fig. 3.23 – Test EEP-CYC 01

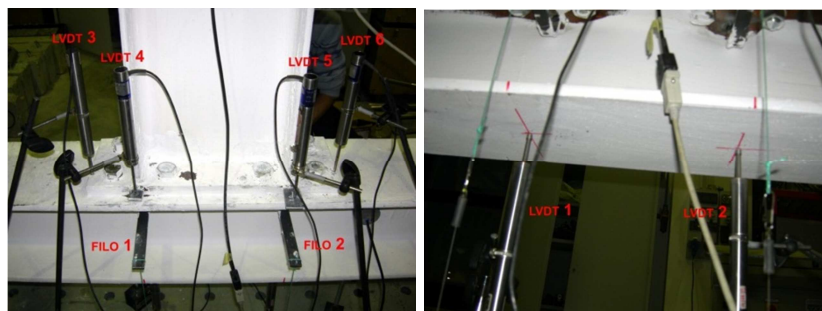


Fig. 3.24 – Measurement devices EEP-CYC 01

Specimen EEP-CYC 01 has exhibited shear panel yielding since the first cycles. In fact, the formation of 45° yield lines on the panel zone has been immediately observed. The use of white wash has allowed yielded zones to be pointed out. According to the adopted design criteria, the end-plate T-stubs have entered in plastic range only under great displacement amplitudes, when the shear panel was almost all yielded (Fig. 3.25).

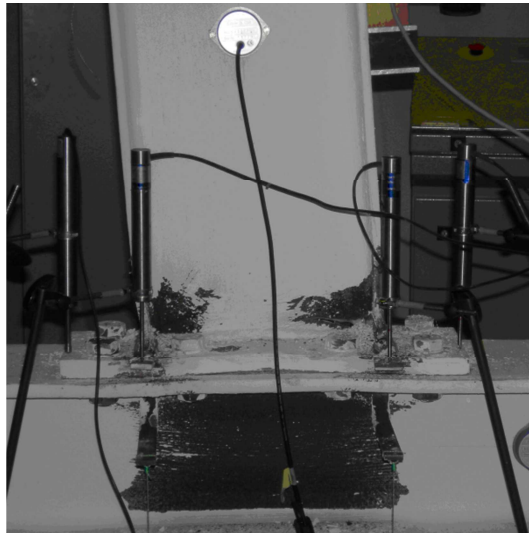


Fig. 3.25 – Measurement devices EEP-CYC 01

It hasn't been noted a significant detachment between the end-plate and the column flange, so that end-plate exhibited a behaviour close to type-1 mechanism. The collapse has been attained due to the brittle failure of the welds connecting the beam flange to the end-plate, when the joint maximum resistance was already achieved. This kind of failure mode is probably due to

the stress concentration arising in the welds in the central zone (Fig. 3.26) close to the beam web of the connected member resulting from the omission of continuity plates and, in addition, to the big deformation reached by the panel zone in shear.

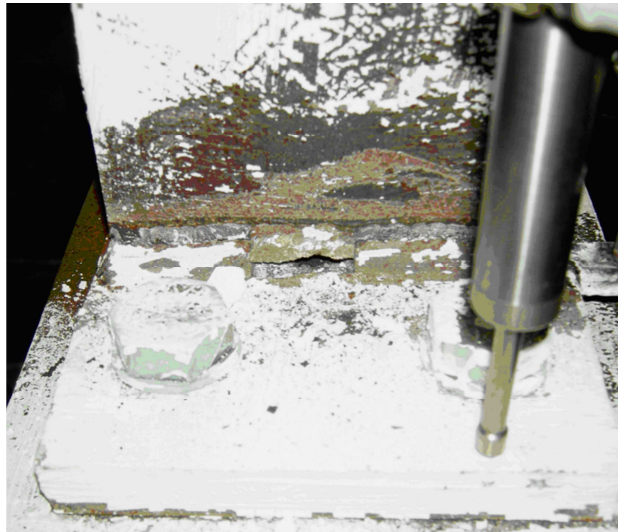


Fig. 3.26 – Failure of EEP-CYC 01 specimen due to brittle collapse of beam flange to end-plate welds

The moment-rotation response of the whole joint is depicted in Fig. 3.27. The participation of the column web, under alternate tension and compression actions, to the energy dissipation has been also observed.

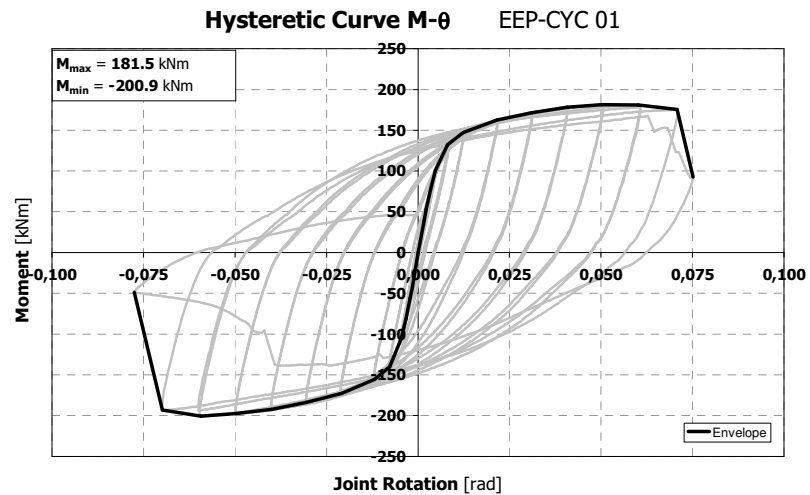


Fig. 3.27 – EEP-CYC 01 Moment-Rotation curve

In particular, as previously described, using the displacements recorded by LVDT 3 to 6, the hysteretic behaviour of the end-plate equivalent T-stubs has been determined (Fig. 3.28). In addition, by means of the measured displacements given by LVDT 1 and 2 and by means of the transducers 1 and 2 the behaviour of the panel components, both the panel zone in shear (Fig. 3.29) and of the column web under alternate transverse tension and compression (Fig. 3.30), has been determined.

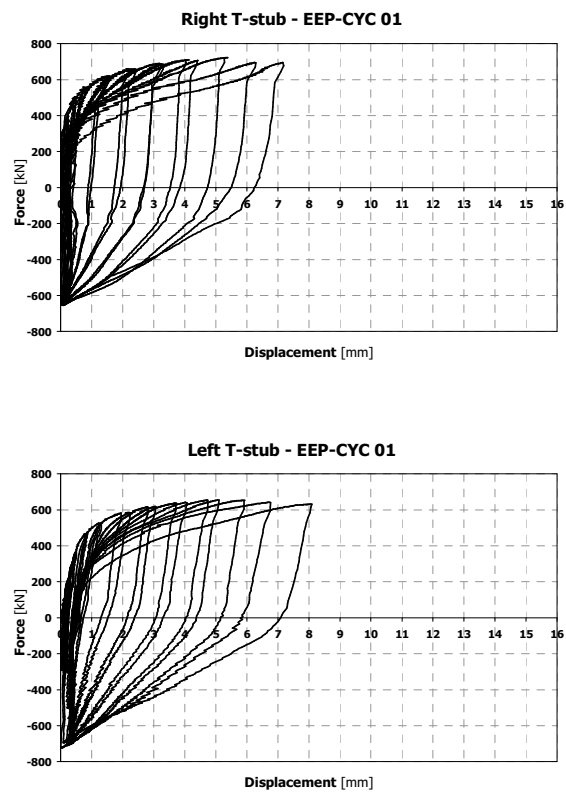


Fig. 3.28 – Hysteretic response of end plate equivalent T-stubs

The measure of the component hysteretic behaviour has pointed out that, as desired by the specimen design process, the dissipation has been mostly governed by the shear panel, with a lower contribution of the end-plate T-stubs and almost negligible contribution of the column web under tension and compression .

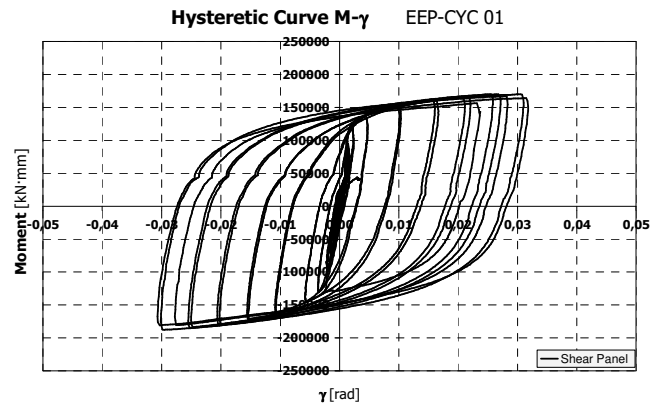


Fig. 3.29 – Cyclic response of column web in shear

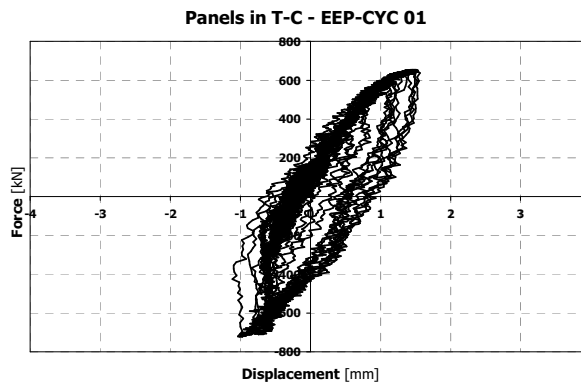


Fig. 3.30 – Cyclic response of column web under alternate tension and compression

Finally, in order to check the correct identification of the joint components and the possibility to extend the component approach to the prediction of the cyclic behaviour of joints, the energy dissipated by the whole joint has been

compared with the sum of the energy dissipated by the single components, clearly obtaining a good agreement (Fig. 3.31).

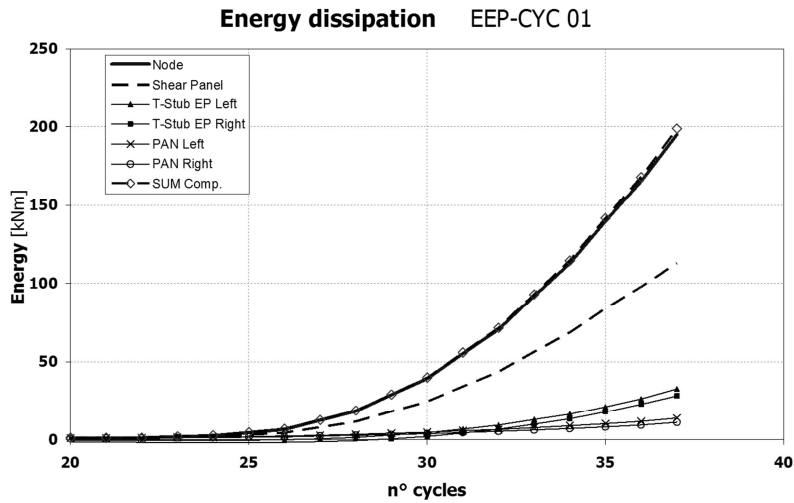


Fig. 3.31 – Energy dissipation of specimen EEP-CY 01

3.4.2 Description of test EEP-CYC 02

The experimental setup and the instruments employed in test EEP-CYC 02 are shown in the following pictures.



Fig. 3.32 – Test EEP-CYC 02

Specimen EEP-CYC 02 has been designed to concentrate the energy dissipation in the end-plate components, so that it represents a joint where panel zone components, including the column web under alternate tension and compression, are designed according to an hierarchy criterion selecting the

end-plate as dissipative element, so that the weakest component is represented by the end-plate T-stubs.

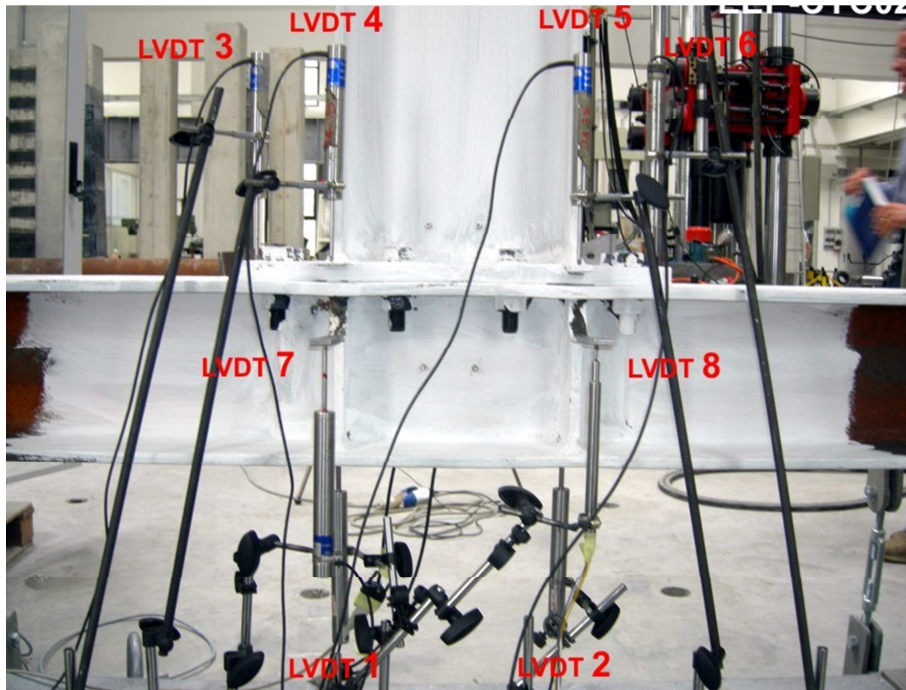


Fig. 3.33 – Measurement devices EEP-CYC 02

As described in the previous Section, in order to reach the design goal, it has been necessary to improve the panel zone detail. In this case, the joint is more rigid than EEP-CYC 01 specimen, because the end-plate in bending is almost the only source of deformability.

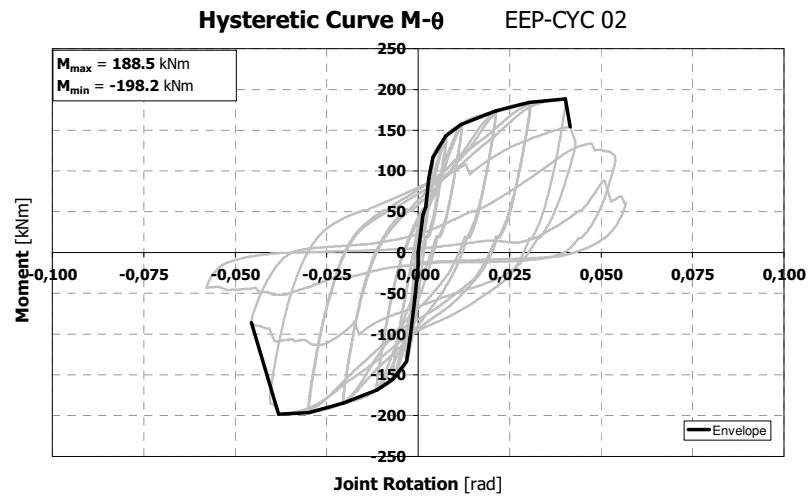
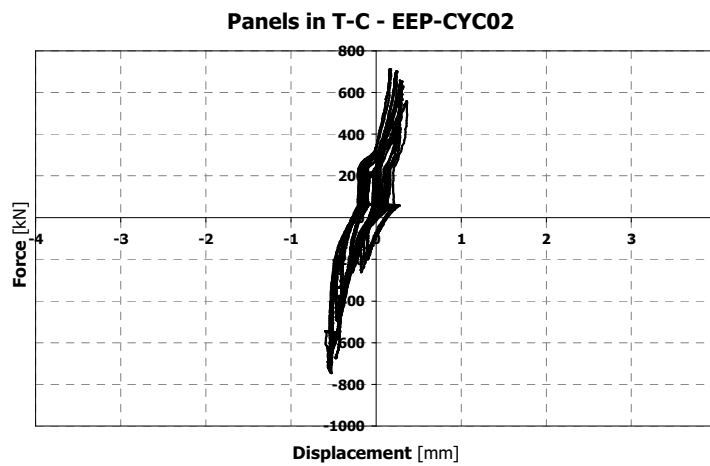
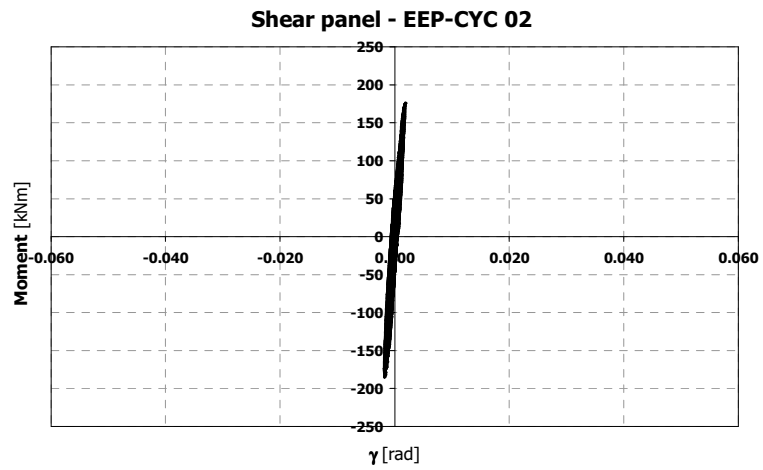


Fig. 3.34 – EEP-CYC 02 Moment-Rotation Curve

In this case, the behaviour is completely different from the one of the previous joint, in fact analyzing both the moment-rotation response of the whole joint (Fig. 3.34) and the force versus displacement response of the single components (Fig. 3.35) it can be recognized that due to the presence of the doubler plates, the shear panel almost remains in elastic range.



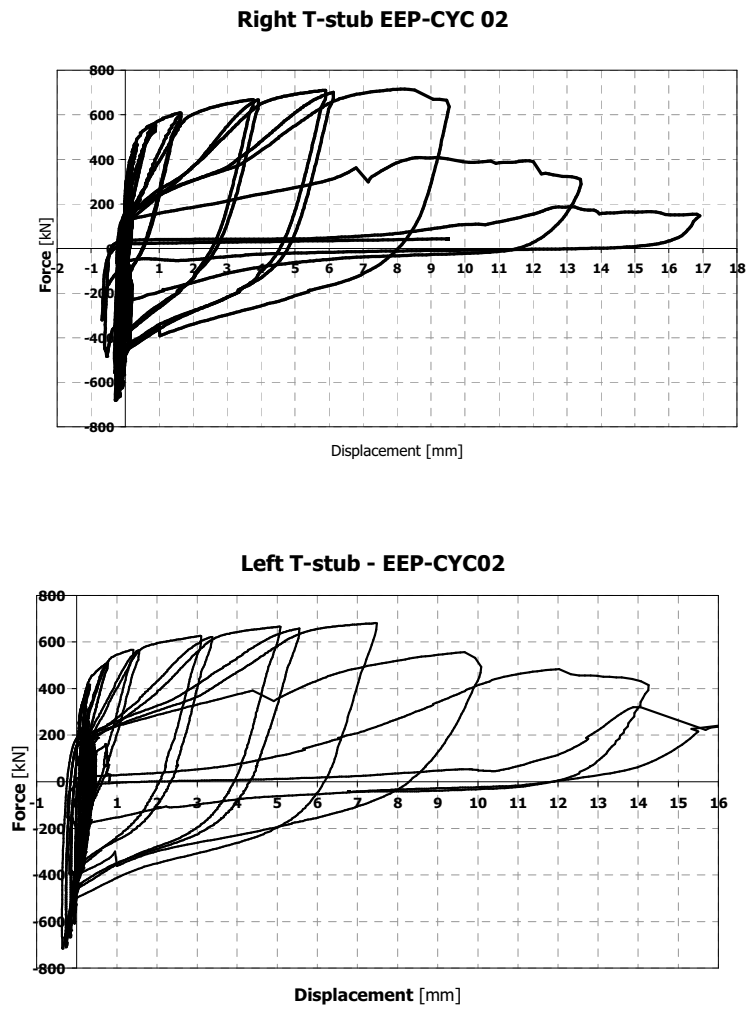


Fig. 3.35 – Component Hysteretic curves for specimen EEP-CYC 02

Similarly, due to the presence of continuity plates, the column web in tension and compression does not provide a significant energy dissipation. Therefore, according to the design purposes, the only components involved in the energy dissipation are the left end-plate and the right end-plate T-stub which also govern the shape of the moment-rotation cyclic response of the joint where some pinching can be observed (Fig. 3.34).



Fig. 3.36 – Formation of the crack in the end-plate

During the test, as the displacement amplitude increased, the plastic engagement of the end-plate at the flange-to-web connection zone increased, leading to the formation of a crack along the whole width of the end-plate

starting from the heat affected zone which progressively propagated along the thickness up to the complete fracture of the end-plate (Fig. 3.36 - Fig. 3.37). This failure mode is consistent with the design purposes of type-1 collapse mechanism. The residual load carrying capacity occurring at the end of the test is due to the final behaviour like a flush end-plate connection.



Fig. 3.37 – Failure of the end-plate

The energy dissipation capacity of this joint, as pointed out by the cyclic moment-rotation response of the whole joint, is quite limited when compared with EEP-CYC 01 specimen. The comparison between the energy dissipated

by the whole joint and the sum of the energy dissipated by the single components (Fig. 3.38) has given even in this case a good agreement, showing the correct identification of the dissipative components and encouraging about the potentialities of the component approach about the prediction of the cyclic response of bolted beam-to-column joints provided that the single components are properly identified and modelled.

Finally, it is also useful to note that the flexural strength and the plastic rotation supply exhibited by the tested specimen fairly good agree with the values adopted into the design process.

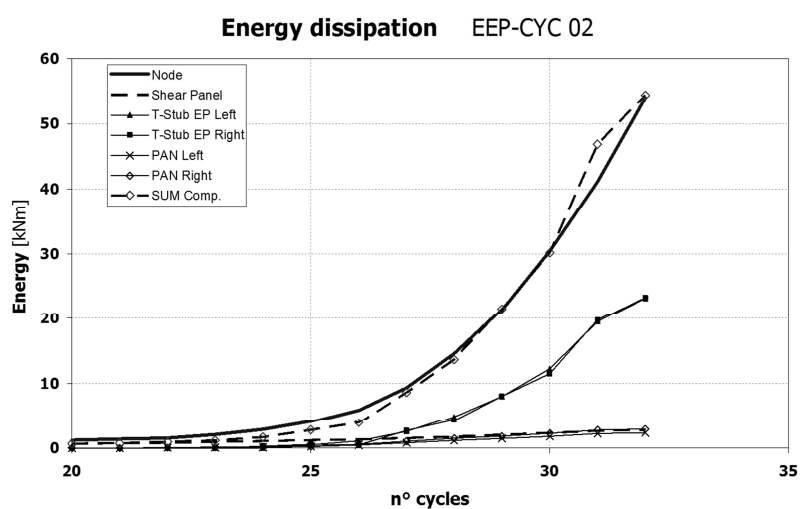


Fig. 3.38 – Energy dissipation of specimen EEP-CYC 02

3.4.3 Description of test EEP-DB-CYC 03

The experimental setup and the instruments used to monitor the joint components and the Reduced Beam Section region are shown in the following pictures.

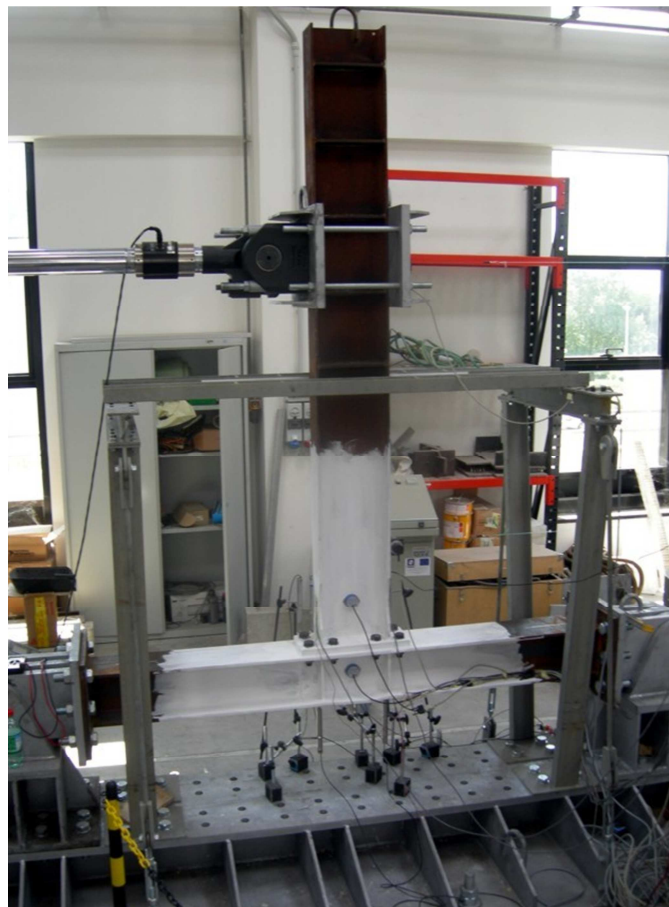


Fig. 3.39 – Setup of test EEP-DB-CYC 03

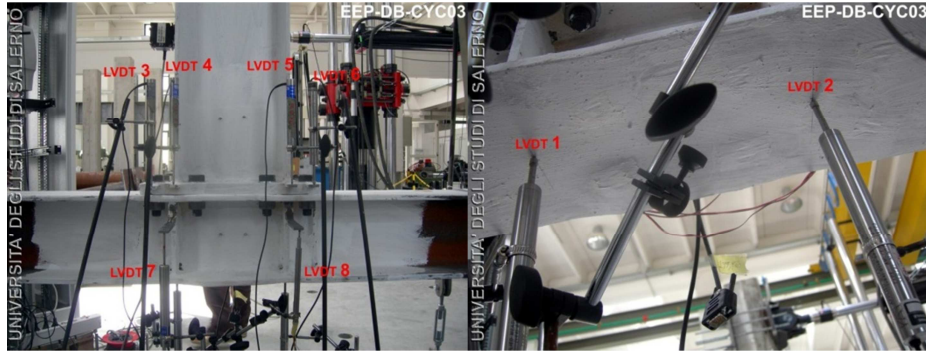


Fig. 3.40 – Measurement instruments used to monitor the joint components

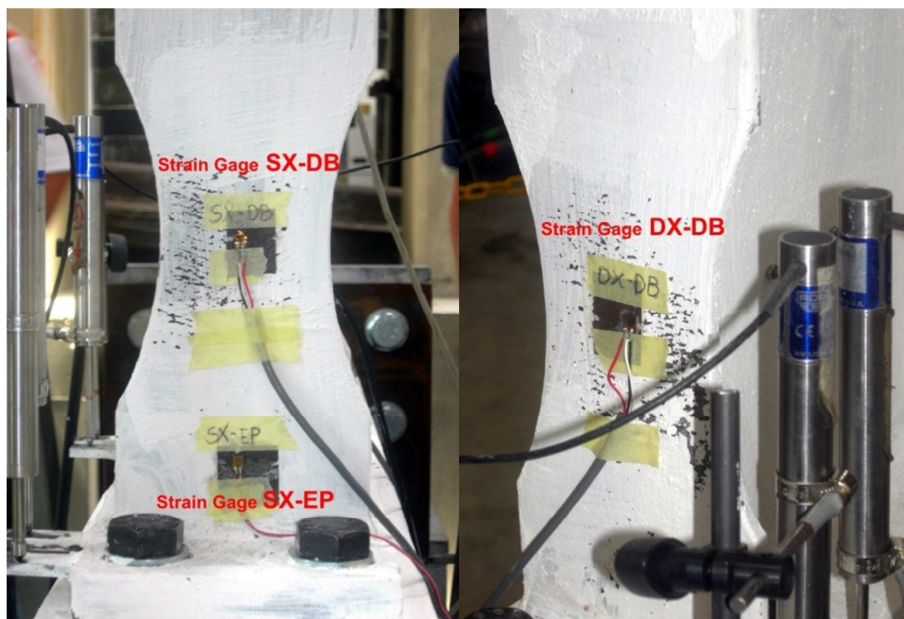


Fig. 3.41 – Strain Gauge used to monitor deformations of the Dog-Bone

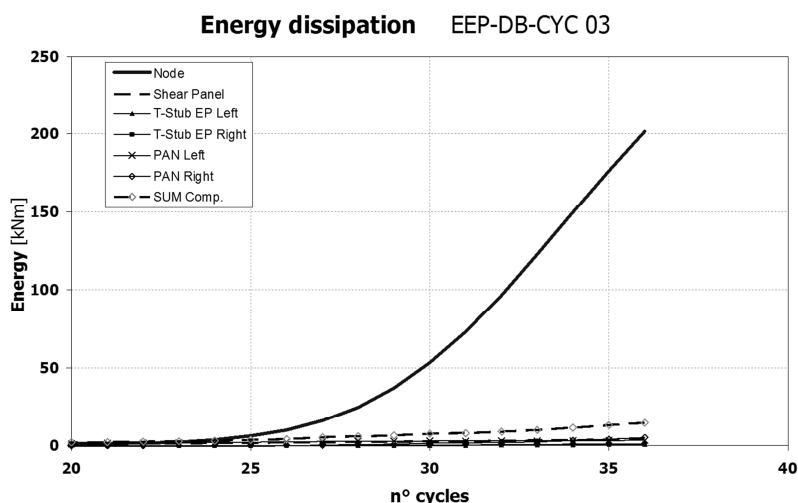


Fig. 3.42 – Energy Dissipation of specimen EEP-DB-CYC 03

The aim of specimen EEP-DB-CYC 03 is to show the dissipation capacity and ductility of a full strength joint, providing a comparison with the previously tested partial strength joints. The adopted design criteria have been presented in the previous section, pointing out the strategy adopted in order to assure that all the components remain in elastic range concentrating yielding in a reduced beam section zone far from the connection zone.

The displacements measured by LVDT registrations confirmed that, according to the design criteria, the connection component contribution is negligible (Fig. 3.42). Yielding has been concentrated in the reduced beam section zone. The failure mechanism is the one typical of steel members with -I section shape. In particular, after yielding of flanges and web and the attainment of the maximum

flexural resistance, flange local buckling occurs accompanied by beam web buckling due to compatibility between flange and web out-of-plane displacements (Fig. 3.43).



Fig. 3.43 – Flange and web buckling

The shape of the cycles of the whole joint is, as well known from the technical literature, wide and stable, guaranteeing a good energy dissipation capacity and significant plastic rotation supply (Fig.23). It is important to underline that RBS connections do not provide dangerous stress concentrations in the welds of the beam flange to column flange connection zone.

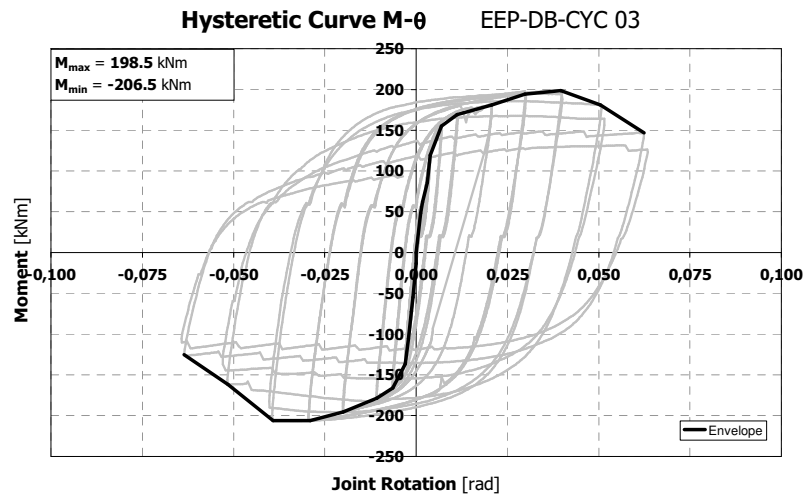


Fig. 3.44 – Flange and web buckling

3.4.4 Description of test TS-CYC 04

Test TS-CYC 04 and the measurement devices are shown in the following.

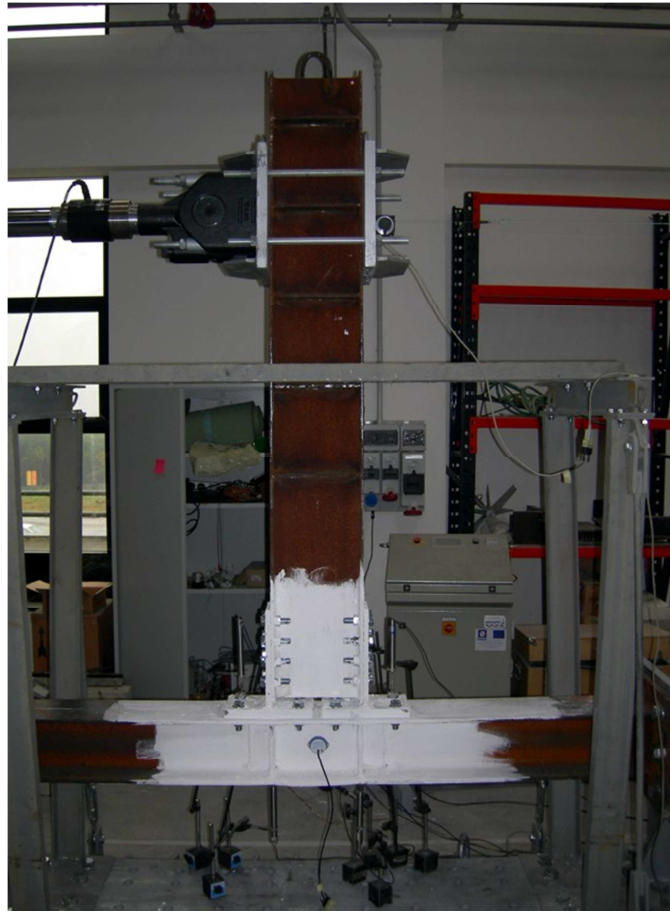


Fig. 3.45 – Test TS-CYC 04

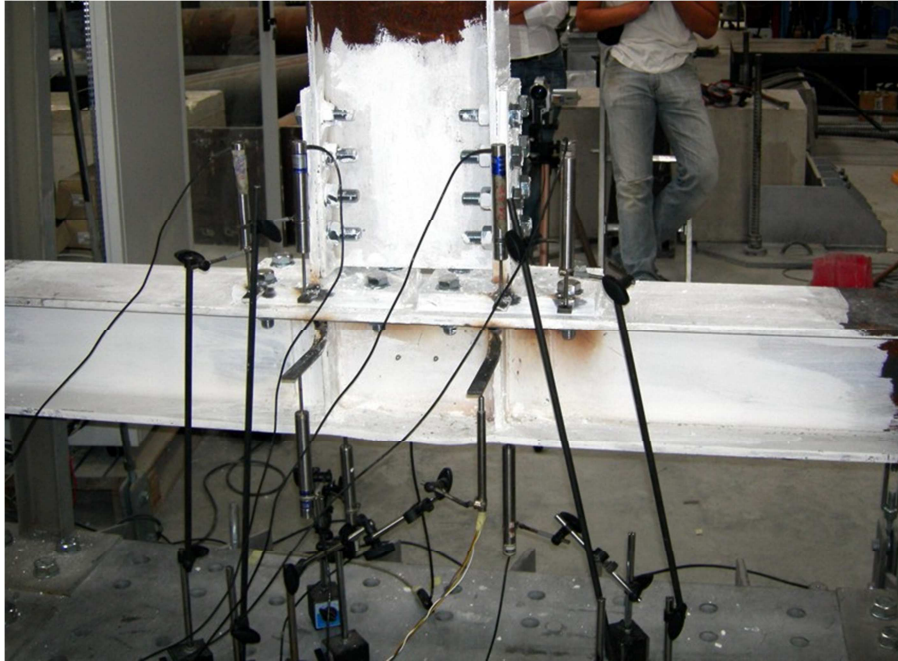


Fig. 3.46 – Measurement devices

TS-CYC 04 is a double tee connection where the only elements involved in the energy dissipation are the top and bottom T-stubs, having four bolts, which are alternatively subjected to tension and compression. The panel components do not provide a significant contribution to the dissipative behaviour of the whole joint

As expected such kind of joint has provided a very good plastic rotation supply, because properly designed, and a good amount of energy dissipation (Fig. 3.47).

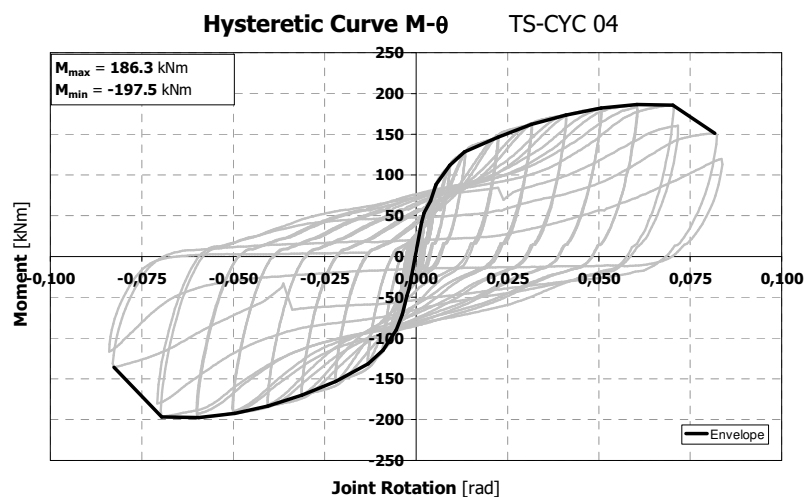


Fig. 3.47 – TS-CYC 04 Moment-Rotation Curve

The shape of the hysteresis loops of double tee connections, designed to dissipate energy in the flanges of tee elements, is similar to the one of extended end-plate connections designed to dissipate energy in the end-plate, because both of them are obviously affected by pinching phenomena. The main advantage of this kind of connection, provided that the weakest joint component is constituted by the tee elements, is due to the fact that the beam end does not exhibit any yielding, so that after a seismic event only the tee elements have to be substituted. It might be said that such a kind of connection could be a good compromise among the setting-up advantages, the detail cheapness and the dissipation and ductility capacity.

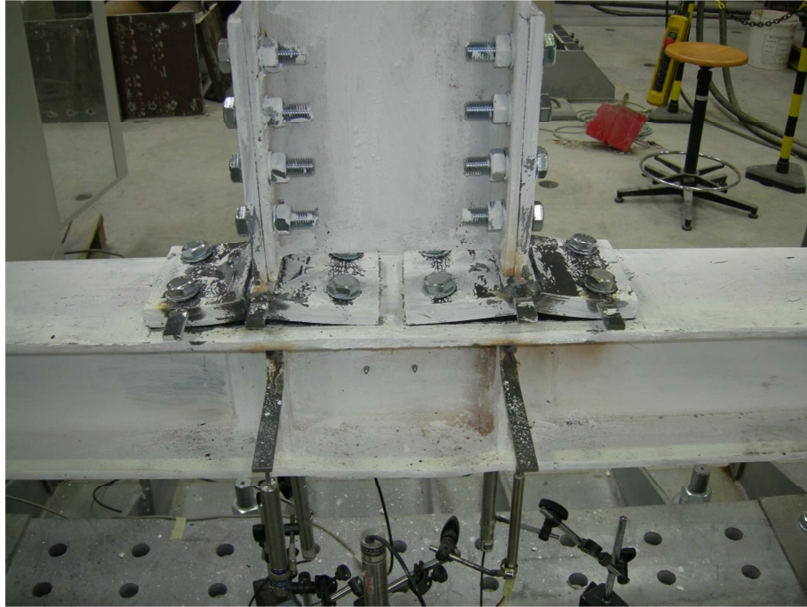


Fig. 3.48 – Formation of the plastic hinges in correspondence of bolts and plate-web tie

The behaviour during the test has been the one expected according to the design based on the component approach. In particular, the plastic engage of the T-stubs only has been observed with the development of plastic hinges at the bolt rows location and at the connection zone between the tee flange and the tee web (Fig. 3.48 - Fig. 3.49).

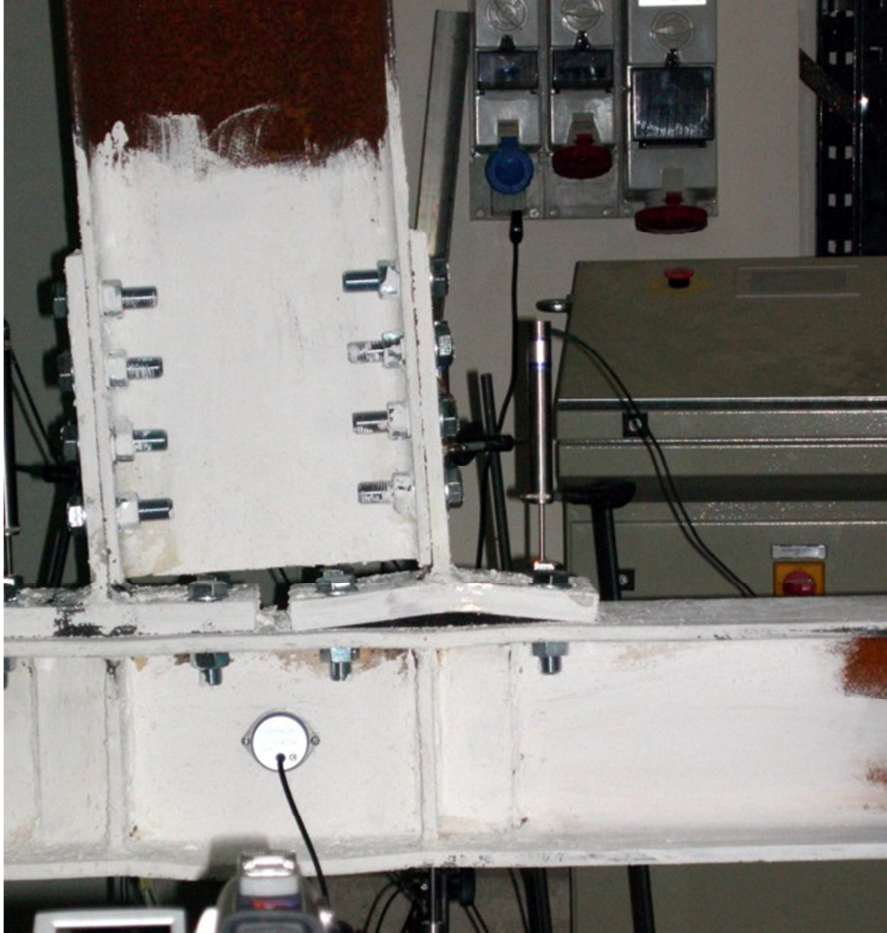


Fig. 3.49 – Plasticization of the Tee elements

Failure occurs due to the development of cracks located in the heat affected zone of the tee flange due to the welded connection with the tee web. These cracks are initially located in a position corresponding to the projection of the bolt axis perpendicular to the tee web. As far as the number of cycles

increases these cracks propagate both toward the inner part of the flange and toward the flange edges leading to complete fracture of the flange.

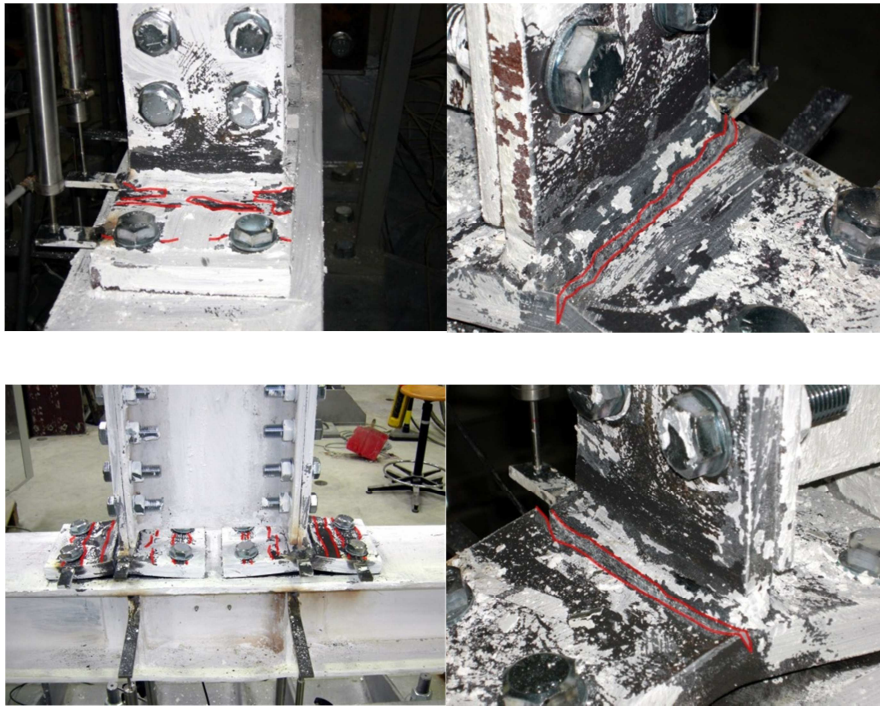


Fig. 3.50 – Development of the plastic hinges and failure of the Tee elements

As previously explained, by means of properly located displacement transducers, the force versus displacement cyclic response of the joint components has been determined. In particular, Fig. 3.51 provides the cyclic response of the two tee elements where the energy dissipation occurs.

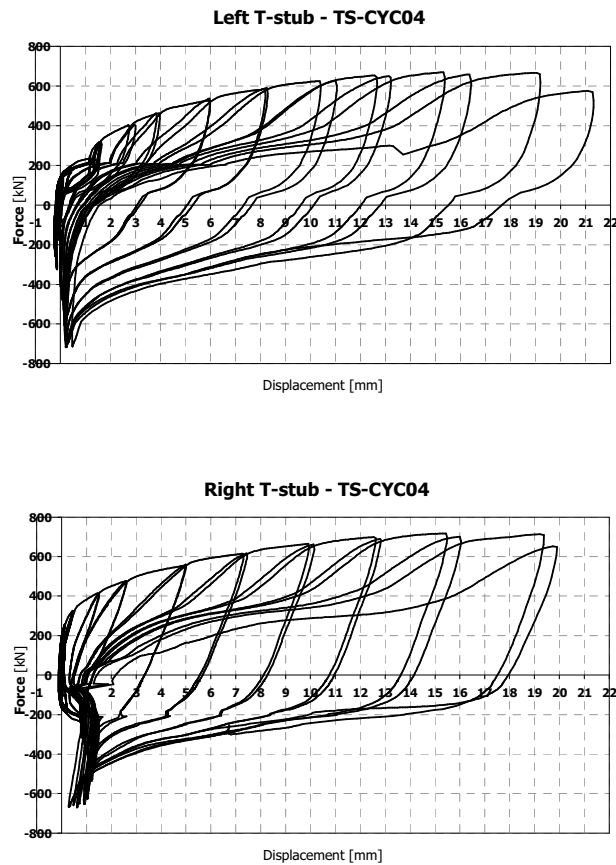


Fig. 3.51 – Components hysteretic curves for specimen TS-CYC 04

Even in this case the comparison between the energy dissipated by the whole joint and the sum of the energy dissipated by the single components (Fig. 3.52) shows that joints components have been properly identified and, in addition, the possibility to apply the component approach for predicting the cyclic behaviour of beam-to-column joints is confirmed.

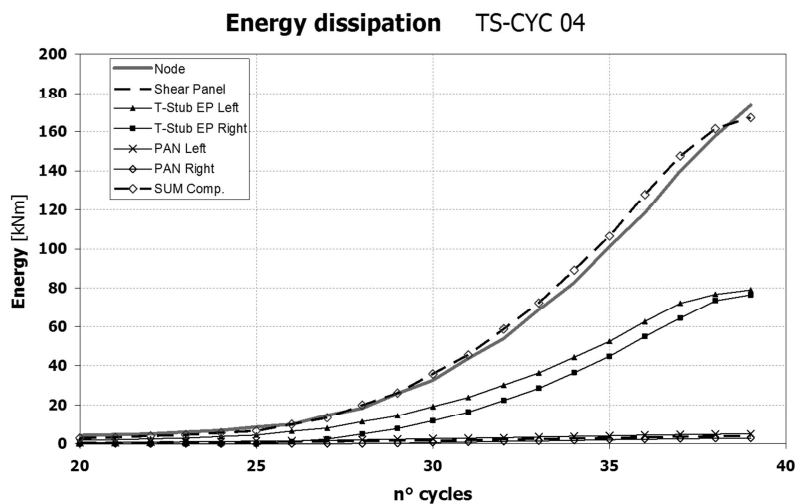


Fig. 3.52 – Energy Dissipation of TS-CYC 04 joint

3.4.5 Geometrical and mechanical properties of the specimens

Plastic deformation supply of compact steel sections is strongly affected by the base material post-elastic behaviour. A typical stress-strain relationship relative to a uni-axial test on a steel specimen is depicted in Fig. 3.53, where four characteristic branches are pointed out: the elastic linear, yield plateau, hardening and softening.

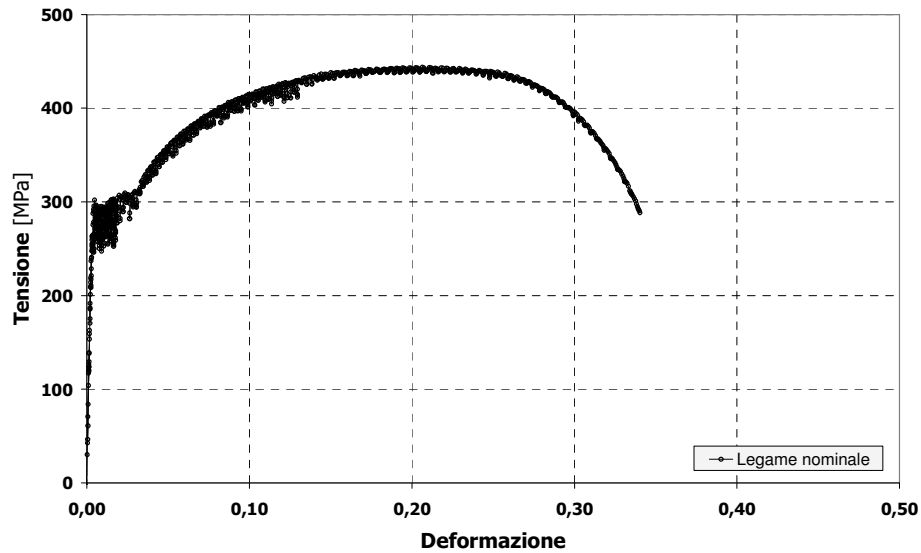


Fig. 3.53 – Experimental results of a coupon tensile test

The modelling of the material properties of end-plates and steel members has been performed with a quadri-linear modelling of the true stress-true strain relation derived from tensile tests.

True stress-true strain relationship is possible to obtain from the following equations:

$$\sigma_t = \sigma_n (1 + \varepsilon_n) \quad (3.56)$$

$$\varepsilon_t = \ln(1 + \varepsilon_n) \quad (3.57)$$

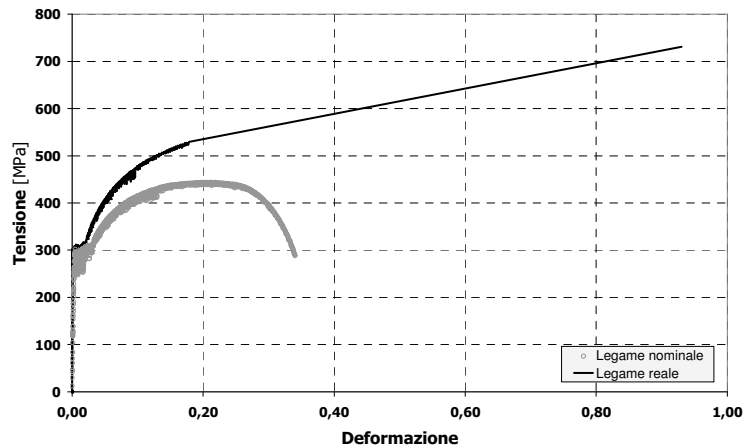


Fig. 3.54 – Comparison between the actual and the engineering stress-strain relationship

where ε_n is the specimen nominal strain, ε_r is the true strain, σ_n is the nominal stress and σ_r is the true stress. Furthermore the knowledge of the ultimate deformation is necessary (RILEM, 1990):

$$\varepsilon_u = \ln \frac{A_0}{A_f} \quad (3.58)$$

where A_0 is the initial cross section of the specimen and A_f is the area at failure, which is measured at the end of the test. In Fig. 3.54 a comparison between the actual and the engineering stress-strain relationship is represented.

All the materials tensile tests have been executed by means of Schenck Hydropuls testing machine with ± 630 kN load capacity and ± 125 mm piston stroke. All the material properties and the geometrical properties of tested specimens are provided in **Table 3.2** to **Table 3.4** with reference to the notation given in Fig. 3.55.

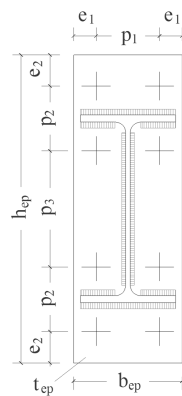


Fig. 3.55 – Notation for the definition of the geometrical properties

Table 3.2 – Tested joints measured properties

Test	Bolts	Pre-loading	Stiffeners	b_{ep}, h_{ep}, t_{ep}	e_1, e_2, p_1, p_2, p_3	HE 200 B	IPE 270
EEP CYC 01	8 M20 (10.9)	550 N·m	none	153.6	30.5, 42.2,	$h_c = 201$	$h_b = 268$
				449.0	91.6, 99.2,	$b_c = 201$	$b_b = 134$
				20.1	160.1	$t_w = 9.2$	$t_w = 6.6$
						$t_f = 15.3$	$t_f = 10.9$

Test	Bolts	Pre-loading	Stiffeners	b_{ep} , h_{ep} , t_{ep}	e_1 , e_2 , p_1 , p_2 , p_3	HE 200 B	IPE 270
EEP CYC 02	8 M20 (10.9)	550 N·m	Continuity	156.7	31.2, 40.5,	$h_c = 198$	$h_b = 271$
			plates +	474.4	94.3, 133.6,	$b_c = 198$	$b_b = 131$
			Doubler plates	20.7	126.2	$t_w = 9.2$	$t_w = 6.8$
						$t_f = 15.5$	$t_f = 10.7$
EEP DB CYC 03	8 M24 (10.9)	800 N·m	Continuity	427.0	36.0, 33.0,	$h_c = 198$	$h_{RBS} = 271$
			plates +	161.0	89.0, 99.0,	$b_c = 198$	$b_{RBS} = 88.8$
			Doubler plates	25.3	163.0	$t_w = 9.2$	$t_w = 6.8$
						$t_f = 15.5$	$t_f = 10.7$
TS CYC 04	8 M20 (10.9)	550 N·m	Continuity	154	30.2, 39,	$h_c = 203$	$h_b = 269$
			plates +	2x257	94.3, 177	$b_c = 200$	$b_b = 132$
			Doubler plates	25.2		$t_w = 9$	$t_w = 6.7$
						$t_f = 15$	$t_f = 10.1$

Table 3.3 – End-plate mechanical properties

Joint	f_y [N/mm ²]	f_u [N/mm ²]	E [N/mm ²]	ϵ_n/ϵ_y	ϵ_u/ϵ_y	E/E _n	E/E _u
EEP-CYC 01	290	493,7	207288	11,3	589	86,5	632,8
EEP-CYC 02	290	493,7	207288	11,3	589	86,5	632,8
TS-CYC 04	295	520	210000	12,2	486	103,4	486

Table 3.4 –Column and Beam mechanical properties

All Joints	$f_{y,f}$ [N/mm ²]	$f_{u,f}$ [N/mm ²]	$f_{y,w}$ [N/mm ²]	$f_{u,w}$ [N/mm ²]
Column	430	523	382,5	522
Beam	405	546	387	534

3.4.6 Comparison among the tests

First of all, it is useful to observe that all the tested specimens exhibited almost the same flexural strength, as desired, and provided energy dissipation mainly in the weakest component according to the adopted design criteria. Therefore, experimental test results confirmed that the component approach can be a powerful tool, even in the framework of seismic design of steel structures, allowing the selection of dissipative elements and the application of hierarchy criteria to design the joint components which have to remain in elastic range.

All the tested specimens have shown that the energy dissipation capacity of the whole joint can be obtained, as expected, by the sum of the energy dissipated by the single joint components, provided that they are properly identified and their cyclic response is properly measured by evaluating the relevant local displacements.

Regarding the amount of energy dissipation capacity exhibited by the tested specimens a comparison is provided in Fig. 3.56 as far as the number of cycles increases. The greatest energy dissipation capacity is exhibited by specimen EEP-DB-CYC 03 adopting the RBS strategy.

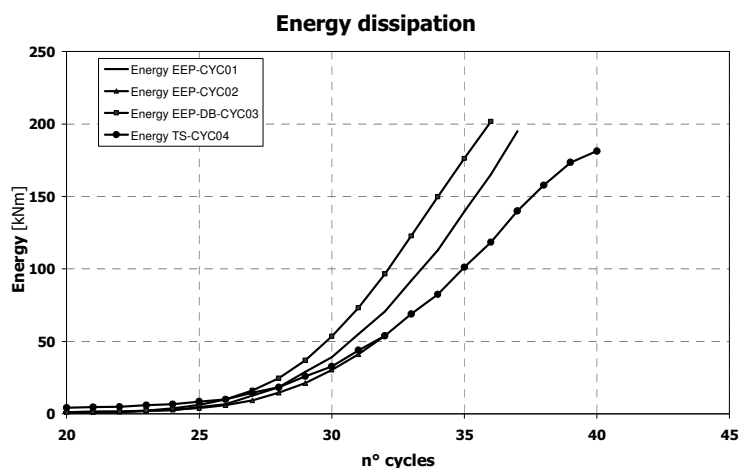


Fig. 3.56 - Energy dissipation capacities of the tested joints

The comparison between specimen EEP-DB-CYC 03 and EEP-CYC 01, where yielding occurs in the panel zone subjected to shear, shows that, in this case, a reduction of about 20% of energy dissipation occurs. Conversely, due to pinching phenomena, specimen EEP-CYC 04 exhibits a reduction of energy dissipation capacity of about 40% when compared with the RBS solution. Finally, poor energy dissipation capacity has been provided by specimen EEP-CYC 02, because it has been designed for an ultimate rotation equal to 0.05 rad under monotonic loading conditions. The monotonic envelopes of the cyclic response of tested specimens are compared in Fig. 3.57.

In **Table 3.5** a comparison between the actual structural performance and the specimen design values, in terms of strength and ductility supply is provided. In particular, the experimental values of the rotational stiffness, of the maximum strength reached during the whole loading process and of the bending moment corresponding to the knee of the moment-rotation envelope are

reported. The knee moment has been determined according to the approach suggested in Eurocode 3 (CEN,2005b), i.e. by evaluating the moment corresponding to a secant stiffness equal to one third of the initial one. The stiffness of joints EEP-CYC 01 and TS-CYC 04 are quite similar; conversely, EEP-CYC 02 and EEP-DB-CYC 03 specimens exhibited an increased stiffness of about 70%. Regarding the strength, the same value of the peak moment has been reached by all the tests while the knee moments are slightly different.

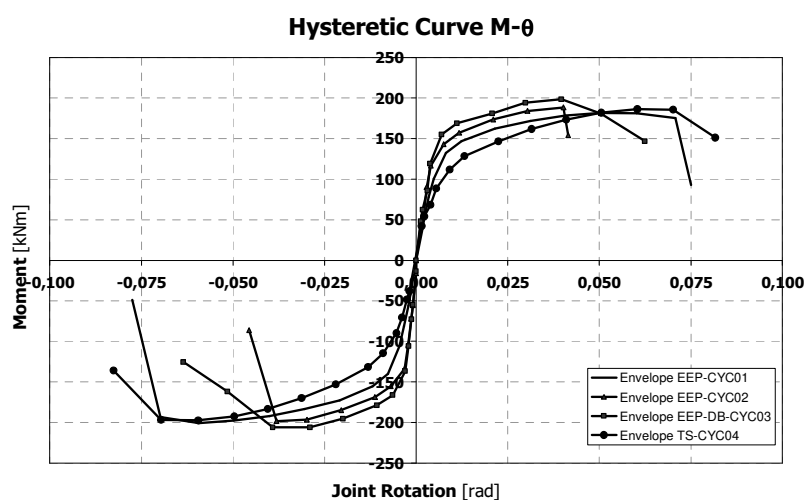


Fig. 3.57 – Comparison among the cyclic curves of the testes specimens

The disagreement between the design values of the flexural resistance and the observed knee value is justified considering that the design process has been carried out using the characteristic values of the yield strength which are lower than the actual ones. In particular, the ratio between the yield strength resulting from coupon tensile tests and the one used during the design, gives an over-resistance of about 10% in case of end plates and of the column web and

flanges and of about 50% in case of beam mechanical properties. This last result justifies the knee moment obtained during test EEP-DB-CYC 03 which is about 50% greater than the design one. Furthermore, with reference to specimens EEP-CYC 01 and EEP-CYC 02 an additional over strength is even due to the design assumptions. In fact, in the former case the moment assumed in the design process corresponds to the shear panel first yielding neglecting contribution of flanges while in the latter case a simplified equivalent T-stub model for the bolt rows in tension has been assumed according to Eurocode 3, which is a conservative simplification, because it does not account for the strengthening action exerted by the beam web with reference to the second bolt row in tension located between the beam flanges.

Table 3.5 – Comparison between experimental and design values of strength and ductility

Joint	$K_{\phi,exp}$ [kNm/rad]	$M_{knee,exp}$ [kNm]	$M_{max,exp}$ [kNm]	M_d [kNm]	$\phi_{u,exp}$ [mrad]	$\phi_{u,d}$ [mrad]
EEP-CYC 01	24931	+159/-173	+181/-201	101	+70.7/ 69.8	-
EEP-CYC 02	41411	+157/-173	+188 /-198	100	+40.2/ 38.1	50
EEP-DB-CYC 03	43420	+169/-182	+198/-206	101.6	+62.5/ 51.5	-
TS-CYC 04	23196	+133.8/ 139	+186/-197	100	+70.2/ 70.7	80

Therefore, as expected, an underestimation of the plastic resistance corresponding to the knee of the moment-rotation envelope is obtained. Regarding the ductility the design values are always slightly greater than the observed values. Such result is obviously consistent with the design assumptions, because the adopted analytical model refers to monotonic loading conditions, so that it represents only an upper bound of the plastic rotation supply under cyclic actions.

Regarding stiffness and strength degradation under cyclic loading, EEP-CYC 01 specimen is characterized by stable hysteresis loops with no significant degradation. Specimens EEP-CYC 02 and TS-CYC 04 are mainly characterized by the pinching of the hysteresis loops and strength degradation after the occurrence of local buckling. The greatest value of the plastic rotation supply is exhibited by TS-CYC 04 specimen. A comparable value is shown by the specimen whose weakest component is the panel zone in shear, while a slightly smaller rotation capacity is obtained adopting the RBS strategy. All these specimens have provided sufficient rotation supply exceeding the benchmark value equal to 0.035 rad suggested by Eurocode 8 with reference to the plastic region. This benchmark is referred to the ratio between the beam deflection at the midspan and the distance between the point of contra-flexure and the beam-to-column joint. Therefore, while the Eurocode 8 benchmark includes also the beam elastic deformation, the presented results are referred to the contribution of the beam-to-column joint only. Therefore, even in the case of specimen EEP-CYC 02, even though the rotation supply in Fig. 3.57 is not clearly greater than 0.035 rad, the Eurocode requirement is fulfilled because of the contribution due to the beam elastic deformation.

3.6 References

Bijlaard, F., 2004. Joints in steel structures based on eurocode 3. In *Steel & Composite Structures (ICSCS'04)*. Yuseong, Korea, 2004. Techno-Press. (TUD).

Carter, C. & Iwankiw, N., 1998. Improved ductility in seismic steel moment frames with dogbone connections. *Journal of Constructional Steel Research*, 46(1-3), p.253.

CEN, 2005a. *Eurocode 3: Design of steel structures - Part 1-1: General rules and rules for buildings*.

CEN, 2005b. *Eurocode 3: Design of steel structures - Part 1-8: Design of joints*.

CEN, 2005c. *Eurocode 8: Design of structures for earthquake resistance - Part 1: General rules, seismic actions and rules for buildings*.

Chen, S., Chu, J. & Chou, Z., 1997. Dynamic behavior of steel frames with beam flanges shaved around connection. *Journal of Constructional Steel Research*, 42(1), pp.49-70.

Chen, S., Yeh, C. & Chu, J., 1996. Ductile steel beam-to-column connections for seismic resistance. *Journal of Structural Engineering ASCE*, 122(11), pp.1292-99.

Clemente, I., Noè, S. & Rassati, G., 2004. Experimental behavior of T-stub connection components for the mechanical modeling of Bare-Steel and

composite partially restrained beam-to-column connections. In *Proceedings of Connections in Steel Structures V*. Amsterdam, 2004.

Dubina, D. et al., 2008. Testing program to evaluate behavior of dual steel connections under monotonic and cyclic loading. In *Proceedings of the 5th European Conference on Steel and Composite Structures*. Graz, Austria, 2008.

Engelhardt, M., Winneberger, T., Zekany, A. & Potyraj, T., 1996. The dogbone connection part II. *Modern Steel Construction*.

Engelhardt, M., Winneberger, T., Zekany, A. & Potyraj, T., 1997. Experimental investigation of dogbone moment connections. In *Proceedings of National Steel Construction Conference*. Chicago, 1997. AISC.

Faella, C., Piluso, V. & Rizzano, G., 1998b. Experimental Analysis of Bolted connections: snug versus preloaded bolts. *Journal of Structural Engineering*, 124(7), pp.765-74.

Faella, C., Piluso, V. & Rizzano, G., 1998a. Cyclic behavior of bolted joint components. *Journal of Constructional Steel Research*, 46(1-3), p.paper number 129.

Faella, C., Piluso, V. & Rizzano, G., 2000. *Structural Steel Semi-Rigid Connections*. Boca Raton: CRC Press.

Jaspart, J., 1991. *Etude de la semi-rigidite des noeuds Poutre-Colonne et son influence sur la resistance et la stabilite des ossature en acier*. PhD Tesis ed. Liege: University of Liege, Belgium.

Jaspart, J.P., 2002. Design of Structural Joints in Building Frames. *Progress in Structural Engineering and Materials*, Vol.4(18-34).

Joh, C. & Chen, W., 1999. Fracture strength of welded flange-bolted web connections. *Journal of Structural Engineering*, 125(5), pp.565-71.

Kim, K. & Engelhardt, M., 2002. Monotonic and cyclic loading models for panel zones in steel moment frames. *Journal of Constructional Steel Research*, 58, pp.605-35.

Mazzolani, F. & Piluso, V., 1996. *Theory and Design of Seismic Resistant Steel Frames*. London: E & FN Spon, an Imprint of Chapman & Hall.

Montuori, R. & Piluso, V., 2000. Plastic design of steel frames with dog-bone beam-to-column joints. In *Third International Conference on Behaviour of Steel Structures in Seismic Areas*. Montreal, 2000. STESSA 2000.

Moore, K., Malley, J. & Engelhardt, M., 1999. Design of Reduced Beam Section (RBD) Moment Frame Connections. *Steel Tips*.

Piluso, V., Faella, C. & Rizzano, G., 2001. Ultimate behavior of bolted T-stubs. Part I: Theoretical model. *Journal of Structural Engineering ASCE*, 127(6), pp.686-93.

Piluso, V. & Rizzano, G., 2008. Experimental Analysis and modelling of bolted T-stubs under cyclic loads. *Journal of Constructional Steel Research*, 64, pp.655-69.

Richard, R., Partridge, J., Allen, J. & Radau, S., 1995. Finite element analysis and tests of beam-to-column connections. *Modern Steel Construction AISC*, 35(10), pp.44-47.

RILEM, 1990. Tension Testing of Metallic Structures for Determining Stress-Strain relations under Monotonic and Uniaxial Tensile Loading. *Material and Structures*, 23, pp.35-46.

Rizzano, G., 1995. *Modellazione nodale e comportamento sismico dei telai in acciaio a nodi semirigidi*. PhD thesis ed. Napoli: Università degli Studi di Napoli.

Rizzano, G., 2006. Seismic Design of Steel Frames with Partial Strength Joints. *Journal of Earthquake Engineering*, 10(5), pp.725-47.

SAC, 1997. *Interim guidelines advisory n°1*. Washington D.C.: Federal Emergency Management Agency.

SAC, 2000a. *Recommended Seismic Design Criteria for New Steel Moment Resisting Frame Buildings*. California: FEMA.

SAC, 2000b. *State of the Art Report on Systems Performance of Steel Moment Frames Subject to Earthquake Ground Shaking*. California, U.S.A.: FEMA.

SAC, 2000c. *State of the Art Report on Past Performance of Steel Moment-Frame Buildings in Earthquakes*. California: FEMA.

Swanson, J. & Leon, R., 2000. Bolted steel connections: tests on T-stub components. *Journal of Structural Engineering ASCE*, 126(1), pp.50-56.

CHAPTER 4 – CYCLIC BEHAVIOR OF BEAM-TO-COLUMN JOINTS: MECHANICAL MODELING

4.1 Introduction

Methods available in technical literature to model the cyclic behavior of beam-to-column joints can be divided into three groups: mathematical models, mechanical models and finite element models. Mathematical models are based on curve fitting of joint moment-rotation curves, so that their limits can be easily understood. In fact, mathematical models can be developed only if experimental tests are available, so that their application is limited to tested structural details.

Conversely, mechanical models are based on an appropriate combination of the cyclic response of the joint dissipative components. The potentialities of such a kind of approach with respect to mathematical modeling can be easily recognized in the variety of connections which can be modeled, provided that the modeling of the cyclic response of the joint components is available and the accuracy of the mechanical model adopted for combining the joint components is verified. The starting point of this approach is the check of the possibility to obtain the dissipation capacity of the whole joint as the sum of those of the single components, as testified in the previous section. In addition, because of the complexity of finite element models and their computational

effort, mechanical models appear to be effective and practical in the prediction of the beam-to-column behavior under cyclic actions.

In this chapter, the prediction of the cyclic rotational response of bolted connections is carried out by means of the mechanical model depicted in Fig. 4.1, with reference to bolted end-plate connections (a) and to bolted tee-stub connections (b). In particular four sources of energy dissipation are considered: column flange in bending (cfb), column web in tension and compression (cwt-c), column web in shear (cws) and end-plate in bending (epb)/ tee-stub in bending (tsb).

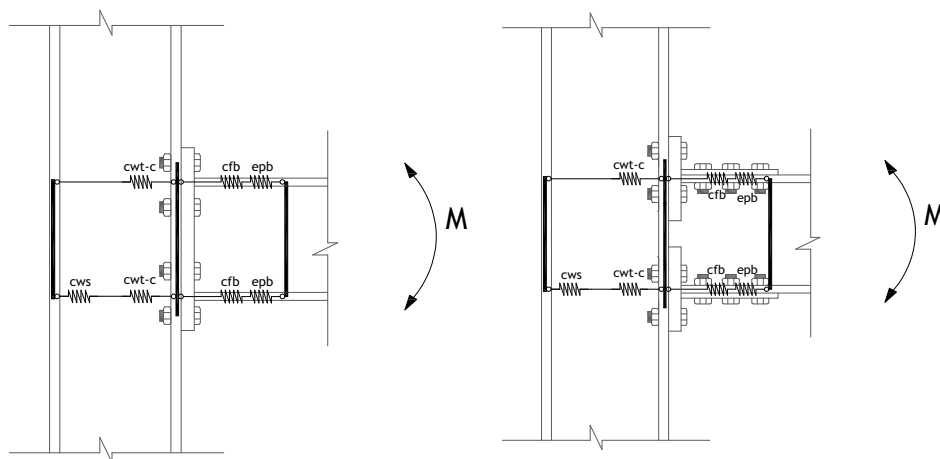


Fig. 4.1 – Mechanical model for bolted connections

The mechanical model is aimed at the prediction of the rotational cyclic response of bolted connections having two bolt rows in tension, because, as depicted in Fig. 4.1, the behavior of the two bolt rows in tension is modeled by

means of only one spring element for each component (cfb and epb or cfb and tsb), represented by an equivalent T-stub.

The use of the mechanical model requires three steps to be performed:

- Modeling of the cyclic behavior of each joint component;
- Assembling of the joint components;
- Evaluation of joint cyclic moment-rotation curve.

In the following sections, further details concerning modeling of the joint components and their assembling are provided. Successively, the proposed model is applied to simulate the joint rotational response of the specimens tested during an experimental program carried out at Salerno University whose results are presented in a companion paper. Finally, the accuracy of the proposed mechanical model is investigated by comparison with test results.

4.2 Cyclic Modeling of the Joint Components: Literature Review

4.2.1 Modeling of the panel zone in shear

As already said in previous chapter, shear panel is represented by the region on the column web panel contained between the flanges of the connected beam. When steel frames are subjected to lateral loads in panel zones arise significant shear actions, so that, if properly designed, this joint component can influence the overall joint response. Therefore, the knowledge of the moment-rotation relationship of shear panels can become of primary importance in the modeling of steel partial strength joints.

Since some seismic codes (CEN, 2005c; AISC, 2005) have allowed yielding of the panel zone prior to the full development of the moment carrying capacity of connected beams, many research efforts have been addressed to the study of the behavior under load reversal of column web panels (Krawinkler et al., 1971; Krawinkler et al., 1973; Davila-Arbona, 2007; Castro et al., 2008; Castro et al., 2005). On the base of the numerous experimental campaign devoted to the study of this component some important observations can be pointed out:

- shear panels develop an ultimate strength significantly greater than the first yielding resistance. This over-strength is mainly due to the steel strain-hardening and to the contribution of the column flanges;
- deformations of the shear panel can provide a significant contribution to the overall joint response;

- shear panel strength and resistance can be increased properly detailing the column web panel. As an example it is possible to add supplementary web panels;
- in plastic range, shear panels exhibit a very ductile behavior both under monotonic and cyclic loads;
- shear panels have been demonstrated to provide wide and stable hysteresis cycles;
- excessive distortion of the web panel zone can lead to concentration of stresses in the welds connecting the beam to the column.

Many models have been proposed in last two decades to account for panel zone behavior under both monotonic and cyclic loading conditions following two different approaches: the analytical modeling and the FEM modeling. In the former case, the panel zone is idealized as a dimensionless region, representing its behaviour by means of a rotational spring connecting two nodes at the same coordinates. Such a kind of approach allows to account for the additional $P-\Delta$ effects on the columns due to the shear deformation of the panel zone provided that rigid end offsets are adopted (Fig. 4.2). In last thirty years, scientific research has gained noteworthy results dealing with the mechanical modeling of panel zones subjected to shear actions. First attempts to provide a model for the prediction of the shear panel response have been done by (Fielding & Huang, 1971) and (Krawinkler et al., 1971). Then, other models, trying to properly account for the post-elastic effects due to the column flanges in case of specimens with thick flanges were proposed by (Wang, 1988; Kim & Engelhardt, 2002).

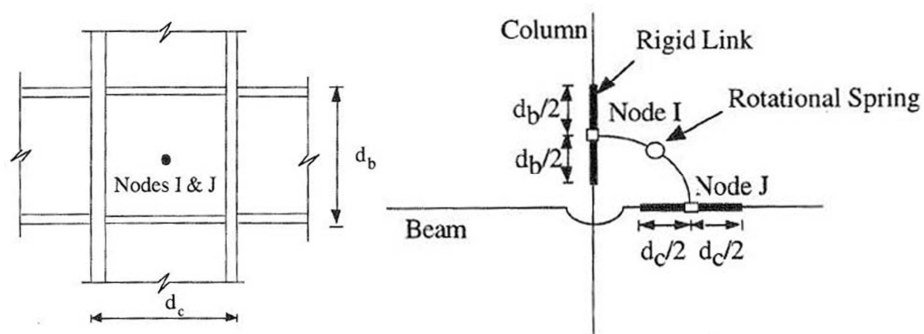


Fig. 4.2 – Modeling of an internal welded joint

On the other hand, FEM models are able to account for the actual dimension of the panel zone by modeling the shear panel response by means of an assemblage of sub-elements representing the deformation modes of the panel zone. First FEM models have been proposed by (Lui, 1985; Lui & Chen, 1986) who proposed a model composed by the assemblage of seven finite elements: a web element, two flange elements and four connecting elements. Even though this model provides a good response with reference to the monotonic loads, in case of cyclic actions does not provide an accurate prediction of the moment rotation response and, in addition, requires a significant computational effort. Another finite element model has been proposed by (Mulas, 2004), where the joint is modeled by means of four elements whose displacements are defined by the translation of the edge nodes (Fig. 4.3).

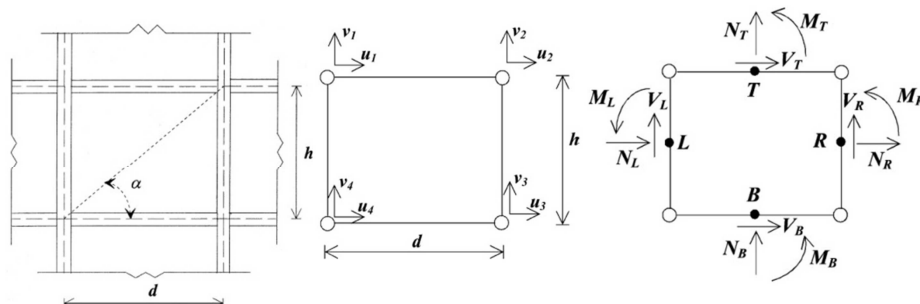


Fig. 4.3 – (Mulas, 2004) FEM model

In the following a review of the existing mechanical model for the prediction of the monotonic and cyclic response of shear panels is reported.

4.2.1.1 Fielding and Huang monotonic model (1971)

Fielding & Huang assume that the in-plane stiffness of beams connected to the column is sufficiently great to consider that constraints at the edges of the panel are rigid. It is for this reason that in this model it is assumed that the stresses are uniformly spread within the panel, even though (Tsai & Popov, 1990) have demonstrated that stresses are greater at the center and lower at the edges of the panel. Fielding and Huang proposed a bi-linear relationship with a first elastic branch with stiffness K_e , and a post-elastic branch of stiffness K_f .

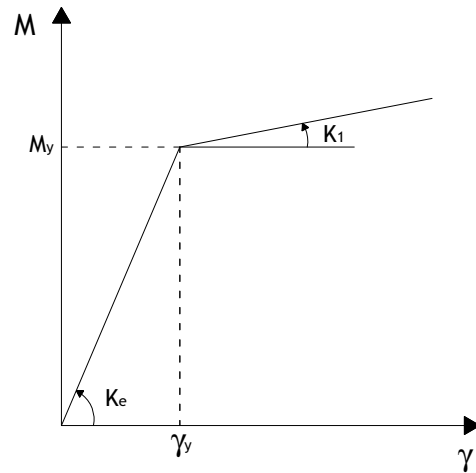


Fig. 4.4 – Bilinear model of Fielding and Huang

One of the main differences among the presented models is related to the definition of the effective shear area. Fielding and Huang assume that the effective shear area is given by:

$$A_{eff,FK} = (d_c - t_{cf})t_{cw} \quad (4.1)$$

where $A_{eff,FK}$ is the effective shear area in models of Fielding & Huang and of Krawinkler, d_c is the column depth, t_{cf} is the thickness of the column flange and t_{cw} is the thickness of the column web. On the base of the reported assumption, in elastic range it is obtained:

$$K_e = \frac{GA_{eff,FK}d_b}{\beta} \quad (4.2)$$

$$M_y = \frac{\tau_y A_{eff,FK} d_b}{\beta} \quad (4.3)$$

$$\tau_y = \frac{f_y}{\sqrt{3}} \sqrt{1 - \left(\frac{\sigma}{\sigma_y} \right)^2} \quad (4.4)$$

$$\gamma_y = \frac{M_y}{K_e} \quad (4.5)$$

where G is the steel shear modulus, d_b is the beam depth, σ is the stress acting in the column, τ_y is the yield shear stress accounting for the normal load, M_y is the moment of first yield of the panel zone, γ_y is the shear panel yielding rotation.

After the elastic range, the two authors obtain the stiffness of the strain-hardening branch introducing the scheme shown in Fig. 4.5. Panel zone post-elastic behavior is derived analyzing the behavior of the two column flanges clamped at the mid-height and connected at the end by a rigid pendulum.

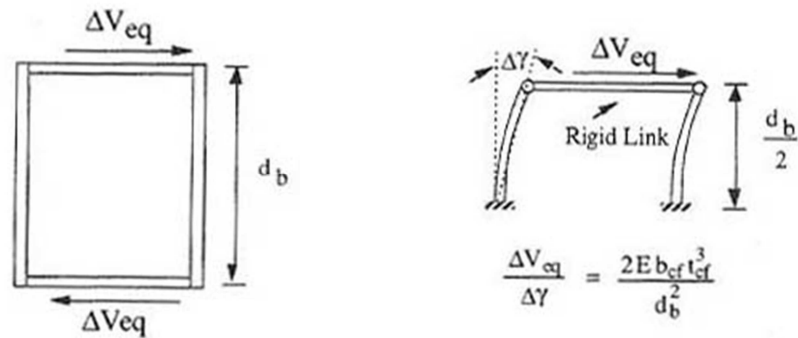


Fig. 4.5 – Post-elastic model of Fielding and Huang (1971)

By means of translational equilibrium shown below is possible to obtain the post-elastic stiffness (Fig. 4.6).

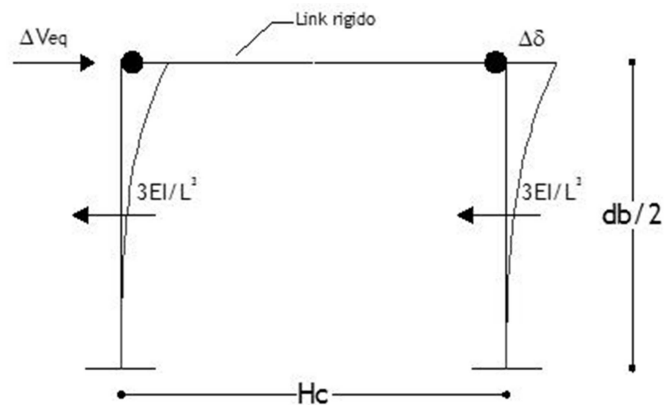


Fig. 4.6 – Translational equilibrium (Fielding model)

$$\frac{6EI}{\left(\frac{d_b}{2}\right)^3} \Delta\delta = \Delta V_{eq} \quad (4.6)$$

$$K_1 = \frac{\Delta V_{eq}}{\Delta\gamma} = \frac{6EI}{\left(\frac{d_b}{2}\right)^2} = \frac{6 \cdot 4E \frac{b_{cf} t_{cf}^3}{12}}{d_b^2} = \frac{2Eb_{cf} t_{cf}^3}{d_b^2} \quad (4.7)$$

where E is the steel elastic modulus, I is the inertia modulus of the column flanges and b_{cf} is the width of the column flanges. The relationship herein presented are applied to model the case of a HEB 200 column and IPE 270 beam made of S275 steel with β equal to 0.92 (Fig. 4.7).

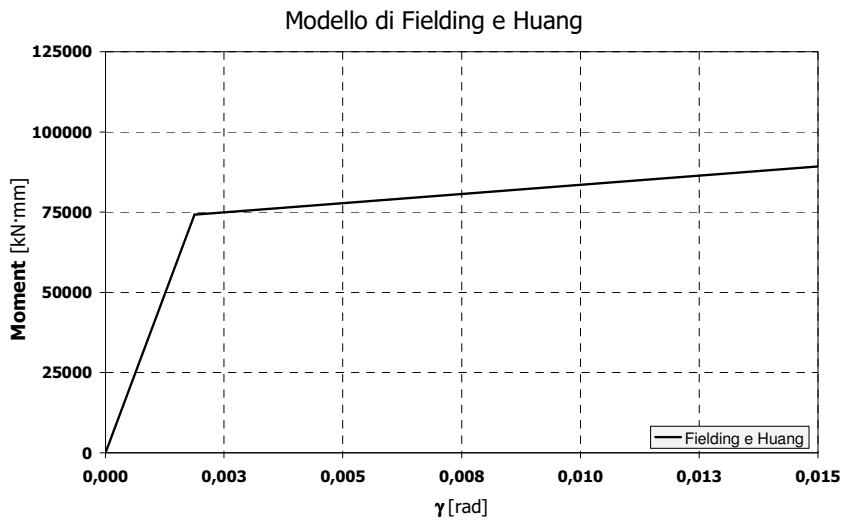


Fig. 4.7 – Application of Fielding & Huang model

4.2.1.2 Krawinkler monotonic model (1971)

In Krawinkler approach the monotonic behavior of a steel panel subjected to shear loads is modeled by means of a tri-linear moment-rotation relationship. The first branch is elastic-linear, the second branch is defined by a slope obtained starting from curve fitting of available experimental data and the third branch is defined by the strain-hardening stiffness (Fig. 4.8).

Elastic phase is only influenced by the definition of the effective shear area. In this model the area is assumed equal to that given in Fielding and Huang model (4.1). Also Eqs.(4.2) - (4.5) can be adopted to calculate the first yielding point, so that there are no differences in the characterization of the elastic behavior in models of Krawinkler and Fielding & Huang.

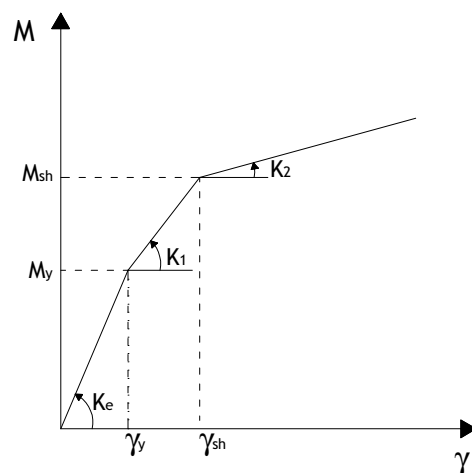


Fig. 4.8 – Tri-linear model of Krawinkler

First post-elastic branch accounts for the contribute of the column flanges and is obtained by means of semi-empirical formulas derived starting from the mechanical model depicted in Fig. 4.9 and by calibration on experimental tests.

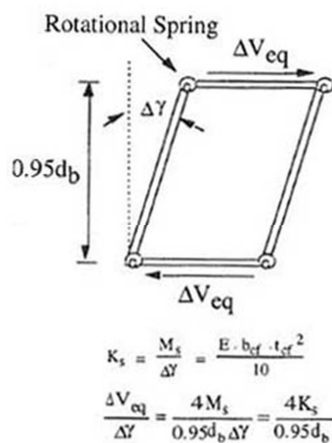


Fig. 4.9 – Post-elastic model (Krawinkler,1971)

The theoretical model is represented by a panel fully restrained at the edges with four rotational springs at the corners. Krawinkler assumes that the springs simulate the resistance of the elements composing the panel zone and in particular the column flanges:

$$K_s = \frac{Eb_{cf}t_{cf}^2}{10} \quad (4.8)$$

the work equation gives:

$$\frac{\Delta V_{eq}}{\Delta \gamma} = \frac{4M_s}{0,95d_b \Delta \gamma} = \frac{4K_s}{0,95d_b} \quad (4.9)$$

from the knowledge of $\Delta M = 0,95d_b \Delta V_{eq} (1 - \rho)$, it is possible to obtain the stiffness of the second branch.

$$K_1 = \frac{\Delta M}{\Delta \gamma} = \frac{4Eb_{cf}t_{cf}^2}{10(1-\rho)} = \frac{4G \cdot 2(1+\nu)b_{cf}t_{cf}^2}{10(1-\rho)} = \frac{1,04Gb_{cf}t_{cf}^2}{(1-\rho)} \quad (4.10)$$

where $(1 - \rho)$ is equal to β . Krawinkler assumes that the strain-hardening phase begins starting from a rotation of the panel equal to $4\gamma_y$. In correspondence of this rotation is possible to find the moment.

$$M_{sh} = M_y + \frac{3,12\tau_y b_{cf}t_{cf}^2}{\beta} \quad (4.11)$$

Last branch of Krawinkler model is described by the strain-hardening modulus of the steel.

$$K_2 = \frac{G_{st} A_{eff,KW} d_b}{\beta} \quad (4.12)$$

In case of S275 steel a typical value of the ratio between G and G_{st} can be equal to $E/E_h=42.8$.

Krawinkler model is currently adopted by several building codes (AISC, 2005; UBC, 1997), even though both Wang and Kim & Engelhardt have shown that the model does not provide a good agreement with the experimental results in case of column flanges thicker than 25 mm. The application of Krawinkler model for the case of HEB 200 column and IPE 270 beam is depicted in Fig. 4.10.

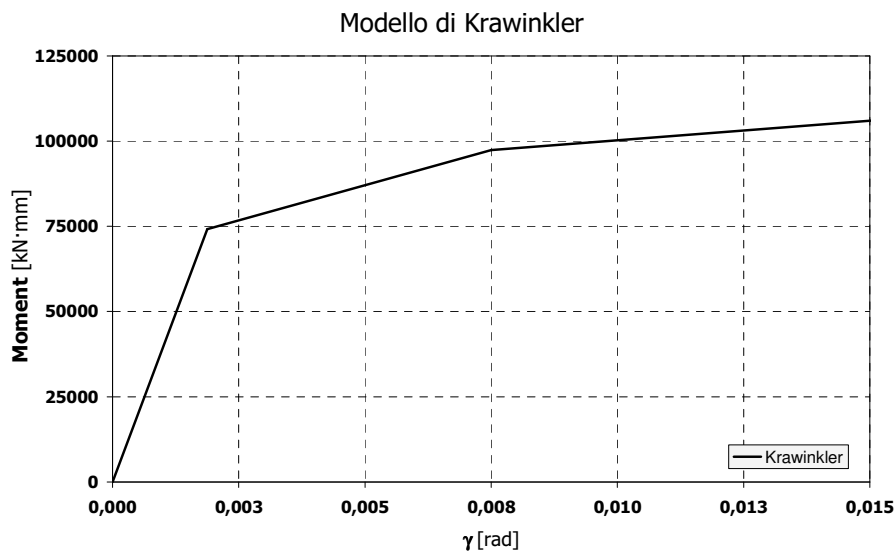


Fig. 4.10 – Krawinkler model in case of HEB 200 column and IPE 270 beam

4.2.1.3 Wang monotonic model (1985)

Wang model is still tri-linear, but differs from Krawinkler approach for the definition of the effective shear area, the first post-elastic stiffness and for the definition of the boundaries between the three zones: elastic, post-elastic and strain-hardening.

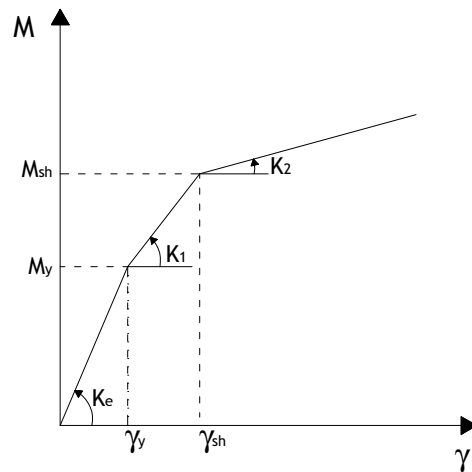


Fig. 4.11 – Shear panel model (Wang, 1985)

The effective shear area is defined as:

$$A_{eff,W} = (d_c - 2t_{cf})t_{cw} \quad (4.13)$$

For the description of the elastic behavior Eqs.(4.2) - (4.5) can be used. The stiffness of the first post-elastic branch are given by means of semi-empirical

formulas and the boundary is defined by the rotation $\gamma_{sh} = 3,5\gamma_y$ and the moment $M_{sh} = M_y + 4M_{pcf}$, where M_{pcf} is the column flange plastic moment.

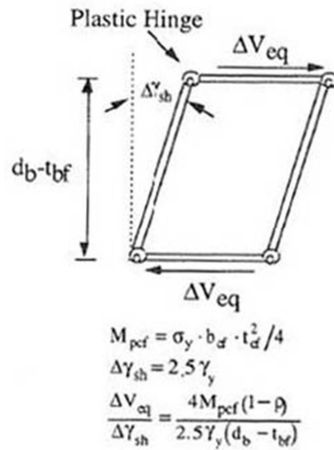


Fig. 4.12 – Wang post-elastic model

Wang assumes that the post-elastic phase begins with the formation of four plastic hinges at the panel corners (Fig. 4.12), so that:

$$K_1 = \frac{\Delta M}{\Delta \gamma} = \frac{(M_{sh} - M_y)}{\gamma_{sh} - \gamma_y} = \frac{4M_{pcf}}{2,5\gamma_y} = \frac{4 \frac{b_{cf} t_{cf}^2}{4} f_y}{2,5 \frac{f_y}{\sqrt{3G}}} = 0,7 G b_{cf} t_{cf} \quad (4.14)$$

The approximation of this model is mainly due to the semi-empirical approach. In fact, the model provides good results only in case of panels with ratio

between thickness of the column flanges and depth of the column close to that used for the calibration of the model.

The strain-hardening branch is defined in the same way of Krawinkler model, but with a different definition of the effective shear area:

$$K_2 = \frac{G_{st} A_{eff,W} d_b}{\beta} \quad (4.15)$$

The representation of the model in case of the coupling HEB200-IPE 270 is reported in Fig. 4.13.

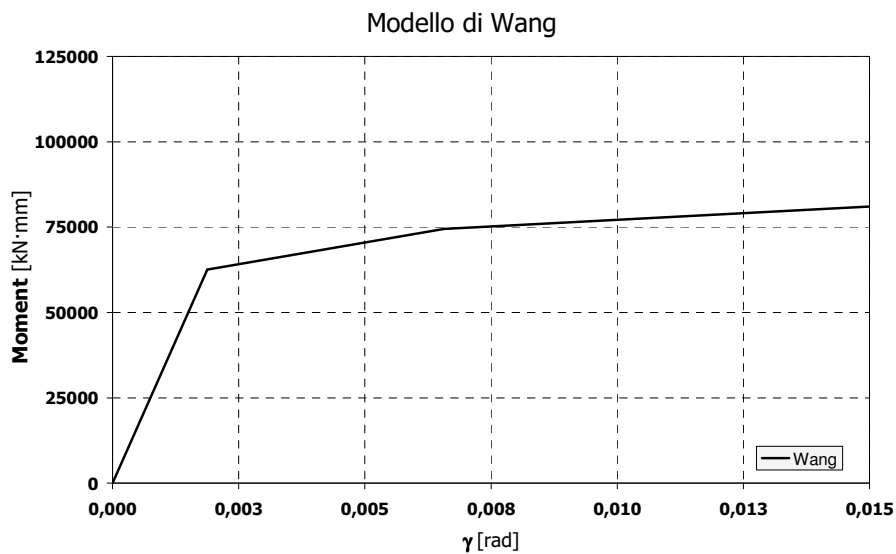


Fig. 4.13 – Wang model

4.2.1.4 Fielding and Wang modified monotonic model (1996)

As already remarked either Fielding, Wang and Krawinkler model provide good agreement with the experimental results only in some cases. The approximation of the models are mainly related to the simplifications made in the basic assumptions or in their semi-empirical character which can lead in case of thick column flanges to unsatisfactory results.

A first attempt to improve the existing models has been made by (Kim & Engelhardt, 1996), providing simple modifications to Fielding and Wang models. The enhancements proposed by the two authors are summarized in the following:

- in both cases the effective shear area is assumed equal to $A_{eff,MOD} = d_c t_{cw}$;
- Fielding model provides good approximation at low rotations but gives unsatisfactory results in case of great rotations, so that the strain hardening is assumed to begin at a rotation equal to $4\gamma_y$.

Some examples of the application of the improved models are here reported to show how the simple modifies significantly enhance the accuracy of the models.

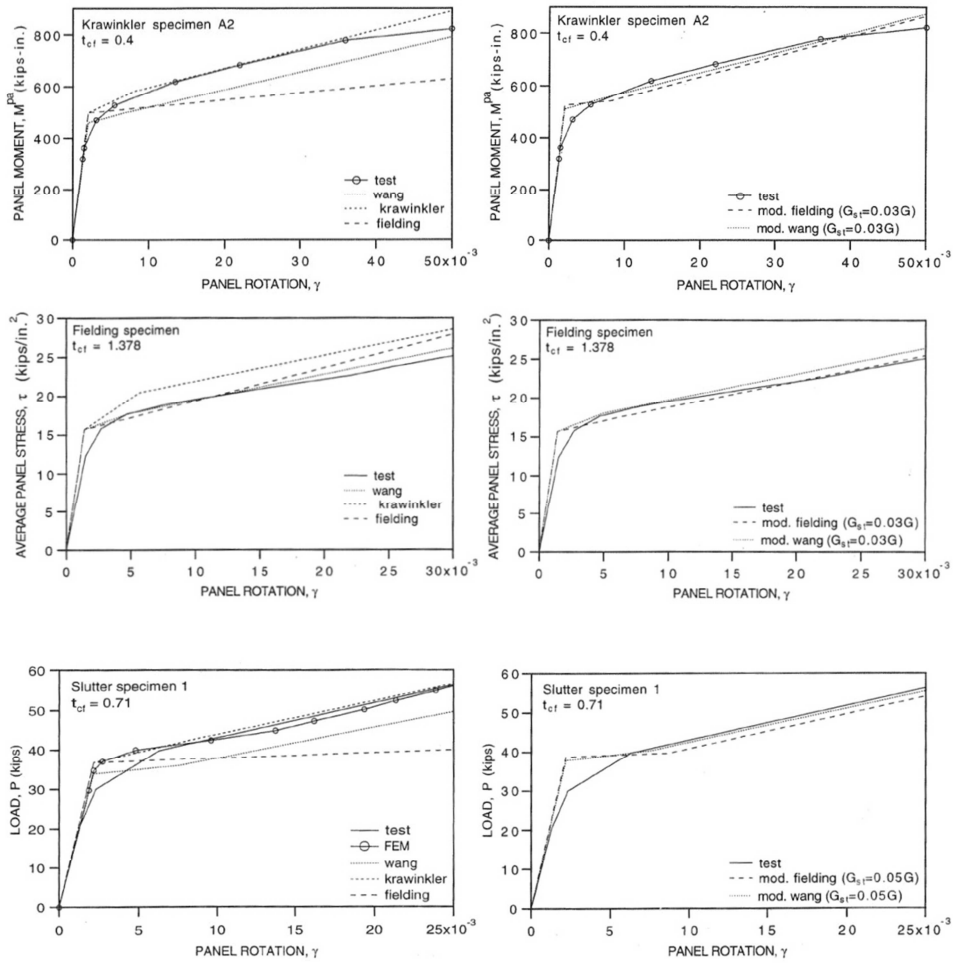


Fig. 4.14 – Comparison between Fielding and Wang models (Left) and Improved Fielding and Wang models (Right)

4.2.1.5 Kim & Engelhardt monotonic model (2002)

As above said, since 1996 Kim & Engelhardt expressed the need to develop a more accurate model for the prediction of the shear panel behavior also in cases of thick column flanges. Thus, in 2002, the two authors on the base of the results obtained in 1996 proposed a new update to the existing models. The main feature of the improved model is that it is able to proper account for shear and flexural effect on the panel zone also in the elastic phase. Therefore, the researchers propose a quadri-linear model constituted by: elastic behavior, first and second post-elastic phase and strain-hardening behavior (Fig. 4.15).

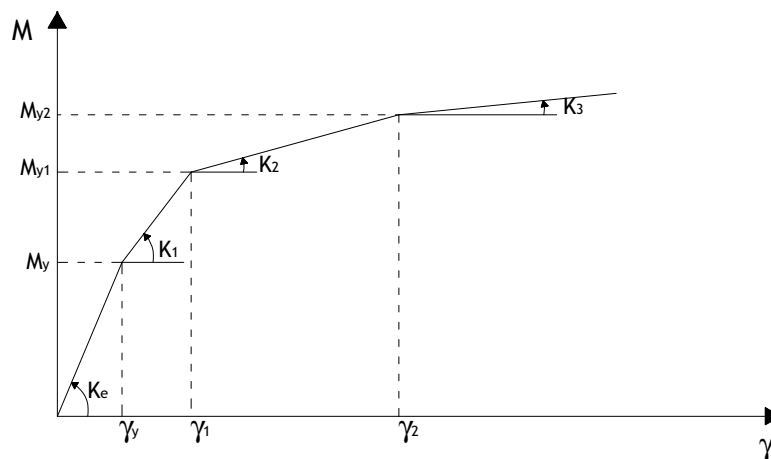


Fig. 4.15 – Quadri-linear model of Kim & Engelhardt

Kim & Engelhardt suggest to model the panel zone dividing the region into two equivalent beams constrained at the beam ends by means of semi-rigid constraints and symmetric with respect to the panel centerline. Consequently,

the displacement of the panel subjected to the shear action V_{eq} can be calculated accounting for the flexural and shear deformability:

$$\delta = (\varepsilon_f + \varepsilon_t) V_{eq} \quad (4.16)$$

where δ is the displacement of the panel zone, ε_f and ε_t are the flexural and shear deformabilities computed as:

$$\varepsilon_f = \frac{[(d_b - t_{bf})/2]^3}{C_r EI_c} \quad (4.17)$$

$$\varepsilon_t = \frac{[(d_b - t_{bf})/2]}{G(d_c t_{cw} + R_f A_{dp})} \quad (4.18)$$

where C_r is a coefficient accounting for the semi-rigidity of the end-constraint, A_{dp} is the area of the doubler plates if adopted, and R_f is a reduction factor accounting for the effectiveness of the doubler plates. The constraining coefficient has to be contained between 12 (fully restrained) and 3 (pinned), the authors by means of FEM analyses propose a coefficient equal to 5. Therefore, considering that the relationship between the moment and the equivalent shear is:

$$\frac{M}{(d_b - t_{bf})} = \frac{V_{eq}}{1 - \frac{(d_b - t_{bf})}{L_c}} \quad (4.19)$$

Eq. (4.16) can be rewritten as:

$$M = V_{eq} \frac{(d_b - t_{bf})}{\beta} = \frac{\varepsilon_1 \varepsilon_2}{\varepsilon_1 + \varepsilon_2} \frac{(d_b - t_{bf})}{2} \frac{(d_b - t_{bf})}{\beta} \gamma \quad (4.20)$$

as a consequence the stiffness of the elastic branch is provided by the next equation.

$$K_e = \frac{\varepsilon_1 \varepsilon_2}{\varepsilon_1 + \varepsilon_2} \frac{(d_b - t_{bf})}{2} \frac{(d_b - t_{bf})}{\beta} \quad (4.21)$$

The first yielding moment is reached when the average shear is equal to:

$$M_y = K_e C_y \gamma_y \quad (4.22)$$

where C_y is a reduction factor accounting for the real stress distribution in the panel zone.

The behavior in the first post-elastic phase is described by means of an approach similar to that adopted by Fielding and Huang, i.e. by modeling the panel as a two T-beams whose height is equal to a quarter of the height of the column web. In this hypothesis Eqs.(4.17)-(4.18) become:

$$\varepsilon_{pf} = \frac{[(d_b - t_{bf})/2]^3}{C_r EI_T} \quad (4.23)$$

$$\varepsilon_{pt} = \frac{[(d_b - t_{bf})/2]}{G \left[\left(\frac{d_c}{2} - d_{yw} \right) t_{cw} + \frac{R_f A_{dp}}{4} \right]} \quad (4.24)$$

where I_T is the inertia modulus of the T-section and d_{yw} is equal to a quarter of the height of the column web. Ultimate moment and stiffness of the second branch are calculated considering the new deformability:

$$K_1 = 2 \frac{\varepsilon_{pf} \varepsilon_{pt}}{\varepsilon_{pf} + \varepsilon_{pt}} \frac{(d_b - t_{bf})}{2} \frac{(d_b - t_{bf})}{\beta} \quad (4.25)$$

$$M_{y1} = \tau_y (d_c t_{cw} + R_f A_{dp}) \frac{(d_b - t_{bf})}{\beta} \quad (4.26)$$

second post-elastic stiffness is related to the condition of fully plasticization of the panel, adopting an approach similar to that used by Krawinkler, i.e. considering the panel restrained by four rotational springs at the corners. The stiffness of the single spring is given by:

$$K_s = \frac{Eb_{cf}t_{cf}^2}{C_s} \quad (4.27)$$

where C_s has to be determined experimentally. With simple calculations is possible to obtain stiffness and ultimate moment of the second branch:

$$K_2 = \frac{4Eb_{cf}t_{cf}^2}{C_s\beta} \quad (4.28)$$

$$M_{y2} = M_{y1} + \bar{\sigma}_y b_{cf} t_{cf}^2 \quad (4.29)$$

where $\bar{\sigma}_y$ is the ultimate stress of the column flanges, accounting for the influence of the normal load. Finally the stiffness of the strain-hardening branch is the same considered by Krawinkler.

$$K_3 = \frac{G_{st} A_{eff} (d_b - t_{bf})}{(1 - \rho)} \quad (4.30)$$

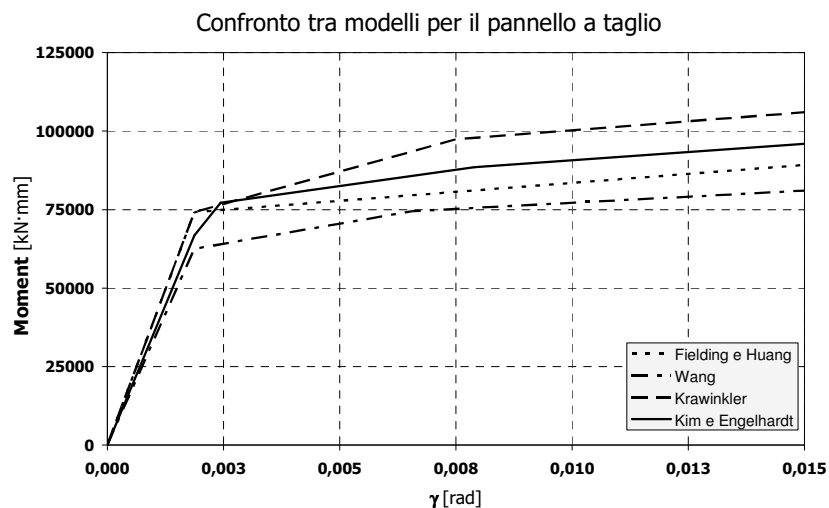


Fig. 4.16 – Comparison among literature models in case of HEB 200-IPE 270 coupling

Considering the coupling HEB 200-IPE 270 and comparing Kim & Engelhardt model, using the coefficients $C_r = 5$, $C_y = 0.9$, $C_s = 20$, as suggested by the authors, with the other literature models is possible to realize that in case of thin flanges (15 mm) the difference between Kim & Engelhardt model and literature model is not so marked.

In order to show the accuracy of Kim & Engelhardt model in case of thick column flanges some charts comparing the accuracy of literature model and Kim & Engelhardt model for FEM analysis and experimental tests carried out by Slutter are shown. From these comparison is possible to realize that Krawinkler model provides accurate results only in case of flanges thinner than 25 mm Fig. 4.17 - Fig. 4.19.

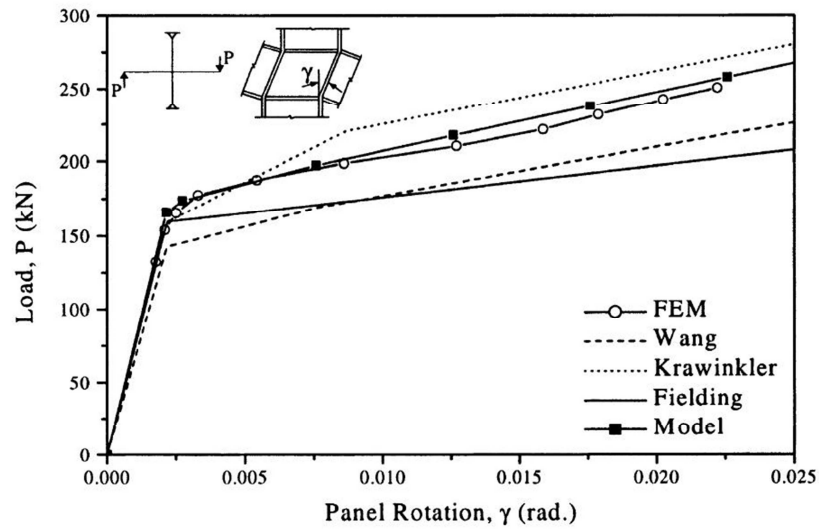


Fig. 4.17 – Comparison among literature models for FEM analysis $t_{cf}=27$ mm

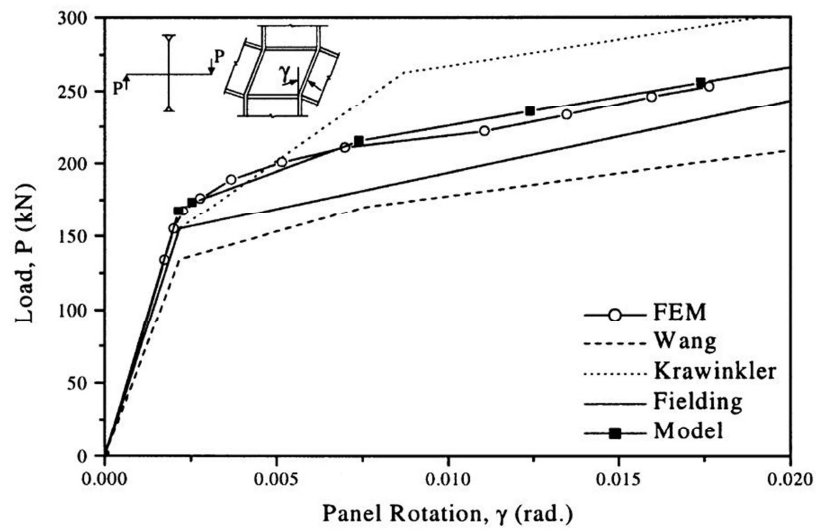


Fig. 4.18 – Comparison among literature models for FEM analysis $t_{cf}=36$ mm

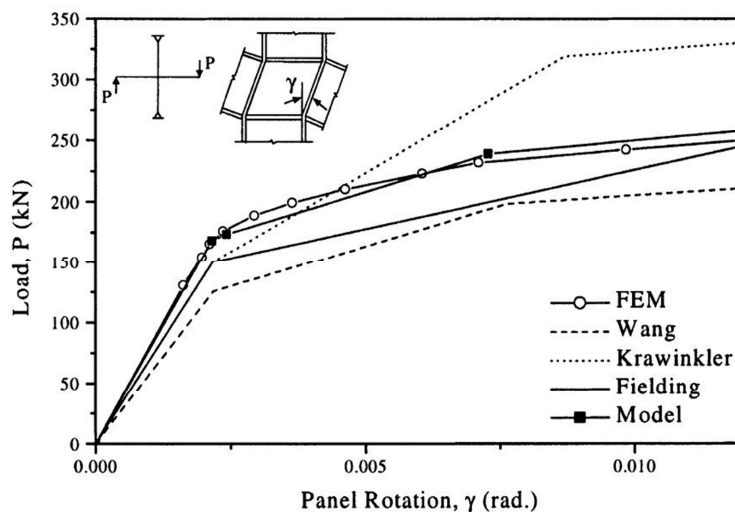


Fig. 4.19 – Comparison among literature models for FEM analysis $t_{cf}=45$ mm

4.2.1.6 Kim & Engelhardt cyclic model (2002)

The number of literature models able to describe the behavior of shear panels is limited. One of the possibilities is represented by the adoption of the kinematic hardening model (Fig. 4.20).

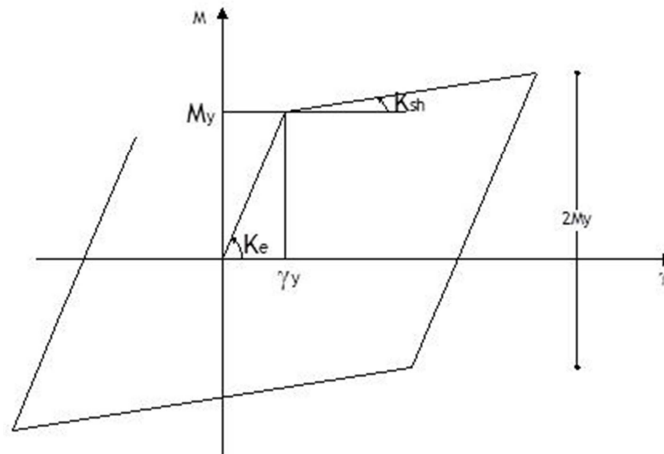


Fig. 4.20 – Kinematic Hardening model

In kinematic hardening model, after the first yielding the panel behavior is represented by means of a strain hardening branch. Past works (Kim & Engelhardt, 1996; Kim & Engelhardt, 2002) have shown that this type of model, in most cases, provides unsatisfactory results. In fact the adoption of kinematic hardening model can lead to underestimation of the dissipated energy of the 80%

In this work, for the importance of the shear panel response in the prediction of the whole moment rotation curve of a joint, Kim and Engelhardt cyclic model has been chosen due to the best agreement with the experimental results (Kim & Engelhardt, 1996; Kim & Engelhardt, 2002).

One of the main features of the model, originally developed by Cofie and Krawinkler to model cyclic stress-strain behaviour of steel, resides in the rules

for the movement of the bound lines. In such a model the cyclic steady state curve, defined as the locus of peak moments obtained by cycling the shear panel at various rotation amplitudes (Fig. 4.22), is used to describe the bound lines shift at the i -th cycle.

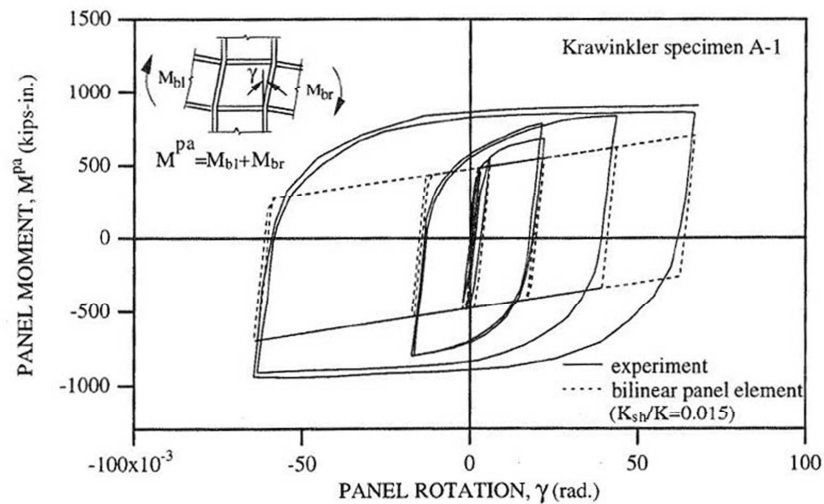


Fig. 4.21 – Application of Kinematic Hardening model to Krawinkler specimen-

A1

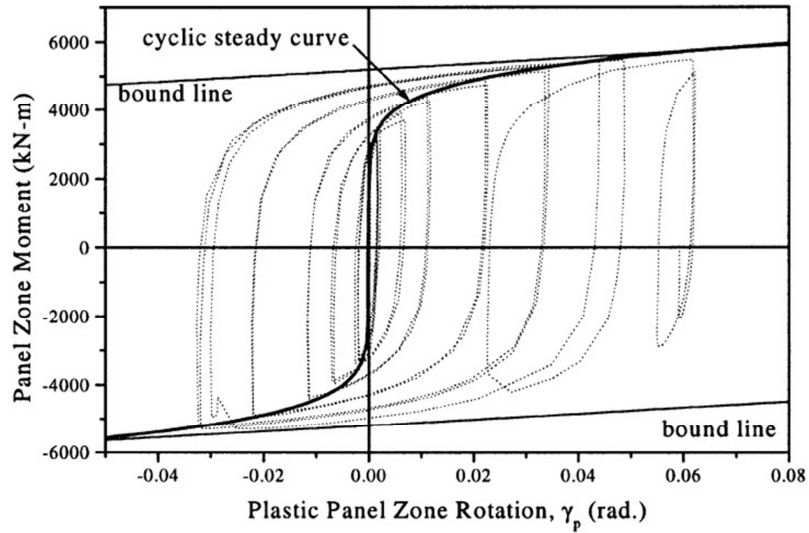


Fig. 4.22 – Cyclic steady state curve

The following expression for the cyclic steady state curve has been proposed by the authors:

$$\frac{\gamma}{\gamma_n} = \frac{M_s}{M_n} + \left(\frac{M_s}{\xi M_n} \right)^c \quad (4.31)$$

where M_s is the ordinate of the cyclic steady state curve, M_n is the normalizing moment assumed equal to the panel zone yield moment plus two times the plastic moment of the column flange, γ_n is the rotation corresponding to the normalizing moment, given by the ratio between the normalizing moment and the panel elastic stiffness evaluated according to Kim and Engelhardt

monotonic model for panel zone in shear and ξ and c are two parameters empirically determined, given in Table 4.1.

Table 4.1 – Empirical parameters for the application of Kim & Engelhardt model

ξ	c	F_H	F_S	F_R
1.1	7	0.45	0.07	0.05

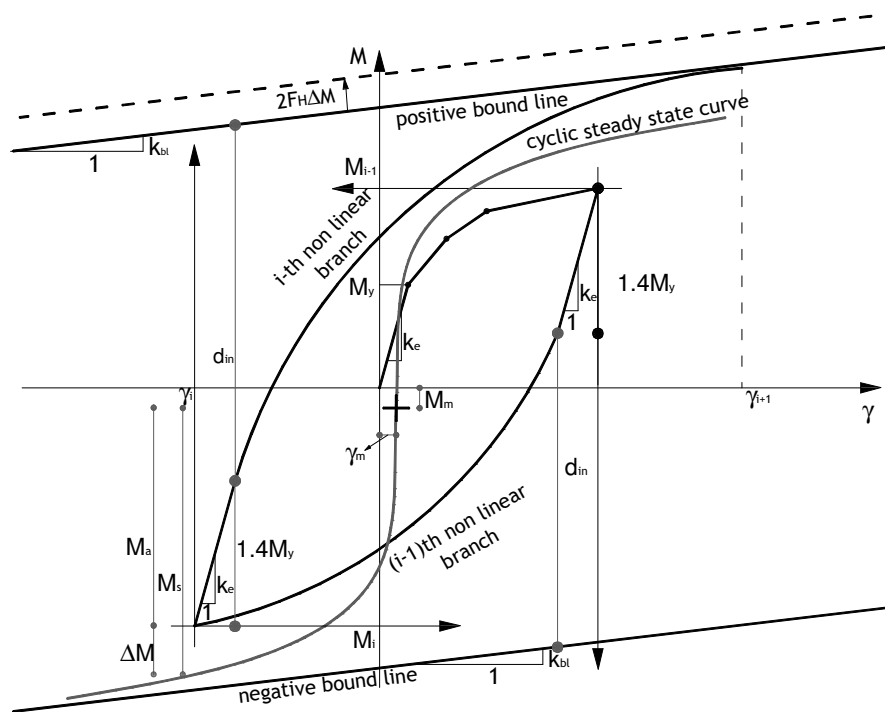


Fig. 4.23 – Shear Panel cyclic curve

The first step to apply the model is the evaluation of the monotonic law for the prediction of the first loading branch. The monotonic moment-rotation relationship is idealized by means of the quadri-linear curve, defined by two post-elastic branches and a strain-hardening branch proposed by (Kim & Engelhardt, 2002) (Fig. 4.15). After the first semi-cycle, the i -th loading or unloading branch is constituted by a linear elastic branch, whose elastic limit factor is equal to 1.4 times the monotonic value M_y (Fig. 4.15) as determined on the basis of available experimental results, followed by a non-linear curve derived according to the expression proposed by (Dafalias, 1975; Dafalias & Popov, 1975; Dafalias & Popov, 1976).

The non-linear branch, according to Dafalias' bounding surface theory, is defined by means of the following parameters:

- the distance d_{in} between the bound line and the end point of the previous linear branch (Fig. 4.23);
- shape factor ψ whose value depends on the accumulated plastic rotation θ_p during the previous loading history;
- the slope K_p^{bl} of the bound line (Fig. 4.23).

In particular, the factor ψ governs the shape of the i -th non-linear branch. Kim and Engelhardt have found that a shape factor equal to 20 for small rotation amplitudes and equal to 40 for large rotation amplitude provides a good agreement with available experimental tests (Kim & Engelhardt, 1996). Thus, a shape factor varying with a Boltzman function has been proposed:

$$\psi = 40 + \frac{(20 - 40)}{\left[1 + e^{\frac{(\theta_p - 0.213)}{0.074}} \right]} \quad (4.32)$$

where θ_p is the accumulated plastic rotation at the i-th cycle.

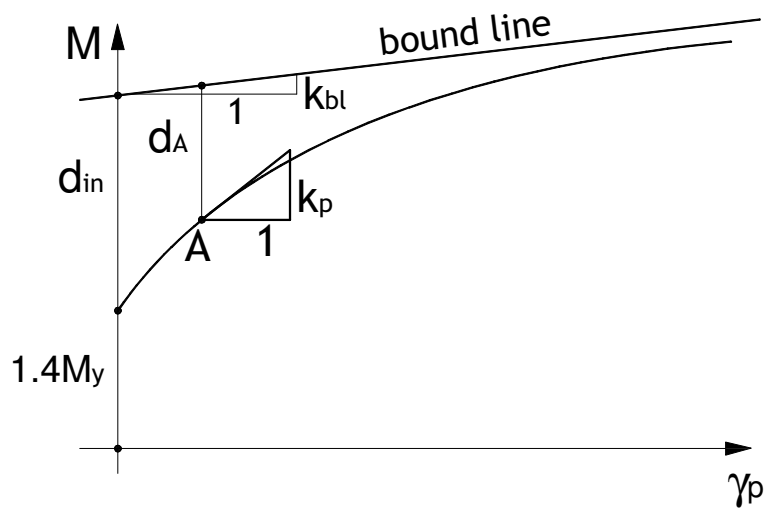


Fig. 4.24 – Dafalias-Popov model for Hysteresis Curve

According to Dafalias' theory, the plastic part of the non-linear curve is defined by means of its plastic stiffness K_p^A (Fig. 4.24).

This is related to the distance from the bound line of the generic point d_A , to d_{in} , to ψ and to the stiffness of the bound line by means of the following expression:

$$K_p^A = K_p^{bl} \left[1 + \psi \frac{d_A}{d_{in} - d_A} \right] \quad (4.33)$$

By means of comparison with experimental data a slope of the bound line $K_p^{bl}=0.008K_e$ is assumed, where K_e is the initial stiffness of the shear panel defined by Kim and Engelhardt monotonic model (Kim & Engelhardt, 2002). Finally, the tangent stiffness at the point A of the inelastic curve is determined accounting for its elastic part by means of the following relationship:

$$K_t^A = \frac{K_e K_p^A}{K_e + K_p^A} \quad (4.34)$$

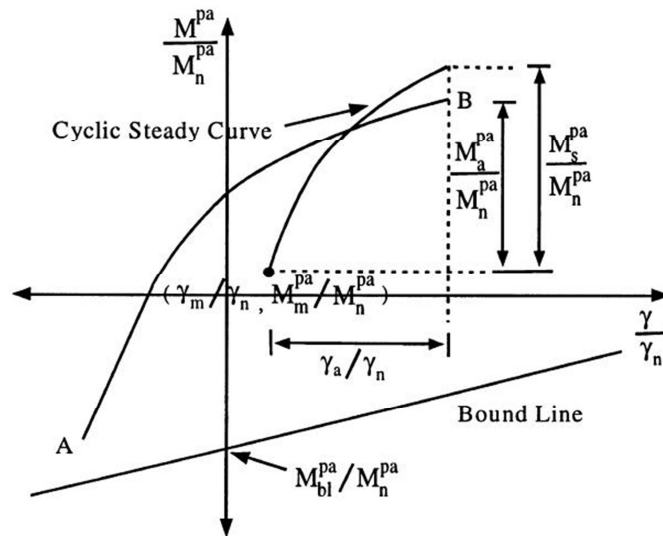


Fig. 4.25 – Procedure for the translation of the bound line

Finally, the procedure to shift the bound line at the i -th loading or unloading cycle can be summarized in the following steps (Fig. 4.25):

- compute the mean value of the bending moment and the mean value of the rotation corresponding to the previous semi-cycle, given by:

$$M_m = \frac{(M_i + M_{i-1})}{2} \quad (4.35)$$

$$\gamma_m = \frac{(\gamma_i + \gamma_{i-1})}{2} \quad (4.36)$$

- compute the semi-amplitude of moment range and rotation range corresponding to the previous semi-cycle, given by:

$$M_a = \frac{|M_i - M_{i-1}|}{2} \quad (4.37)$$

$$\gamma_a = \frac{|\gamma_i - \gamma_{i-1}|}{2} \quad (4.38)$$

- calculate the difference ΔM between the moment amplitude M_a and M_s , which is defined as the moment on the cyclic steady state curve corresponding to the rotation amplitude γ_a ;
- if ΔM is positive cyclic hardening is predicted and bound lines are moved outward by an amount equal to $2F_H\Delta M$;

- if ΔM is negative cyclic softening is predicted and bound lines are moved inward by an amount equal to $2F_S\Delta M$;
- finally bound lines are moved to account for the mean moment relaxation by an amount equal to $F_R M_m$.

The hardening, softening and mean moment relaxation coefficients, namely F_H, F_S and F_R respectively, are given in **Table 4.1** as experimentally evaluated by (Cofie & Krawinkler, 1985).

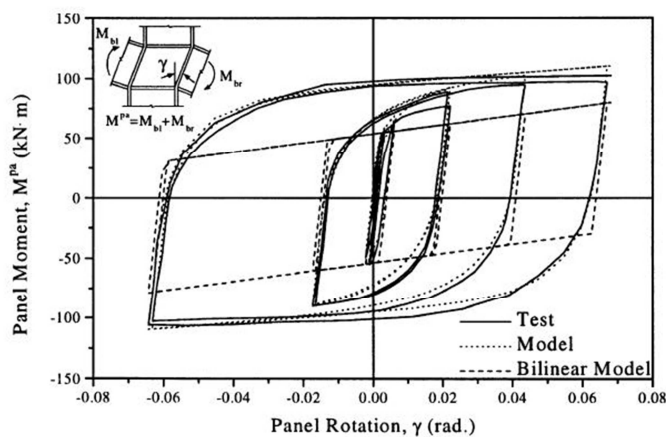


Fig. 4.26 – Comparison with Krawinkler test A1

The accuracy of the model is shown with reference to Krawinkler specimen A1 and A2 (Fig. 4.26 - Fig. 4.27). In the first case also the comparison with respect to the kinematic hardening model is shown and the different ability of the two models to simulate the shear panel response under cyclic loads is pointed out.

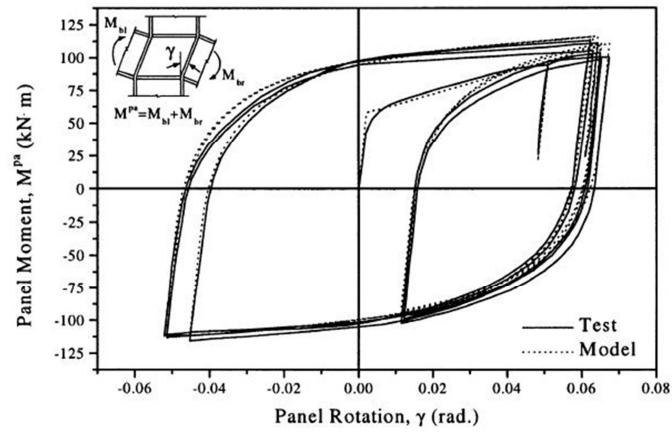


Fig. 4.27 – Comparison with Krawinkler test A2

4.2.2 Modeling of column web panels under tension and compression

Generally, in beam-to-column connections, the column web is subjected to concentrated tension/compression loads due to the normal action transmitted by the beam flanges. Such forces produce local effects which have to be properly accounted in terms of local deformations. These actions, as shown in Fig. 4.28 - Fig. 4.29 have to be added to the shear and the vertical loads.

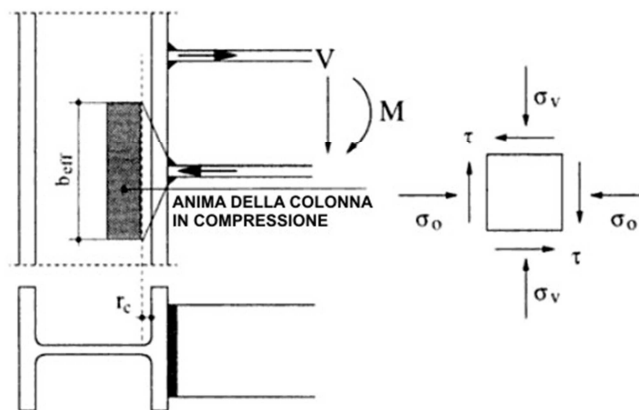


Fig. 4.28 – Column web subjected to compression

Moreover, the behaviour of the column web subjected to tension/compression is strongly affected by the diffusion of the loads through the connecting plates and the column flange, and by the interaction with the other tangential and/or vertical stresses. In addition, the collapse of a panel in compression can arise both for attainment of the squash load or for local buckling, so that second order effects have to be carefully evaluated.

The behavior of panels subjected to monotonic loads has been widely characterized in the past and is at the present time codified in (CEN, 2005b). In the same manner, the behavior of panels subjected to load reversal has been studied in past and, in particular, in the following the model proposed by (Cofie & Krawinkler, 1985) will be illustrated.

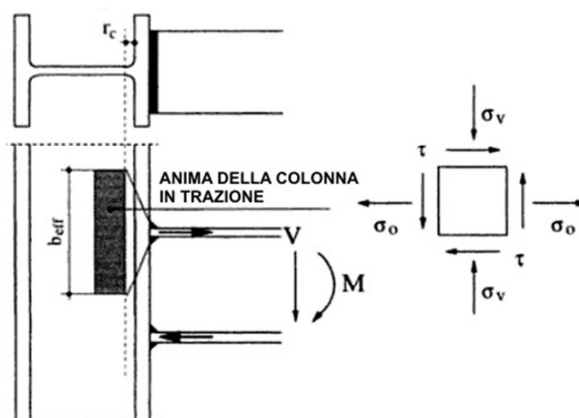


Fig. 4.29 – Column web subjected to tension

Generally speaking, the behavior of panels under alternate tension/compression can be studied starting from the knowledge of the cyclic behavior of structural steel. Mechanical response of a material subjected to cyclic reversal is not uniform during the loading process. In fact, three phases can be individuated: the first phase, namely transitory phase, where a variation of the response at the increase of the number of cycles can be observed, the second phase, namely saturation phase, where the response of the elements is constant as the number of cycles increases and the third phase, namely near collapse phase, where the response is again variable up to the failure of the element.

In the transitory phase, two types of behavior, which depend on the material and on the loading history, can be found: cyclic hardening or softening. These behaviors are reflected in the increase/reduction of the peak stress (Fig. 4.30). Successively, response become stable and for each cycle of loading/unloading the cyclic curve assume the same shape. In case of structural steel this phase is the most important, because it is the greatest part of the material life.

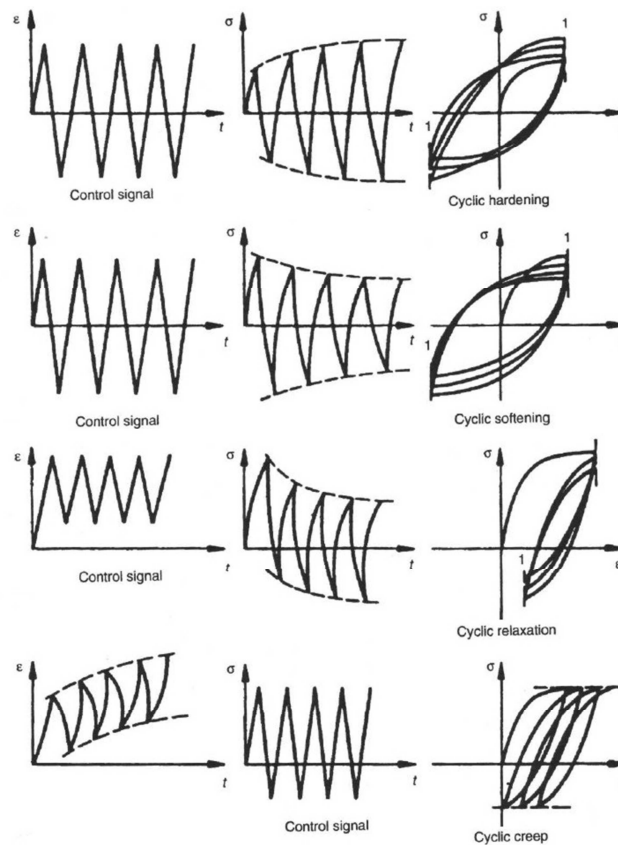


Fig. 4.30 – Transitory phase

Usually, the best way to predict the cyclic response of the structural steel is the knowledge of the locus of the peak response in the saturation phase, i.e. the cyclic steady state curve. The knowledge of this curve is of fundamental importance because steel tends to follow CSSC whatever the loading history. The best way to provide the shape of CSSC is to arrange constant amplitude tests finding for each test the value of the stabilized peak stress. In Fig. 4.31 is depicted the case of a test where after the monotonic cycle the specimen is subjected to a series of constant amplitude cycle with mean value equal to the amplitude. It is worth note that cycles tends to follow the CSSC (dashed line) after the transitory phase.

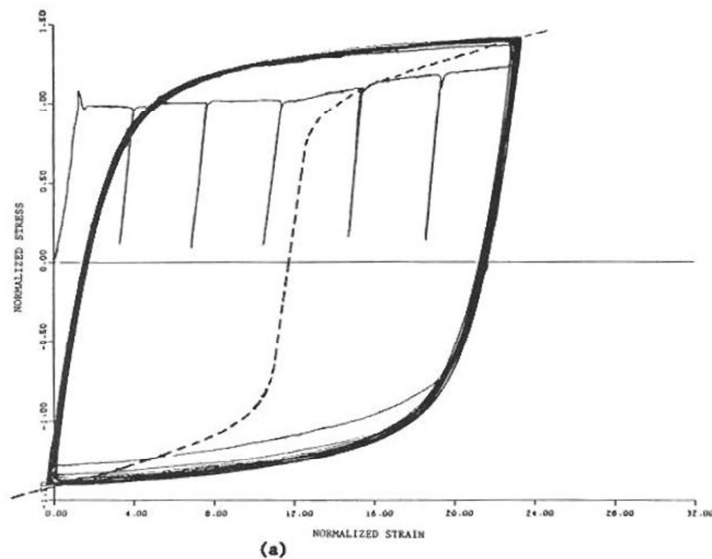


Fig. 4.31 – Stabilized response

In Fig. 4.32 other two cases where the peak stress goes above the saturation curve and then, by means of a transitory softening phase, goes back to the CSSC are represented.

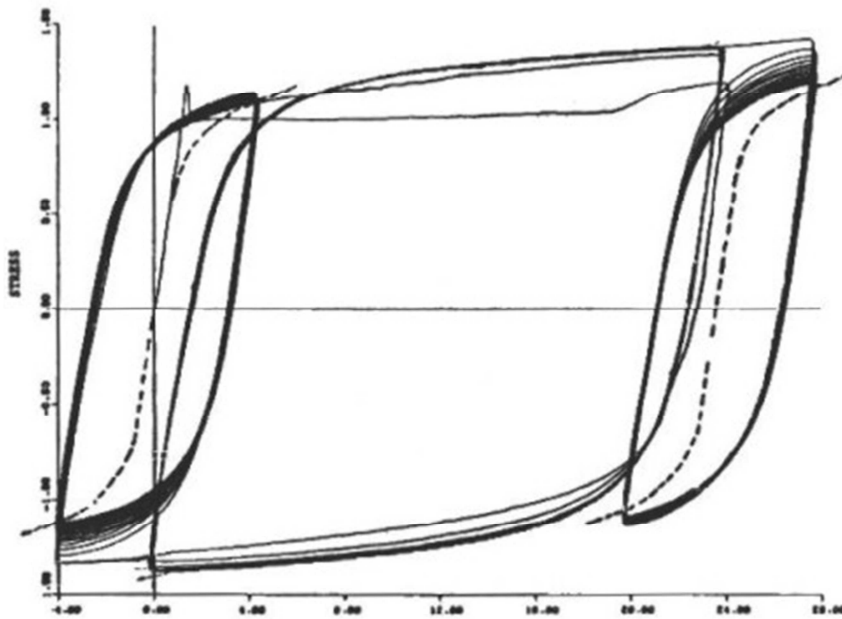


Fig. 4.32 – Stabilized response after softening

In addition, studies by Cofie have evidenced that, in case of steel, hardening is a relatively fast process, whilst softening and relaxation of the mean stress are relatively slow process. In Cofie studies, these three behavior are accounted for by means of three coefficients: hardening coefficient (F_H), softening factor (F_S) and relaxation of the mean stress factor (F_R).

Hardening factor represents the utilization rate for each excursion of the available hardening. Available hardening (H_a) is defined as the difference between the peak stress at the i -th cycle (σ_a) and the saturation stress corresponding to the cycle amplitude (σ_s):

$$H_a = \sigma_s - \sigma_a \quad (4.39)$$

as a consequence the hardening factor is obtained as:

$$F_{H,n} = \frac{H_{a,n-1} - H_{a,n}}{H_{a,n-1}} = 1 - \frac{H_{a,n}}{H_{a,n-1}} \quad (4.40)$$

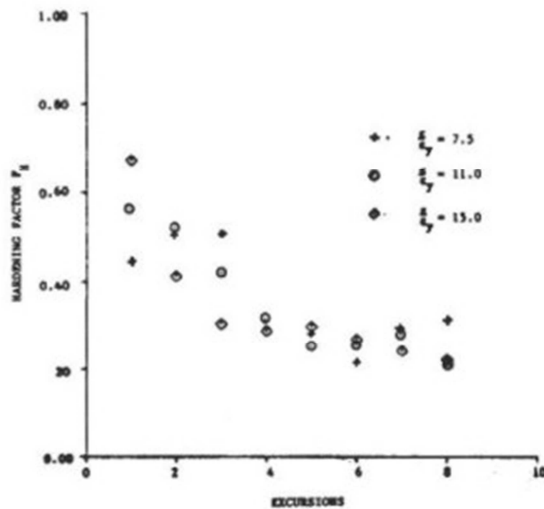


Fig. 4.33 – Hardening factor

the hardening coefficient has been obtained by Coffie on the base of constant amplitude tests on A36 steel. In Fig. 4.33 are reported Coffie's results which evidence that hardening factor decreases as the number of cycle increases.

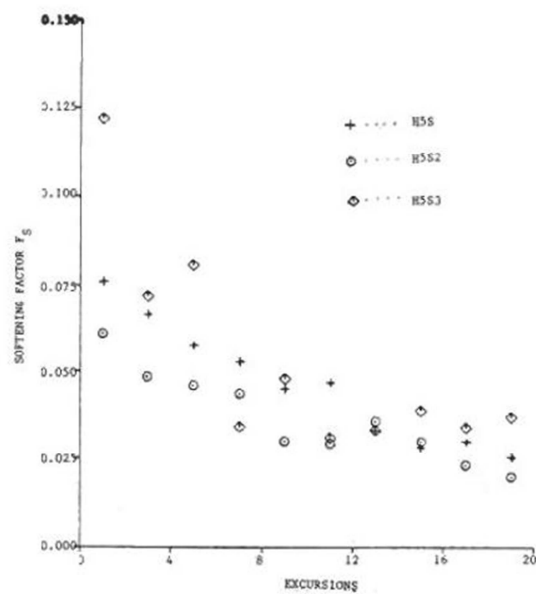


Fig. 4.34 – Softening factor

Conversely softening factor measures the ability of the material to return, during the transitory phase, to the saturation curve. Coefficient is expressed by means of the available softening.

$$S_a = \sigma_a - \sigma_s \quad (4.41)$$

$$F_{S,n} = \frac{S_{a,n-1} - S_{a,n}}{S_{a,n-1}} = 1 - \frac{S_{a,n}}{S_{a,n-1}} \quad (4.42)$$

Analogously to Fig. 4.33 in Fig. 4.34 results obtained by Cofie for the softening factor are represented. It is evidenced how the softening process is slower compared to hardening process.

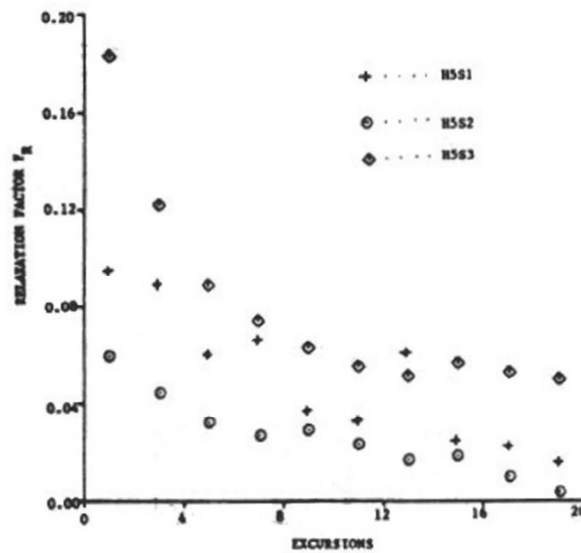


Fig. 4.35 – Relaxation factor

When the mean deformation of the generic cycle is not equal to zero hardening and softening phenomena are also affected by the mean relaxation of the material, which is defined as the ability of the material to reset to zero the mean stress in a determined number of cycles. In are reported the results of Cofie work.

Model of Cofie and Krawinkler is analogous to the one of Kim and Engelhardt for the shear panel. The main differences between the above models are constituted by the assumption of a constant shape factor ψ and of a non-linear monotonic law. Three curves are needed to apply the model: the monotonic curve, the cyclic steady state curve and the hysteretic curve consistent with Dafalias' bounding surface theory.

The monotonic curve is constituted by means of a linear branch followed by a yield plateau branch and a non linear hardening branch defined by a Ramberg-Osgood relationship. The branch are given by the following equations:

$$\sigma = E\varepsilon \quad \text{for} \quad 0 < \varepsilon < \varepsilon_y \quad (4.43)$$

$$\sigma = f_y \quad \text{for} \quad \varepsilon_y < \varepsilon < 14\varepsilon_y \quad (4.44)$$

$$\frac{\varepsilon}{\varepsilon_y} = \frac{\sigma}{f_y} + \left(\frac{\sigma}{Kf_y} \right)^{1/n} \quad \text{for} \quad \varepsilon > 14\varepsilon_y \quad (4.45)$$

where the coefficients K and n given in **Table 4.2**, as obtained from curve fitting of experimental data reported in Krawinkler et al. studies on A36 steel.

Table 4.2 – Empirical parameters for the application of Cofie & Krawinkler model

K	n	K'	n'	h	F _H	F _S	F _R
0.51	0.23	0.90	0.19	45	0.45	0.07	0.05

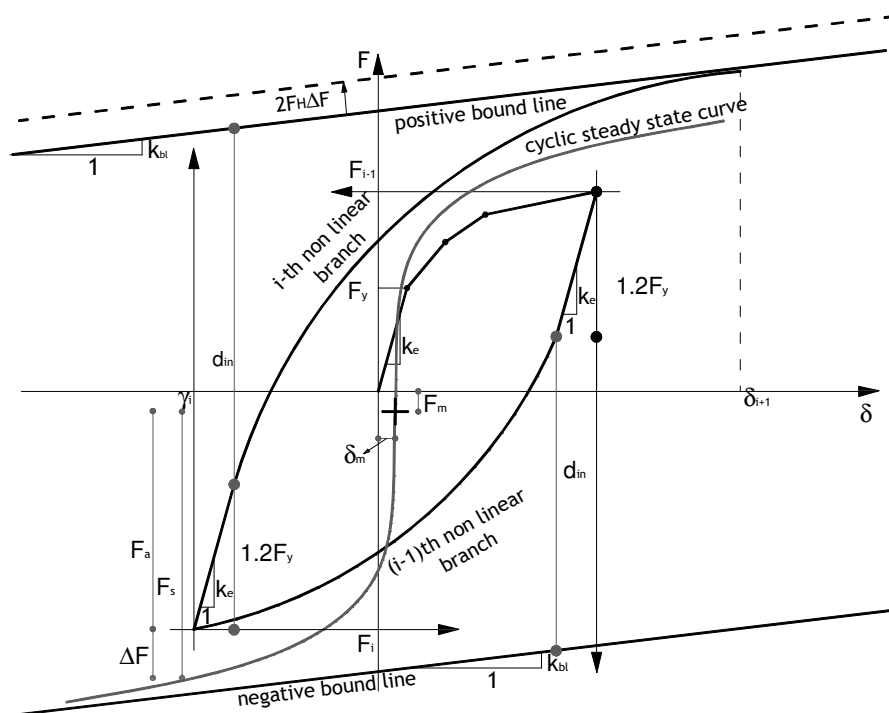


Fig. 4.36 – Cyclic curve at the i -th cycle for panels in tension and compression

As already seen for the modelling of the shear panel, the cyclic steady state curve is a stable reference curve during the whole cyclic loading history representing the saturation curve of the material (Fig. 4.36).

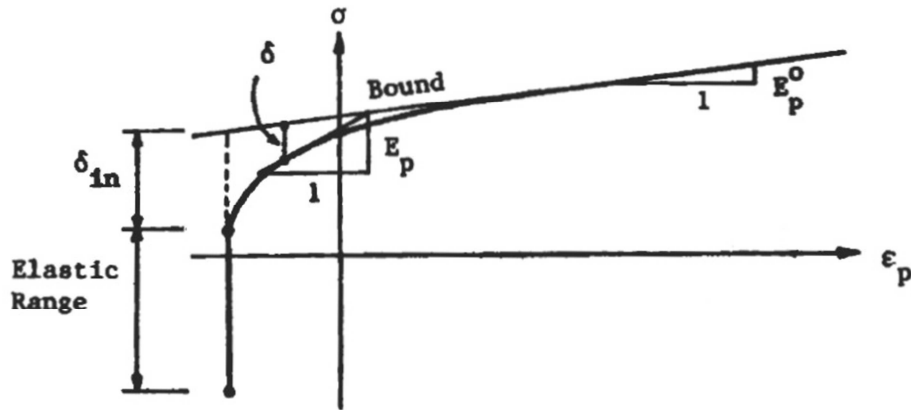


Fig. 4.37 – Hysteresis curve in Cofie model

This has been determined by Cofie and Krawinkler by means of constant amplitude cycles and it is described by a Ramberg-Osgood relationship:

$$\frac{\varepsilon}{\varepsilon_y} = \frac{\sigma}{f_y} + \left(\frac{\sigma}{K' f_y} \right)^{1/n'} \quad (4.46)$$

the parameters K' and n' are given in **Table 4.2**. Further details on the application of the model can be found in the original work of the authors.

Hysteresis curve is defined according to Dafalias' bounding surface theory.

$$E_p = \frac{d\sigma}{d\varepsilon_p} = E_{bl} \left[1 + h \left(\frac{\delta}{\delta_{in} - \delta} \right) \right] \quad (4.47)$$

The accuracy of the model is shown in the following figures.

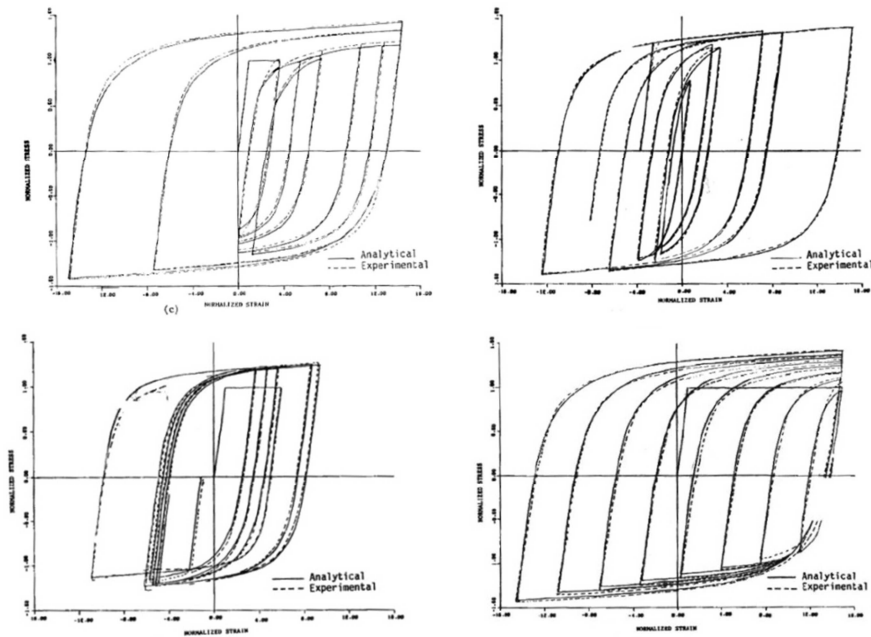


Fig. 4.38 – Theoretical-experimental comparisons

4.2.3 Modeling of the T-stub in tension

Following the same approach of Eurocode 3 (CEN, 2005a; CEN, 2005b), bolted joint components such as the end-plate in bending, the column flange in bending and the tee-stub in bending can be modelled by means of an “equivalent T-stub”. Aiming to develop a model for the prediction of the cyclic behaviour of bolted steel connections, it is of paramount importance the use of a cyclic model sufficiently reliable for predicting T-stub response under cyclic

actions. In this work, the model proposed by (Faella et al., 2000; Piluso & Rizzano, 2008) is applied.

According to such model the main parameter to define degradation laws of stiffness and strength is the energy cumulated at collapse under cyclic conditions. This is related to the energy absorbed under monotonic loads up to a displacement equal to the displacement amplitude of the i -th cycle, of the displacement history under investigation, by means of a non-dimensional parameter. Such non-dimensional parameter is a function of the ratio between the ultimate displacement of the T-stub under monotonic loading conditions and the plastic part of the displacement occurring in the i -th cycle. The ultimate displacement under monotonic loading conditions can be evaluated depending on the material mechanical properties, by means of a coefficient C , and on the geometrical properties of the T-stub, namely m and n , that are respectively defined as the distance between the bolt axis and the plastic hinge corresponding to the flange-to-web connection and the distance between the prying force and the bolt axis, and t_f , i.e. the plate thickness (Piluso et al., 2001).

By means of a regression analysis of experimental data dealing with isolated bolted T-stubs (i.e. the single joint component) under cyclic actions, the following relationship has been proposed by (Piluso & Rizzano, 2008):

$$\frac{E_{cc}}{E_0} = a_0 \left(\frac{t_f \delta_p}{2Cm^2} \right)^{-b_0} \quad (4.48)$$

where E_{cc} is the energy cumulated at collapse, assuming the conventional collapse as the attainment of 50% deterioration of energy dissipation capacity, E_0 is the area below the monotonic curve (i.e. the absorbed energy) up to a displacement equal to the one corresponding to the i -th cycle, C is a parameter depending on the material mechanical properties (Piluso et al., 2001), δ_p is the plastic part of the displacement corresponding to the i -th cycle and a_0 and b_0 are two regression parameters, given in **Table 4.3**.

Table 4.3 – Empirical parameters for definition of stiffness and strength degradation laws

a_0	b_0	a_1	a_2	a_3	b_1	b_2	b_3
1.1	1.212	0.345	0.158	4.595	0.849	0.053	0.137

The implementation of the model requires the preliminary evaluation of monotonic force-displacement curve by means of the theoretical approach proposed by (Piluso et al., 2001), starting from the knowledge of the geometrical and mechanical properties of the equivalent T-stub.

As soon as the T-stub monotonic behaviour has been theoretically predicted, for a given displacement amplitude the hysteresis loop is modelled by means of a multilinear approximation.

On the basis of experimental results on isolated T-stubs, the authors have observed that in constant amplitude cyclic tests, the points corresponding to the load inversion remain practically unchanged during loading and unloading process. These points, i.e. A and D in Fig. 4.39, can be identified starting from the maximum displacement achieved at the i -th cycle and the corresponding load on the monotonic force-displacement curve, as depicted in the same figure.

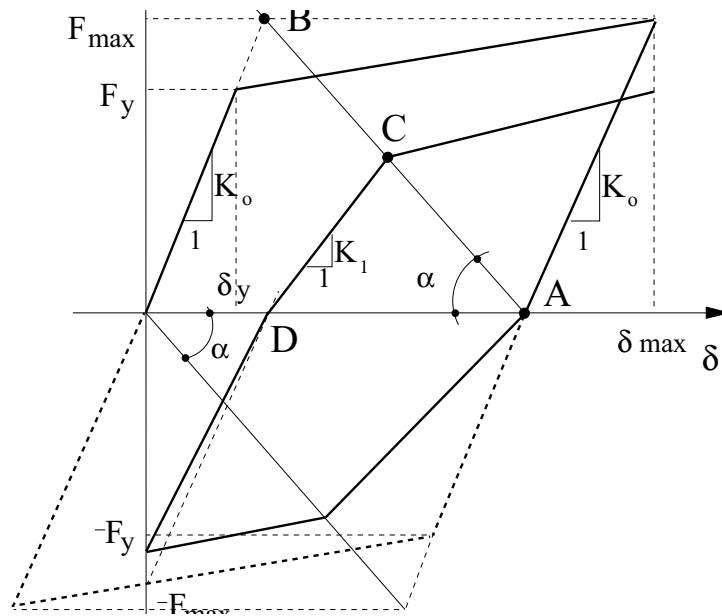


Fig. 4.39 – Piluso et al. model

As mentioned before, the characteristic points of the generic loading or unloading branch are defined provided that stiffness and strength degradation laws are known. Such degradation laws have been derived by means of a regression analysis of experimental data on isolated T-stubs, relating the degradation to the ratio between the maximum displacement of the i -th cycle (δ_{max}) and the threshold amplitude ($2\delta_y$) and to the ratio between the energy dissipated in the previous loading history up to the i -th cycle and the energy cumulated at collapse, derived by means of (4.48):

$$\frac{F_i}{F_{\max}} = 1 - a_1 \left(\frac{\delta_{\max}}{2\delta_y} \right)^{a_2} \left(\frac{E_{ic}}{E_{cc}} \right)^{a_3} \quad (4.49)$$

$$\frac{K_i}{K_0} = 1 - b_1 \left(\frac{\delta_{\max}}{2\delta_y} \right)^{b_2} \left(\frac{E_{ic}}{E_{cc}} \right)^{b_3} \quad (4.50)$$

where F_i and K_i are the force and stiffness at the i -th cycle, F_{\max} is T-stub strength corresponding on the monotonic curve to the displacement δ_{\max} of the i -th cycle, K_0 is the initial stiffness of the T-stub without bolt preloading (Faella et al., 1998b; Faella et al., 2000), δ_y is the yield displacement, E_{ic} is the energy dissipated up to the i -th cycle and a_1 , a_2 , a_3 , b_1 , b_2 , b_3 are regression parameters obtained by curve fitting of test data on isolated T-stubs. The values of the regression parameters required for the application of the model are reported in **Table 4.3**.

The main steps for the application of the model for predicting the cyclic response of the equivalent T-stub can be summarized as follows:

1. Prediction of monotonic force-displacement curve by means of (Piluso et al., 2001);
2. Computation of the energy E_0 absorbed under monotonic loads up to a displacement δ_{\max} equal to the one of the i -th cycle:

3. Computation of the energy dissipation capacity E_{cc} corresponding to the displacement δ_{max} of the i -th cycle by means of (4.48);
4. Evaluation of the force F_{max} corresponding to δ_{max} on the monotonic force-displacement curve;
5. Definition of the strength degradation law by means of (4.49);
6. Definition of the stiffness degradation law by means of (4.50);
7. Evaluation of the degraded values of the force F_i and of the stiffness K_i for the current cycle;
8. Definition of the current bilinear branch of the cyclic response.

4.3 Assembly and accuracy of the model

In order to obtain the cyclic moment-rotation curve of bolted beam-to-column joints starting from the knowledge of the cyclic force-displacement behaviour of the joint components, a computer program has been developed.

The computer program is constituted by a series of subroutines, corresponding to the different joint components, providing the component displacement for a given force level. With reference to the loading phase of the cyclic response, the main program working step-by-step for increasing values of the bending moment compute the force level in each joint component, because of the knowledge of the lever arm. Therefore, for each joint component the displacement corresponding to the given force level can be computed, accounting for the rules governing their cyclic behaviour. The knowledge of the displacements of each joint component allows the evaluation of the joint rotation according to the mechanical models previously presented. This process is carried out step-by-step, increasing the bending moment, until the computed rotation assumes a value equal to the one corresponding to the end of the loading semi-cycle of the applied history.

Similarly, regarding the unloading phase, the analysis is carried out by progressively decreasing the bending moment and computing the force levels in the joint components. The computation of the component displacements, accounting for the previous loading history, allows the evaluation of the corresponding rotation values. This process continues up to the rotation value corresponding to the end of the unloading phase, as fixed by the applied rotation history.

The above procedure is repeated for the following loading-unloading cycles to compute the numerical prediction of the joint cyclic flexural response corresponding to a given rotation history.

In order to verify the accuracy of the proposed model, the numerical simulation of the cyclic rotational response of the beam-to-column connections tested at the University of Salerno has been carried out. In addition, to enlarge the experimental sample for model validation, other three tests collected from the technical literature have been considered.

Regarding tests carried out at the University of Salerno, attention has been focused on three partial strength bolted beam-to-column connections. As already said, all the specimens are characterized by the same coupling of beam and column, but with different details of the connection elements. In particular, HEB200 and IPE270 profiles have been used for the column and the beam, respectively. The first joint, namely EEP-CYC01 (Fig. 4.40), is characterized by a panel zone without continuity plates and by an end-plate whose resistance has been calibrated to significantly reduce its plastic engage so that, as confirmed by experimental evidence the energy dissipation mainly occurs in the shear panel.

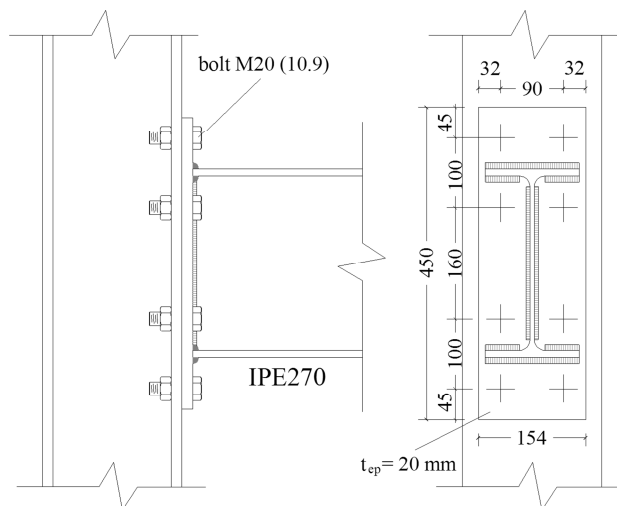


Fig. 4.40 – Geometry of EEP-CYC 01 specimen

The second and the third joint, namely EEP-CYC02 (Fig. 4.41) and TS-CYC04 (Fig. 4.42) have been designed aiming to engage in plastic range the end-plate in bending, in case of EEP-CYC 02 specimen, and the tee-stub in bending, in case of TS-CYC04 specimen.

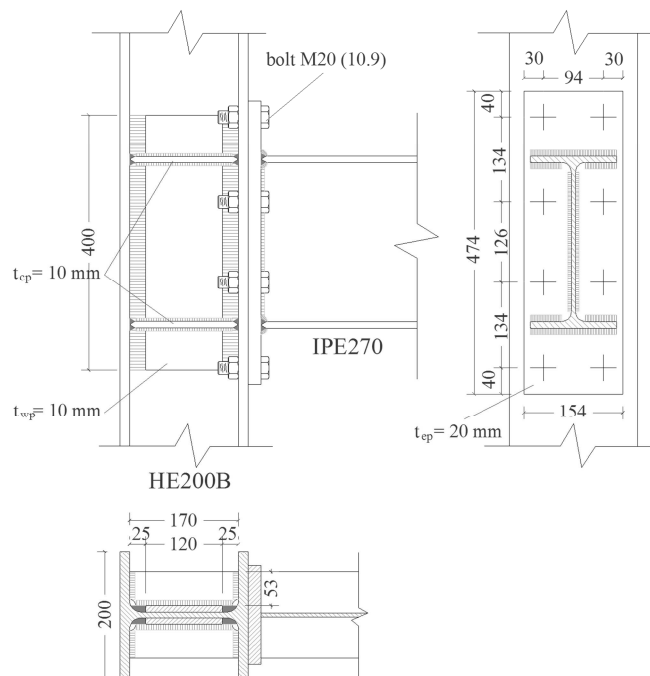


Fig. 4.41 – Geometry of EEP-CYC 02 specimen

To this scope, continuity plates and supplementary web plates have been added to the panel zone. The equivalent T-stubs modelling the end-plate and the tee-stub, respectively, of these two joints are characterized by flanges having different thickness and bolt location.

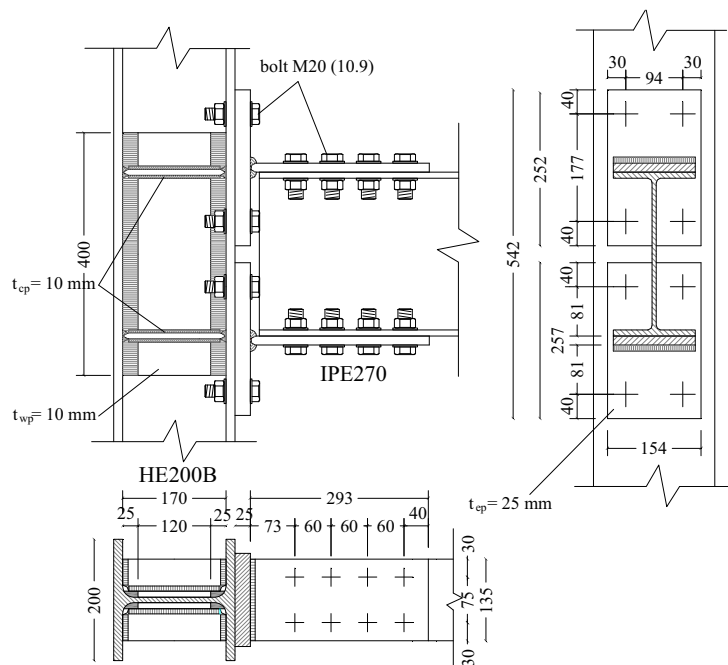


Fig. 4.42 – Geometry of TS-CYC 04 specimen

Regarding the experimental tests collected from technical literature, those performed by (Bernuzzi et al., 1996; Nogueiro et al., 2006; Yang & Kim, 2006) have been considered. The joints under investigation are characterized by different details. In particular, Bernuzzi test, namely FPC/B (Fig. 4.43), consists of a beam stub of an IPE 300 section connected by means of a flush end-plate connection to a rigid counterbeam. This testing condition approximately reproduces the case of a beam-to-column joint with negligible column deformability.

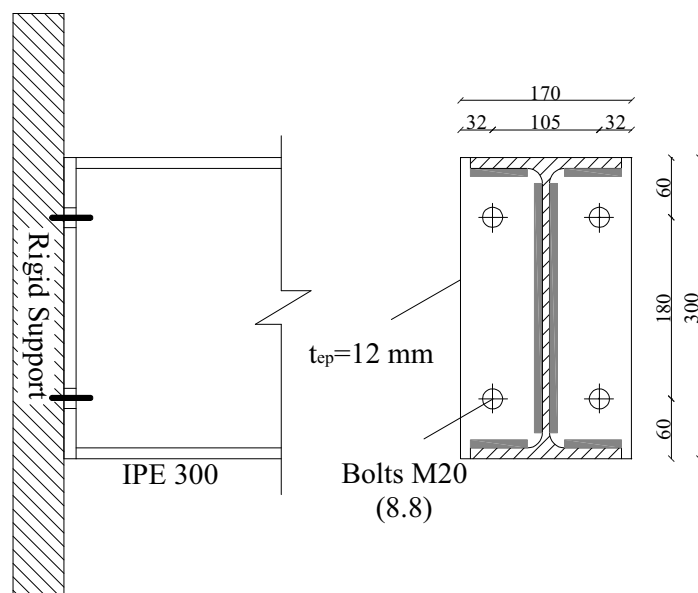


Fig. 4.43 – Geometry of FPC/B specimen (Bernuzzi et al., 1996)

Nogueiro et al. test, namely J-1.3 (Fig. 4.44), is composed by the assemblage of an IPE 360 beam and an HEA 320 column coupled with an extended end-plate connection whose end-plate thickness is equal to 18 mm fastened with eight M24 bolts (10.9 grade). The steel grades of plates and members is S355. The column panel zone is strengthened by means of 15 mm continuity plates.

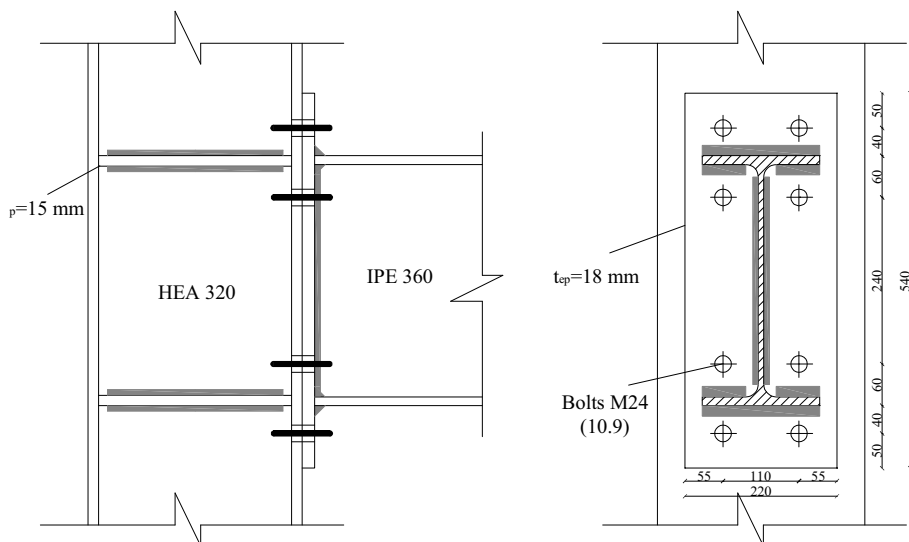


Fig. 4.44 – Geometry of J-1.3 specimen (Nogueiro et al., 2006)

In this case, the experimental test has evidenced that the joint response of this specimen has been mainly governed by the shear panel plastic engagement with a minor contribution of the end-plate. Finally, Yang & Kim test, namely FW (Fig. 4.45), is constituted by H-250x125x6x9 beam fully welded to a H-125x125x6.5x9 column without stiffeners on the column panel zone, i.e. with neither supplementary web plates nor continuity plates. All welds were checked by means of magnetic particle testing to assure the absence of defects.

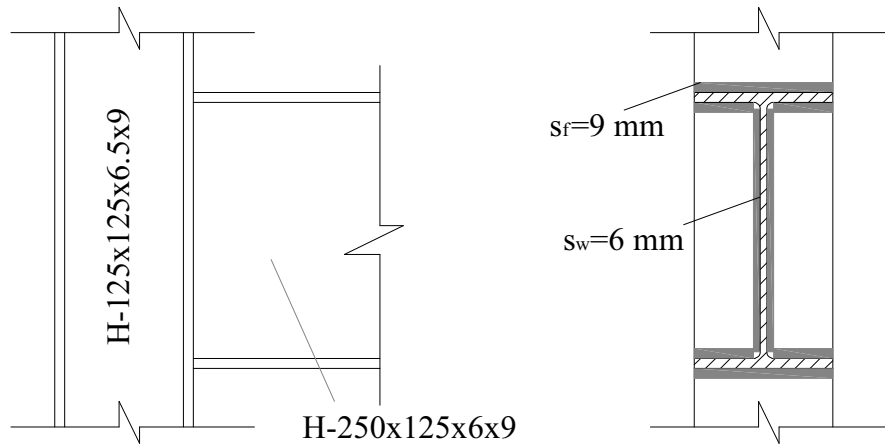


Fig. 4.45 – Geometry of FW specimen (Yang & Kim, 2006)

The base material of plates and steel members is SS400. The test is characterized by a dissipation mainly concentrated in the panels in tension and compression and in the shear panel.

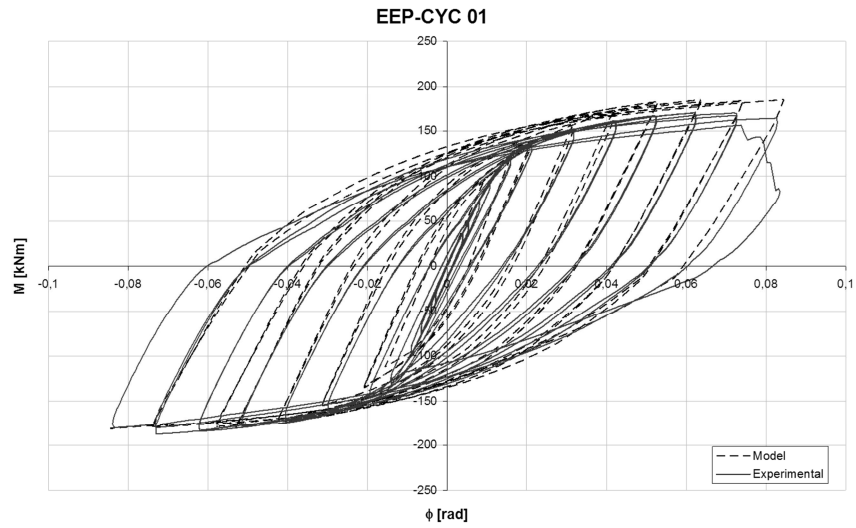


Fig. 4.46 – Theoretical-Experimental comparison for specimen EEP-CYC 01

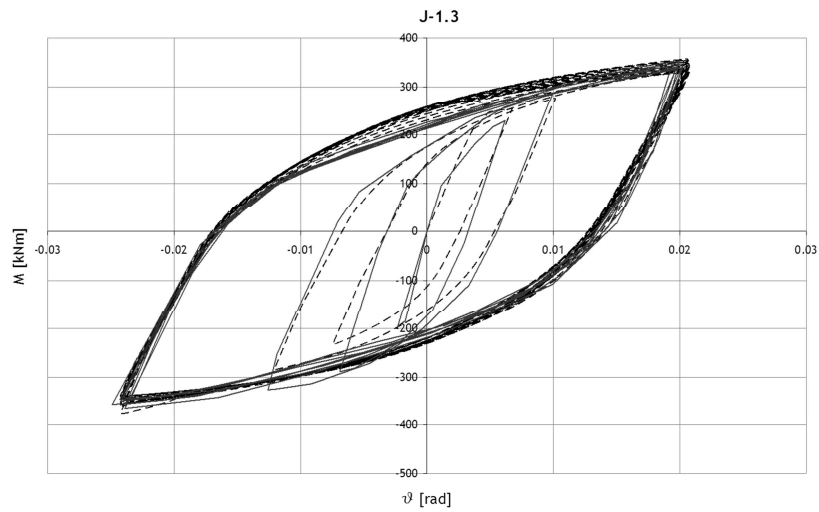


Fig. 4.47 – Theoretical-Experimental comparison for specimen J-1.3

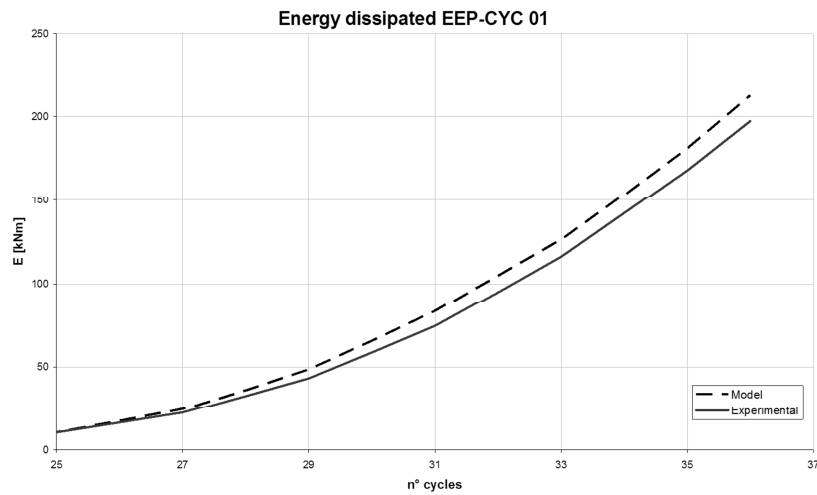


Fig. 4.48 – Comparison of the energy dissipated for specimen EEP-CYC 01

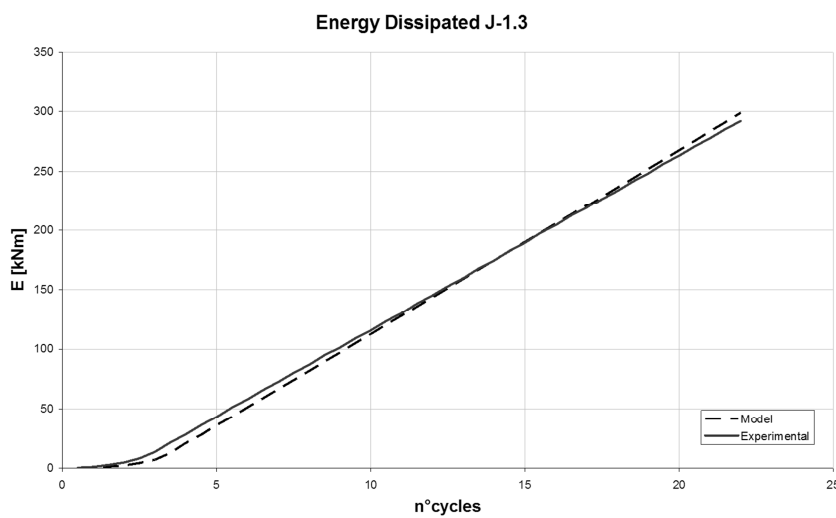


Fig. 4.49 – Comparison of the energy dissipated for specimen J-1.3

The comparison between the experimental results and the numerical results deriving from application of the developed mechanical model shows a good agreement both in terms of cyclic moment-rotation curves and in terms of energy dissipation. Obviously, the accuracy of the developed mechanical model in predicting the cyclic rotational behaviour of beam-to-column joints is mainly related to the accuracy in the modelling of the cyclic force-displacement response of the weakest joint component. Therefore, in the case of specimen EEP-CYC 01 and J-1.3, where dissipation mainly occurs in the shear panel, the good accuracy (Fig. 4.46 - Fig. 4.47) testifies the goodness of Kim and Engelhardt model adopted for the modelling of the panel zone in shear.

In both cases the shape of the hysteresis loops is accurately predicted in terms of stiffness and peak moment. Notwithstanding, a slight overestimation of the energy dissipation capacity occurs (Fig. 4.48 - Fig. 4.49), because of a slight overestimation of resistance in the monotonic envelope. In addition, the accuracy of simulation of FW test is mainly governed by the accuracy of the modelling of shear panel and panels in tension/compression which are the two components engaged in plastic range (Fig. 4.50). The comparison in terms of energy dissipation indicates that beyond Kim and Engelhardt model, even Cofie and Krawinkler model is sufficiently reliable, allowing a satisfactory prediction of the joint rotational response (Fig. 4.51).

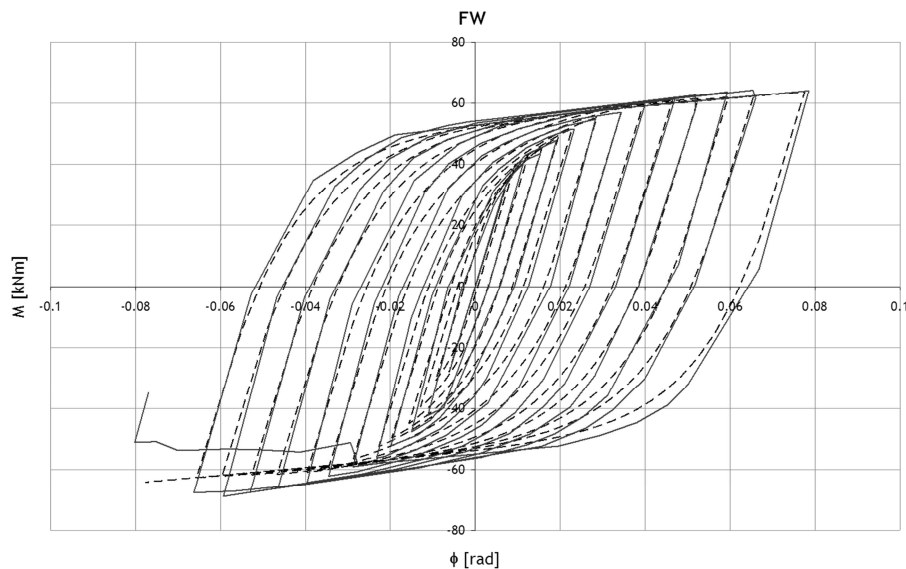


Fig. 4.50 – Theoretical-Experimental comparison for specimen FW

Furthermore, regarding the accuracy in the modelling of the cyclic response of specimens EEP-CYC 02 (Fig. 4.52), TS-CYC 04 (Fig. 4.53) and FPC/B (Fig. 4.54), it is mainly related to the accuracy in the modelling of the cyclic force-displacement response of the equivalent T-stub modelling the end-plate in bending and the tee-stub in bending, respectively. In fact, the two specimens are characterized by the plastic engage of the T-stub representing the weakest joint component.

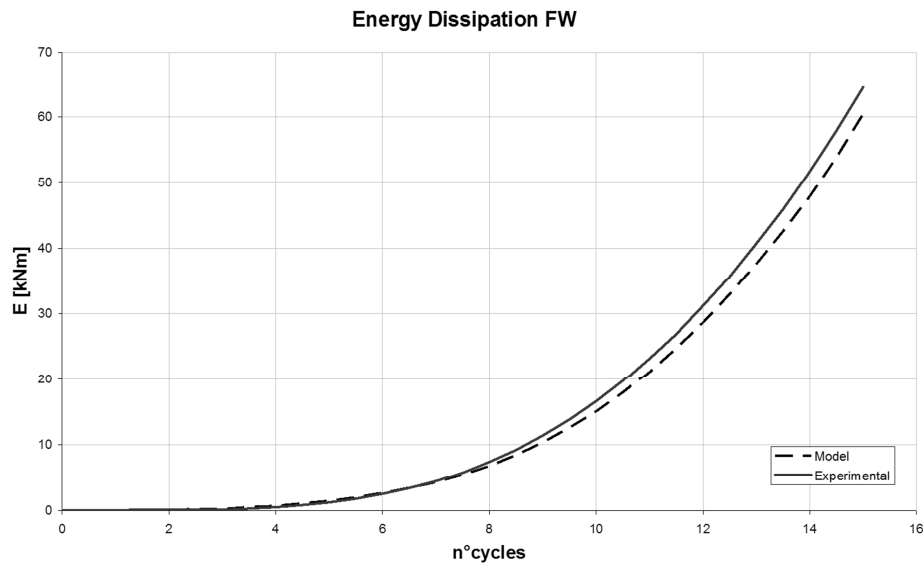


Fig. 4.51 – Comparison of the energy dissipated for specimen FW

In particular, the experimental cyclic response is characterized by a more significant pinching of hysteresis loops compared to the numerical prediction. The pinching of the hysteresis loops is due to the whole reloading branch, not only to the initial reloading stiffness.

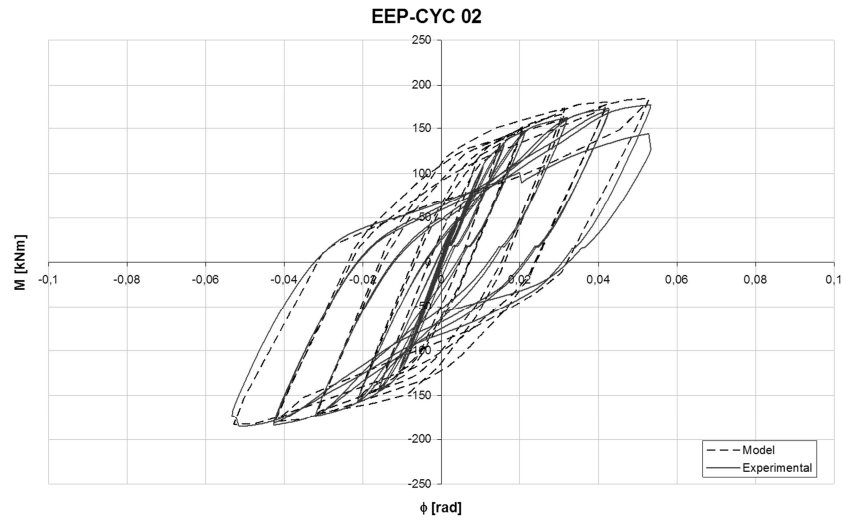


Fig. 4.52 – Theoretical-Experimental comparison for specimen EEP-CYC 02

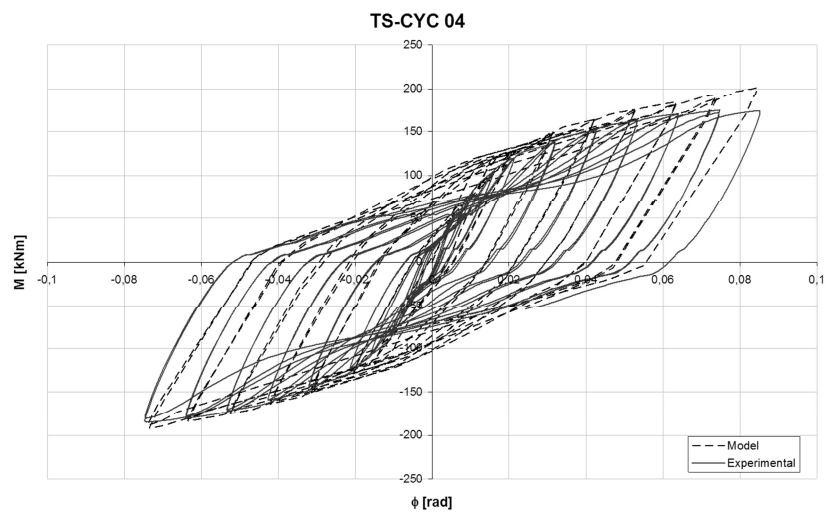


Fig. 4.53 – Theoretical-Experimental comparison for specimen TS-CYC 04

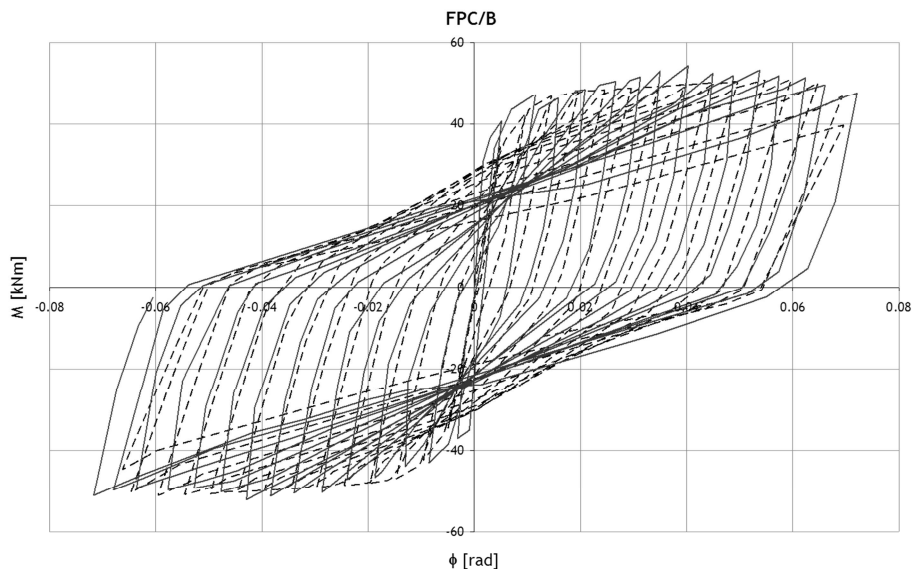


Fig. 4.54 – Theoretical-Experimental comparison for specimen FPC/B

Therefore, such pinching is affected by the degradation of stiffness and strength as the number of cycles increases. It is a highly complicated phenomenon, because it is affected not only by the geometrical properties, but also by the fabrication process which, in turn, affects stiffness and strength degradation rules. This is confirmed not only by the experimental results presented in this work, but also by experimental tests dealing with isolated T-stubs carried out both by the authors (Piluso & Rizzano, 2008) and by other researchers (Clemente et al., 2004; Clemente et al., 2005).

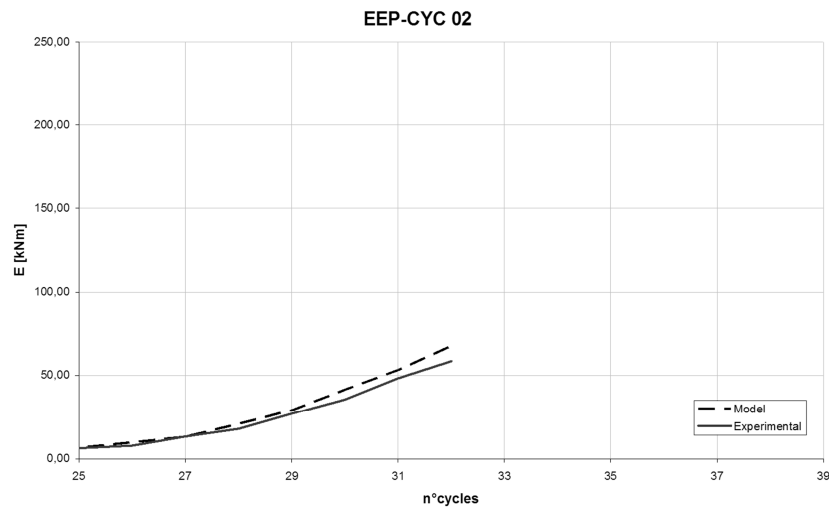


Fig. 4.55 – Comparison of the energy dissipated for specimen EEP-CYC 02

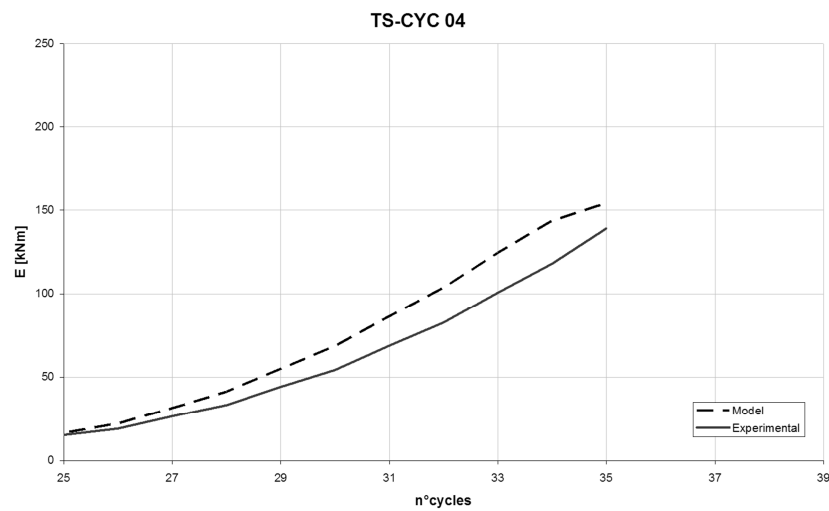


Fig. 4.56 – Comparison of the energy dissipated for specimen TS-CYC 04

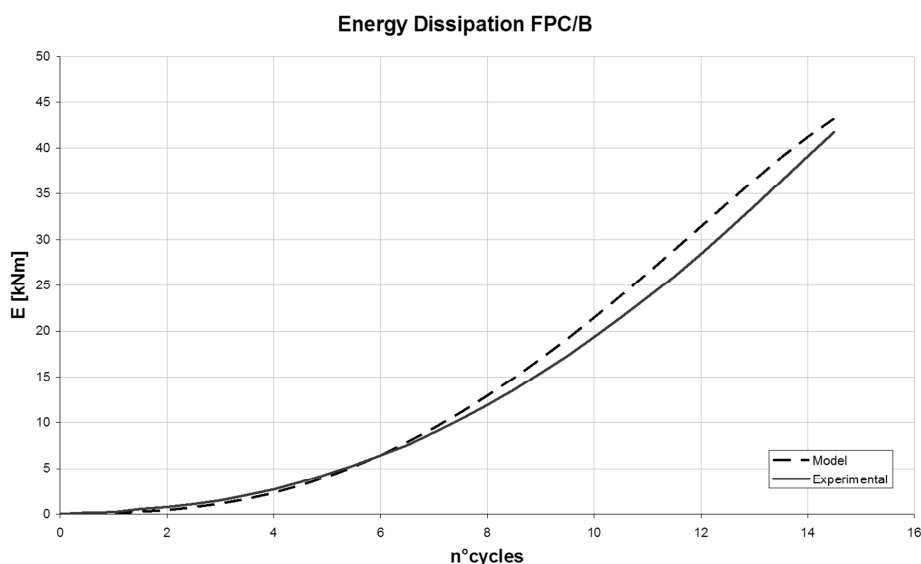


Fig. 4.57 – Comparison of the energy dissipated for specimen FPC/B

In particular, according to (Clemente et al., 2005; Clemente et al., 2004), experimental results on the cyclic response of isolated T-stubs can be classified under three different aspects: *a)* behavioral differences among same-sized T-stubs fabricated with different methods; *b)* behavioral differences among different-sized T-stubs with the same fabrication method; *c)* differences between the cyclic and the monotonic behavior of the specimens. As far as issue *a)* is concerned (Clemente et al., 2005; Clemente et al., 2004) have found results in agreement with those presented in this paper stating that force-displacement curves of same sized T-stubs obtained from hot rolled shapes and by welding of plates are characterized by different amount of pinching. This is caused by localized plastic deformations of the T-stub flanges which tend to pull away from the plate surface. In addition, welded T-stubs

show early signs of stiffness and strength degradation, mostly due to the formation of cracks in the welds. Therefore, experimental evidence shows that stiffness and strength degradation rules are significantly affected by the fabrication process, because of the heat affected zone.

In this framework, it is useful to observe that the model for the cyclic response of the equivalent T-stub was mainly calibrated on the basis of the experimental tests regarding the cyclic response of isolated T-stubs made of rolled profiles. Therefore, as already underlined in (Piluso & Rizzano, 2008), an improvement of the model could be expected provided that additional experimental tests on isolated T-stubs composed by welding are carried out.

Table 4.4 – Comparison between model and experimental dissipated energy

Joint	Typology	$E_{diss,mod}$ [kNm]	$E_{diss,exp}$ [kNm]	$\frac{E_{diss,mod}}{E_{diss,exp}}$ [kNm]
EEP-CYC 01	Extended end-plate	210	197	1.07
J-1.3	Extended end-plate	299	292	1.02
FW	Fully welded	60	64	0.94
EEP-CYC 02	Extended end-plate	67	58	1.15
TS-CYC 04	Extended end-plate	154	139	1.10
FPC/B	Flush end-plate	43	42	1.04

As a result of the more marked pinching occurring in the experimental hysteresis loops, the mechanical model provides also in these cases a slight overestimation of the energy dissipation, as depicted in Fig. 4.55 for EEP-CYC 02 specimen, in Fig. 4.56 for specimen TS-CYC 04 and in Fig. 4.57 for Bernuzzi et al. test FPC/B. Moreover, the maximum ratios between the

dissipated energy predicted by the model and that provided by experimental evidence are summarized in **Table 4.4** for the six tests considered.

Finally, in order to give a more complete picture of the joint model performance, the comparison has been extended to the peak moment response and to the stiffness evaluated at each semi-cycle on unloading branches (Figs. 25-28). In all cases the model appears to be sufficiently reliable providing a good correlation with the experimental results.

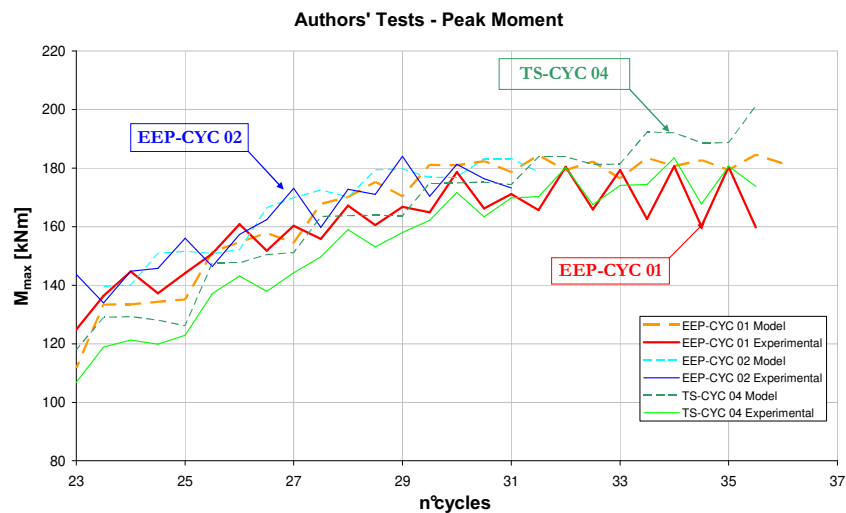


Fig. 4.58 – Model performance - Peak Moment for Authors' Tests

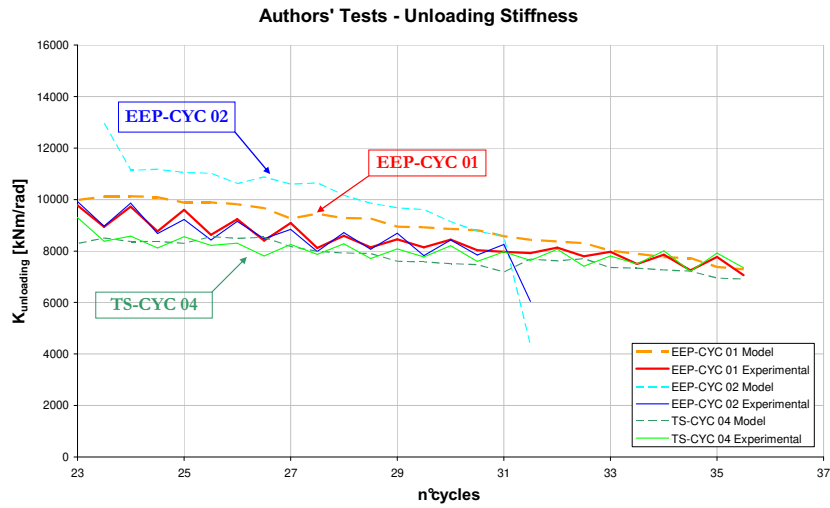


Fig. 4.59 – Model performance - Unloading Stiffness for Authors' Tests

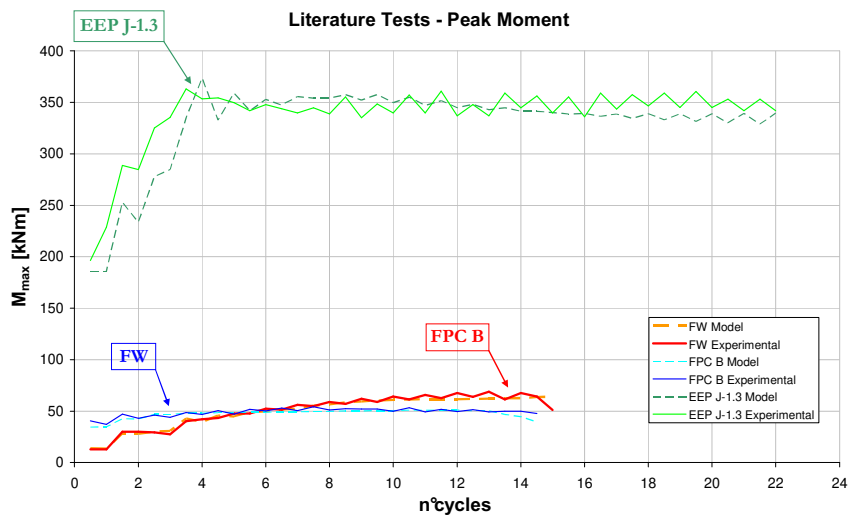


Fig. 4.60 – Model performance - Peak Moment for Literature Tests

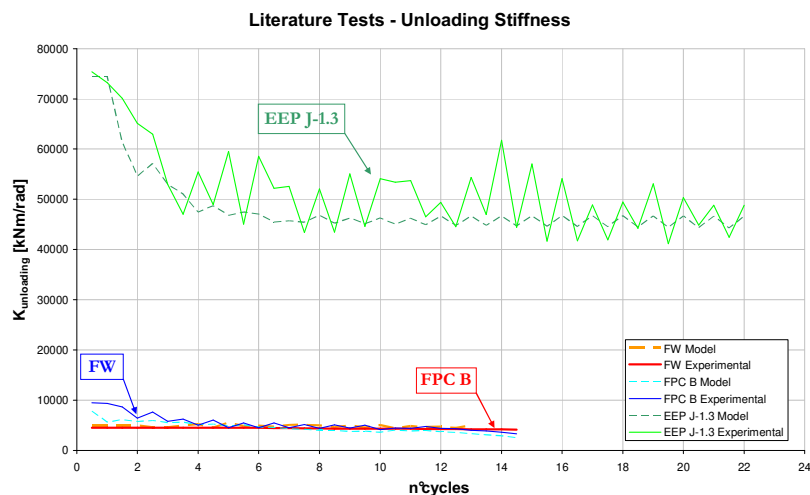


Fig. 4.61 – Model performance - Unloading Stiffness for Literature Tests

The results are really encouraging about the possibility of accurately predicting the cyclic response of bolted connections by means of the component approach. The accuracy of the developed mechanical model can be improved provided that additional test results on the cyclic response of isolated joint components are available to improve the modelling of the cyclic force versus displacement behaviour of the joint components. Moreover, considering that the cyclic model relies on empirical parameters calibrated on the basis of cyclic experimental tests with only a symmetrical loading history, other tests with generic loading history are necessary to prove the sufficiency of the model for any loading history.

4.4 References

AISC, 2005. *Seismic Provisions for Structural Steel Buildings*. Chicago, Illinois.

Bernuzzi, C., Zandonini, R. & Zanon, P., 1996. Experimental analysis and modelling of semi-rigid steel joints under cyclic reversal loading. *Journal of Constructional Steel Research*, 2, pp.95-123.

Castro, J., Davila-Arbona, F. & Elghazouli, A., 2008. Seismic design approaches for panel zones in steel moment frames. *Journal of Earthquake Engineering*, 12(S1), pp.35-51.

Castro, J., Elghazouli, A. & Izzudin, B., 2005. Modelling of the panel zone in steel and composite moment frames. *Engineering Structures*, 27, pp.129-44.

CEN, 2005a. *Eurocode 3: Design of steel structures - Part 1-1: General rules and rules for buildings*.

CEN, 2005b. *Eurocode 3: Design of steel structures - Part 1-8: Design of joints*.

CEN, 2005c. *Eurocode 8: Design of structures for earthquake resistance - Part 1: General rules, seismic actions and rules for buildings*.

Clemente, I., Noè, S. & Rassati, G., 2004. Experimental behavior of T-stub connection components for the mechanical modeling of Bare-Steel and composite partially restrained beam-to-column connections. In *Proceedings of Connections in Steel Structures V*. Amsterdam, 2004.

Clemente, I., Noè, S. & Rassati, G., 2005. Experimental and Numerical Analysis of the Cyclic Behaviour of T-stub Components. In *Proceedings of XX CTA Conference*. Ischia, 2005.

Cofie, N. & Krawinkler, H., 1985. Uniaxial Cyclic Stress-Strain Behavior of Structural Steel. *Journal of Engineering Mechanics*, 111(9), pp.1105-20.

Dafalias, Y., 1975. *On Cyclic and Anisotropic Plasticity: I) A General Model Including Material Behavior Under Stress Reversals, II) Anisotropic*. Berkeley: University of California.

Dafalias, Y. & Popov, E., 1975. A model of nonlinearly hardening material for complex loading. *Acta Mechanica ASME*, 21, pp.173-92.

Dafalias, Y. & Popov, E., 1976. Plastic Internal Variables Formalism of Cyclic Plasticity. *Journal of Applied Mechanics ASME*, 43, pp.645-51.

Davila-Arbona, F., 2007. *Panel Zone Behaviour in Steel Moment Resisting Frames*. Pavia: European School for Advanced Studies in Reduction of Seismic Risk.

Faella, C., Piluso, V. & Rizzano, G., 1998b. Experimental Analysis of Bolted connections: snug versus preloaded bolts. *Journal of Structural Engineering*, 124(7), pp.765-74.

Faella, C., Piluso, V. & Rizzano, G., 2000. *Structural Steel Semi-Rigid Connections*. Boca Raton: CRC Press.

Fielding, D. & Huang, J., 1971. Shear in steel beam-to-column connections. *Welding J.*, 50(7), pp.313-26.

Kim, K. & Engelhardt, M., 1996. *Development of analytical models for earthquake analysis of steel moment frames*. Berkeley: National Science Foundation and American Institute of Steel Construction University of California.

Kim, K. & Engelhardt, M., 2002. Monotonic and cyclic loading models for panel zones in steel moment frames. *Journal of Constructional Steel Research*, 58, pp.605-35.

Krawinkler, H., Bertermo, V. & Popov, E., 1971. *Inelastic behavior of beam to column subassemblages*. Report UCB/EERC-71/7. Berkeley: University of California Earthquake Engineering Research Center.

Krawinkler, H., Bertero, V. & Popov, E., 1973. *Further studies on seismic behavior of steel beam-column subassemblages*. UCB/EERC-73/27. Berkeley: University of California Earthquake Engineering Research Center.

Lui, E., 1985. *Effects of Connection Flexibility and Panel Zone Deformation on the Behavior of Panel Steel Frames*. Indiana, USA: Purdue University West Lafayette.

Lui, E. & Chen, W., 1986. Analysis and Behavior of Flexibly-Jointed Frames. *Engineering Structures*, 8(2), pp.107-18.

Mulas, M., 2004. A structural model for panel zones in non linear seismic analysis of steel moment-resisting frames. *Engineering Structures*, 26, pp.363-80.

Nogueiro, P., Simoes Da Silva, L., Bento, R. & Simoes, R., 2006. Experimental Behaviour of standardised European end-plate beam-to-column steel joints under arbitrary cyclic loading. In *Proceedings of SDSS'06-International Colloquium on Stability and Ductility of Steel Structures*. Lisboa, Portugal, 2006.

Piluso, V., Faella, C. & Rizzano, G., 2001. Ultimate behavior of bolted T-stubs. Part I: Theoretical model. *Journal of Structural Engineering ASCE*, 127(6), pp.686-93.

Piluso, V. & Rizzano, G., 2008. Experimental Analysis and modelling of Bolted T-stubs under Cyclic Loads. *Journal of Constructional Steel Research*, pp.vol.64 pp.655-669.

Tsai, K. & Popov, E., 1990. Cyclic behavior of end-plate moment connections. *Journal of Structural Engineering ASCE*, 116(11), pp.2917-30.

UBC, 1997. *Uniform Building Code*. Whittier, CA: International Conference of Building Officials.

Wang, S., 1988. *Seismic Response of Steel Buildings Frames with inelastic Joint Deformation*. Bethlehem, PA: Department of Civil Engineering.

Yang, C. & Kim, Y., 2006. Cyclic Behaviour of Bolted and welded beam-to-column joints. *International Journal of Mechanical Sciences*, pp.vol.49, pp.635-649.

CHAPTER 5 – APPLICATION OF DISSIPATIVE DEVICES TO BEAM-TO-COLUMN JOINTS

5.1 Energetic Approaches: Main Features

It is well known in technical literature that the equation of motion of an inelastic single degree of freedom system (SDOF) characterized by mass m , viscous damping coefficient c and restoring force f_s subjected to a seismic ground motion can be written as:

$$m\ddot{x}(t) + c\dot{x}(t) + f_s(x, \dot{x}) = -m\ddot{x}_g(t) \quad (5.1)$$

where $x(t)$, $\dot{x}(t)$ and $\ddot{x}(t)$ are respectively the global displacement, velocity and acceleration relative to the moving base at time t and $\ddot{x}_g(t)$ is the horizontal acceleration of the ground at time t .

By means of integration of Eq. (5.1) it is possible to derive the classical energetic formulation, obtained integrating the work done by each element over an increment of the global structural displacement dx :

$$\int_0^x m\ddot{x}(t)dx + \int_0^x c\dot{x}(t)dx + \int_0^x f_s(x, \dot{x})dx = \quad (5.2)$$

$$= - \int_0^x m \ddot{x}_g(t) dx$$

the first term on the left side of Eq.(5.2) is commonly called kinetic energy of the mass associated with its motion relative to the ground which can be rewritten as:

$$E_k(t) = \int_0^x m \dot{x}(t) dx = \int_0^x m \dot{x}(t) d\dot{x} = \frac{m\dot{u}^2}{2} \quad (5.3)$$

the second term on the left side of Eq.(5.2) is the energy dissipated by viscous damping:

$$E_{vd}(t) = \int_0^x c \dot{x}(t) dx = \int_0^x f_D dx \quad (5.4)$$

The third term on the left side of Eq.(5.2) is the sum of the energy dissipated by yielding and the recoverable strain energy of the system:

$$E_a(t) = \int_0^x f_s(x, \dot{x}) dx \quad (5.5)$$

thus the energy dissipated by yielding is given by:

$$E_h(t) = \int_0^x f_s(x, \dot{x}) dx - E_{es}(t) \quad (5.6)$$

on the base of the obtained expressions is possible to rewrite Eq.(5.2) in terms of energetic balance of the structural system:

$$E_I(t) = E_k(t) + E_{vd}(t) + E_{es}(t) + E_h(t) \quad (5.7)$$

consequently, during a seismic event, the earthquake input energy has to be equal to the sum of the contributes given on the right side of Eq.(5.7), i.e. the kinetic energy, the energy dissipated by viscous damping, the energy dissipated by inelasticity of structure (hysteresis) and the elastic strain energy.

It can be demonstrated that the viscous damping energy monotonically increases during the time-history whilst the absorbed energy, given by the sum of the elastic strain and the hysteretic energy fluctuates while increasing. This last behavior is caused by the elastic strain energy, which is first absorbed and then released by the system.

As an example, in Fig. 5.1 (Chopra, 1995) is depicted the variation of the energy dissipated by viscous, elastic and hysteretic damping for two systems subjected to El Centro ground motion: the first elastic with natural period $T_n=0,5$ sec, damping ratio $\zeta=0.05$ and the second inelastic with the same elastic properties and behavior factor equal to 4.

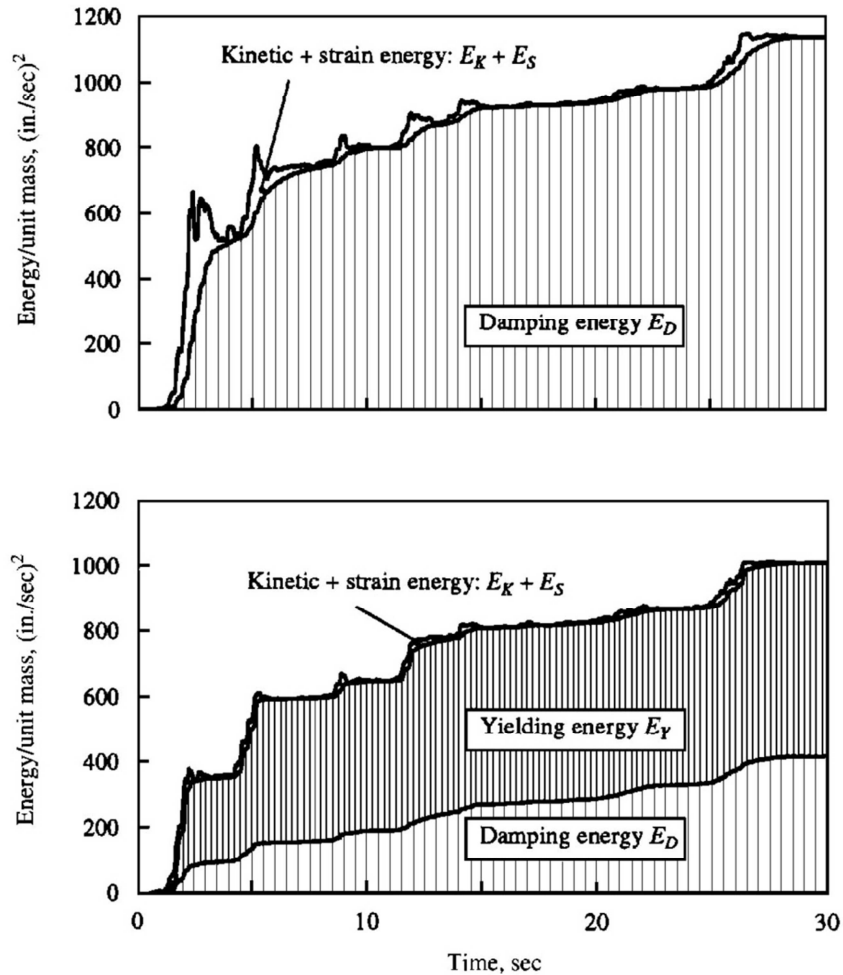


Fig. 5.1 – Time variation of the energy dissipated by viscous damping of an elastic (top) and inelastic system (bottom)

The results given show that in case of elastic system the structure dissipates all the energy supplied by means of damping, conversely in case of inelastic system both hysteretic and viscous damping provide the dissipation of the seismic input energy. In the inelastic case, less damping is required to

withstand the seismic action, therefore the velocities of the inelastic system are smaller compared to that of the elastic one. In addition, the comparison of the two figures points out that the two systems attract different amounts of input energy even though possess the same elastic properties. In fact, inelasticity causes a decrease of the structural effective stiffness and, as a consequence, the elongation of the effective period of vibration. In conclusion, the yielding energy shown in Fig. 5.1 indicates that if the inelastic system is able to dissipate through yielding of structural elements the imposed energy demand, can be designed only for one-fourth of the force developed in the corresponding linear system.

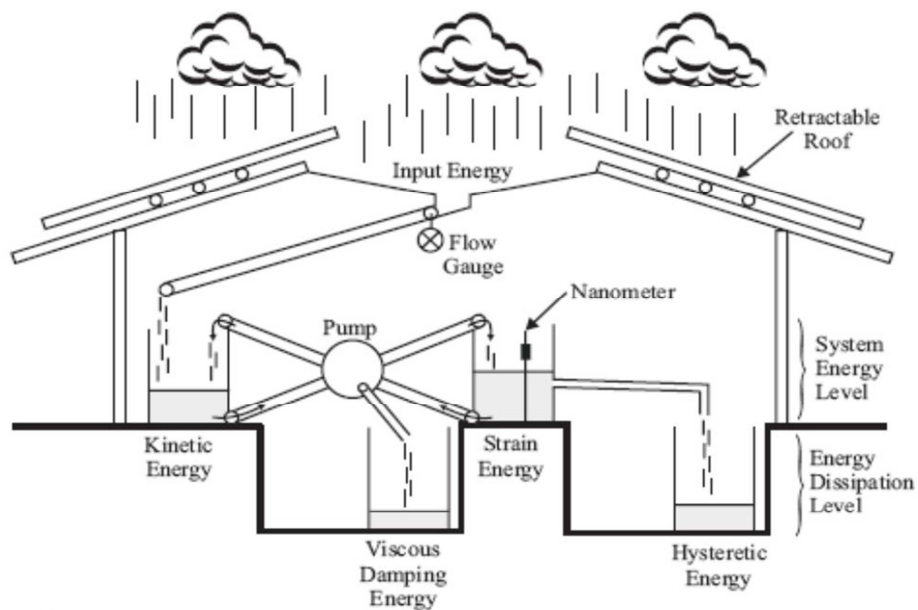


Fig. 5.2 – Rain flow analogy

The concepts expressed by the classical equation of the energetic balance can be effectively visualized through the so-called rain flow analogy shown in Fig. 5.2 (Christopoulos & Filiatrault, 2006). In this figure is represented a hangar with a retractable roof subjected to a rainstorm. The rainstorm symbolize the earthquake and the amount of water entering into the hangar represents the seismic input energy. The retractable roof symbolize the dynamic properties of the structure because the amount of roof opening changes the amount of entering water. If the roof is completely open, all the energy generated by the ground motion at the site is transferred to the structure. Conversely, if the roof is completely closed means that no water can enter into the hangar and the structure is perfectly isolated. The entering water is collected below the roof and sent to the pail of the kinetic energy. This pail characterizes the amount of input energy transformed in kinetic energy due to the inertia masses of the structure. The rain water which slides down on the roof is the energy generated at the site which is not transferred to the structure. As the masses vibrate the structural elements deform and absorb strain energy, at the end of each cycle all the kinetic energy becomes strain energy. This process is symbolized by a two-ways pump which connects the kinetic pail and the strain pail. The flow rate of the pump is associated with the effective period of vibration of the structure. This pump is active as long as rain water is present both in kinetic or strain pail. Hence, the vibration of the structure is connected with a continuous transformation of kinetic energy in strain energy and vice-versa.

The equivalent viscous damping is symbolized as a loss of water of the pump proportional to the flow rate. This loss is analogous to the velocity dependence of the viscous damping. The amount of lost water is collected in a viscous pail. If the behavior of the system is indefinitely linear the seismic input energy is

dissipated only through viscous damping and at the end of the rain storm all the entering water is collected in the viscous pail Fig. 5.1. Conversely, if the system is inelastic, over a certain level some of the water contained in the strain pail is drained permanently to the hysteretic pail. In this last case, at the end of the shaking, the entering water is distributed between viscous and hysteretic pail.

From the rain flow analogy, which represents the symbolic expression of Eq.(5.7) is clear that the strategies to improve the seismic performances of a structure are two. The first strategy consists of minimizing the amount of water collected by the hysteresis pail that is directly related to the structural damage. This goal can be achieved by adding supplemental dissipating mechanisms, both viscous and hysteretic. The other strategy consists of minimizing the amount of entering water. This strategy symbolize the function of a seismic isolation system which properly filters the input energy to the structure.

Dealing with the first strategy, the development of supplemental damping devices started in New Zealand about 40 years ago (Kelly et al., 1972; Skinner et al., 1975). As already said, dampers are usually adopted to dissipate a part of the seismic input energy reducing the seismic demand on the structural elements. Supplemental damping devices are often coupled to bracing systems or strong walls that are employed to limit the structural response in terms of sway displacement under Serviceability Limit States. Dampers are typically distributed along the height of the structure to absorb the kinetic energy transferred by the ground during the seismic event.

Generally speaking, supplemental damping devices can be categorized in (Fig. 5.3) (Soong & Spencer Jr, 2002):

- Passive;
- Active;
- Semi-active;
- Hybrid.

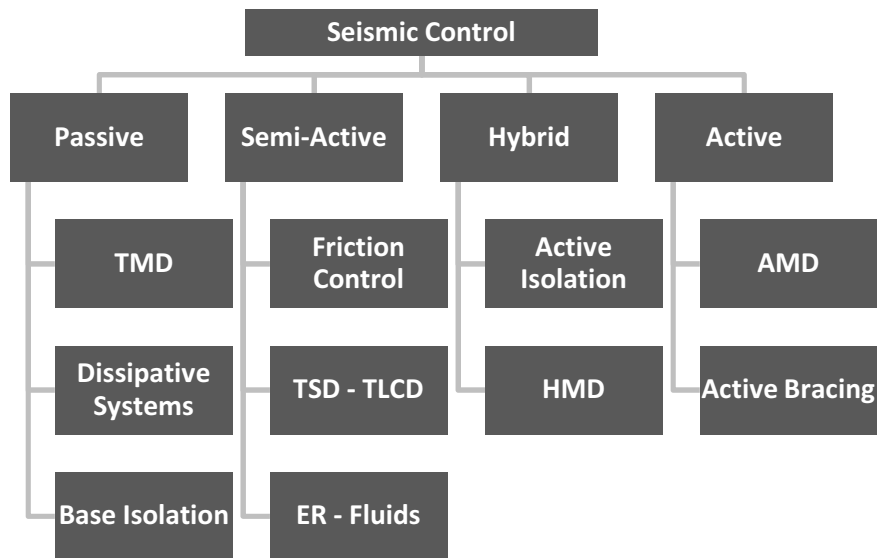


Fig. 5.3 – Seismic Control Systems

Passive control systems are based on mechanical elements that are intended to operate without external power supply. Passive systems do not necessitate of computers or actuators but, unfortunately, have properties that cannot be modified before, during and after the seismic event. Passive systems can be classified in:

- base isolation systems;
- dissipative systems;

- tuned mass dampers (Fig. 5.5).

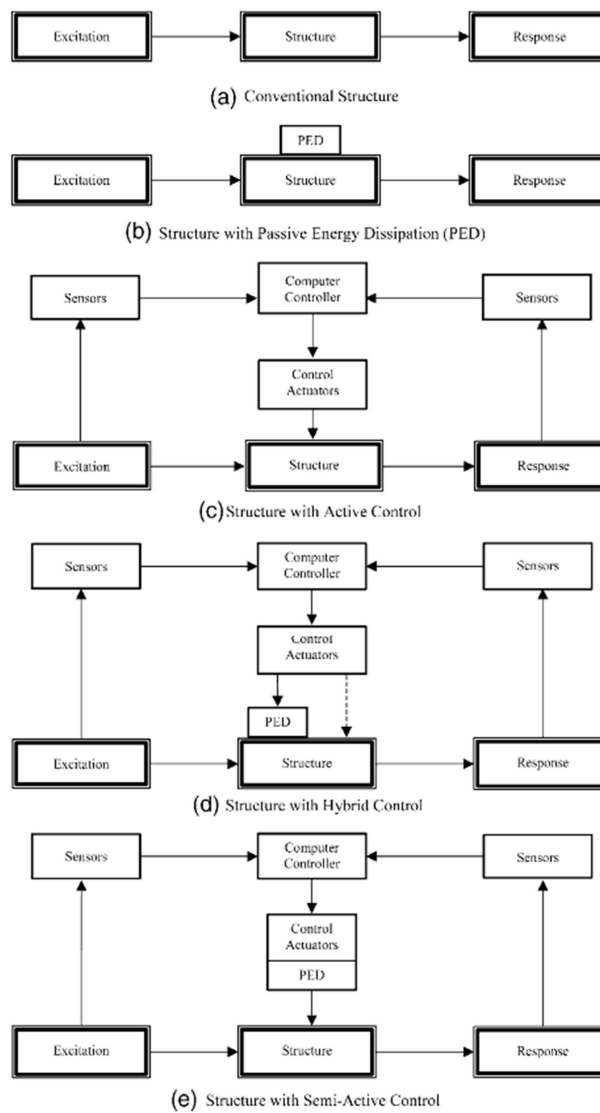


Fig. 5.4 – Control Schemes

Active control systems are usually constituted by three integrated components: a *monitoring system* able to control the state of the structure and to acquire the data collected through an electronic system; a *control system* that, on the base of the results given by the measurement devices decide on the countermeasures to be applied to the structure; an *actuating system* that through the supply of external energy, applies the forces or displacements required by the control system. An example of active control is the so-called “Active Mass Damper” (Spencer & Sain, 1998). With this system a mass, usually not more than 1% of the total structural mass, is installed on the roof of the building and connected through an actuator to the structure. During the seismic event, on the base of an adequate algorithm the mass is properly moved to counteract the seismic action by means of its inertia, reducing the structural response within acceptable values. Compared to passive systems, active systems have numerous advantages, above all:

- better effectiveness in controlling the structural response;
- less sensitivity to local site conditions;
- same system can be used for different goals. As an example an active control system can be efficiently applied either for controlling displacements under SLS and to limit the structural response under a severe seismic event.

Despite the indisputable advantages, active control systems usually provide also several disadvantages:

- high initial and maintenance cost;
- require a continuous energy supply;

- dynamic response of a building with high number of degree of freedom is complex and its control can become onerous in terms of applied sensors and actuators and difficult in terms of prediction of the structural response.

Semi-active control systems are very similar to active systems except that they require a small amount of energetic supply because do not need continuous monitoring and employ low cost mechanical devices. Some of the semi-active control techniques are: the variable friction, the movement of liquid masses contained in tanks (Tuned Sloshing Dampers) or columns into the building (Tuned Liquid Dampers) (Fig. 5.5), the use of hydraulic or oleodynamic devices with variable local properties or actuators containing fluids with variable viscosity according to electromagnetic fields.

Hybrid systems are the combination of active and passive systems. The seismic control is obtained starting from the application of both mechanical elements and actuators. Hybrid systems are supposed to work better of active systems for different reasons:

- in case of failure of the active system the passive components continue to work;
- energetic supply is lower.

Some examples of hybrid control systems that have obtained great attention by the scientific community are the so-called Hybrid Mass Damper and the base isolation with active control of the base displacement. Hybrid mass damper combines the use of a passive Tuned Mass Damper with actuators called to enhance the efficiency of the system. Base isolation with active control

combines the adoption of base isolation, which decouples ground and structure movement, with an actuator that has to limit the movement at the base of the building.

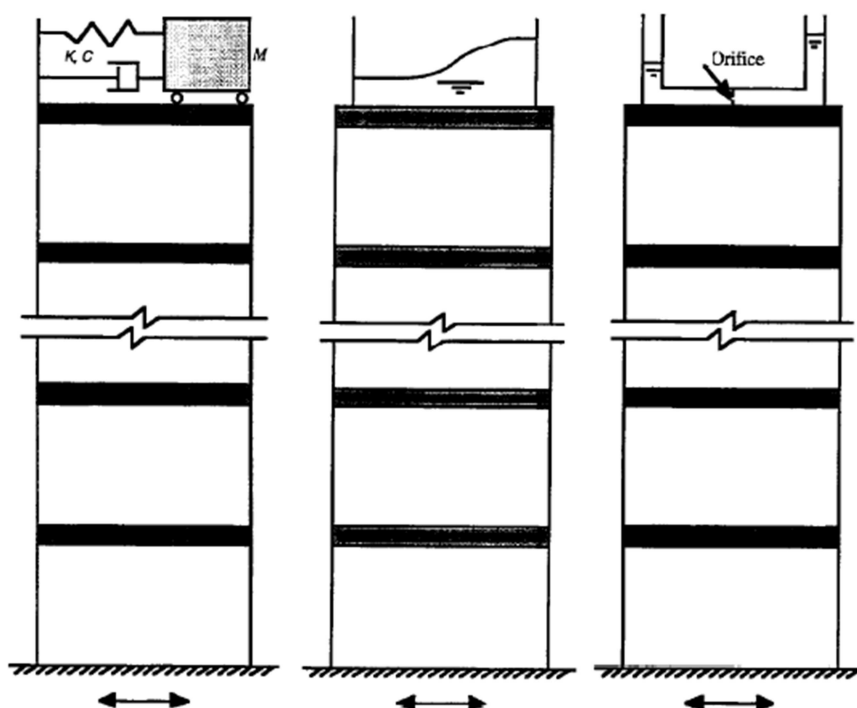


Fig. 5.5 – Tuned Mass Damper - Tuned Sloshing Damper – Tuned Liquid Damper

In this work reference is made to passive systems, so that in the following other systems are not discussed further. In the next paragraphs, the attention will be mainly focused on description of the main features of passive devices.

5.1.1 Passive Energy Dissipating System

A large number of passive control systems has been developed and installed in structures worldwide in last thirty years. Up to now, in U.S. PED devices have been installed approximately 100 building and bridges, either for retrofit and for new constructions.

As already discussed, the addition of a passive energy dissipation system changes the structural properties and, in particular, modifies the energy balance during the seismic event. Recalling the energy balance, the addition of a passive supplemental damping device leads to the following expression:

$$E_I(t) = E_k(t) + E_{vd}(t) + E_{es}(t) + E_h(t) + E_{sd}(t) \quad (5.8)$$

where $E_{sd}(t)$ is the energy dissipated by the supplemental damping device at time t . It is worth note that, generally, the most desirable response of a structure equipped with supplemental damping devices does not necessarily corresponds to the maximum energy dissipated by the devices. In fact, considering the expression of the vibrational energy, defined as the part of seismic input energy which has not been yet dissipated by viscous or supplemental damping at time t and that can potentially cause damage to the structural elements:

$$E_{vb}(t) = E_k(t) + E_{es}(t) + E_h(t) \quad (5.9)$$

comes out that the structure is best protected when the vibrational energy is minimized. In particular, Eqs. (5.8)-(5.9) yield:

$$E_{vb}(t) = E_{in}(t) - E_{vd}(t) - E_{sd}(t) \quad (5.10)$$

Eq.(5.10) clearly shows that maximizing the supplemental damped energy does not necessarily lead to the minimum vibrational energy, since the amount of input energy can also significantly increase. As a result, the best design strategy of passive control systems should consist in minimizing the difference between the input energy and the energy dissipated by the dampers. Eq.(5.10) also suggests that the optimum design of an energy dissipating system is usually un-trivial as far as depends both on the characteristics of dampers and of the input earthquake.

In general, passive energy dissipating devices can be categorized according to the following classification:

- displacement activated devices;
- velocity activated devices;
- motion activated devices.

Displacement activated device dissipate seismic input energy through the relative displacement occurring between two connected points. These dampers possess characteristic independent on the frequency of motion. In addition, the forces arising in displacement activated devices are usually in phase with the forces generated within the structure, i.e. the maximum actions generated in dampers take place simultaneously with maximum forces and

displacements occurring in other structural elements. Two examples of dampers belonging to this category are: metallic dampers and friction dampers.

Velocity activated dampers dissipate energy through the relative velocities occurring between the connected points. These dampers have characteristics dependent on the earthquake frequency. Moreover, the maximum forces generated in the dampers are usually not in phase with the maximum structural response. In fact, in general, the maximum forces generated in velocity activated dampers are not contemporary to the maximum forces and deformations arising in the structure. This results in lower design forces for structural members and foundation. Typical dampers falling in this category are viscous and visco-elastic dampers.

Motion activated devices alter the seismic input energy in the structure through a secondary system. An example of motion activated device is the Tuned Mass Damper (TMD). In case of TMD a mass-spring-dashpot system is attached to the structure aiming to reduce its structural response. The secondary system is designed to be resonant with the first-mode of vibration of the structure, so that under a dynamic excitation the inertia forces of the TMD dissipate the input energy. These kinds of systems have been demonstrated to be effective in reducing the wind vibration and more recently have been considered for the reduction of the actions induced by a seismic event.

5.1.2 Basic Response of Structures Equipped with Hysteretic Dampers

Before analyzing the effects on the global structural response of the application of hysteretic dampers is useful to recall the results of the analysis of a viscous damped Single Degree of Freedom (SDoF) system subjected to an harmonic excitation. It is well known that the differential equation governing the response of this type of systems is:

$$m\ddot{x}(t) + c\dot{x}(t) + ku(t) = p_o \sin(\omega t) \quad (5.11)$$

where ω is the ground excitation circular frequency and p_o is the amplitude of the equivalent applied load. The equation is to be solved subjected to the initial conditions:

$$u = u(0) \quad \dot{u} = \dot{u}(0) \quad (5.12)$$

the complete solution of the equation given by the sum of the complementary and particular solution is given by:

$$u(t) = e^{-\zeta \omega_n t} [A \cos(\omega_D t) + B \sin(\omega_D t)] + C \sin(\omega t) + D \cos(\omega t) \quad (5.13)$$

where $\omega_D = \omega_n \sqrt{1 - \zeta^2}$, ω_n is the natural circular frequency of vibration, ζ is the damping ration and A, B, C, D are four constants.

$$A = u(0)$$

$$B = \frac{\dot{u}(0) + \zeta \omega_n u(0)}{\omega_D}$$

$$C = \frac{p_0}{k} \frac{1 - (\omega/\omega_n)^2}{[1 - (\omega/\omega_n)^2]^2 + [2\zeta(\omega/\omega_n)]^2} \quad (5.14)$$

$$D = \frac{p_0}{k} \frac{-2\zeta(\omega/\omega_n)}{[1 - (\omega/\omega_n)^2]^2 + [2\zeta(\omega/\omega_n)]^2}$$

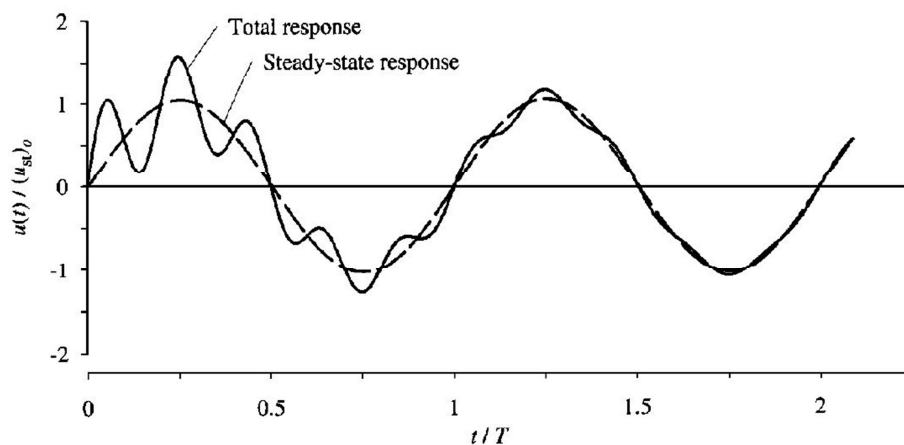


Fig. 5.6 – Response of damped system subjected to harmonic forces

Eq.(5.13) is plotted in Fig. 5.6 where is shown that the response of the system is given by two contributes: the transient response obtained as the sum of first two terms of Eq.(5.13) and the steady-state response given by the sum of last two terms of Eq.(5.13). If reference is made only to the steady-state response,

it can be demonstrated that this part of the system response can be rewritten in terms of peak response deformation R_d and phase angle φ :

$$u(t) = u_0 \sin(\omega t - \varphi) = \frac{p_0}{k} R_d \sin(\omega t - \varphi) \quad (5.15)$$

where:

$$R_d = \frac{u_0}{(u_{st})_0} = \frac{1}{[1 - (\omega/\omega_n)^2]^2 + [2\zeta(\omega/\omega_n)]^2} \quad (5.16)$$

In Fig. 5.7 the plot of the amplitude of response against the excitation frequency, usually called frequency-response curve, is depicted. From this picture it can be observed that:

- if the frequency ratio is minor than 1, the force is defined as slowly varying and the structural response is close to the static response;
- if the ratio is greater than 1, the force is defined rapidly varying and the response tends to zero as the frequency ratio increases;
- if the frequency ratio is equal to one the natural frequency of the system is equal to the harmonic force frequency and the system maximum response is obtained (resonance condition).

To study the effect of hysteretic dampers on the dynamic response of structures, a generic hysteretic device is added to the simple single degree-of-

freedom linear system subjected to ground acceleration $\ddot{x}_g(t)$ as shown in Fig. 5.8.

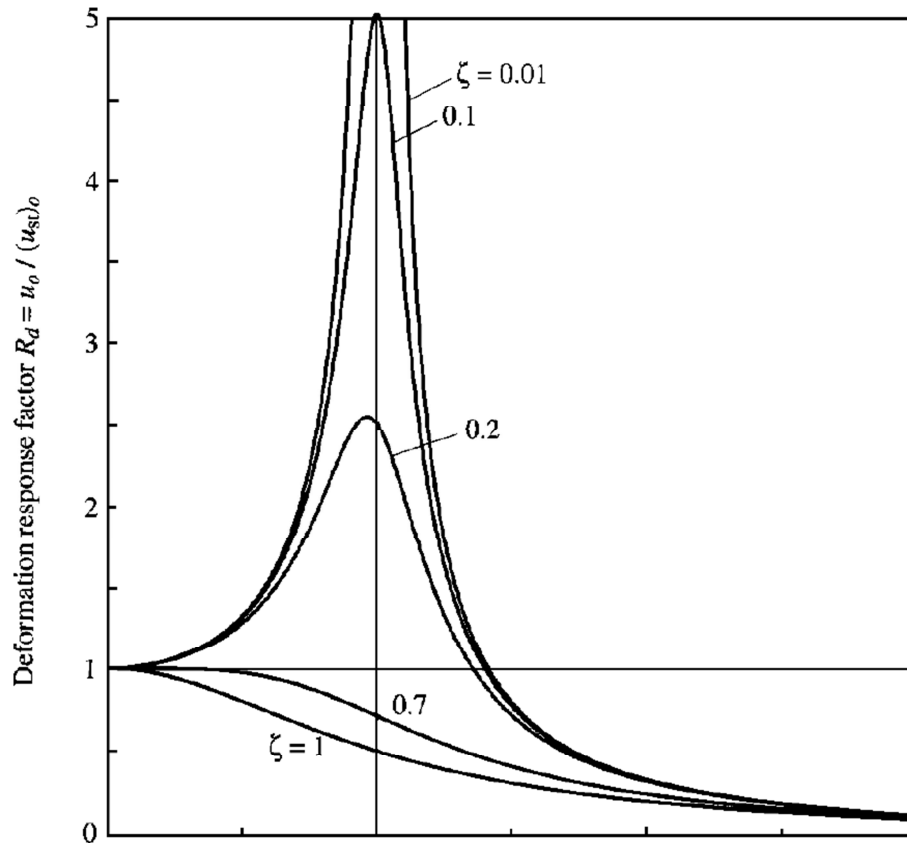


Fig. 5.7 – Deformation response factor for damped system (harmonic force)

In this case, the equation of motion of the combined system can be written as:

$$m\ddot{x}(t) + c\dot{x}(t) + kx(t) + F_{hd}(t) = -m\ddot{x}_g(t) \quad (5.17)$$

where $F_{hd}(t)$ is the nonlinear horizontal force provided by the hysteretic damper.

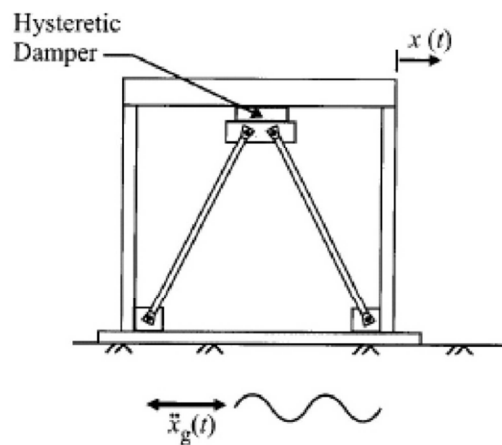


Fig. 5.8 – Single-degree-of-freedom system incorporating hysteretic damper

Assuming that the structure has no inherent viscous damping, and is subjected to harmonic base excitation given by:

$$\ddot{x}_g(t) = -\frac{p_o}{m} \sin(\omega t) \quad (5.18)$$

By nonlinear time-history dynamic analyses, the amplitude of the steady-state response can be obtained. If the amplitude of the response is normalized with respect to the excitation amplitude, the different effects of the added hysteretic damper on the response of the main structure can be seen.

First, the frequency ratio σ is defined as:

$$\sigma = \frac{\omega}{\omega_0} \quad (5.19)$$

where:

$$\omega_0 = \sqrt{\frac{k + k_d}{m}} \quad (5.20)$$

and where ω_0 is the natural circular frequency of the structure equipped with the damper before the damper is activated, k is the lateral stiffness of the bare frame and k_d is the lateral stiffness provided by the added damper before it is activated.

The equivalent static lateral displacement of the structure x_{st} is defined as:

$$x_{st} = \frac{p_0}{k} \quad (5.21)$$

Finally, the lateral deflection of the system required to activate the hysteretic damper x_0 can be expressed in terms of the activation load of the damper:

$$x_o = \frac{F_{lat}}{k_d} \quad (5.22)$$

where F_{lat} is the horizontal lateral load that activates the damper.

In Fig. 5.9, the amplitude of the response A normalized by x_{st} , is shown for systems with $k_d/k = 0.55$ for different values of x_{st}/x_o . The ratio x_{st}/x_o can be expressed as:

$$\Lambda_{hd} = \frac{x_{st}}{x_o} = \frac{k_d p_o}{k F_{lat}} \quad (5.23)$$

The hysteretically damped system's parameter Λ_{hd} is expressed as a function of both the lateral stiffness of the added damper with respect to the stiffness of the original structure (k_d/k) and of the activation load of the damper relative to the amplitude of the applied excitation (p_o/F_{lat}).

As can be seen in Fig. 5.9 (for $k_d/k = 0.55$) for values of Λ_{hd} above 0.85, the apparent natural frequency of the system with the hysteretic damper is similar to that of the initial system. The effect of the added damper is similar to an increase in the amount of viscous damping, with lower amplitudes of vibration for lower values of Λ_{hd} . However, for values of Λ_{hd} below 0.85, the apparent natural frequency of the system is affected by the addition of the hysteretic damper. The effect of the added damper is both to increase the amount of

damping in the system and to alter its dynamic properties. The amount of damping also increases for decreasing values of Λ_{hd} .

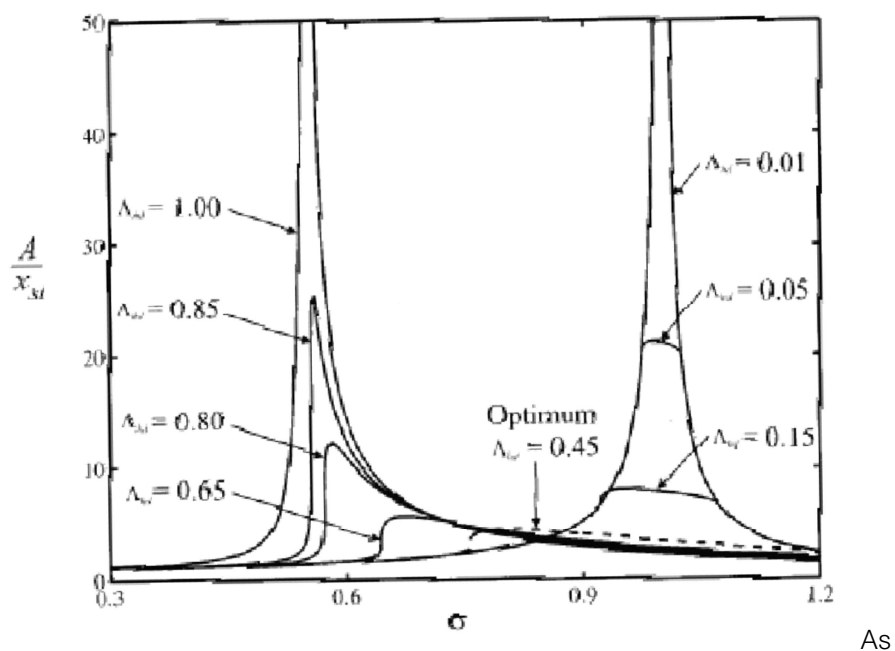


Fig. 5.9 – Steady-state response amplitude of single-degree-of-freedom with hysteretic damper under harmonic base excitation, $k_d/k = 0.55$

When Λ_{hd} is lower than 0.15, the natural period of the system becomes similar to that of the fully braced system. In this range, however, lower values of Λ_{hd} result in higher response amplitudes. In Fig. 5.9, the system corresponding to the value of $\Lambda_{hd} \approx 0.45$, which exhibits the lowest response amplitude, is shown in dashed lines. The theoretical derivation leading to this optimal value

is presented in the following paragraphs. Based on the above numerical results, the addition of hysteretic dampers to a system can be envisioned as having three possible effects:

- the addition of supplemental damping without significantly modifying the dynamic properties of the system (0.85 in Fig. 5.9);
- the addition of supplemental damping along with a modification of the dynamic properties of the system that optimizes the use of the added damper ($\Lambda_{hd} = 0.45$ in Fig. 5.9);
- the addition of supplemental damping along with a significant effect on the dynamic properties of the system. This modification is the equivalent of adding a brace to the system ($\Lambda_{hd} < 0.15$).

From the results shown in Fig. 5.9, it may be tempting to replace a nonlinear structure equipped with hysteretic dampers by a linear system with equivalent viscous damping. This equivalent viscous damping could be calculated from the amplitude of the nonlinear system at resonance (Filiatrault, 2002).

Linearization of the nonlinear system greatly simplifies the problem and provides an approximate estimate of the response of a structure equipped with hysteretic dampers for preliminary assessment for design purposes. This approach is reflected in current design and analysis guidelines for structures incorporating passive energy dissipation systems (ASCE, 2000; BSSC, 2003). It must be clearly understood, however, that this equivalent linearization for structures incorporating hysteretic dampers should be used only for preliminary design and for estimating the dynamic response. The addition of this equivalent viscous damping will always cause a reduction of the dynamic

response of a single-degree-of-freedom system for any seismic input signal. Because of the nonlinear nature of actual hysteretic devices, the results obtained with the linear system with equivalent viscous damping can be non-conservative.

A linearization of the structure can be made by computing the effective period of vibration and the equivalent viscous damping for an equivalent single-degree-of-freedom system. For this purpose, a pushover analysis of the rehabilitated structure is carried out under a lateral load distribution consistent with the first mode shape of the structure in its fully braced condition. The effective stiffness can be calculated graphically, and the effective period can be computed using the effective lateral stiffness and the first modal weight of the structure:

Nonlinear time-history dynamic analyses are required in order to fully assess the effects of hysteretic supplemental damping devices on the dynamic response of civil engineering structures.

5.1.3 Metallic and Friction Dampers

Metallic and friction devices fall into the category of displacement activated dampers. Metal dampers take advantage of the hysteretic behavior of metals when deformed into the post-elastic range to dissipate energy. On the other hand, friction devices dissipate the seismic input energy through the friction developed between the relative movements of two sliding surfaces. In general both the behavior of hysteretic and friction devices can be characterized by an

elastic-plastic behavior. In case of metallic dampers the cyclic response can be defined starting from the knowledge of elastic stiffness, yield load and cyclic ductility of the damper. Conversely, in case of friction dampers, the cyclic characteristics of dissipating devices can be described through the knowledge of the slip load and of the elastic stiffness. This last parameter is, in truth, in many cases very steep, so that behavior of friction devices is usually associated with a rigid-plastic response. Most friction devices are used in bracing configuration and, as a consequence, the stiffness of the bracing-damper system is in general associated with the stiffness of the connecting bracing elements. As a result, metallic and friction dampers, in technical literature, are usually referred to as the family of the hysteretic devices and, when speaking of the influence of hysteretic dampers on the global structural response, reference is usually made either to metallic and friction dampers.

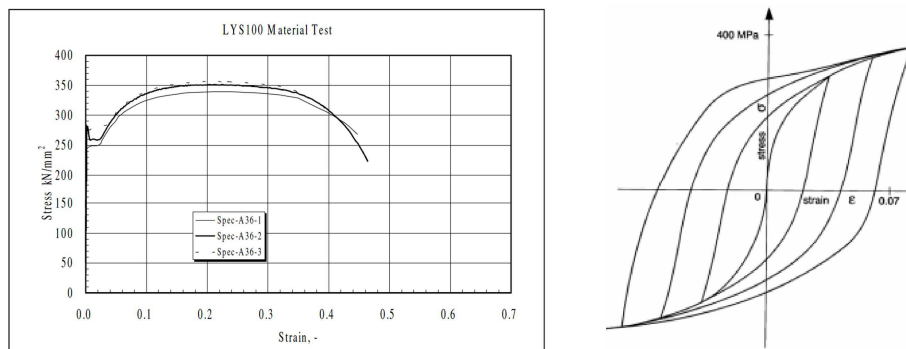


Fig. 5.10 – Typical response of metals subjected to monotonic and cyclic loads

Metallic dampers are devices which have been found to be most economic and suitable to apply passive control strategies. Their behavior under cyclic loads can be described starting from the knowledge of the response of metals

under uniaxial loading conditions. In Fig. 5.10 the stress-strain curve of a metal in simple tension is shown. In the elastic phase the stress is proportional to the strain and the constant of proportionality is the Young's modulus E . In the elastic region the equation of state is given below.

$$\sigma = E\varepsilon \quad (5.24)$$

An increase of deformation over the elastic limit leads to the plasticization of the material and to the exhibition of a yielding plateau phase. The knowledge of the stress leading to the first material plasticization is of great importance in engineer. A further increase of deformation results in a strain hardening phase, where the material develops larger stresses than the yield stress. If the material is subjected to cyclic load reversal after it has exceeded the linear elastic range, it exhibits several properties. When material is unloaded recovers its elastic modulus E and when is loaded in the opposite direction starts to yield at a stress lower than the yield stress. This effect is known as Bauschinger effect. Since material is subjected to loads within the elastic range yield stress remain unchanged. Conversely, if the material is stressed beyond yield plateau, it unloads following the initial elastic stiffness and the Bauschinger effect becomes more pronounced as the maximum strain is increased. In case of cyclic loads the yield plateau disappears and the material exhibit a certain post-yield stiffness.

To understand the behavior of a metal as it is plastically deformed, it is necessary to look at it on an atomic scale. Previous to the 1930's, the plastic deformation of a metal was not understood, and theoretical calculations predicted yield stresses and strains very different from those observed in

practice. It was calculated that a perfect crystal, with its atoms in well-defined positions, should have a shearing yield stress f_y of the order of 10^{10} Pa, and should break in a brittle fashion, like a piece of chalk, at a shear strain ϵ_y of the order of 0.1. In reality, metal single crystals start to yield at a stress of 10^6 to 10^7 Pa (a strain of 10^{-4} to 10^{-3}) and continue to yield plastically up to strains of 0.01 to 0.1 or more. The weakness of real metal crystals could in part be attributed to minute cracks within the crystal, but the model failed in that it did not indicate how the crystal could be deformed plastically.

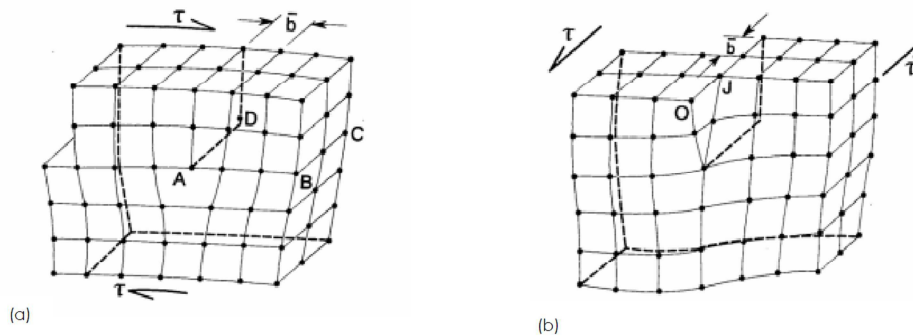


Fig. 5.11 – Atomic arrangements corresponding to: a) edge dislocation; b) screw dislocation

The dislocation model was then revised and overcame these difficulties. Since its inception the dislocation model has been extremely successful in explaining the strength, deformability and related properties of metal single crystals and poly-crystals. The plastic deformation in a crystalline solid occurs by planes of atoms sliding over one another like cards in a pack. In a dislocation-free solid it would be necessary for this slip to occur uniformly in one movement, with all the bonds between atoms on one slip plane stretching equally and finally

breaking at the same instant, where the bond density is of the order of 10^{16} bonds per square centimeter. In most crystals, however, this slip, or deformation, is not uniform over the whole slip plane but is concentrated at dislocations.

Fig. 5.11(a) is a schematic drawing of the simplest of many types of dislocation, namely an edge dislocation with the solid spheres representing atoms. The edge dislocation itself is along the line AD and it is in the region of this line that most of the crystal distortion occurs. Under the application of the shear stress this dislocation line will move across the slip plane ADCB, allowing the crystal to deform plastically. The bonds, which must be broken as the dislocation moves, are of the order of 10^8 per centimeter, and are concentrated at the dislocation core, thus enabling the dislocation to move under a relatively low shear stress. As the dislocation moves from the left-hand edge of the crystal Fig. 5.11 (a) it leaves a step in the crystal surface, which is finally transmitted to the right-hand side. Fig. 5.11 (b) shows the other major type of dislocation, namely a simple screw dislocation, which may also transmit plastic deformation by moving across the crystal.

The dislocations in crystals may be observed using electron microscopy, while the ends of dislocations are readily seen with the optical microscope after the surface of the crystal has been suitably etched. Typical dislocation densities are 10^8 dislocations per square centimeter in a deformed metal and about 10^5 per square centimeter in an annealed metal, namely one which has been heated and cooled slowly to produce softening. Dislocations are held immobile at points where a number of them meet, and also at points where impurity atoms are clustered.

The three main regions of a typical stress-strain curve are interpreted on the dislocation model as follows:

- Initial elastic behavior is due to the motion of atoms in their respective potential wells; existing dislocations are able to bend a little, causing micro plasticity.
- A sharp reduction in gradient at the yield stress is due to the movement of dislocations.
- An extended plastic region, whose gradient is the plastic modulus or strain-hardening coefficient, occurs when further dislocations are being generated and proceed to move. As they tangle with one another, and interact with impurity atoms, they cause work hardening.

It is also possible to model a polycrystalline metal as a set of interconnected domains, each with different hysteretic features of the type conferred by dislocations, which give the general stress-strain features displayed by the hysteresis loops of Fig. 5.10.

Since dislocations are not in thermal equilibrium in a metal, but are a result of the metal's history, there is no equation of state which can be used to predict accurately the stress-strain behavior of the metal. However, the behavior of a metal may be approximately predicted in particular situations, if the history and deformation are reasonably well characterized.

A classification of metallic dampers can be made according to the actions that have to withstand in:

- flexural dissipating devices;

- shear dissipating devices;
- torsional dissipating devices.

In the following, some of the most interesting structural application proposed in past years by different authors is exposed.

5.1.3.1 Metallic Flexural dissipating devices

In past thirty years, several devices designed to dissipate seismic energy exploiting the flexural behavior of metallic elements have been proposed.

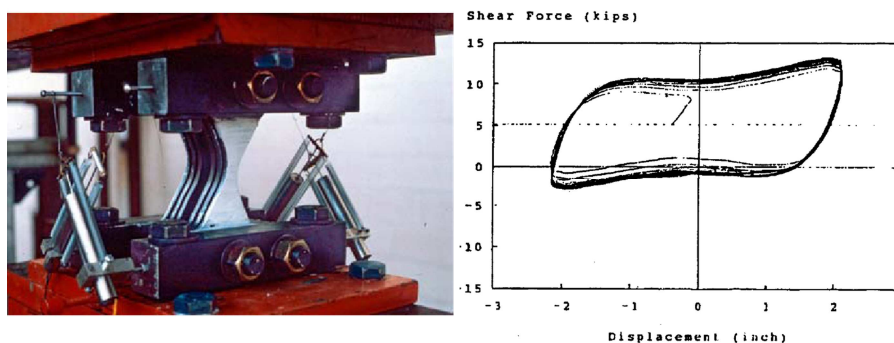


Fig. 5.12 – Cyclic response of ADAS devices

One of the most famous and most studied types of damper is known with the name of ADAS (Added Damping and Stiffness) (Fig. 5.12) (Whittaker et al., 1989; Whittaker et al., 1990; Yang & Popov, 1995; Alonso, 1989; Scholl, 1990; Su & Hanson, 1990). It is a device constituted by the assemblage of a number

of plates with constant thickness and hourglass section usually positioned between the top of a chevron bracing system and the lower part of the beam. The number of plates is variable depending on the desired force-displacement characteristics. The choice of the number of plates allows to adjust the characteristics of the device on the base of the characteristics of the structure in which the device is incorporated. ADAS plates are positioned so that structural displacements generate bending actions symmetric, with point of contra-flexure at the mid-height of the device. The basic idea is that plates have to possess a shape varying accordingly with the bending moment, so that, ideally, yielding takes place contemporary in all plate sections (Fig. 5.13).

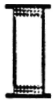
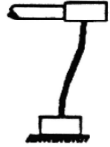

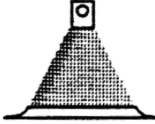



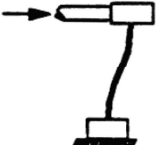

<u>PLATE CONFIGURATION</u>	<u>PROFILE</u>	<u>DEFORMATION</u>	<u>STRESS DISTRIBUTION</u>	<u>COMMENTS</u>
Rectangle			 $+f_y+$	Non-Workable due to local yielding only
Triangle			 $+f_y+$	Workable
X Shape			 $+f_y+$	Workable

Fig. 5.13 – Curvatures developed for different plate geometry

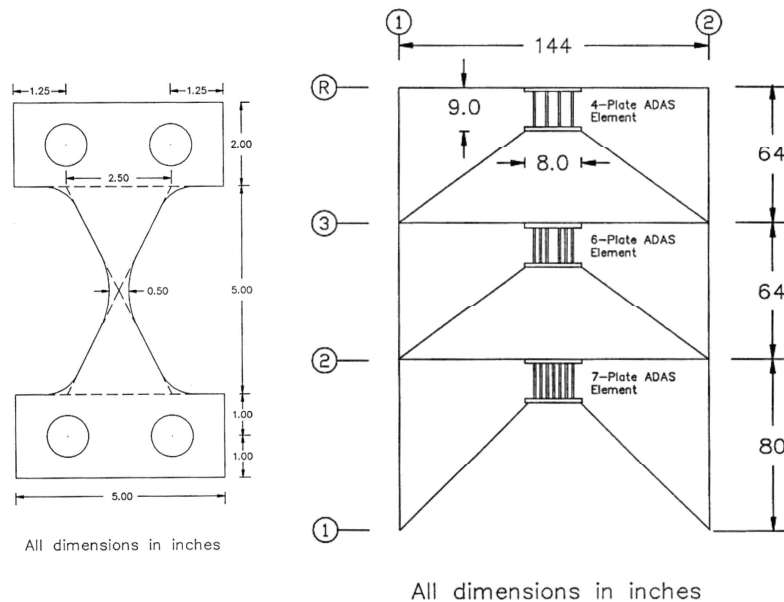


Fig. 5.14 – Application of ADAS device to a three stories steel MRFs

In this way, the ductility demand is spread along the whole plate and a better distribution of the plasticization is obtained. In past experimental works, the cyclic behavior of ADAS devices has been shown to be wide and stable. Shake table tests of a three stories moment resisting steel frame structure demonstrated that the presence of ADAS devices improved the behavior under seismic loads enhancing the stiffness, strength and ability to dissipate energy (Fig. 5.14). The inter-storey drifts were reduced by 30 to 70 percent with the addition of the ADAS elements. The ratios of base shears in the structure equipped with ADAS elements to those without dampers ranged from 0.6 to 1.25. In addition, it was pointed out that shear forces were resisted primarily by

ADAS and the supporting braces. Therefore, ADAS plasticized while the bare frame was prevented by excessive ductility demands.

After few years from the first experimental campaign carried out by (Whittaker et al., 1989) ADAS devices found a number of application worldwide. Some implementations of ADAS dampers in buildings occurred in New Zealand, Japan, Mexico and U.S.A.

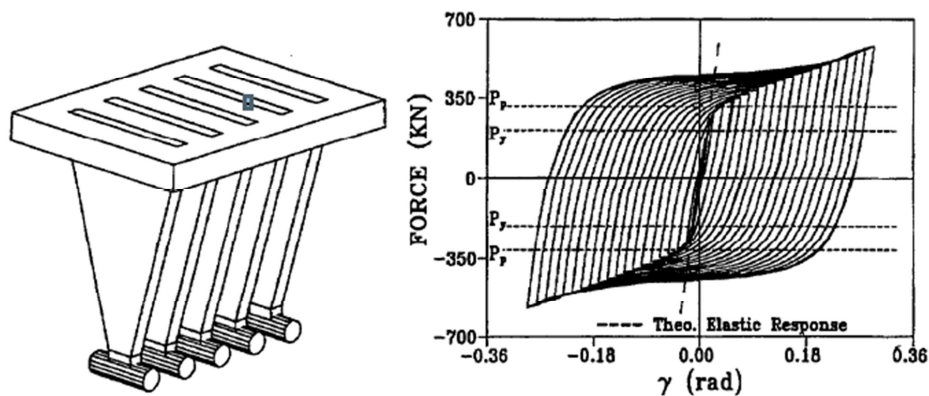


Fig. 5.15 – Geometry and Response of T-ADAS devices

Later, triangular dissipators were used also in the form of Tapered or Triangular ADAS (T-ADAS). T-ADAS system is constituted by the assemblage of a number of trapezoidal plates positioned between a chevron bracing system and the beam of a MRF. The behavior of T-ADAS system is similar to that of ADAS dampers. In fact T-ADAS plates are properly constrained in order to develop a bending moment diagram analogous to that of a cantilever beam. The section of maximum width is usually rigidly connected to the beam of the MRF and the section of minimum width is connected to the bracing system

through a slotted base plate. The main advantage of T-ADAS devices compared to ADAS devices is that they are not affected by gravity loads because of the slotted holes in the base plate. However, the assemblage of a T-ADAS is usually much more complicated than an ADAS. Experimental results on T-ADAS tests have shown that also the behavior of T-ADAS device is wide and stable with almost no degradation under cyclic reversals. Pseudo-dynamic tests on frames equipped with Tapered dampers showed the ability of these devices to improve the response under seismic loads (Tsai et al., 1993).

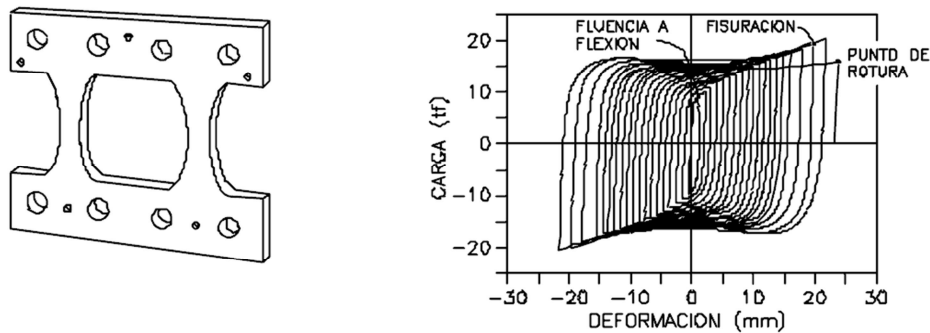


Fig. 5.16 – Geometry and Response of Honeycomb devices

Another system which relies on the geometry and, in particular, on the development of a uniform plasticization along a steel plate is the Honeycomb system, developed in Japan by Kajima Corporation (Kobori et al., 1992). Honeycomb damper consists of single or multiple X-shaped plates loaded in the plane orthogonal to the usual loading direction of ADAS devices. Typical results of experimental testing on Honeycomb devices is reported in Fig. 5.16.

5.1.3.2 Metallic Shear Dissipating Devices

It is well known in technical literature that steel panels subjected to shear loads can develop wide and stable hysteretic response. It is for this reason that, in past years, a number of steel dissipating systems working under shear loads has been developed (Popov, 1980; Kasai & Popov, 1986; Rai & Wallace, 1998; Tsai & Wang, 1998; Nakashima, 1995; Cahis et al., 1997).

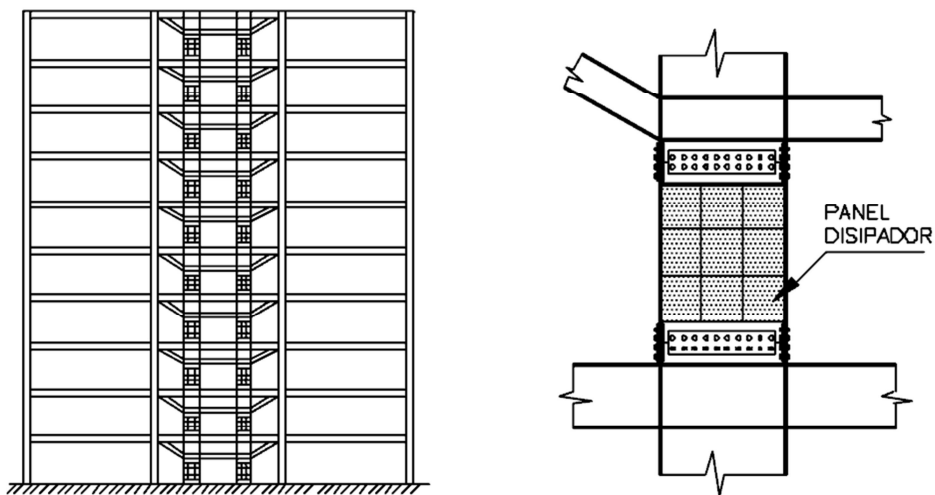


Fig. 5.17 – Distribution of Shear Panels in MRFs (Nakashima, 1995)

Usually, shear systems relying on steel hysteresis are constituted by short H-sections stubs properly stiffened to prevent local buckling of web panels. As far as these kind of devices belong to the category of displacement activated devices, they are usually applied in combination with bracing systems to exploit the relative movement arising during a seismic event between two

stories. Behavior of steel shear panels has been extensively studied in past and some criteria to establish design rules to determine the optimum geometry of stiffeners to avoid web buckling have been proposed.

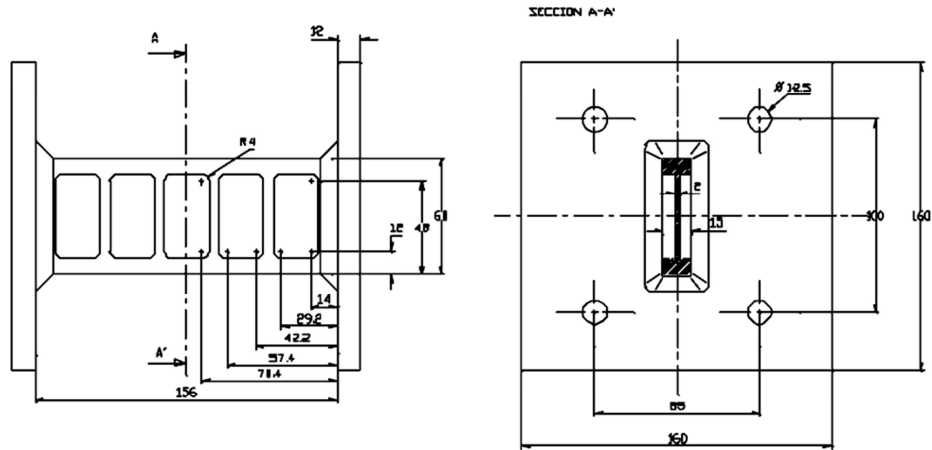


Fig. 5.18 – Shear Damper proposed by (Cahis et al., 1997)

In many cases, the basic principles applied to develop shear based dissipative systems are the same used to define geometry of flexural devices such as ADAS or TADAS. As an example, in case of the damper proposed by (Tsai & Wang, 1998) a tapered H-section stub is used to dissipate the seismic input energy between a chevron bracing and MRF beam. As in case of TADAS device, the tapered H-section stub is assembled to be rigidly fixed to the beam and pinned to the bracing system. In this way, a constant shear and linear bending moment is developed on the tapered damper.

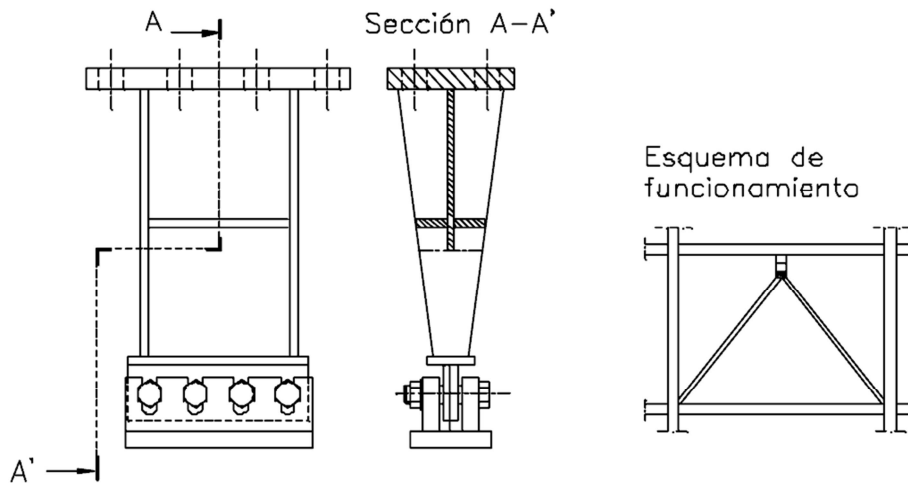


Fig. 5.19 – Shear Damper proposed by (Tsai) (Tsai & Wang, 1998)

More recently, shear dissipating systems employing low-yield high-ductility steel (80 MPa yield stress – 60% elongation) have attracted the attention of the scientific community. The adoption of low-yield steel allows to obtain, for a fixed shear, sections with higher thickness, in this way, the adoption of stiffeners is not necessary.

5.1.3.3 Friction Dissipating Devices

As already underlined, friction dampers dissipate seismic input energy through the slippage of two surfaces in contact on which is applied an adjustable normal action. Obtained hysteresis cycles are analogous to that of elastic-plastic dampers with high initial stiffness. This is a great advantage of friction

devices, in fact they can be designed aiming to remain in elastic range under serviceability limit state and to plasticize under ultimate conditions. In this way, because of their steep elastic behavior, under SLS can be used to work as displacement reducers and under ULS can be employed to dissipate the seismic input energy. Solid friction is a phenomenon, which has been studied by illustrious scientists such as Leonardo Da Vinci, Newton and Coulomb.

Classical theory of dry friction is based on the following three postulates:

- Total frictional force is independent of the apparent surface area of contact;
- total frictional force that can be developed is proportional to the normal action applied;
- in case of slow sliding velocities, the total frictional force is independent on the sliding velocity.

During slippage, the classical relationship to compute the tangential force acting at the sliding interface in the direction opposed to the motion is the Coulomb friction equation, named after Charles-Augustin de Coulomb.

$$T = \mu N \quad (5.25)$$

where T is the sliding force, N is the normal action and μ is the friction coefficient. In case of dry friction, two main kinds of frictional behaviors can be individuated: static friction and kinetic friction. In the former case friction is developed between two surfaces which are not moving each other. As an example static friction is the phenomenon that prevents a body to slip down a

sloped surface. Usually static friction coefficient is greater than kinematic friction coefficient, so that when no slide occurs friction force can assume values from zero up to the maximum force that is expressed as:

$$T_{max} = \mu_s N \quad (5.26)$$

where μ_s is the static friction coefficient. Any force smaller than T_{max} is not able to cause slippage. Any force larger than T_{max} overcomes the force of static friction and cause sliding to occur. After the instant sliding occurs static friction is no longer applicable and the phenomena is called kinetic friction. The maximum value of static friction is often called limiting friction or sometimes traction.

Many systems relying on friction have been proposed in past. The most famous is probably the Pall friction damper, where the relative sliding of steel plates within an X-shaped bracing system provides the energy dissipation.

5.2 Development of Dissipative T-stubs

As pointed out in the introduction, behavior of steel moment resisting frames under the seismic events occurred in last years evidenced a significant loss of resistance and ductility deriving from the premature fracture of welds. In fact, even though welded beam-to-column joints can be detailed to obtain full strength connections theoretically able to provide steel frames with adequate dissipation capacities, the difficulties deriving from the in situ manufacturing of the welds play a basic role leading often to a brittle behavior of the connections and, as a consequence, to an unsatisfactory behavior of the whole frame. From this point of view, bolted connections should be preferred in design of seismic-resistant steel frames provided that joints are designed to ensure the engagement in plastic range of beam ends rather than connections. The dissipation capacity of steel frames with bolted connections has already been investigated in order to verify the possibility of using this kind of frame as an alternative to welded moment frame (SAC, 2000a; Leon & Swanson, 2000; Faella et al., 2000; Latour et al., 2008; Rizzano, 2006) In particular, with reference to Ductility Class High Frames (CEN, 2005c), a design criterion able to obtain full strength extended end-plate connections has already been proposed and validated by (Piluso & Rizzano, 2003) on the basis of a probabilistic analysis accounting for random material variability of the connecting elements, i.e. beam, column, end-plate, bolts.

As an alternative, the latest version of Eurocode 8 (CEN, 2005c) allows to design Steel Moment Resisting Frames with partial strength joints, provided that connecting elements possess adequate ductility and dissipation capacities under cyclic loads. Within this framework, some attempts to provide detailed rules for designing dissipative joints have already been proposed in

technical literature (Fleischman & Hoskisson, 2000; Rizzano, 2006; Kim et al., 2007). This topic has also been investigated in previous works of (Latour et al., 2008; Iannone et al., 2011), where an experimental program devoted to point out the behavior under cyclic loads of different joint typologies has been carried out. In particular, design criteria able to engage in plastic range specific joint components, in order to govern the joint dissipation capacity, and to assure a desired value of stiffness, strength and plastic rotation supply have been pointed out.

In recent years, a growing interest of the scientific community has been addressed to structural systems able to perform adequately during seismic events and, at the same time, easy to replace after the earthquake (Aiken et al., 1993b; Kelly, 1979). Within this framework the approach usually adopted consists on equipping the structure with supplemental damping devices able to dissipate a part of the seismic input energy reducing the seismic demand on the structural elements. Many works have been carried out in recent studies on this topic, leading to relevant results and to the development of a large number of high dissipation capacity dampers, either of friction or of yielding type (Aiken et al., 1993a; Constantinou et al., 1998; Christopoulos & Filiatrault, 2006; Kim et al., 2007).

In this paper, an innovative approach is followed. The advantages provided by the introduction in the structure of supplemental damping devices easy to be substituted after the earthquake are added to those typical of dissipative steel frames in which a large number of dissipative zones is expected at beam ends. This goal can be achieved designing partial strength joints and providing joints with ductile and simple replaceable elements. In addition, it is important to underline that in designing steel frames with global collapse

mechanism the use of partial strength joints can lead to a significant reduction of the structural cost (Faella et al., 1998). In fact, in many cases columns design is governed by the satisfaction of members' hierarchy criterion rather than by resistance and deformability checks. In (Faella et al., 1998), it has been demonstrated that the use of partial strength connections in frames designed to fail according to a global collapse mechanism, can lead to a reduction of the structural cost up to 25% in case of frames with long span and few storeys.

A partial strength joint typology particularly appropriate to this purpose is the Double Split Tee Connection in which the connecting elements are clearly identified and easily replaceable. The behavior of this type of connection is strictly related to that of a T-stub subjected to axial load, which models the top and bottom tee. In past, many scientific efforts have been devoted to understand and model the behavior of simple rectangular T-stubs under cyclic loads (Piluso & Rizzano, 2008). Such behavior, as pointed out in scientific literature, is affected by significant pinching due to many factors, such as the plastic deformation of bolts and contact phenomena. Moreover, the plastic mechanism of rectangular T-stubs is characterized by the concentration of plastic strain in two small areas of the flange corresponding to the flange-to-web connection and to the bolt axes. Such plastic mechanism concentrates strain demand in limited zones and, consequently, under cyclic loads quickly leads to the deterioration of stiffness, strength and energy dissipation capacity (Whittaker et al., 1989). Aiming to increase the energy dissipation capacity of T-stubs, in this work, starting from results obtained by (Piluso & Rizzano, 2008; Latour et al., 2008) concerning monotonic and cyclic behavior of T-stubs, concepts usually adopted for ADAS devices have been applied developing a dissipative T-stub.

This typology of damper can be easily used in beam-to-column joints in substitution of classic rectangular T-stub of Double Split Tee Connection.

5.2.1 Mechanical Modeling

5.2.1.1 Rectangular T-stubs – Piluso et al. Model (1997)

In order to analyze the energy dissipation capacity of T-stub connections, the plastic behavior of classic rectangular T-stub should be preliminary considered.

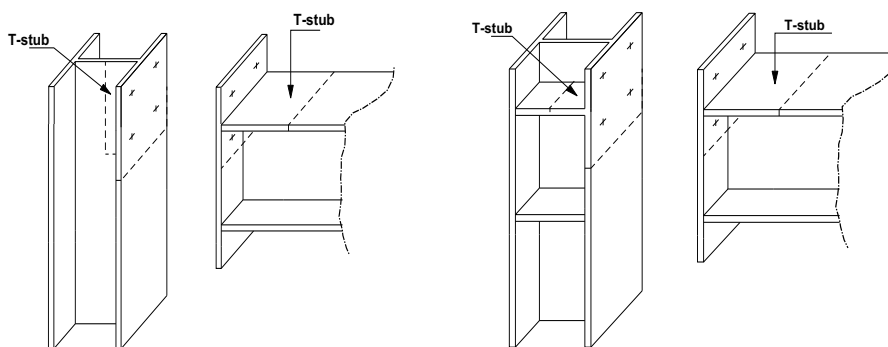


Fig. 5.20 – T-stub Identification in case of Extended end plate Connections

It is well known in scientific literature that equivalent T-stub is constituted by the coupling of two or more T elements fastened through one or more bolt rows in correspondence of the flanges. First studies dealing with modeling of T-stubs are by (Yee & Melchers, 1986). The two authors developed a method for the prediction of the moment rotation curve of extended end-plate connections Fig. 5.20. As far as basic principles governing behavior of T-stubs are of

concern the most simple case can be considered, i.e. the case of a simple two bolts T-stub subjected to uniaxial loads.

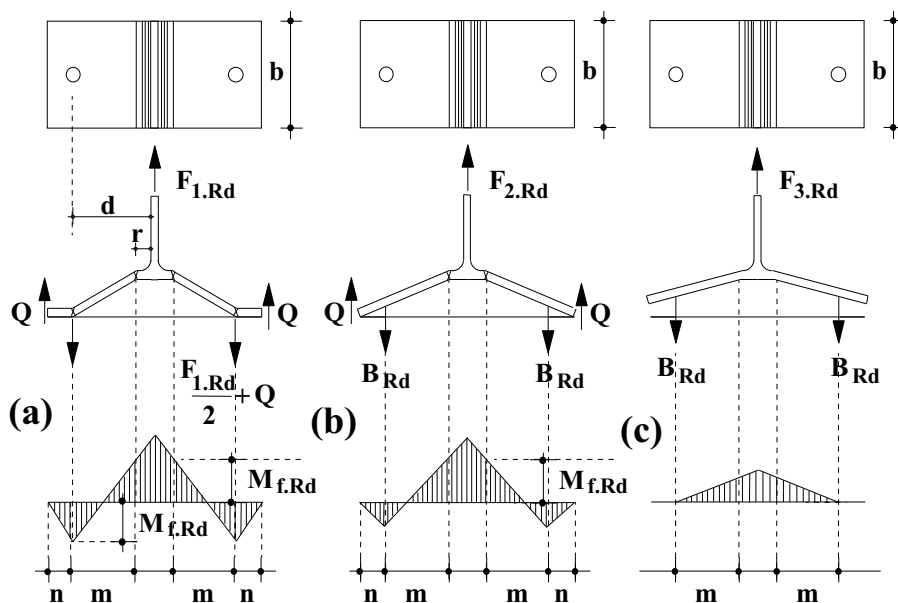


Fig. 5.21 – Failure modes of bolted T-stubs

In this case, depending on the ratio between the flexural strength of the flanges and the axial strength of the bolt (Faella et al., 2000), it is possible to individuate three different failure mechanisms (Fig. 5.21).

In the following reference is made to the notation given in Fig. 5.22.

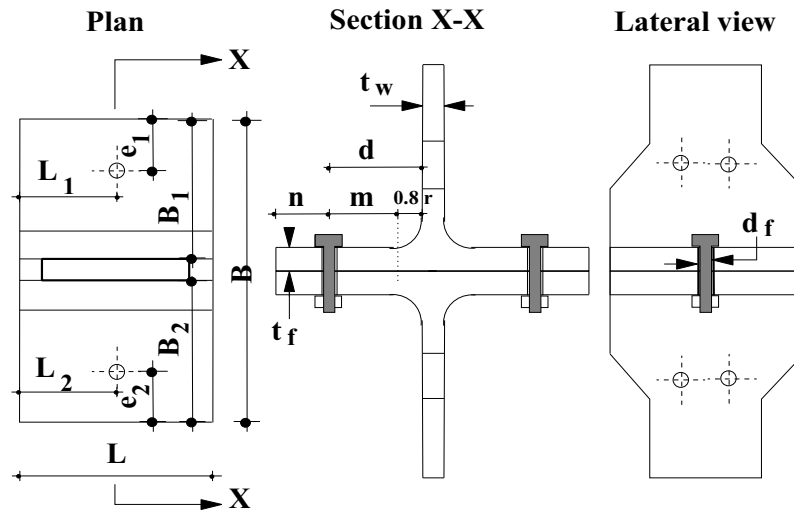


Fig. 5.22 – Adopted Notation

Mechanism type 1

The most dissipative failure mechanism (type-1) is characterized by the formation of four plastic hinges, two in correspondence of the bolt line and two in correspondence of the flange-web connection. According to EC3 distance between bolt and plastic hinge can be defined as $m = d - 0,8r$, where d is the distance between bolt axis and T-stub web.

Starting from the bending moment diagram given in Fig. 5.21 it is easy to recognize that plastic resistance in this hypothesis is equal to:

$$F_1 = \frac{4M_f}{m} \quad (5.27)$$

where M_f is the plastic resistance of the flange.

Mechanism type 2

Mechanism type 2 is characterized by the contemporary formation of two plastic hinges in correspondence of the flange-web connection and fracture of bolts. In this case, contact forces lead to an increase of axial load in the bolts, which fail prior of the development of the plastic hinges in correspondence of the bolt line. Flanges yield condition allows determining:

$$Bm - Q(n + m) = M_f \quad (5.28)$$

as a result:

$$Q = \frac{Bm - M_f}{m + n} \quad (5.29)$$

where n is the distance between the bolt axis and the contact forces, which are assumed to act at the end of the plate. From the translational equilibrium derives:

$$F_2 = 2(B - Q) = \frac{2M_f + 2Bn}{m + n} \quad (5.30)$$

Mechanism type 3

In this case, weak elements are bolts, which attain the failure condition prior of the plasticization of the plate. In this case it is not possible the development of contact forces and, as a consequence, T-elements are completely disconnected at failure. In this case, plastic resistance coincides with the resistance of the two bolts.

$$F_3 = 2B \quad (5.31)$$

Starting from the geometrical and mechanical characteristics of the T-stubs, plastic resistance is given by:

$$F = \min\{F_1, F_2, F_3\} \quad (5.32)$$

Three collapse mechanisms are clearly influenced by the ratio between the flexural strength of the plate and axial resistance of the bolts. It is worth note that parameter:

$$\beta = \frac{4M_f}{2B \cdot m} \quad (5.33)$$

which represents the ratio between resistance provided by mechanism type 1 and mechanism type 3, is the parameter governing the failure mechanism.

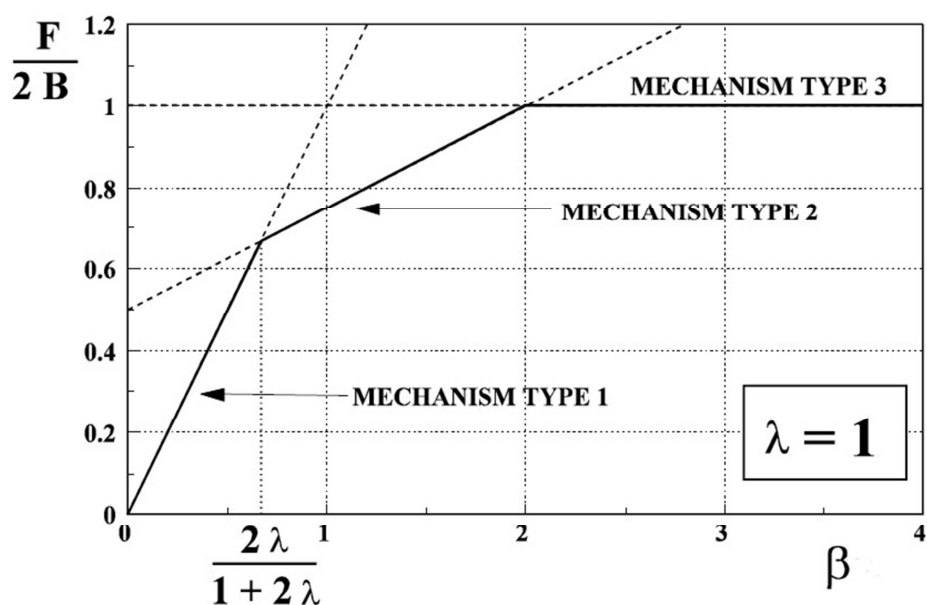


Fig. 5.23 – Influence of parameter β on the collapse mechanism

By introducing adimensional parameter $\lambda = n/m$ and equating resistances of mechanisms 1-2 and 2-3 it is possible to individuate three ranges:

- mechanism type 1 (flange collapse): $\beta < \frac{2\lambda}{1+\lambda}$;
- mechanism type 2 (flange collapse and bolt failure): $\frac{2\lambda}{1+\lambda} < \beta < 2$;
- mechanism type 3 (bolt failure): $\beta > 2$.

Design resistance for the three mechanism can be represented in adimensional form in Fig. 5.23. Practically, first mechanism is typical of T-stubs

with thin flanges and strong bolts, third mechanism is typical of elements with thick flanges and weak bolts.

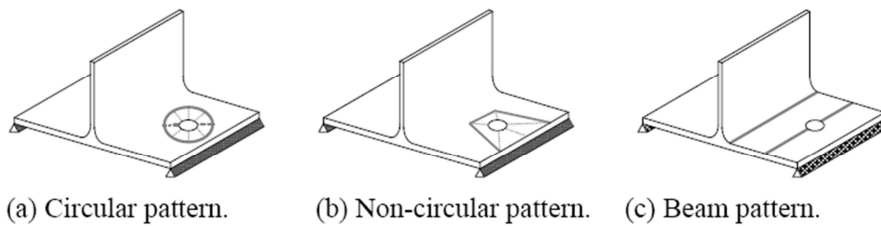


Fig. 5.24 – Yield lines for T-stubs with only one bolt row

In previous expressions flange plastic moment has been used. Generally this is expressed as:

$$M_f = \frac{b_{eff} t_f^2}{4} f_y \quad (5.34)$$

where b_{eff} is the effective width. This width classically is determined by using the yield line approach. As evidenced in Fig. 5.24, generally three possible mechanisms are considered:

- Circular pattern: $b_{eff,1} = 2\pi m$;
- Non-circular pattern: $b_{eff,2} = 4m + 1,25n$;
- Beam pattern: $b_{eff,2} = b$.

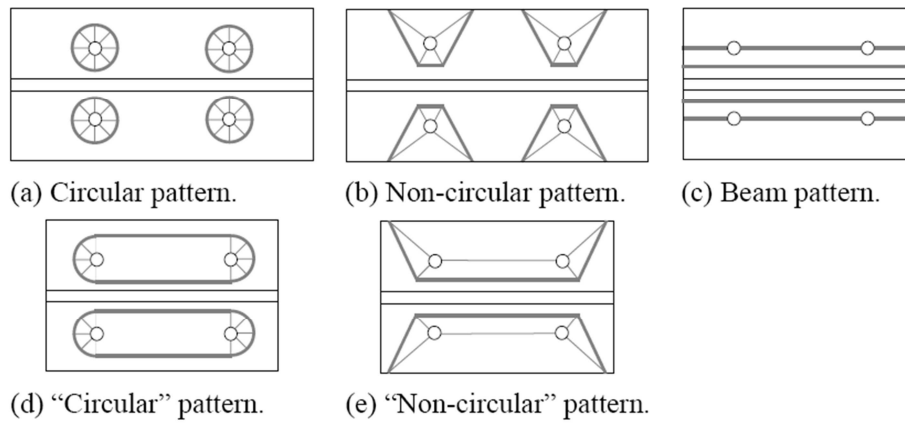


Fig. 5.25 – Yield lines in case of group of bolts

It is evident that failure mechanism with minimum effective width will be activated:

$$b_{eff} = \min\{b_{eff,1}, b_{eff,2}, b_{eff,3}\} \quad (5.35)$$

Values of the effective width previously reported are referred to the case of two bolts T-stubs. In general, especially when end-plates are considered, it is required to account for group behaviors. With reference to it is possible to obtain the following:

- Circular pattern: $b_{eff,4} = \pi m + 0.5 p$;
- Non circular pattern: $b_{eff,5} = 2m + 0.625n + 0.5 p$.

Accounting also for bolt group mechanisms the effective width to adopt in calculations is:

$$b_{eff} = \min \{ b_{eff,1}, b_{eff,2}, b_{eff,3}, b_{eff,4}, b_{eff,5} \} \quad (5.36)$$

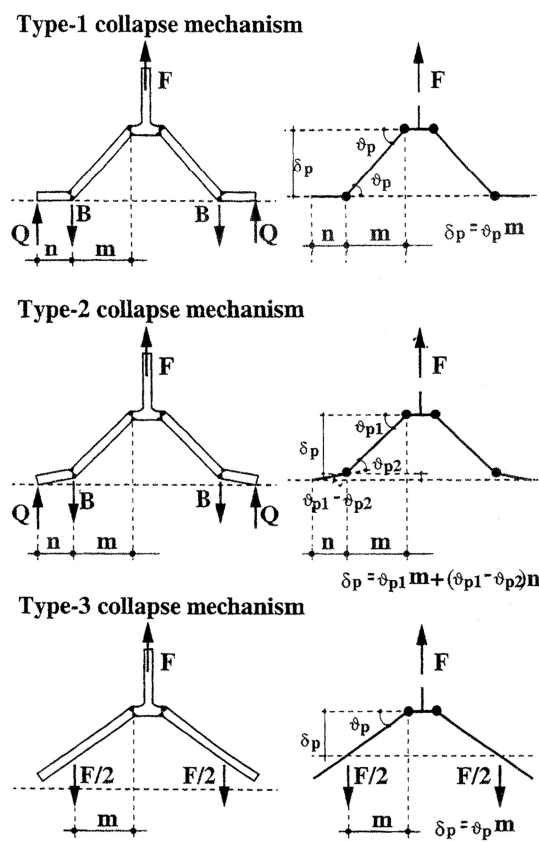


Fig. 5.26 – Collapse mechanisms according to Piluso et al. model

Piluso et al. model is developed assuming that during the loading process bending moment distribution is analogous to that acting in the elastic case, i.e. the internal actions previously described. Therefore, model is based on the idea that starting from the knowledge of the bending moment, by integration, it is possible to determine the corresponding curvatures and, as a consequence, rotation and displacement of the T-stub.

It is worth note that, in general, prediction of the force-displacement curve of bolted T-stubs is untrivial because of the numerous sources of uncertainty due to different aspects. In particular, nature of the problem is tridimensional, geometrical non-linearities can arise and contact phenomena are involved. Piluso et al. mathematical model is based on the following assumptions:

- Model is uni-dimensional and 3-D effects are neglected;
- geometric non-linearity is neglected;
- moment-shear interaction is neglected;
- contact forces are assumed to act at the plate end;
- steel uni-axial behavior is modeled assuming that ultimate condition is attained at the ultimate strain in the flanges.

Under these hypothesis it is easy to understand that definition of the ultimate displacement depends on the definition of the ultimate rotation of a compact section by means of integration of its moment-curvature diagram.

Therefore, definition of the model strongly depends on the evaluation of steel true stress- true strain. In this model, material uniaxial behavior is represented by means of a quadri-linear approximation.

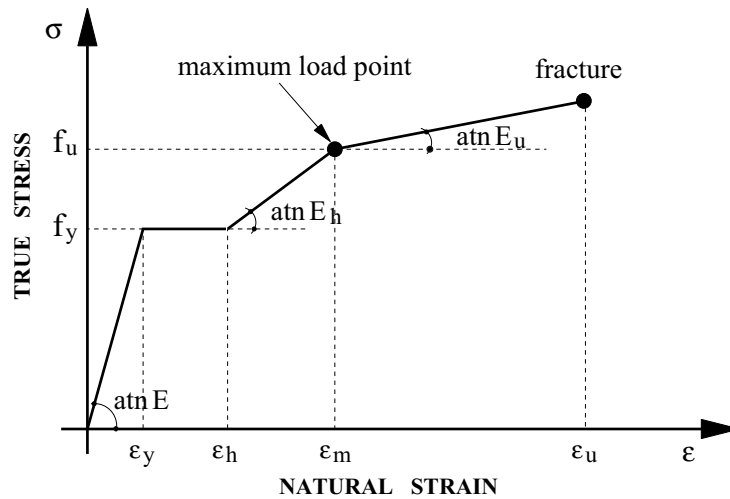


Fig. 5.27 – Material Uni-axial behavior

Steel behavior is completely defined starting from the following parameters:

- ϵ_y , true strain at yielding;
- ϵ_h , true strain at the beginning of strain hardening;
- ϵ_m , maximum strain at maximum load;
- ϵ_u , strain at collapse;
- f_y , true stress at yielding;
- f_u , ultimate stress;
- f_b , stress at collapse;
- E , elastic modulus;
- E_h , hardening modulus ;
- E_u , ultimate modulus.

Moment curvature diagram of a rectangular section can be obtained under the hypothesis previously described and in particular modeling the material by means of a quadri-linear approximation.

In general curvature χ relative to a determined level of strain of the section extreme fiber ε , and moment relative to yielding can be defined as:

$$\chi = \frac{2\varepsilon}{t_f} \quad (5.37)$$

$$M_y = \frac{b_{eff} t_f^2}{6} f_y \quad (5.38)$$

Considering the following curvatures:

$$\chi_y = \frac{2\varepsilon_y}{t_f} \quad (5.39)$$

$$\chi_h = \frac{2\varepsilon_h}{t_f} \quad (5.40)$$

$$\chi_m = \frac{2\varepsilon_m}{t_f} \quad (5.41)$$

$$\chi_u = \frac{2\varepsilon_u}{t_f} \quad (5.42)$$

it is possible to define the moment-curvature diagram in adimensional form by means of equilibria equations:

$$\begin{aligned} & \chi/\chi_y < 1 \\ \text{Elastic branch} & \quad , \\ \chi_y & = \frac{2\varepsilon_y}{t_f} \end{aligned} \quad (5.43)$$

$$\begin{aligned} & 1 < \chi/\chi_y < \chi_h/\chi_y \\ \text{Yield plateau} & \quad , \\ \frac{M}{M_y} & = \frac{1}{2} \left[3 - \left(\frac{\chi}{\chi_y} \right)^2 \right] \end{aligned} \quad (5.44)$$

$$\begin{aligned} & \chi_h/\chi_y < \chi/\chi_y < \chi_m/\chi_y \\ \text{Hardening} & \quad , \\ \frac{M}{M_y} & = \frac{1}{2} \left[3 - \left(\frac{\chi}{\chi_y} \right)^2 \right] + \frac{1}{2} \frac{E_h}{E} \left(\frac{\chi - \chi_h}{\chi_y} \right) \left(1 - \frac{\chi_h}{\chi} \right) \left(2 + \frac{\chi_h}{\chi} \right) \end{aligned} \quad (5.45)$$

$$\begin{aligned} & \chi_m/\chi_y < \chi/\chi_y < \chi_u/\chi_y \\ \text{Ultimate Branch} & \quad , \\ \frac{M}{M_y} & = \frac{1}{2} \left[3 - \left(\frac{\chi}{\chi_y} \right)^2 \right] + \frac{1}{2} \frac{E_h}{E} \left(\frac{\chi - \chi_h}{\chi_y} \right) \left(1 - \frac{\chi_h}{\chi} \right) \left(2 + \frac{\chi_h}{\chi} \right) + \\ & - \frac{1}{2} \left(\frac{E_h - E_u}{E} \right) \left(\frac{\chi - \chi_m}{\chi_y} \right) \left(1 - \frac{\chi_m}{\chi} \right) \left(2 + \frac{\chi_m}{\chi} \right) \end{aligned} \quad (5.46)$$

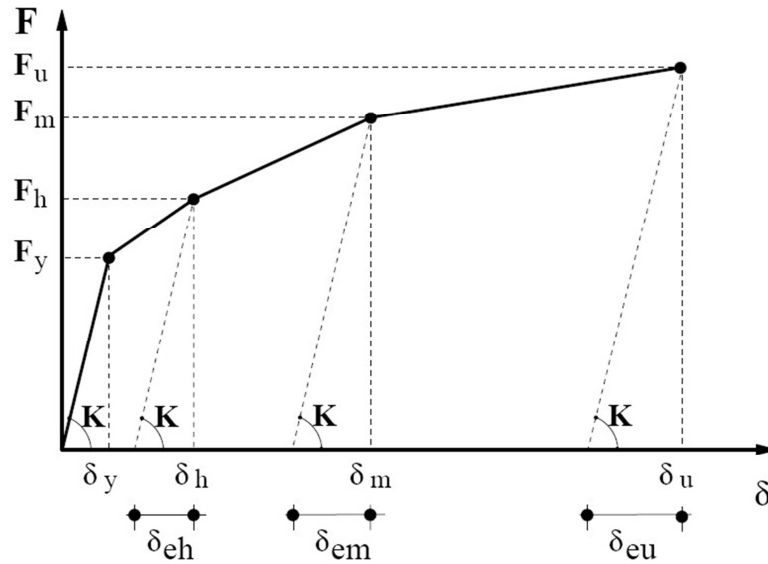


Fig. 5.28 – Quadrilinear force-displacement curve

Parameter which individuate the type of mechanisms is β , which with reference to ultimate conditions becomes:

$$\beta_u = \frac{4M_u}{B_u m} \quad (5.47)$$

where:

$$M_u = M_y \cdot \left(\frac{M}{M_y} \right)_{|\chi=\chi_u} = \frac{b_{eff} t_f^2}{6} f_y \cdot \left(\frac{M}{M_y} \right)_{|\chi=\chi_u} \quad (5.48)$$

$$B_u = A_{rb} f_{ub} \quad (5.49)$$

Depending on the collapse mechanism individuated by coefficient β_u Piluso et al. model force-displacement curve by means of a quadrilinear curve (Fig. 5.28).

Mechanism type 1

This mechanism occurs when $\beta_u < \frac{2\lambda}{1+2\lambda}$. In this case, considering the influence of the washer under the bolt head ultimate resistance is given by:

$$F_{1,u} = \frac{M_u \cdot (32n - 2d_w)}{8mn - (m+n) \cdot d_w} \quad (5.50)$$

This expression provides the ordinates of the other three points of the quadrilinear curve, if specialized for moments corresponding to the attainment of the limit curvatures: χ_y , χ_h , χ_m .

Displacements corresponding to the four points of the quadrilinear force-displacement curve can be obtained by integrating curvatures along T-stub flange. Displacement corresponding to first yielding can be calculated on the base of the expression for the initial stiffness obtained by Piluso et al.:

$$K = 0,5E \frac{b'_{eff} t_f^3}{m^3} \quad (5.51)$$

Where b'_{eff} is equal to:

$$b'_{eff} = 2m + d_h < b \quad (5.52)$$

displacement at elastic limit is obtained as:

$$\delta_y = 2 \frac{F_y}{K} + \delta_{b,y} \quad (5.53)$$

where $\delta_{b,y}$ is the bolt elongation given by:

$$\delta_{b,y} = \frac{B}{EA_b/L_b} = \frac{\frac{F_y}{2} + \frac{M_y}{n}}{EA_b/L_b} \quad (5.54)$$

and L_b is the bolt conventional length:

$$L_b = 2t_f + 2t_{wh} + \frac{t_{bh} + t_n}{2} \quad (5.55)$$

where t_{wf} is the thickness of the washer, t_{bh} is the thickness of the bolt head and t_n is the thickness of the nut.

Displacement corresponding to force F_h , i.e. to the beginning of strain-hardening phase is computed as sum of the elastic and plastic part:

$$\delta_h = \delta_{eh} + 2\delta_{ph} \quad (5.56)$$

where δ_{eh} is evaluated as:

$$\delta_{eh} = \frac{F_h}{K_i} \quad (5.57)$$

and δ_{ph} is the plastic part of the displacement of a single T element, which can be obtained by means of function $D(\xi)$ defined starting from integration of curvatures:

$$D(\xi) = \varepsilon_y \left[2 \frac{\chi_\xi}{\chi_y} - \frac{1}{\xi} \frac{M_y}{M_u} \left(3 \frac{\chi_\xi}{\chi_y} + \frac{\chi_y}{\chi_\xi} - 3 \right) - 1 \right] \quad (5.58)$$

$$\delta_{ph} = \frac{m^2}{2t_f} D(\xi_2) \quad (5.59)$$

where $D(\xi_2)$ is the value of function for $\xi_2 = \frac{M_h}{M_u}$ and $\chi_\xi = \chi_h$.

Displacement δ_m can be obtained in the same way. In this case:

$$\delta_m = \delta_{em} + 2\delta_{pm} \quad (5.60)$$

where the elastic part is expressed by:

$$\delta_{em} = \frac{F_m}{K_i} \quad (5.61)$$

while the plastic part is given by:

$$F(\xi) = \varepsilon_y \left[2 \frac{\chi_\xi}{\chi_y} - \frac{1}{\xi} \frac{M_y}{M_u} \left(3 \frac{\chi_\xi}{\chi_y} + \frac{\chi_y}{\chi_\xi} - 3 + \frac{E_h}{E} \frac{(\chi_\xi - \chi_h)^2}{\chi_\xi \chi_y^2} \right) - 1 \right] \quad (5.62)$$

$$\delta_{pm} = \frac{m^2}{2t_f} F(\xi_3) \quad (5.63)$$

where $F(\xi_3)$ is the value of the function in correspondence of $\xi_3 = \frac{M_m}{M_u}$ and

$$\chi_\xi = \chi_m.$$

Finally, ultimate displacement can be obtained from:

$$\delta_u = \delta_{eu} + 2\delta_{pu} \quad (5.64)$$

where the elastic part is given by:

$$\delta_{eu} = \frac{F_u}{K_i} \quad (5.65)$$

and the plastic part is calculated by means of the following relationship:

$$C = 2 \left\{ \bar{\varepsilon}_u - \frac{1}{2(M_u/M_y)} \left(3\bar{\varepsilon}_u + \frac{1}{\bar{\varepsilon}_u} - 3 + \frac{E_h}{E} C_h + \frac{E_u}{E} C_u \right) - \frac{1}{2} \right\} \varepsilon_y \quad (5.66)$$

$$C_h = \frac{\bar{\varepsilon}_m^3}{\bar{\varepsilon}_u} + 3\bar{\varepsilon}_m \bar{\varepsilon}_u - 3\bar{\varepsilon}_m^2 + 3\bar{\varepsilon}_h^2 - 3\bar{\varepsilon}_h \bar{\varepsilon}_m - \frac{\bar{\varepsilon}_h^3}{\bar{\varepsilon}_u} \quad (5.67)$$

$$C_u = \bar{\varepsilon}_u^2 - 3\bar{\varepsilon}_m \bar{\varepsilon}_u + 3\bar{\varepsilon}_m^2 - \frac{\bar{\varepsilon}_m^3}{\bar{\varepsilon}_u} \quad (5.68)$$

$$\delta_{pu} = \frac{m^2}{2t_f} C \quad (5.69)$$

It is important to observe that parameters $D(\xi_2)$, $F(\xi_3)$ and C depend only on the material properties.

Mechanism type 2

Mechanism type 2 is verified for values of $\frac{2\lambda}{1+2\lambda} < \beta_u < 2$. In this case T-stub ultimate resistance can be expressed through M_u and parameter ξ .

$$F_{u,2} = \frac{2M_u}{m}(1 + \xi) \quad (5.70)$$

where:

$$\xi = \frac{(2 - \beta_u)\lambda}{\beta_u(1 + \lambda)} \quad (5.71)$$

Assuming that the point of zero moment remains unchanged during the loading process, expression (5.70) evaluated for the bending moments corresponding to curvatures χ_y , χ_h , χ_m provides ordinates of the T-stub quadrilinear force-displacement curve. Concerning displacement corresponding to the elastic limit, Eq.(5.65) can be applied also in this case, but bolt contribution has to be computed as:

$$\delta_{b,y} = \frac{B}{EA_b/L_b} = \frac{\frac{F_y}{2} + \frac{\xi M_y}{n}}{EA_b/L_b} \quad (5.72)$$

Second point, corresponding to the strain-hardening condition, can be obtained by the difference of the two plastic rotations ϑ_{p1} and ϑ_{p2} . Integration of curvatures gives:

$$\vartheta_{p1h} = \frac{m}{t_f(1+\xi)} D(\xi_2) \quad (5.73)$$

$$\text{If } \xi_2^* < \xi_1 \quad \vartheta_{p2h} = 0$$

$$\text{If } \xi_2^* > \xi_1 \quad \vartheta_{p2h} = \frac{m}{t_f} \left(\frac{\xi}{1+\xi} + \lambda \right) D(\xi_2^*)$$

where is $D(\xi_2^*)$ expressed by means of function (5.58) with $\xi_2^* = \xi \frac{M_h}{M_u}$ and χ_ξ equal to the curvature corresponding to bending moment $\xi_2^* M_u$.

By means of obtained rotations plastic displacement δ_{ph} is computed as:

$$\text{if } \vartheta_{p1h} > \vartheta_{p2h} \quad \delta_{ph} = \vartheta_{p1h} (n+m) - \vartheta_{p2h} n \quad (5.74)$$

$$\text{if } \vartheta_{p1h} < \vartheta_{p2h} \quad \delta_{ph} = \vartheta_{p2h} n \quad (5.75)$$

Concerning displacement δ_m corresponding to the attainment of force F_m , same steps followed to compute displacement δ_h can be applied.

$$\vartheta_{p1m} = \frac{m}{t_f(1+\xi)} F(\xi_3) \quad (5.76)$$

$$\text{if } \xi_3^* < \xi_1 \quad \vartheta_{p2m} = 0 \quad (5.77)$$

$$\text{if } \xi_1 < \xi_3^* < \xi_2 \quad \vartheta_{p2m} = \frac{m}{t_f} \left(\frac{\xi}{1+\xi} + \lambda \right) D(\xi_2^*) \quad (5.78)$$

$$\text{if } \xi_2 < \xi_3^* < \xi_3 \quad \vartheta_{p2m} = \frac{m}{t_f} \left(\frac{\xi}{1+\xi} + \lambda \right) F(\xi_3^*) \quad (5.79)$$

Even in this case $D(\xi_3^*)$ and $F(\xi_3^*)$ are values of functions (5.58)-(5.62)

evaluated in correspondence of $\xi_3^* = \xi \frac{M_m}{M_u}$ and χ_ξ , which is the curvature

relative to moment $\xi_3^* M_u$. With the same procedure previously applied results:

$$\text{if } \vartheta_{p1m} > \vartheta_{p2m} \quad \delta_{pm} = \vartheta_{p1m}(n+m) - \vartheta_{p2m}n \quad (5.80)$$

$$\text{if } \vartheta_{p1m} < \vartheta_{p2m} \quad \delta_{pm} = \vartheta_{p1m}m \quad (5.81)$$

As a conclusion ultimate displacement can be computed applying (5.63),

where plastic rotation ϑ_{p1u} is obtained by means of:

$$\vartheta_{p1u} = \frac{m}{t_f(1+\xi)} C \quad (5.82)$$

Rotation in the zone between bolt axis and the free edge depends on the corresponding value of bending moment ξM_u identified on the base of the following four cases:

$$\text{if } \xi < \xi_1 \quad \vartheta_{p2u} = 0 \quad (5.83)$$

$$\text{if } \xi_1 < \xi < \xi_2 \quad \vartheta_{p2u} = \frac{m}{t_f} \left(\frac{\xi}{1+\xi} + \lambda \right) D(\xi) \quad (5.84)$$

$$\text{if } \xi_2 < \xi < \xi_3 \quad \vartheta_{p2u} = \frac{m}{t_f} \left(\frac{\xi}{1+\xi} + \lambda \right) F(\xi) \quad (5.85)$$

$$\text{if } \xi_3 < \xi < \xi_1 \quad \vartheta_{p2u} = \frac{m}{t_f} \left(\frac{\xi}{1+\xi} + \lambda \right) G(\xi) \quad (5.86)$$

Where function $G(\xi)$ is defined as:

$$G(\xi) = \varepsilon_y \left\{ 2 \frac{\chi_\xi}{\chi_y} - \frac{1}{\xi} \frac{M_y}{M_u} \left[3 \frac{\chi_\xi}{\chi_y} + \frac{\chi_y}{\chi_\xi} - 3 + \frac{E_h}{E} G_h + \frac{E_u}{E} G_u \right] - 1 \right\} \quad (5.87)$$

$$G_h = \frac{\chi_m^3}{\chi_\xi \chi_y^2} + 3 \frac{\chi_m \chi_\xi}{\chi_y^2} - 3 \frac{\chi_m^2}{\chi_y^2} + 3 \frac{\chi_h^2}{\chi_y^2} - 3 \frac{\chi_h \chi_\xi}{\chi_y^2} - \frac{\chi_h^3}{\chi_\xi \chi_y^2} \quad (5.88)$$

$$G_u = \frac{\chi_\xi^2}{\chi_y^2} + 3 \frac{\chi_m^2}{\chi_y^2} - 3 \frac{\chi_m \chi_\xi}{\chi_y^2} - \frac{\chi_m^3}{\chi_\xi \chi_y^2} \quad (5.89)$$

Hence:

$$\text{if } \vartheta_{p1u} > \vartheta_{p2u} \quad \delta_{pu} = \vartheta_{p1u}(n+m) - \vartheta_{p2u}n \quad (5.90)$$

$$\text{if } \vartheta_{p1u} < \vartheta_{p2u} \quad \delta_{pu} = \vartheta_{p1u}m \quad (5.91)$$

Mechanism type 3

In this case, formulation is analogous to that of mechanism type 1. Main difference is that T-stub rotation is given by Eq.(5.84), where in this case coefficient is:

$$\delta_p = \vartheta_p m \quad (5.92)$$

$$\xi = \frac{M}{M_u} = \frac{B_u m}{M_u} = \frac{2}{\beta_u} \quad (5.93)$$

Expressions previously obtained for sake of clarity are here recalled.

$$\delta_y = \frac{F_y}{K} \quad (5.94)$$

$$\delta_h = \frac{F_h}{K} + \frac{m^2}{t_f} D(\xi_2) \quad (5.95)$$

$$\delta_m = \frac{F_m}{K} + \frac{m^2}{t_f} F(\xi_3) \quad (5.96)$$

$$\delta_u = \frac{F_u}{K} + \frac{m^2}{t_f} G(\xi) \quad (5.97)$$

5.2.1.2 Dissipative T-stubs – Proposed Model

As above said, the most dissipative failure mechanism (type 1 mechanism) arises in case of strong bolt and weak flange. It is characterized by the formation of four plastic hinges in the T-stub flanges, two in correspondence of the bolts axes due to the bending moment caused by the prying force, and two located at the sections corresponding to the flange-to-web connection (Fig. 5.21).

In this case, the bending moment diagram along the flange of the T-stub is linear throughout the entire process of loading with two equal values of the moment at the section where the plastic hinges arise. It is clear that the classic rectangular shape of the T-stub flange does not allow to engage the whole plate in plastic range because it yields only in the most stressed parts, i.e. the plastic hinge zones, confining the plastic deformations in finite regions. Therefore, the resulting curvature and strain demand is extremely high. In order to increase the energy dissipation capacity of T-stub connections, it is easy to understand that an ideal X-shaped element subjected to a linear

bending moment diagram yields along the whole plate extension providing plastic deformation and strain demand over the plate length (Fig. 5.29).

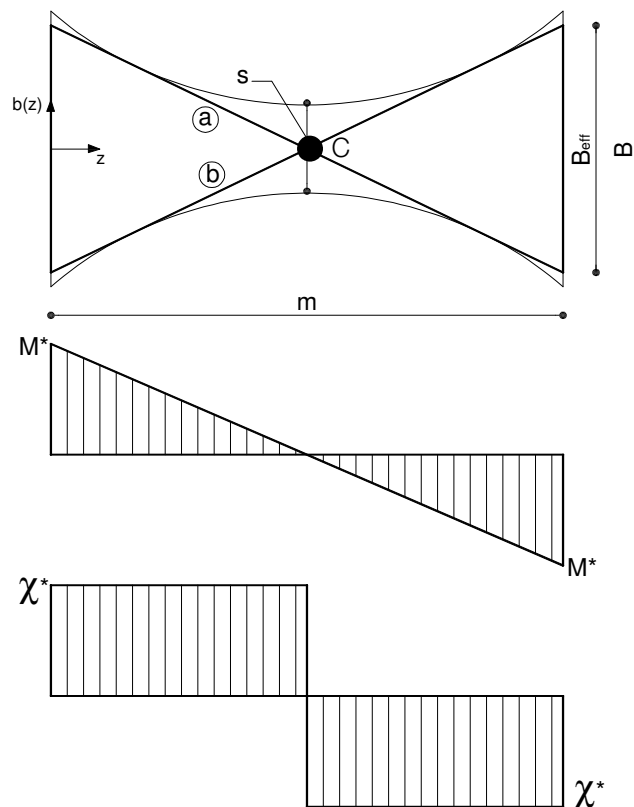


Fig. 5.29 – Definition of geometry, curvature and bending moment diagrams

This approach is mainly followed in the design of steel hysteretic dampers working in double curvature such as ADAS devices, which are elements usually adopted in combination with chevron bracing systems (Fig. 5.14). The

shape of ADAS devices must differ from the ideal X shape, first of all because a proper dimension of the mid-section of the element is required to withstand axial and shear actions. In fact, in the modeling of such a kind of metallic dampers two effects should be considered: the moment-shear interaction and the catenary effects due to geometric non linearity. In particular, the latter effect, at high displacements, can lead to significant axial stresses in the plate and, as a consequence, to a reduction of the ductility supply.

For this reason, usually ADAS devices are characterized by the so-called "hourglass shape", whose geometry is defined by means of an exponential function. The mathematical formulations describing the ADAS devices shape have been empirically determined by (Tena-Colunga, 1997) starting from the results of tests carried out at the University of Berkeley by (Whittaker et al., 1989). With reference to the notation of Fig. 2, the hourglass shape is described by the following exponential function (Tena-Colunga, 1997):

$$\begin{cases} b(z) = Be^{-\alpha z} & 0 \leq z \leq m/2 \\ b(z) = s \cdot e^{\alpha(z-m/2)} & m/2 \leq z \leq m \end{cases} \quad (5.98)$$

$$\alpha = \frac{2}{m} \ln\left(\frac{B}{s}\right) \quad (5.99)$$

where s is the width of the mid-section, B is the width of the clamped section and m is the distance between the sections stressed by the maximum level of bending moment which, in the case of T-stub, is represented by the distance between the bolt axis and the section corresponding to the flange-to-web fillet Fig. 5.21. This distance can be assumed, according to Eurocode 3 (CEN,

2005b), as $m=d-0.8r$, where d is the distance between the bolt axis and the face of the T-stub web and r is the radius of the flange-to-web connection in the case of rolled T-stub or $r=a_c\sqrt{2}$ in the case of welded T-stub with a_c equal to the weld throat thickness.

In order to model the force-displacement curve of a device with an hourglass shape the prediction of stiffness, resistance and ductility is required. Such prediction, for the complexity of the hourglass shape, is untrivial in a closed form solution. Hence, generally, simplified models are assumed to predict both the elastic behavior (initial stiffness) and the inelastic behavior (resistance and ductility).

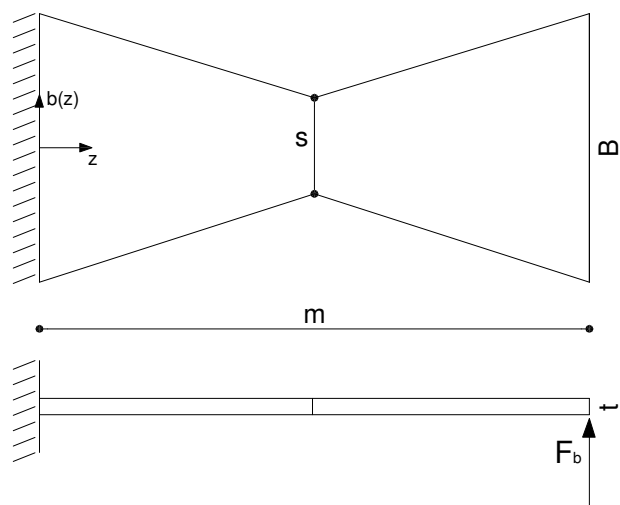


Fig. 5.30 – Simplified model for stiffness prediction

Regarding the elastic behavior, initial stiffness of the hourglass T-stub can be evaluated following the same approach provided in (Faella et al., 1998b), where the stiffness of the T-stub is determined by means of a mechanical approach based on an equivalent cantilever model. In particular, taking into account the width of the mid-section necessary to withstand the axial and shear actions, a simplified trapezoidal model has been adopted for the hourglass shape of the T-stub.

In order to determine the stiffness of the trapezoidal element, the scheme given in Fig. 5.30 loaded by a unitary force has been considered. In this scheme, deflection at the free-end is equal to the deformability of the element and, therefore, its inverse represents the stiffness. As far as the unknown is the displacement at the free-end, Mohr Theorem has been applied. To apply Mohr approach it is preliminary necessary to evaluate moment and curvatures on the actual scheme given in Fig. 5.30 loaded by a unitary force.

It is well known that curvature is given by the ratio between bending moment and flexural stiffness. As far as flexural stiffness depends on the width of the element, which varies along the element length, it is preliminary necessary to describe the variation law of the plate width. In particular, the shape of the device can be described through the following two expressions relative to the linear segments starting respectively from zero to the mid-section and from the mid-section to the free-end:

$$0 < z < m / 2 \quad B_1(z) = B + \frac{2(s - B)}{m} z \quad (5.100)$$

$$m/2 < z < m \quad B_2(z) = (2s - B) - \frac{2(s - B)}{m} z \quad (5.101)$$

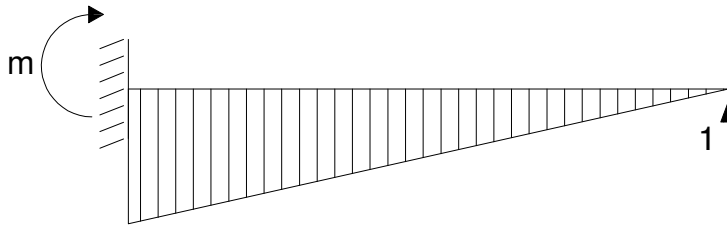


Fig. 5.31 – Moment on the cantilever

In case of cantilever beam loaded by a unitary force, bending moment diagram is described through (Fig. 5.31):

$$M(z) = (m - z) \quad (5.102)$$

from Eqs.(5.100)-(5.102) it is possible to evaluate the curvatures in the two segments:

$$0 < z < m/2 \quad \chi_1(z) = \frac{12}{Et^3} \left[\frac{(m - z)}{B - \frac{2(B - s)}{m} z} \right] \quad (5.103)$$

$$m/2 < z < m \quad \chi_2(z) = \frac{12}{Et^3} \left[\frac{(m-z)}{2s-B + \frac{2(B-s)}{m}z} \right] \quad (5.104)$$

On the base of Mohr's Theorem, deflection under the unitary force, which represents the deformability of the element, is equal to the moment at the clamped section of the fictitious scheme of Fig. 5.32. In such a scheme, clamped section and free-end are inverted and the cantilever beam is subjected to a load equal to the inverse of the curvatures. Aiming to determine this moment it is necessary to calculate resultant forces R_1 and R_2 and the position of their barycenter y_1 and y_2 .

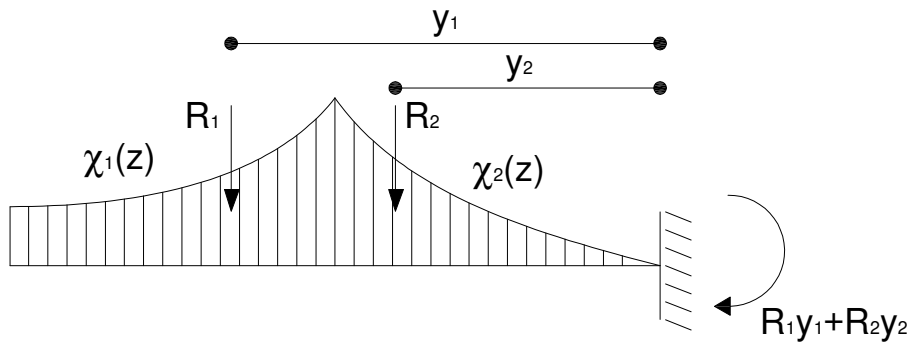


Fig. 5.32 – Diagram of Curvatures in the fictitious scheme

From Eqs.(5.103)-(5.104)resultants R_1 and R_2 are equal to the integral of the curvatures.

$$R_1 = \int_0^{m/2} \chi_1(z) dz \quad (5.105)$$

$$R_2 = \int_{m/2}^m \chi_2(z) dz \quad (5.106)$$

Eqs. (5.103)-(5.106)yield:

$$\begin{aligned} R_1 &= \frac{12}{Et^3} \frac{m^2 \left[(B-s) + (B-2s) \ln \left| \frac{B}{s} \right| \right]}{4(B-s)^2} = \\ &= \frac{3m^2}{E(B-s)^2 t^3} \left[(B-s) + (B-2s) \ln \left| \frac{B}{s} \right| \right] = \frac{3m^2}{E(B-s)^2 t^3} A_1 \end{aligned} \quad (5.107)$$

$$\begin{aligned} R_2 &= \frac{12}{Et^3} \frac{m^2 \left[s - B + B \ln \left| \frac{B}{s} \right| \right]}{4(B-s)^2} = \\ &= \frac{3m^2}{E(B-s)^2 t^3} \left[s - B + B \ln \left| \frac{B}{s} \right| \right] = \frac{3m^2}{E(B-s)^2 t^3} A_2 \end{aligned} \quad (5.108)$$

Barycenter of the two resultant forces R_1 and R_2 can be evaluated through the knowledge of the ratio between the first moment of area and the resultant. Expressions of the statical moments of area calculated with respect to the free-end of the fictitious scheme are given by:

$$\begin{aligned}
S_1 &= \int_0^{m/2} \chi_1(z) \cdot z \, dz = \frac{12}{Et^3} \frac{m^3 \left[(3s - B)(B - s) + 2B(B - 2s) \ln \left| \frac{B}{s} \right| \right]}{16(B - s)^3} \\
&= \frac{3m^3}{4E(B - s)^3 t^3} \left[(3s - B)(B - s) + 2B(B - 2s) \ln \left| \frac{B}{s} \right| \right] = \quad (5.109) \\
&= \frac{3m^3}{4E(B - s)^3 t^3} A_3
\end{aligned}$$

$$\begin{aligned}
S_2 &= \int_{m/2}^m \chi_2(z) \cdot z \, dz = \frac{12}{Et^3} \frac{m^3 \left[(3s - B)(B - s) + 2B(B - 2s) \ln \left| \frac{B}{s} \right| \right]}{16(B - s)^3} \\
&= \frac{3m^3}{4E(B - s)^3 t^3} \left[(3s - B)(B - s) + 2B(B - 2s) \ln \left| \frac{B}{s} \right| \right] = \quad (5.110) \\
&= \frac{3m^3}{4E(B - s)^3 t^3} A_3
\end{aligned}$$

Consequently, the position of the barycenter of the two resultant forces with respect to the clamped section of the fictitious scheme can be expressed as:

$$y_1 = \frac{R_1}{m - \frac{S_1}{R_1}} = m \left[1 - \frac{A_3}{4A_1(A_3 - s)} \right] \quad (5.111)$$

$$y_2 = \frac{R_1}{m - \frac{S_1}{R_1}} = m \left[1 - \frac{A_3}{4A_2(A_3 - s)} \right] \quad (5.112)$$

Finally deflection at the free-end of the cantilever beam defined in Fig. 5.30 is given by:

$$\delta = R_1 y_1 + R_2 y_2 = \frac{3m^3}{4E(B-s)t^3} \left[\frac{A_1}{(B-s)} + \frac{A_2}{(B-s)} - \frac{2A_3}{4(B-s)^2} \right] \quad (5.113)$$

On the base of the obtained results, considering that the force acting in the bolt of a simple T-stub with two bolts is equal to $F/2$, the initial stiffness of the Hourglass T-stub ($K_{0,HS}$) has been determined and expressed by means of a formulation formally coincident with that of a simple rectangular T-stub. In particular, the following relationship has been obtained, where ζ is a factor depending on the ratio between the width at the mid-section (s) and the width at the clamped section (B), and t is the thickness of the plate:

$$K_{0,HS} = \zeta \frac{EBt^3}{m^3} \quad (5.114)$$

where:

$$\left\{ \begin{array}{l} \zeta = \frac{2(B-s)}{3B} \frac{4(B-s)^2}{4(B-s)A_1 + 4(B-s)A_2 - 2A_3} \\ A_1 = [(B-s) + (B-2s)\ln(B/s)] \\ A_2 = [(s-B) + B\ln(B/s)] \\ A_3 = [(3s-B)(B-s) + 2B(B-2s)\ln(B/s)] \end{array} \right. \quad (5.115)$$

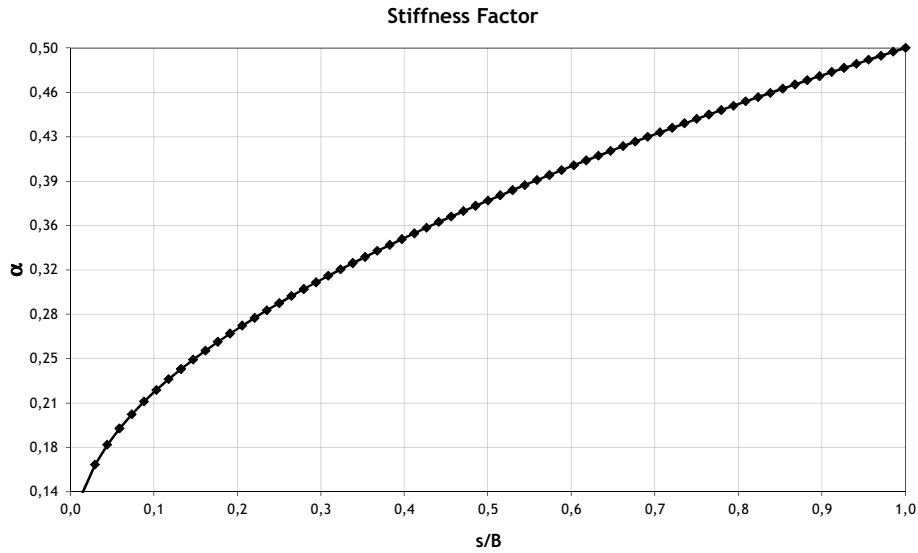


Fig. 5.33 – Correlation between ζ factor and the ratio s/B

The value of ζ corresponding to $s/B=1$ provides the well-known solution $\zeta = 0.5$ available for the T-stub with rectangular flange. Besides, considering s/B ratios adopted in tests of Whittaker et al. (1989), which vary from 0.1 to 0.2, the value of ζ ranges between 0.22 and 0.27 according to the non-linear law

given in Fig. 5.33. Therefore, for design purposes, the average value $\zeta = 0.25$ can be adopted.

Bolt pretension effects on the initial stiffness of the hourglass T-stub have been modeled according to the approach given in (Faella et al., 1998b). In particular, in this approach the influence of the preloading level on the degree of flexural constraint exhibited by the bolts is accounted for. In fact, in case of very thick plates, the bolts are not able to prevent the detachment of the connected flanges and, therefore, the bolt restraining action can be modeled as simple supports located at the bolts axis. In the case of very thin T-stub flanges, the bolt preloading prevents the detachment of the plates at the edge line of the bolt head. In such a case, bolts can be considered as clamps. In intermediate cases, the location of the prying forces moves away from the axis of bolt as the plate thickness-to-bolt diameter ratio increases. Restraining action of the bolts depends, in these cases, on their axial and flexural stiffness. It is clear that the actual behavior is intermediate between the two extreme cases. In the first case, stiffness of the T-stub can be evaluated by means of Eq.(5.114), in the second case, by means of the following:

$$K_{0,HS} = 4\zeta \frac{EBt^3}{\left(m - \frac{d_h}{2}\right)^3} \quad (5.116)$$

In all intermediate cases the two equations has to be replaced by an equation accounting for two effects: the variation of degree of restraint from 1 (simple

supports) to 4 (clamped sections), and the reduction of m due to the bolt head restraining action.

On the basis of the analysis of experimental data, in (Faella et al., 1998b) this effects have been considered by properly correcting the formulation of the initial stiffness by means of a coefficient ψ depending on the ratio between the flexural stiffness of the flanges and the bolt axial stiffness. Therefore, in the case of preloaded bolts, the stiffness of the hourglass T-stub can be computed by replacing Eq. (5.114) with the following relationship:

$$K_{0,HS} = \psi \zeta \frac{EBt^3}{m^3} \quad (5.117)$$

where ψ is given, in case of a preloading level equal to 80%, which is the value suggested for high strength bolts, by (Faella et al., 1998b):

$$\psi = 0.57 \left(\frac{t}{d_b \sqrt{m/d_b}} \right)^{-1.28} \quad (5.118)$$

with d_b equal to the bolt diameter.

Regarding the inelastic behaviour of the Hourglass T-stub, the prediction of the whole monotonic force-deflection curve can be performed by increasing step-by-step the bending moment level on the T-stub and assuming that the point of zero moment remains during the loading process located at the middle section between the bolt axis and the flange-to-web connection, according to the

$$B_1(z) = Be^{-\alpha z} \quad (5.119)$$

$$B_2(z) = B_{eff} - \frac{2B_{eff}}{m} z \quad (5.120)$$

By deriving the last two relationships, the following are obtained:

$$B'_1(z) = -\alpha Be^{-\alpha z} \quad (5.121)$$

$$B'_2(z) = \frac{2B_{eff}}{m} \quad (5.122)$$

since in tangent point, the slope of the bi-triangular X-shape has to be equal to the slope of the hourglass shape it is possible to determine the value of abscissa z^* defined in Fig. 5.34.

$$B'_1(z) = B'_2(z) \quad (5.123)$$

as a result:

$$\alpha Be^{-\alpha z^*} = \frac{2B_{eff}}{m} \quad (5.124)$$

which leads to:

$$z^* = -\frac{1}{\alpha} \ln\left(\frac{2B_{eff}}{\alpha m B}\right) \quad (5.125)$$

Thus, by the knowledge of abscissa z^* it is possible to determine the expression of the effective width. By imposing, for the linearity of the bi-triangular X-shape, that the ratio between the effective width and $m/2$ is equal to the ratio between the width $B_1(z)$ evaluated in correspondence of z^* and $m/2 - z^*$, comes:

$$\frac{2B_{eff}}{2m} = \frac{B_1(z^*)}{2\left(\frac{m}{2} - z^*\right)} \quad (5.126)$$

for sake of clarity, all analytical developments are given.

$$\frac{2B_{eff}}{m} \left[\frac{m}{2} + \frac{1}{\alpha} \ln\left(\frac{2B_{eff}}{\alpha B m}\right) \right] = \frac{1}{\alpha} \quad (5.127)$$

$$\frac{\alpha m}{2} + \ln\left(\frac{2B_{eff}}{\alpha B m}\right) = 1$$

$$\ln\left(\frac{2B_{eff}}{\alpha B m}\right) = 1 - \frac{\alpha m}{2}$$

$$\frac{2B_{eff}}{\alpha B m} = e^{(1-\frac{\alpha m}{2})}$$

$$B_{eff} = \frac{\alpha B m}{2} e^{(1-\frac{\alpha m}{2})} \quad (5.128)$$

By substituting Eq.(5.99) in (5.128) a further simplification is possible:

$$B_{eff} = B \cdot e \cdot \left(\frac{s}{B}\right) \cdot \ln\left(\frac{B}{s}\right) \quad (5.129)$$

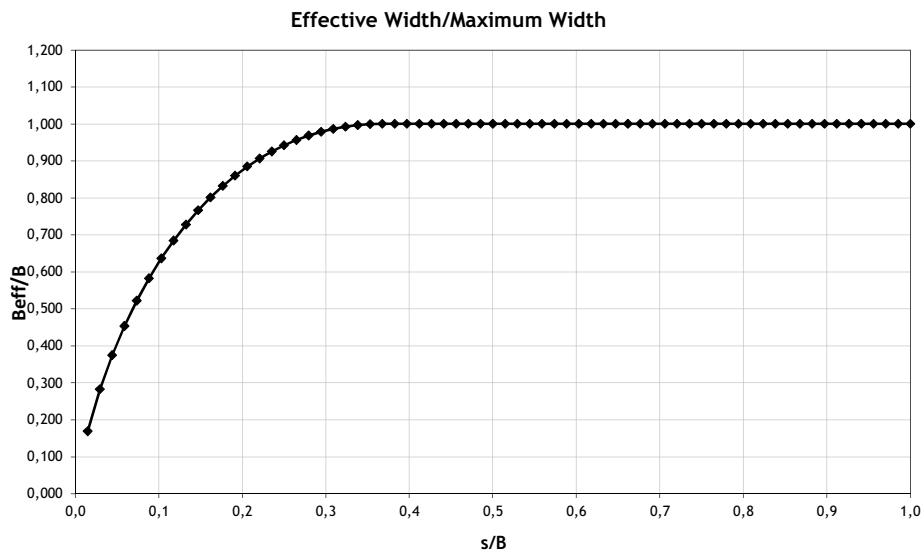


Fig. 5.35 – Ratio between effective and maximum plate width

It is worth note that the effective width depends only on some of the geometrical properties of the plate and in particular on the width at the mid-section and the maximum width. It can be interesting to determine the condition which leads to development of the maximum width, namely what is the optimum geometry which allows to obtain $B_{eff}=B$. Imposing this condition in Eq.(5.128) it is possible to find:

$$B = B \cdot e \cdot \left(\frac{s}{B}\right) \cdot \ln\left(\frac{B}{s}\right) \quad (5.130)$$

$$\ln\left(\frac{B}{s}\right) = \frac{B}{s \cdot e} \quad (5.131)$$

By deriving with respect to B/s on both sides derives:

$$\frac{s}{B} = \frac{1}{e} \quad (5.132)$$

Eq.(5.132) means that starting from a value of s/B equal to $1/e=0.368$ effective width is coincident with maximum width. For current values of s/B , as for example that used in Whittaker tests, effective width assumes values lower than the maximum plate width. In particular for $s/B=0.1$: $B_{eff}=0.636B$ and for $s/B=0.2$: $B_{eff}=0.884B$. A diagram of the ratio between effective and maximum plate width is depicted in Fig. 5.35.

The evaluation of the force-displacement curve is significantly simplified in the case of X-shaped T-stub because, assuming an ideal linear shape, for each assigned moment distribution the curvatures are constant along the plate (Fig. 5.29). Therefore, taking into account that the curvature χ_i corresponding to the i -th moment distribution can be expressed as a function of the strain ε_i of the extreme fiber ($\chi_i = 2\varepsilon_i/t$), the following expressions have been obtained:

$$\delta_i = \frac{F_i}{K_{0,HS}} \quad 0 \leq \delta \leq \delta_y \quad (5.133)$$

$$\delta_i = \frac{F_i}{K_{0,HS}} + \frac{(\varepsilon_i - \varepsilon_y)m^2}{t} \quad \delta_y \leq \delta \leq \delta_u \quad (5.134)$$

where F_i is the axial force acting on the T-stub which is defined, for a single T-stub with weak plate and strong bolts, by the following relation (Fig. 5.21):

$$F_i = \frac{4M_i}{m} \quad (5.135)$$

and ε_y is the yielding strain of the steel, δ_y is the displacement corresponding to the first yielding given by (5.133) with $F_i = F_y$ and δ_u is given by (5.134) for ε_i equal to the steel ultimate strain ε_u . F_y is given by:

$$F_y = \frac{4M_y}{m} = \frac{2}{3} \cdot \frac{B_{eff} t^2 f_y}{m} \quad (5.136)$$

Eqs. (5.133), (5.134) and (5.135) allow to predict the whole inelastic branch of the F - δ curve of the hourglass T-stub up to failure.

5.2.2 Experimental Behavior under Cyclic Loads

In order to verify the benefits provided by the proposed device in terms of energy dissipation capacity, an experimental program on rectangular and hourglass T-stubs under monotonic and cyclic loading conditions has been performed (Fig. 5.36).

Concepts of ADAS devices has already been applied to beam-to-column connections by Fleischman & Hoskisson (2000), where modular connectors produced as cast piece were proposed and analyzed. In this work, in order to simplify the manufacturing of the dissipative T-stub, ADAS concept is applied manufacturing the hourglass shape, by means of flame cutting, that is the main and easiest method for cutting steel. This technique even though provides cut surface with striated structure and some burring, minimizing the additional processing costs for the construction of the dissipative T-stubs can lead to advantageous structural solutions due to the reduction of the global cost as already underlined in (Faella et al., 1998).

The design of the tested specimens has been performed by using both the mechanical model above described and the Finite Element model carried out in ABAQUS code. In particular, with reference to the mechanical models, Eqs. (3)-(11) have been used in the case of hourglass T-stub, while the Piluso et al. model (2001) has been applied for designing the rectangular T-stubs.

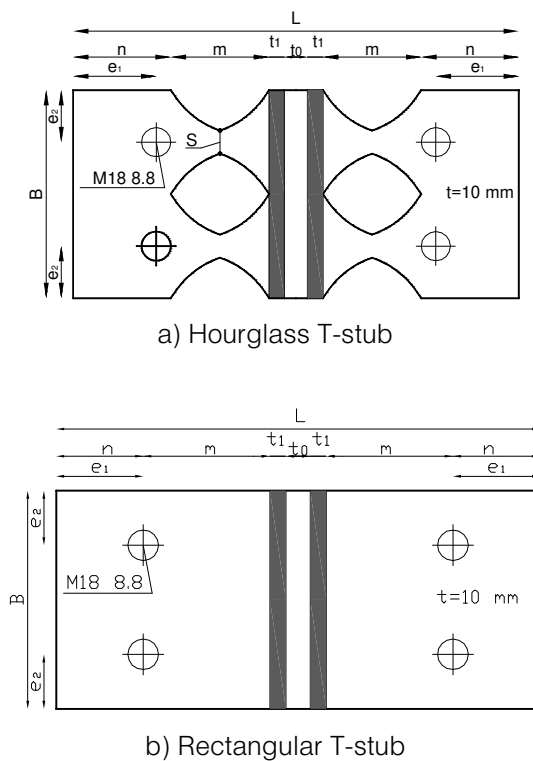


Fig. 5.36 – Typologies of Tested Specimens

Aiming to obtain a solid three-dimensional model the library element C3D8R, i.e. 8-node linear brick, with reduced integration and instability mesh control has been adopted. The choice of this type of element comes from the following considerations. First of all, aiming to reduce the computational effort, a first order element (linear brick) has been chosen, taking into account that, although second order element provide higher accuracy than the first order element, in presence of complicated phenomena, such as contacts and slips, the computational effort exponentially grow. In addition, in order to reduce the

processing time, a "reduced integration element", using a lower order integration to form the element stiffness, has been adopted. In case of eight node bricks, integration points are reduced from eight to one. In this way, element assembly is approximately eight times less costly compared to the case of full-integration elements. This choice do not reduce accuracy of the analysis provided that an instability mesh control is simultaneously applied.

Full integration elements may undergo shear and volumetric locking due to their numerical formulation, which gives rise to shear strains that do not really exist, while reduced integration elements can exhibit the mesh instability phenomena often known as hourglassing (Kosloff & Frazie, 1978). This is a special case of the phenomenon known in finite elements as kinematic modes or spurious zero-energy modes. Practically, since the elements have only one integration point, it is possible for them to distort in such a way that the strains calculated at the integration point are all zero which, in turn, leads to uncontrolled distortion of the mesh. In order to control this phenomenon the viscous approach of ABAQUS code has been employed in the FE modeling. The effects due to the axial stiffness of the plate and to the catenary actions arising at large displacements have been accounted for by means of a static non-linear analysis. The geometric non linearity has been properly accounted for to grasp the full post elastic behavior of tested T-stubs, which are characterized, at large displacements, by considerable second order effects. To this scope, the stiffness matrix is formulated considering the current configuration of the nodal position. Furthermore, in FE model, the interactions between the plates and between hole and bolt have been modeled by means of a frictionless formulation and the bolt pretension effect has been modeled by imposing, in a preliminary loading step, an appropriate thermal distortion.

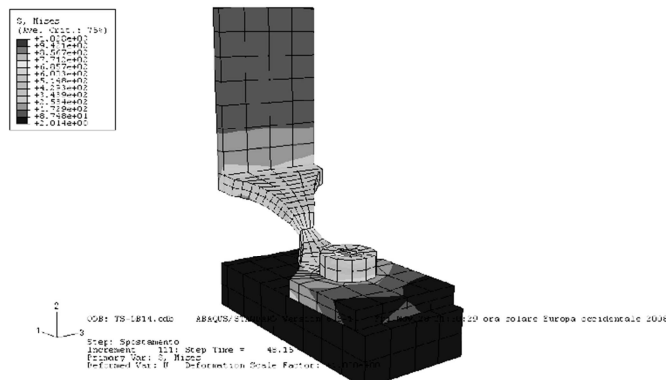


Fig. 5.37 – Finite Element Model

As already underlined, an experimental analysis has been planned to verify the possibility to increase the energy dissipation capacity under cyclic loads of T-stubs by adopting an hourglass shape. The purpose of the study has been comparative. In fact, basic idea was to show that rectangular and hourglass T-stubs can be properly designed in order to obtain the same monotonic force-displacement response, i.e. same stiffness and resistance, but different dissipative behaviors under cyclic loads.

To this goal, by applying a trial and error procedure the following design conditions have been imposed:

- the initial stiffness of the hourglass T-stub $K_{0,HS}$ is equal to that of the corresponding T-stub with rectangular flange;
- the energy dissipation capacity of the hourglass T-stub is maximized by properly cutting the T-stub flanges;
- the inelastic branch of the $F-\bar{\delta}$ curve of hourglass T-stub fits that of the corresponding rectangular T-stub up to its ultimate displacement.

In order to achieve the design goals, within the design process, the following three geometrical parameters have been considered: the distance m between the bolt and the plastic hinge, the width of the plate B , and the thickness of the plate t . These three parameters have been chosen as main design parameters because they strongly affect the T-stub overall behavior and, in particular, initial stiffness, resistance and the ductility. In fact, as already examined in (Faella et al., 2000), the initial stiffness is related to the ratio $(Bt^3)/m^3$, the plastic resistance corresponding to the knee of the force-displacement curve of the T-stub depends mainly on the parameter (Bt^2/m) and the ductility is governed by the parameter m^2/t . It is clear that the reduction of the section width along the plate due to the hourglass shape leads mainly to a reduction of the T-stub stiffness which can be recovered by increasing width B and thickness t and reducing the distance m . The simultaneous respect of the three previous design condition provided the most appropriate combination of values of the three geometrical design parameters.

The whole experimental program consists of 21 welded T-stub specimens, 11 with rectangular plates and 10 with hourglass plates. The elements have been connected through the flanges by means of four M18 bolts of 8.8 class (CEN, 2005b) with a preloading level equal to 80% of the yield stress. Two type of steel grade have been used: S275 and S355 (CEN, 2005a).

The specimens are divided into two series. The first one is constituted by twelve specimens which have been realized connecting the T-stubs to a rigid and strong flange. Four specimens have been tested under monotonic load and eight under constant amplitude cyclic loads. The second series is composed by nine specimens constituted by two equal T-elements. Also in this

case both monotonic tests (two specimens) and cyclic tests (seven specimens) have been performed.

The identity tag of the specimens allows to identify all the examined cases. After symbol TS, which is the abbreviation of T-Stub, the presence or absence of letter D (Double) differentiates specimens of the second series (Coupled T-stubs) from the elements of the first series (T-stubs on rigid support). Symbol –XS, which is the acronym of X-Shaped, identifies hourglass T-stubs. Finally, symbols –M or –C individuate, respectively, monotonic tests and cyclic tests. Moreover, with reference to cyclic tests, after letter C, constant cyclic amplitude is also specified. The values of the geometrical properties of the specimens are given in Table 5.1, with reference to symbols of Fig. 5.36.

The goal of cyclic tests under different constant amplitudes was the evaluation of the low cycle fatigue curves, in order to compare the dissipative capacities of the X-shaped elements with respect to the rectangular ones. The experimental tests were carried out at the Materials and Structures Laboratory of the Department of Civil Engineering of Salerno University. All the specimens were subjected to a tensile axial force, applied under displacement control to the webs by the jaws of the testing machine, a Schenck Hydropuls S56 (maximum test load 630 kN, piston stroke ± 125 mm). Monotonic tests were executed by applying the tensile load at speed of ± 0.01 mm/s. The same speed has been adopted in cyclic tests, which have been executed under displacement control adopting a triangular waveform. Each cyclic test is characterized by a sequence of tensile loading up to the cyclic displacement amplitude, unloading and compressive loading up to the zero displacement.

In addition, coupon tensile tests have been performed to establish the mechanical properties of the material. The values of the mechanical properties are given in Table 5.2.

Table 5.1 –Specimens' Geometry

Specimen	n [mm]	m [mm]	s [mm]	t [mm]	t ₁ [mm]	t ₀ [mm]	B [mm]	e ₁ [mm]	e ₂ [mm]
TS01	54	80.5	-	10	10	15	108	54	20
TS02	54	80.5	-	10	10	15	108	54	20
TS01-XS	63.5	63.9	15.1	10	10	15	136	54	34
TS02-XS	63.5	63.9	15.1	10	10	15	136	54	34
TSD	54	80.5	-	10	10	15	108	54	20
TSD-XS	63.5	63.9	15.1	10	10	15	136	54	34

Table 5.2 –Steel Mechanical Properties

Specimen	f _y [MPa]	f _u [MPa]	ε _y [%]	ε _h [%]	ε _m [%]	ε _u [%]
TS01	272	441	0.13	1.87	9.88	45.3
TS02	391	626	0.18	2.37	7.4	40.8
TS01-XS	282	490	0.13	1.72	17.6	52.2
TS02-XS	456	663	0.18	2.37	8.5	66.4

Specimen	f_y [MPa]	f_u [MPa]	ϵ_y [%]	ϵ_h [%]	ϵ_m [%]	ϵ_u [%]
TSD	272	441	0.13	1.87	9.88	45.3
TSD-XS	272	441	0.13	1.87	9.88	45.3

5.2.2.1 Monotonic Tests - T-stubs on rigid support

The experimental tests (Fig. 5.38 -Fig. 5.39) on T-stubs connected to rigid support evidenced a good reliability of the design procedure previously described.



Fig. 5.38 – Experimental test on hourglass T-stub on rigid Support

Monotonic tests show that the experimental curves of the hourglass T-stub are close to that of the rectangular ones (Fig. 5.40- Fig. 5.41). In addition, it can be observed that monotonic behavior is significantly influenced by the axial forces due to the presence of the rigid support which represents a shear constraint for the bolts. This effect is greatest in the case of T-stub connected to a very rigid support. In fact, during the loading process, T-stub deforms while the rigid support remains in elastic range, not exhibiting significant deformations. Therefore, in this case, shear actions on the bolt become prevalent and significant axial force arises in the fastened plate (Fig. 5.42a). On the contrary, in the case of two equal T-stubs connected through the flanges, during the loading process the bolt axes follows the flange deformation and therefore shear actions in bolts are negligible (Fig. 5.42b).



Fig. 5.39 – Experimental test on rectangular T-stub on rigid Support

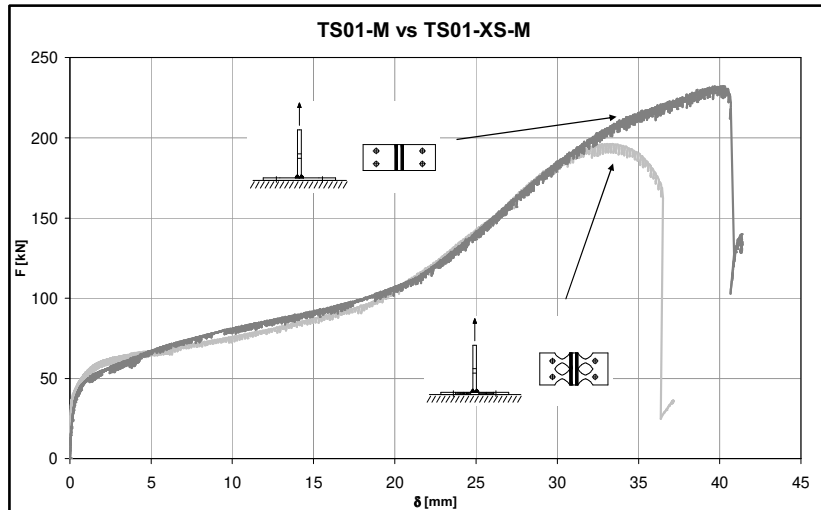


Fig. 5.40 – TS01-M vs TS01-XS-M: monotonic tests comparison

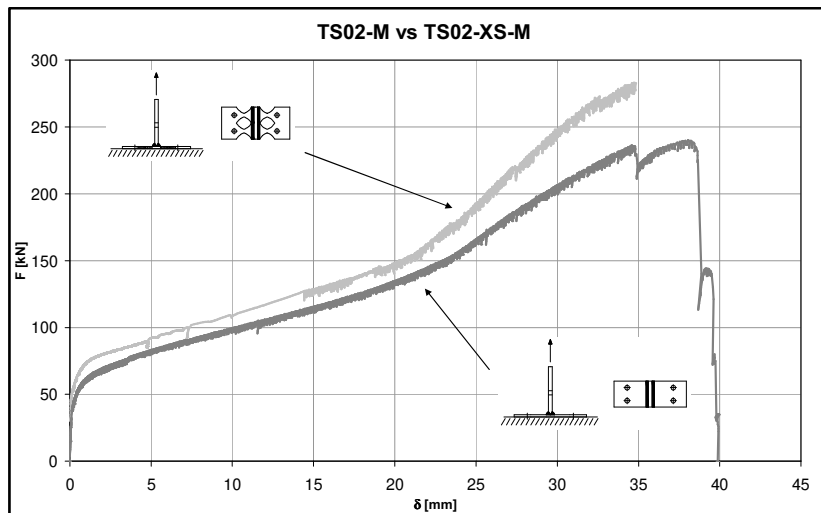


Fig. 5.41 – TS02-M vs TS02-XS-M: monotonic tests comparison

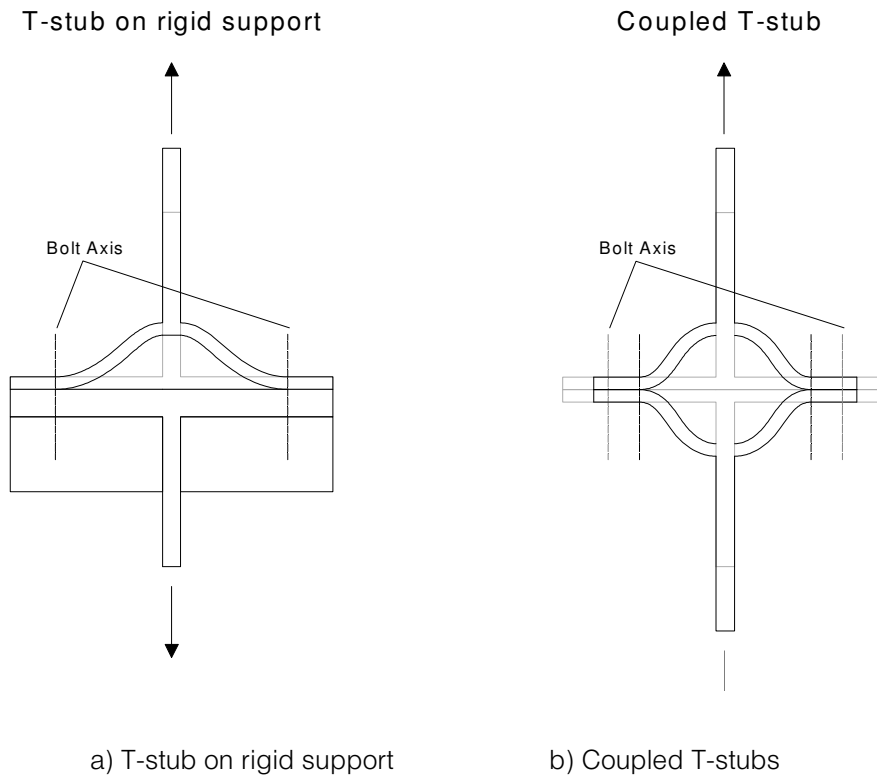


Fig. 5.42 – Deformed shape of T-stub on rigid support and Coupled T-stubs

Failure of specimens TS01-M, TS02-M, TS01-XS-M and TS02-XS-M was caused by axial stresses in the flange: in case of TS-M specimens bolt shear failure arose (Fig. 5.43) and in case of TS-XS-M specimens fracture of the hourglass mid-section occurred (Fig. 5.44). Fig. 5.45 - Fig. 5.46 show the comparisons between monotonic experimental curves and the predicted ones. As already underlined, prediction of the $F-\delta$ curve has been computed by means of the model proposed by Piluso et al. (2001), for rectangular T-stubs.

Conversely, the model derived in section 2 has been applied for the hourglass T-stub.

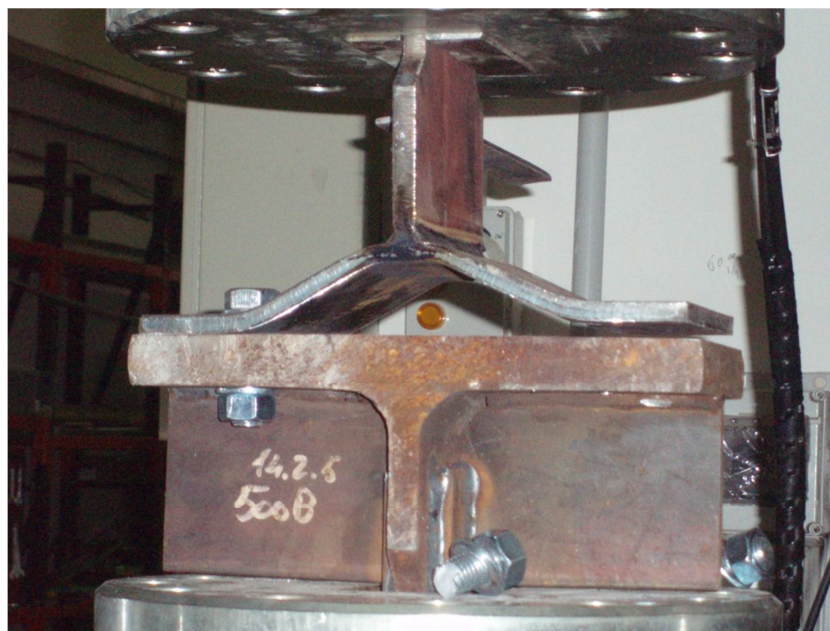


Fig. 5.43 – Typical failure of rectangular T-stubs on rigid support under monotonic loads

It can be observed that both the mechanical model and the FE model provide a very accurate prediction of the monotonic behavior either for rectangular T-stub and for hourglass T-stub. Regarding the mechanical model, as it does not account for the influence of second order effects, it results sufficiently accurate only up to the T-stub displacement corresponding to the hardening branch due to the second order effects. Nevertheless, such approximation does not represent a problem, because this displacement is greater than the displacement expected from a structural point of view. In fact, it can be

observed from Fig. 5.40-Fig. 5.41 that second order effects became important for T-stub displacement greater than 20 mm.

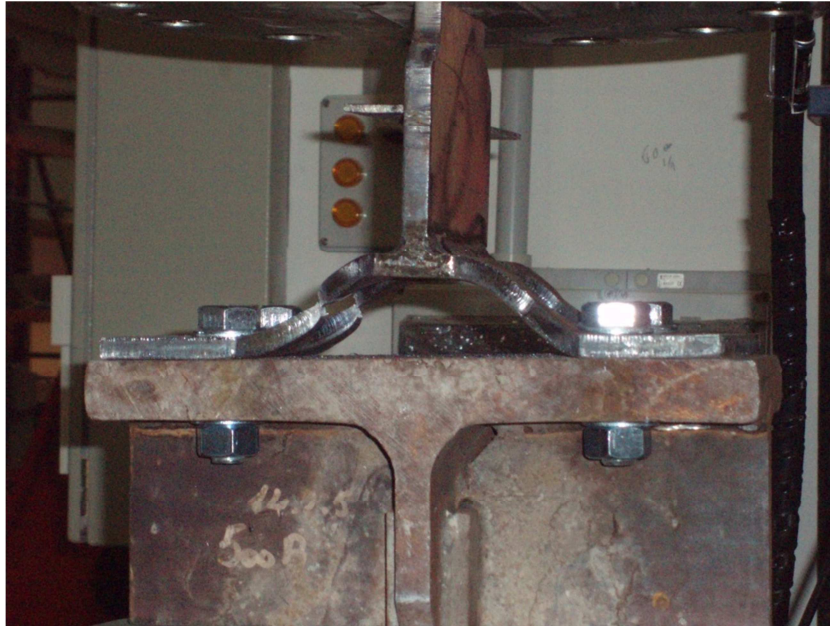


Fig. 5.44 – Typical failure of hourglass T-stubs on rigid support under monotonic loads

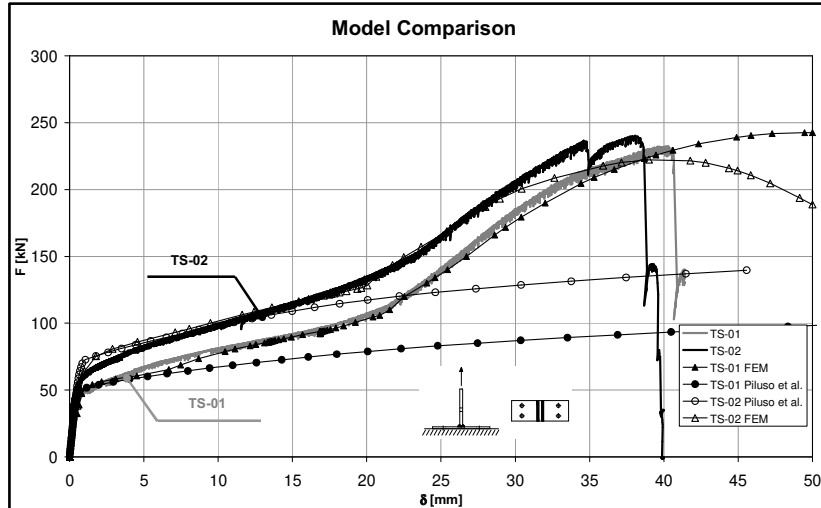


Fig. 5.45 – Rectangular T-stub – Model Comparison

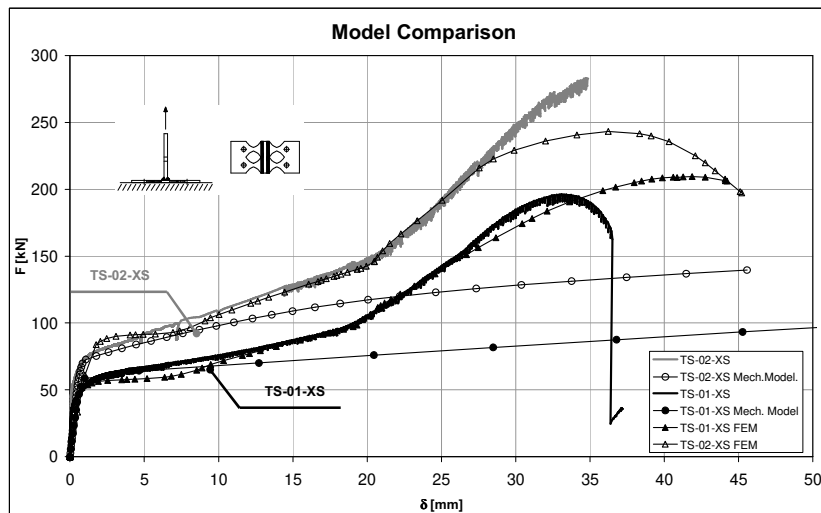


Fig. 5.46 – Hourglass T-stub – Model Comparison

If we consider the T-stub as the element connecting the beam to the column in correspondence of the upper and lower flange of the beam (Double Split Tee Connection), the T-stub displacement equal to 20 mm provides a beam rotation equal to 0.05 rad and 0.04 rad for a beam depth equal to 400 mm and 500 mm respectively. These values are greater than the structural demand of the joint rotation capacity required by the codes. In fact, with reference to the Near Collapse limit state, Vision 2000 Report (SEAOC, 1995) provides a mean value equal to 0.025 rad, while Eurocode 8 (CEN, 2005b), for High Ductility Class, requires a minimum value of the plastic rotation supply of connections equal to 0.035 rad.

5.2.2.2 Monotonic Tests - Coupled T-stubs

The experimental analysis on coupled rectangular T-stubs (Fig. 5.47) and hourglass T-stubs (Fig. 5.48) simulates the structural situation in which the thickness of the T-stub flange is similar to that of the support. Two monotonic tests TSD-M and TSD-XS-M have been performed on coupled T-stubs. The experimental results show a very ductile behavior (Fig. 5.49 - Fig. 5.50). The comparison between the experimental results on T-stubs on rigid support and on coupled T-stubs shows that the influence of the axial forces in coupled T-stubs is significantly reduced with respect to that of T-stub on rigid support both with reference to rectangular T-stubs and to hourglass T-stubs. It can be recognized that the displacement corresponding to the increase of the slope of the hardening branch in the case of coupled T-stub is about 40 mm, which is approximately equal to two times that of the T-stub on rigid support. This is

due, as already underlined, to the reduction of the shear restraining action exerted on T-stub bolts in the case of coupled T-stub.

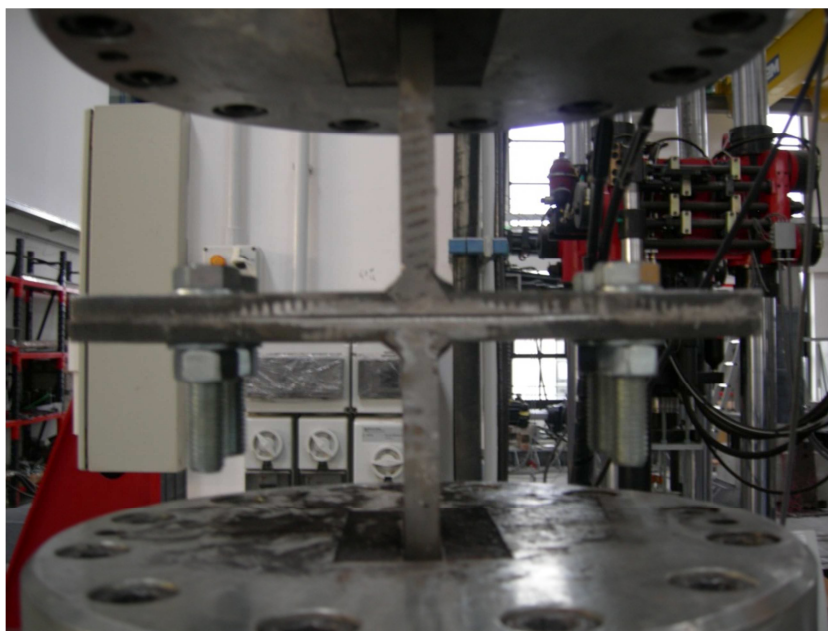


Fig. 5.47 – TSD series

In Fig. 5.49 - Fig. 5.50 the comparison between the Force-Displacement curves provided by the experimental tests and those obtained by means of mechanical modeling and FE models previously described is also shown. It can be observed, as already underlined with reference to T-stubs on rigid support, that the predictions provided by the mechanical models and FE model are very satisfactory and accurate in the range of interest.



Fig. 5.48 – TSD-XS series

In particular, it can be observed that the FE model is able to accurately predict the force-displacement curve also in the range of high displacements because it accounts for the geometrical non-linearity. Conversely, the mechanical models, neglecting the influence of axial stresses, cannot be applied to the high displacement range which, as already underlined in the case of T-stub on rigid support, is not significant from a structural point of view.

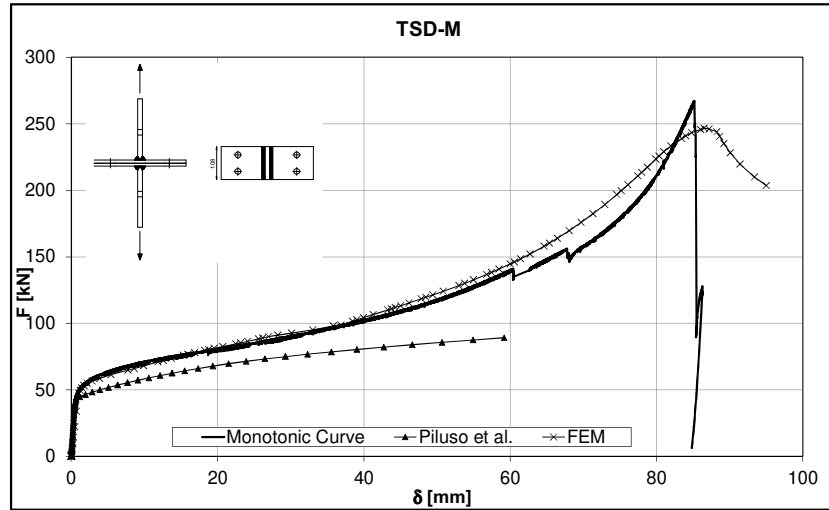


Fig. 5.49 – TSD test result and models comparison

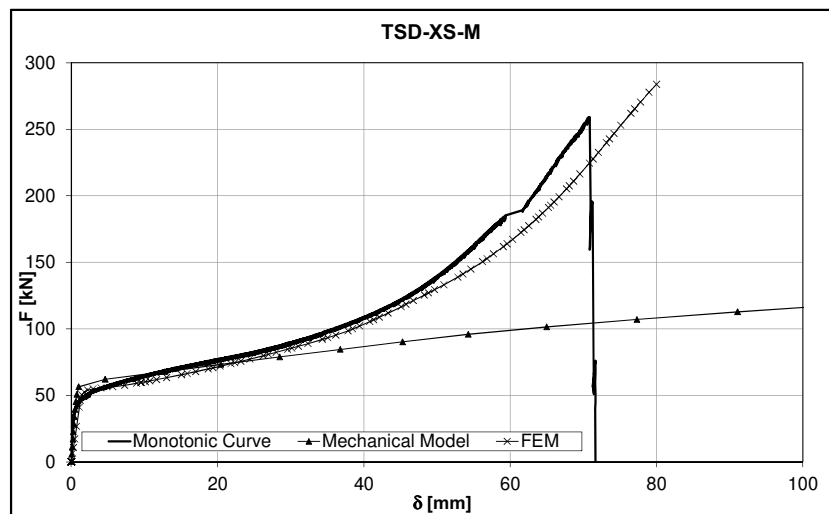


Fig. 5.50 – TSD-XS test results and model comparison



Fig. 5.51 – Typical failure of TSD specimens



Fig. 5.52 – Typical failure of TSD-XS specimens

5.2.2.3 Cyclic Tests – T-stubs on Rigid Support

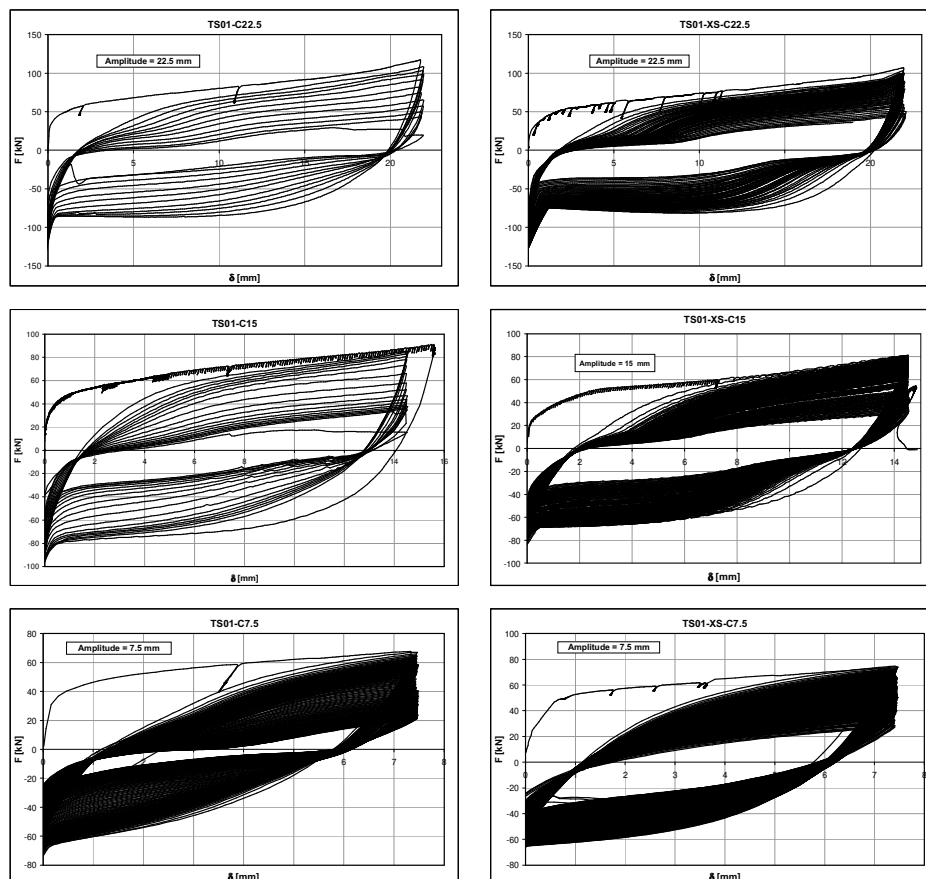


Fig. 5.53 – TS01-C and TS01-XS-C test results

Aiming to the analysis of low cycle fatigue, T-stubs have been subjected to constant amplitude cyclic tests. Regarding T-stub on rigid support, three cyclic tests under constant amplitude have been performed both for rectangular T-stub and for hourglass T-stub. The displacement amplitudes of the tests, equal for the three tests to 7.5, 15 and 22.5 mm (Fig. 5.53 - Fig. 5.54), have been

chosen aiming to cover a range of displacements significant for structural applications. In fact, as already underlined with reference to monotonic tests, the adopted maximum value of the T-stub displacement in cyclic tests equal to 22.5 mm leads to a joint rotation greater than the value of the rotation capacity required both by Vision 2000 Report (SEAOC, 1995) and by Eurocode 8 (CEN, 2005c).

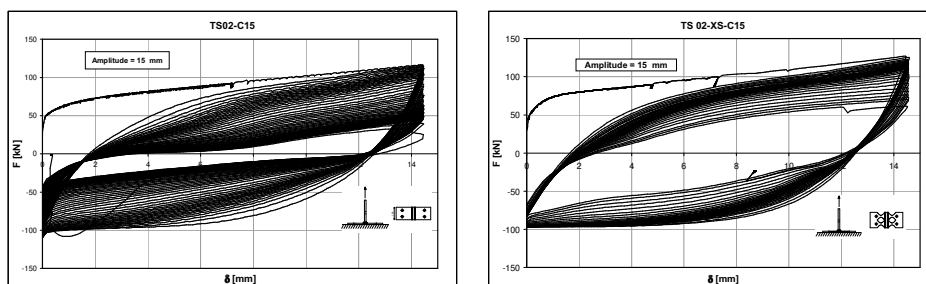


Fig. 5.54 – TS02-C15 and TS02-XS-C15 test results

All rectangular T-stubs exhibit the same failure mode regardless of the imposed displacement amplitude. Cracking of flanges initially developed at welds and progressively propagated along the flange width and thickness up to the complete fracture of the flange, which produced the complete loss of the load-carrying capacity. The behavior gave rise to a progressive deterioration, up to failure, of axial strength, stiffness and energy dissipation capacity.

The hourglass T-stubs showed the same failure mode characterized by the complete fracture of the flange. Moreover, cyclic behaviors of hourglass T-stubs are very different compared to that of rectangular T-stubs in terms of spread of plasticity and, as a consequence, of energy dissipation capacity.



Fig. 5.55 – Propagation of the heat along the flanges – Hourglass T-stub



Fig. 5.56 – Propagation of the heat along the flanges – Rectangular T-stub

This is firstly confirmed by the experimental evidence provided by the monitoring of the specimens during the test by means of thermal camera (Fig. 5.55-Fig. 5.56). The measurement of the heat on the T-stub flanges during the second cycle both for rectangular and hourglass T-stub confirms the expected mechanism of plasticization of the metal. In fact, in the case of rectangular T-stub, a significant gradient of temperature has been measured along the flange confirming the concentration of the energy dissipation in correspondence of the bolts and of the flange-to-web connection (Fig. 5.56). In the case of the hourglass element the diffusion of the plasticization is evidenced by the reported shot, which shows a uniform thermal state in the whole flange (Fig. 5.55).

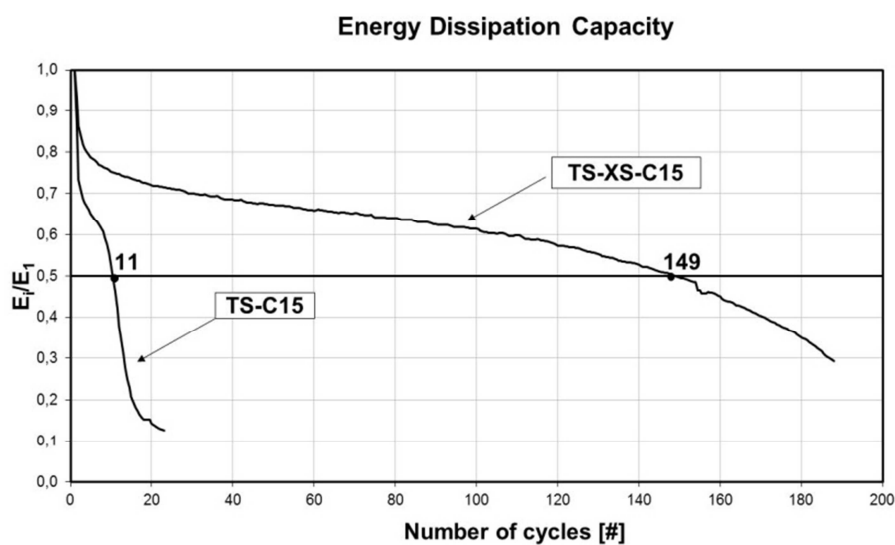


Fig. 5.57 – Definition of the conventional collapse

In order to completely point out the different plastic behavior under cyclic loads of the two details, low cycle fatigue curves have been carried out. To this scope, it is preliminary necessary to establish the conventional collapse condition, as there is no universally recognized failure criterion. Generally, in scientific literature collapse condition is identified in correspondence of a given value α of degradation of strength, stiffness or energy dissipation capacity. In this work the failure condition has been identified checking the degradation of Energy Dissipation Capacity, because it is able to account for the overall behavior of the T-stubs, including also the reduction of stiffness and strength. Castiglioni and Calado (1996), with reference to the degradation of energy dissipation capacity, i.e. the ratio between the energy dissipated during the generic cycle and that dissipated during the first cycle, have pointed out that after a few cycles of quick deterioration there is a phase of stabilization, characterized by a relatively small gradient, which is followed by an abrupt reduction of the energy dissipation capacity corresponding to failure. Therefore, Castiglioni and Calado (1996), suggest to assume a value of $\alpha=0.5$ as the conventional level of deterioration corresponding to failure. In fact, this degradation limit provides, on the average, a number of cycle corresponding to the abrupt reduction of the energy dissipation capacity. Thus, in the following, it is assumed that the collapse is reached when the condition $E_i/E_1=0.5$ is satisfied, where E_i is the energy dissipated during the i -th cycle and E_1 is the corresponding value recorded during the first cycle (Fig. 5.57).

First of all, it has been observed that in all cyclic tests the hourglass T-stub attained the collapse after a number of cycles much higher than that provided by rectangular T-stub. As shown, for example, in Fig. 5.57 with reference to cyclic tests under constant amplitude of 15 mm, the number of cycles to

conventional failure of hourglass T-stub is equal to 149 instead of 11 of rectangular T-stub.

As well known, low cycle fatigue curves can be represented by means of straight lines in bi-logarithmic scales. The number of plastic reversal to failure N_f is related to the total displacement amplitude Δv by means of the following relationship:

$$\Delta v = aN_f^b \quad (5.137)$$

on the base of the results of cyclic tests under different values of constant amplitude displacement (Fig. 5.53) low-cycle fatigue curves have been defined evaluating through least square fitting parameters a and b . First of all, it can be observed that, in the examined case, the monotonic points are not well aligned with the low-cycle fatigue curves.

This behavior is related to the different failure mechanisms occurring under cyclic and monotonic loading. In fact in the case of cyclic tests, as the cyclic amplitudes are contained in a displacement range in which second order effects do not have relevance, the failure of the element is due to the fracture of the plate while in the case of monotonic tests, as above underlined, the constraining action of the rigid support caused the premature shear failure of the bolt. The low cycle fatigue curves depicted in Fig. 5.58 show the significant improvement of the energy dissipation capacity provided by the hourglass T-stub. The ratio between the energy dissipated up to the conventional failure by hourglass T-stub and by the rectangular T-stub is equal, on the average, to 7.5. As the two curves are characterized by the same slope and the curve of

hourglass T-stub is above that of the rectangular T-stub, the enhancement in terms of number of cycles up to failure is significant in the whole range of the investigated cyclic displacement amplitudes resulting always greater than 650%.

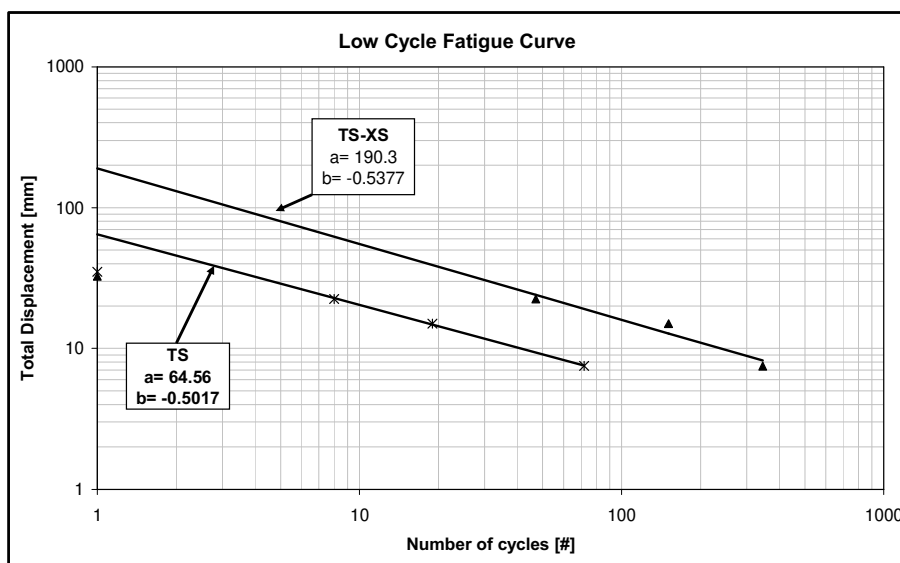
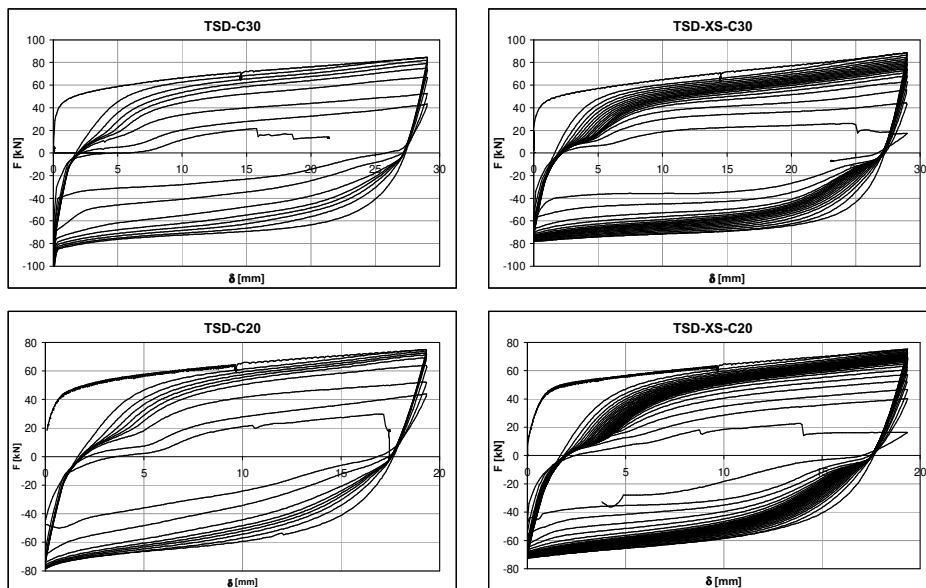


Fig. 5.58 – TS and TS-XS low-cycle fatigue curves

5.2.2.4 Cyclic Tests – Coupled T-stubs

The results of cyclic tests on coupled rectangular and hourglass T-stubs are depicted in Fig. 5.59, which confirm that also in the case of coupled T-stubs the enhancement of the device response under cyclic loading conditions is very significant. In Fig. 5.60 low-cycle fatigue curves of rectangular and

hourglass T-Stubs are depicted. Even in this case, the monotonic points are not well aligned with the curves obtained by means of regression analysis of the three cyclic points. As already underlined with reference to T-stubs on rigid support, this behavior arises because in the cyclic tests the second order effects do not have relevance, so that the failure modes under cyclic and monotonic conditions are different. The comparison between the low-cycle fatigue curve of the rectangular T-stubs and that of the hourglass T-stubs shows the significant increase of the energy dissipation capacity obtained by properly cutting the T-stub flanges also in the case of coupled T-stubs.



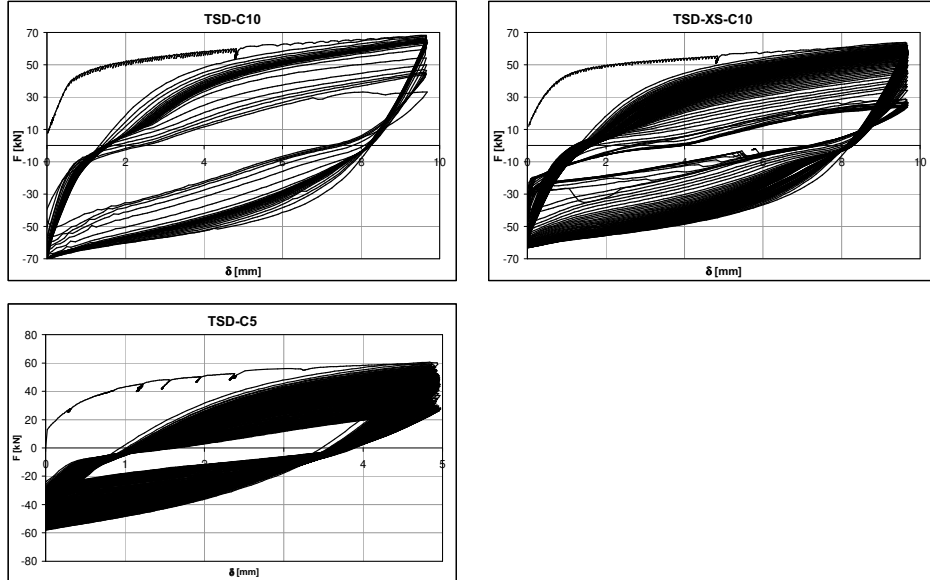


Fig. 5.59 – TSD and TSD-XS series – Cyclic Tests

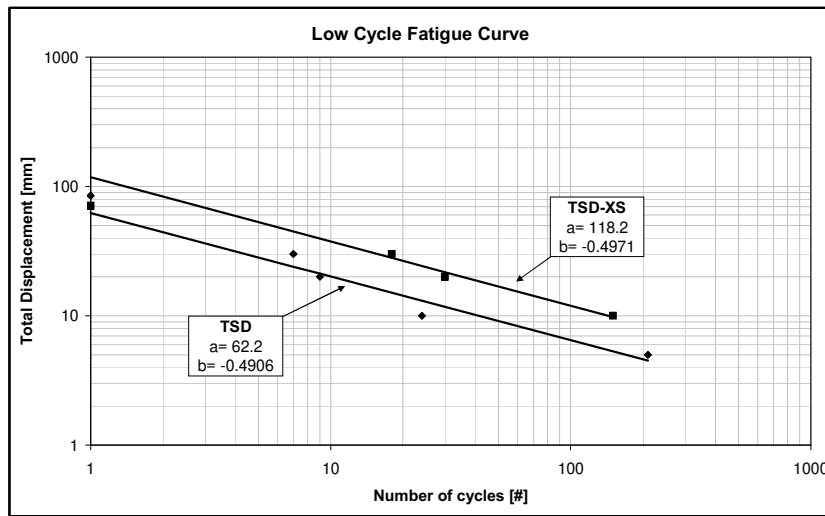


Fig. 5.60 – TSD and TSD-XS – low cycle fatigue curves

In particular, the ratio between the energy dissipated up to failure of hourglass and rectangular T-stub is equal, on the average, to 2.8. Finally, Fig. 5.61 evidences that low cycle fatigue curves in the cases of rigid support and coupled elements are characterized by the same slope which is approximately equal to 0.5. The intersection of low cycle fatigue curves with the vertical axis is almost the same in the case of rectangular element while, in the case of the hourglass T-stub, a higher value is shown by T-stubs on rigid support. This testifies that the benefit provided by the hourglass configuration in terms of energy dissipation capacity increases as far as the thickness of the connected plate increases.

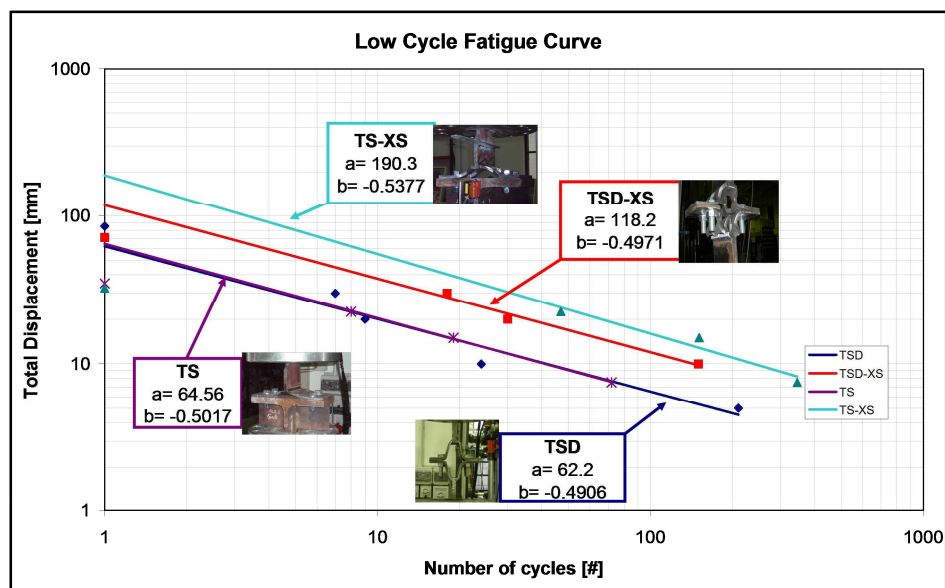


Fig. 5.61 – Comparison among low cycle fatigue curves

5.3 Application of Dissipative T-stubs to Double Split Tee Joints

As already remarked several times, dissipative behavior of MRFs designed to involve in plastic range connections rather than beam ends strongly depends on the dissipative capacities of the elements designed to be plasticized. In chapter 3 and 4 an experimental analysis dealing with the characterization of the cyclic behavior of beam-to-column connections detailed to engage in plastic range different joint components has been presented. In particular, four joints have been tested and the main characteristics of their behavior under cyclic loads have been pointed out. Main results of this experimental campaign can be summarized as follows:

- energy dissipation capacity of the whole beam-to-column joint strongly depends on the dissipation capacity of the weakest joint component;
- component method can be a useful support in establishing a joint component hierarchy criterion. Modeling of joint elements can represent an effective tool for designing joints failing according to a desired mechanism. In fact, a proper modeling of the response of the single joint components allows to select the dissipative element and to overstrength non-dissipative components which have to be designed to remain in elastic range.
- as demonstrated by the experimental analysis, if a proper design approach is adopted, sufficient plastic rotation supply can be obtained;
- joint adopting RBS strategy and joint engaging in plastic range mainly the shear panel, namely EEP-DB-CYC-03 and EEP-CYC 01, exhibited

wide and stable response under cyclic loads. Moreover, both joints provided a large amount of dissipated energy;

- joints involving in the dissipative mechanism mainly bolted components, i.e. EEP-CYC 02 and TS-CYC 04, gave a response under cyclic loads affected by significant pinching mainly due to stiffness degradation. This last behavior led to a lower dissipation capacity compared to the case of joints adopting RBS strategy or detailed to plasticize shear panel. Nonetheless, both joints provided sufficient plastic rotation supply.
- dealing with maintenance of steel buildings subjected to a severe earthquake, damage and, as a consequence plasticization, should be concentrated in elements easy to replace. From this standpoint, it is inconceivable to concentrate dissipation in panel zones and in many cases also the recovery of beam ends and/or end plates can be difficult. In fact, restoring welded elements obviously requires field flame cutting and field welding. Therefore, bolted solutions should be preferred, such as that adopting field bolted top and bottom T-stubs, namely the case of joint TS-CYC 04.

As far as this last point is of concern, it is easy to understand that, in order to make attractive to designers a joint solution adopting elements easy to replace after a seismic event, its characteristics under cyclic loads should also be comparable to that of joints involving in plastic mechanism beam ends or panel zones.

As already outlined, joints adopting T-stubs as dissipative elements provide many advantages. Concerning the total structural cost, as already demonstrated by (Faella et al., 1998), MRFs implementing partial strength

joints can lead to significant savings, particularly in cases where beams design is governed by vertical loads, i.e the case of low-rise/long spans buildings. Next, partial strength T-stub joints are less costly compared to other joint typologies. MRFs adopting bolted Double Split Tee Connections are fast to erect. In addition, bolted joints avoid the adoption of field welds which have been demonstrated, on the base of past experiences, to be unreliable and expensive because require inspections and good weather conditions to be executed. Moreover, after a severe ground motion, in case of damages bolted elements can be easily and quickly recovered. T-stub behavior, which is used to model also bolted components, is studied since many years, so that its monotonic and cyclic behavior can be clearly identified and predicted through various existing mechanical and FE models. In this work and in scientific literature it is widely demonstrated that bolted components, either end-plates and T-stubs, allow to govern the design process through three parameters, namely width and thickness of the flange plate and distance of bolts from the plastic hinge arising in correspondence of the web welds. Therefore, through a proper combination of these parameters it is possible to detail joints with certain stiffness, resistance and ductility supply.

On the other hand, joints involving bolted components in plastic range provide also some disadvantages. In particular, even though extensive past experimental studies showed that bolted connections are able to dissipate significant amounts of energy, it has to be recognized that their ability to dissipate seismic input energy is limited compared to that of other joint typologies or to the hysteretic behavior of H-shaped sections. This is mainly due to the presence of the well-known pinching phenomena. In addition, it is well known that performances of connections are strongly influenced by the depth of the connected beam. In fact, it is obvious that, for a given plastic

rotation, the plastic engage of the component at the tension flange level increases as the beam depth increases. In past experimental works, in case of end-plate connections, the energy dissipation capacity, in non-dimensional form, has been demonstrated to decrease as the beam depth increases.

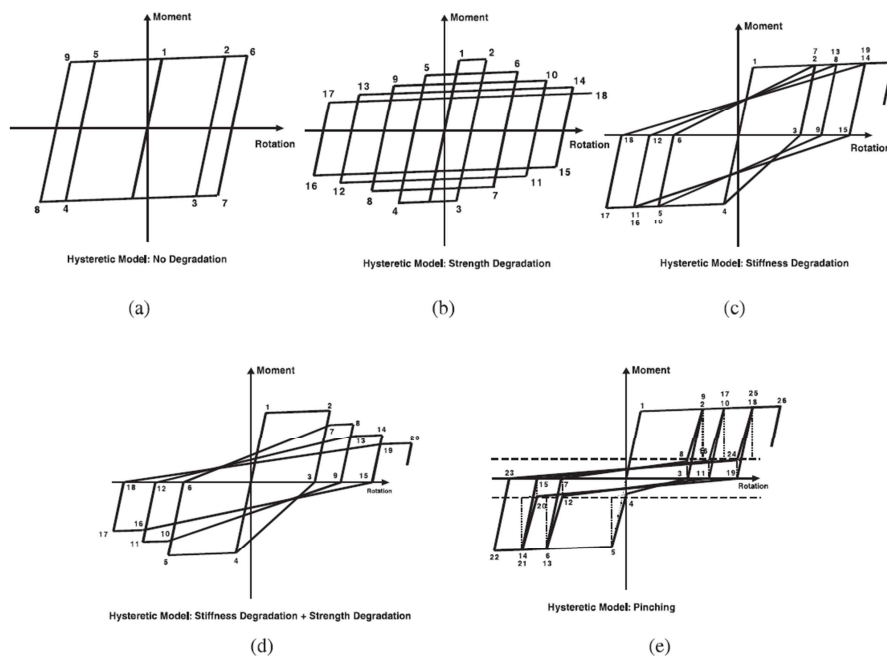


Fig. 5.62 – Different joint hysteretic behaviors

This result becomes clear making reference to a T-stub Joint. In fact, considering the case of two Double Split Tee Connections with same connection elements fastening beams with different height, it is clear that, for a given rotation history, the displacement demand at the T-stub level becomes higher as the beam depth increases. Therefore, a greater ductility demand is related to a higher engagement in plastic range of T-stubs, which, in turn,

accentuates phenomena associated with stiffness and strength degradation, and, as a consequence, reduces the energy dissipation capacity. As a result, in case of connections relying on dissipation of bolted components, even more than other joint typologies, ductility capacity/demand ratio has to be carefully evaluated.

As already said, concerning cyclic behavior of connections, it is clear that when T-stub or end-plate connections are employed, significant pinching phenomena, involving strength and stiffness degradation, are expected. Dealing with this topic, at present time, the role of hysteresis type on the global behavior of Steel Moment Resisting Frames is still a subject under discussion. In a recent work, (Huang & Foutch, 2009) aiming to evaluate the influence of the joint hysteretic behavior on the global drift limit of steel MRFs, have studied 3, 9 and 20 storey steel moment resisting frames employing five different hysteresis models (Fig. 5.62). In particular, their studies have pointed out that structural drift Capacity/Demand ratio is, generally, negatively influenced by strength degradation. Conversely, in case of joints affected by pinching phenomena Capacity/Demand ratio is not significantly different from the case of MRFs dissipating seismic input energy at beam-ends, which are known to be characterized by full hysteresis loops (Fig. 5.63). This last result, that a first glance may appear unexpected, is mainly due to the decrease of the effective structural period, which shifts MRFs to spectral zones with lower input energy. Therefore, although the energy dissipated per cycle decreases, the effective period increases, so that these two features offset each other. On the base of these results, due to the worse behavior exhibited by MRFs adopting joints affected by strength degradation, moment connections should be detailed aiming to avoid these phenomena. In addition, in spite of the conventional view, (Huang & Foutch, 2009) work demonstrates that pinching phenomena

does not negatively influence the response of MRFs. Thus, when connections are detailed to dissipate in bolted components, even though stiffness degradation and/or pinching phenomena are involved, in order to obtain a satisfactory behavior, it is of fundamental importance to prevent strength degradation up to plastic rotations compatible with the design inter-storey drifts. In part, the negative role played by a beam/joint hysteretic response characterized by strength degradation is already recognized by the codes. In fact, dealing with MRFs, EC3 requires that rotation of plastic hinges has to be ensured without stiffness and strength degradation greater than 20%.

TABLE 7 Capacity/demand ratios (20% criteria)

	BL	10%SD	25%SD	40%SD	KD	KD+10%SD	KD+25%SD	KD+40%SD	20%Pinch	50%Pinch	70%Pinch
3-story											
Demand	.0312	.0320	.0346	.0359	.0342	.0351	.0374	.0441	.0339	.0348	.0356
Capacity	.200	.200	.200	.199	.200	.199	.198	.193	.196	.200	.200
C/D	6.4	6.3	5.8	5.5	5.8	5.7	5.3	4.4	5.8	5.7	5.6
%	100%	98%	91%	86%	91%	89%	83%	69%	91%	89%	88%
9-story											
Demand	.0249	.0253	.0254	.0261	.0256	.0260	.0274	.0331	.0256	.0256	.0261
Capacity	.101	.086	.065	.059	.115	.102	.074	.061	.100	.101	.108
C/D	4.1	3.4	2.6	2.3	4.5	3.9	2.7	1.8	3.9	3.9	4.1
%	100%	83%	63%	56%	110%	95%	66%	44%	95%	95%	100%
20-story											
Demand	.0194		.0219		.0201		.0232				
Capacity	.096		.074		.123		.074				
C/D	4.9		3.4		6.1		3.2				
%	100%		69%		124%		65%				

Fig. 5.63 (Huang & Foutch, 2009) results

As a conclusion, the application of joints having bolted elements as weak components is definitely more complicated, but for the above reported reasons in many cases can be convenient. When bolted connections are adopted, detailing has to be carefully evaluated paying attention both to the monotonic and to the cyclic response. In case of dissipative joints, if the monotonic response can be accurately governed by properly detailing the geometrical parameters defining the end-plate/T-stub, the same cannot be said for the

cyclic response. In fact, stiffness and strength degradation are not as easy to calibrate as initial stiffness and/or plastic resistance and, as a consequence cyclic behavior of joints designed to dissipate in bolted components in some cases may result unsatisfactory. As a result, aiming to apply these joint typologies to MRFs systems their dissipative behavior should be improved. In last years, in order to enhance the dissipative behavior of bolted joints, several authors have proposed systems involving the addition of supplemental damping devices.

In previous paragraphs, cyclic characteristics of classical T-stubs have been compared to those of innovative dissipative T-stubs. Experimental results have demonstrated that this supplemental damping device can dissipate significant amounts of energy. In particular, experimental results have shown that, in the considered cases, hourglass T-stubs have dissipated from three to seven times more energy compared to rectangular T-stubs with same initial stiffness and plastic resistance. In addition, the increase of energy dissipation capacity has been combined with an improvement of the cyclic behavior in terms of stiffness and strength degradation. Within the framework of dissipative joints, this result is noteworthy and useful to the development of dissipative systems to be applied to bolted joints.

In the following the results of an experimental campaign dealing with the application of dissipative T-stubs to two real scale beam-to-column joints is presented. Also in this case, the scope of the research program is comparative. In fact, the main goal is to show a procedure to design dissipative T-stub joints with same monotonic characteristics of a classical T-stub joint, i.e. stiffness and resistance, but with greater capacity to dissipate the seismic input energy. The objective of the work is to obtain a joint providing

the same response of a classical detail under service loads and dissipating a larger amount of energy under Ultimate Limit State Conditions.

5.3.1 The Role of Moment-Shear Interaction

5.3.1.1 Effect of Moment-Shear Interaction on the Value of the Plastic Moment

Formulations previously derived for computing design resistance of hourglass T-stubs do not account for moment-shear interaction effect. Therefore, before analyzing the procedure applied to design the tested specimens it is necessary to evaluate the role played by the moment-shear interaction on the ultimate resistance of dissipative T-stubs.

Dealing with the force-displacement response of classical rectangular T-stubs, in (Faella et al., 2000), effect of shear on the plastic moment has been modeled by identifying more complete formulations, based on an approximate approach employing a moment-shear interaction domain. (Faella et al., 2000) have determined that, when the ratio between the lever arm and the plate thickness is greater than 2.5 the reduction of resistance is less than 10% in case of mechanisms type-1, while in case of mechanism type-2 is lower than 4%. On the base of these results it is easy to conclude that, in current applications, the effect of moment-shear interaction on the resistance of rectangular T-stubs can be neglected. In case of dissipative T-stubs the same result cannot be taken for granted. In fact, the particular shape of the plate, which is tapered in the region between the bolt and the T-stub web, if not properly dimensioned, could lead to substantial decreases of strength. It is well known that, in case of hourglass T-stubs, the bending moment diagram varies accordingly with the breadth of the plate leading to normal stresses approximately constant along

the plate extension. Conversely, the shear action is constant and, as a consequence, the variability of the plate width results in a variable response in terms of tangential stresses along the device extension. Therefore, although the plate is dimensioned to plasticize contemporary in all sections for bending, if the shape of the plate is not properly designed to withstand shear, moment-shear interaction can significantly affect the dissipative behavior by influencing the distribution of plasticization and, as a result, decreasing the ultimate resistance of the X-shaped T-stub.

The effect of moment-shear interaction is a high complicated phenomenon, because it depends on the constraints and on the shape of loads on the entire beam. In general, the problem is untrivial in a closed form solution, in fact, as observed by (Drucker, 1956) there is no reason to expect that the problem possesses a unique solution expressed in the form:

$$f\left(\frac{M}{M_p}, \frac{V}{V_p}\right) = 0 \quad (5.138)$$

because the variables moment (M) and shear (V) are not independent. As an example, considering a simple cantilever beam, even though the situation at the clamped section is the same, there is no reason to suppose that the solution in case of end-load is equal to that of a uniform distributed load. Despite this, in technical literature benchmark cases are studied and the obtained results, expressed in the form of Eq.(5.138) are extended to other structural situations. This cannot be strictly justified, but fortunately the effects of shear force are small in practical cases. The most studied case is that of the

end-loaded cantilever made of perfectly plastic material. Generally, aiming to obtain lower bound solutions, the problem is studied exploiting the static theorem, which is expressed as follows:

An external load computed on the basis of an assumed distribution of internal forces, in which the forces are bounded by limit values and in equilibrium is less than or equal to the true collapse load.

Following the approach already proposed by (Faella et al., 2000) a more complete formulation for those details where moment-shear interaction is not negligible can be identified. Considering the plate cross-section, external fibers are assumed to withstand the bending moment, while the internal ones are supposed to be subjected to shear stress only. According to the static theorem of the plastic collapse this assumption leads to safe results. With reference to Fig. 5.66 by considering Hencky-Von Mises yield criterion, at the generic section \bar{z} , internal equilibrium conditions provide:

$$M_f = f_y a \cdot (t - a) b(\bar{z}) \quad (5.139)$$

$$V_f = \frac{f_y}{\sqrt{3}} (t - 2a) b(\bar{z}) \quad (5.140)$$

From Eq.(5.140) parameter a , which obviously depends on the considered abscissa, derives:

$$a = \frac{t}{2} - \frac{\sqrt{3}}{2} \frac{V_f}{b(\bar{z})f_y} \quad (5.141)$$

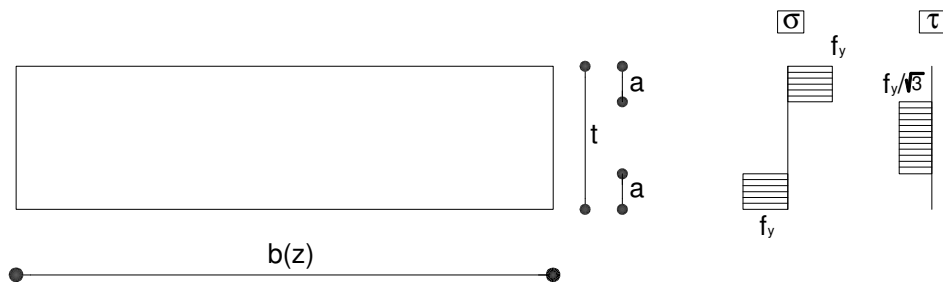


Fig. 5.64 – Distribution on internal stresses in the yielding condition under bending moment and shear

by substituting Eq.(5.141) into Eq.(5.140) yields:

$$M_f = M_{f,Rd} - \frac{3}{4} \frac{V_f^2}{b(\bar{z})f_y} \quad (5.142)$$

where $M_{f,Rd}$ is the design value of the pure plastic moment.

$$M_{f,Rd} = \frac{b(\bar{z}) \cdot t^2}{4} f_y \quad (5.143)$$

By introducing the design value of the pure plastic shear evaluated according to Hencky-Von Mises yield criterion:

$$V_{f,Rd} = b(\bar{z}) \cdot t \frac{f_y}{\sqrt{3}} \quad (5.144)$$

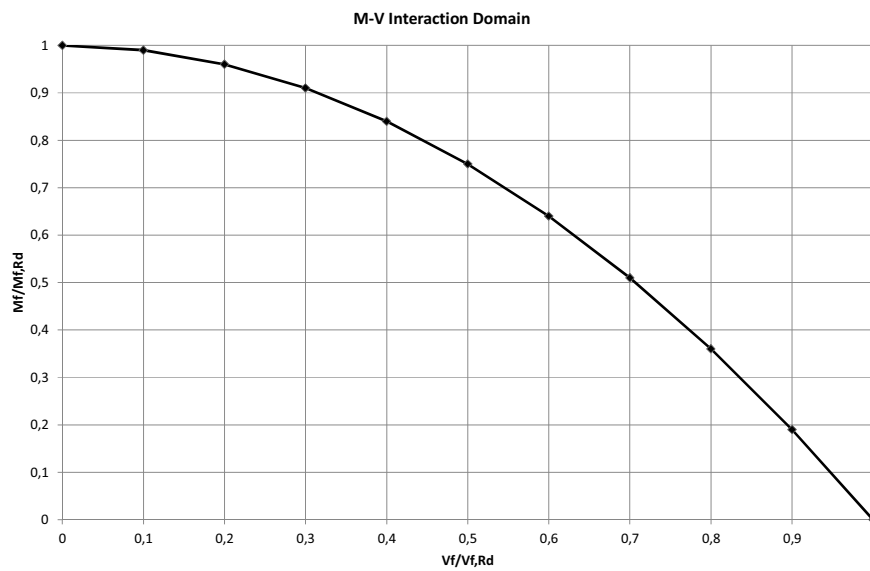


Fig. 5.65 – Representation of M-V Interaction Domain

the yielding condition (5.142) can be rearranged in the following form. For sake of clarity analytical developments are reported.

$$\frac{M_f}{M_{f,Rd}} + \frac{3}{4} \frac{V_f^2}{b(\bar{z})f_y M_{f,Rd}} = 1 \quad (5.145)$$

$$\frac{M_f}{M_{f,Rd}} + \frac{3}{4} \frac{4 \cdot V_f^2}{b(\bar{z})f_y \sqrt{3} \cdot t \cdot V_{f,Rd}} \cdot \frac{b(\bar{z}) \cdot t \cdot f_y}{\sqrt{3} \cdot V_{f,Rd}} = 1$$

$$\frac{M_f}{M_{f,Rd}} + \frac{V_f^2}{V_{f,Rd}^2} = 1 \quad (5.146)$$

Starting from the obtained moment-shear interaction domain (Fig. 5.65), a new expression of resistance of dissipative T-stub accounting for shear forces can be obtained. Moreover, in next paragraph, assuming the plate width unknown, the plate optimum shape, accounting both for bending and shear will be characterized.

Let us first consider the hourglass shape described by Eqs.(5.98)-(5.99). In hypothesis of mechanism type-1, which is the most dissipative failure mechanism, it is well known that on the T-stub flange act a linear bending moment with point of zero moment in the mid-section and a constant shear, described in analytical form by the following expressions (Fig. 5.66):

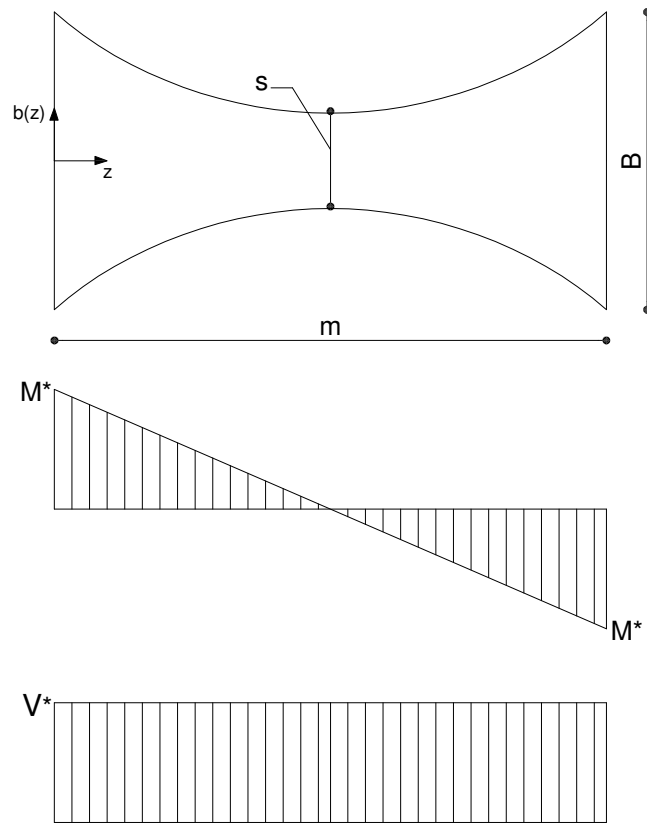


Fig. 5.66 – Distribution of internal forces on an X-shaped T-stub

$$M_f(z) = M^* \left(1 - \frac{2z}{m} \right) \quad (5.147)$$

$$V_f(z) = \frac{2M^*}{m} \quad (5.148)$$

by considering that the relationship between plate bending and shear resistance is:

$$M_{f,Rd}(z) = \frac{\sqrt{3}}{4} V_{f,Rd}(z)t \quad (5.149)$$

and by combining Eqs.(5.148)-(5.149), the yielding condition can be rewritten in the following form:

$$\frac{M_f(z)}{M_{f,Rd}(z)} + \frac{V_f^2(z)}{V_{f,Rd}^2(z)} = 1 \quad (5.150)$$

$$\frac{V_f(z) \cdot m \left(\frac{m-2z}{m} \right)}{2} \cdot \frac{4}{\sqrt{3}V_{f,Rd}(z)t} + \frac{V_f^2(z)}{V_{f,Rd}^2(z)} = 1 \quad (5.151)$$

$$\frac{V_f(z)}{V_{f,Rd}(z)} \cdot \frac{2 \cdot (m-2z)}{\sqrt{3}t} + \frac{V_f^2(z)}{V_{f,Rd}^2(z)} = 1 \quad (5.152)$$

By solving with respect to $\frac{V_f(z)}{V_{f,Rd}(z)}$ the following expression of the shear

carried by the device at abscissa z is obtained.

$$\frac{V_f(z)}{V_{f,Rd}(z)} = \frac{(2z-m)}{\sqrt{3t}} \left[1 - \sqrt{\left(1 + \frac{3t^2}{(2z-m)^2} \right)} \right] \quad (5.153)$$

Considering that last expression is evaluated on a single damper, in case of a two bolts T-stub, the total resistance $F(z)$ is equal to:

$$F(z) = \frac{2 \cdot V_{f,Rd}(z) \cdot (2z-m)}{\sqrt{3t}} \left[1 - \sqrt{\left(1 + \frac{3t^2}{(2z-m)^2} \right)} \right] \quad (5.154)$$

by substituting $V_{f,Rd}(z)$ with its expression and considering the equation defining the hourglass shape derives:

$$F(z) = \frac{2 \cdot B \cdot e^{-\frac{2}{m} \ln\left(\frac{B}{s}\right)z} \cdot f_y \cdot (2z-m)}{3} \left[1 - \sqrt{\left(1 + \frac{3t^2}{(2z-m)^2} \right)} \right] \quad (5.155)$$

Therefore, the force carried by the cross section at the generic section z is given by Eq.(5.155). Thus, as the external shear force acting on the device is constant, the maximum force carried by the T-stub is given by the minimum of function $F(z)$. Such a minimum value individuates the section of minimum resistance accounting for both bending moment and shear. Deriving Eq.(5.155) provides:

$$\begin{aligned}
F'(z) = & \frac{2 \cdot B \cdot e^{-\frac{2}{m} \ln\left(\frac{B}{s}\right)z} \cdot f_y}{3} \left\{ \left[1 - \sqrt{1 + \frac{3t^2}{(m-2z)^2}} \right] + \right. \\
& + \frac{6t^2}{\sqrt{\left(1 + \frac{3t^2}{(m-2z)^2}\right)}(m-2z)^2} + \\
& \left. + \alpha \left[1 - \sqrt{1 + \frac{3t^2}{(m-2z)^2}} \right] (m-2z) \right\}
\end{aligned} \tag{5.156}$$

condition $F'(z) = 0$ in range $0 < z < m/2$ gives the following solution:

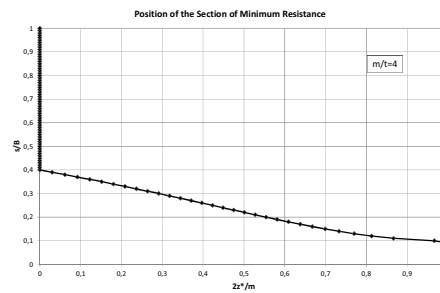
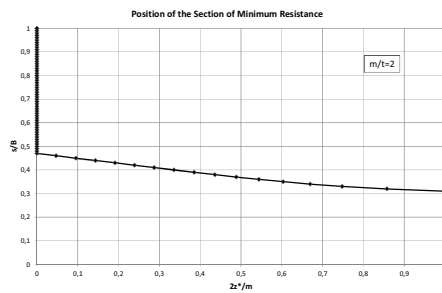
$$z^* = 0 \quad \text{if} \quad \frac{B}{s} < e^{m\sqrt{\frac{1}{m^2+3t^2}}} \tag{5.157}$$

$$z^* = \frac{\alpha^2 m - \sqrt{4\alpha^2 - 3\alpha^4 t^2}}{2\alpha^2} \quad \text{if} \quad e^{m\sqrt{\frac{1}{m^2+3t^2}}} < \frac{B}{s} < e^{\frac{m}{\sqrt{3}t}} \tag{5.158}$$

$$z^* = m/2 \quad \text{if} \quad \frac{B}{s} > e^{\frac{m}{\sqrt{3}t}} \tag{5.159}$$

where α is given by Eq.(5.99). Last equation represents the expression of the abscissa of the cross-section of minimum resistance accounting both for shear and bending moment that is, from the theoretical standpoint, the section where plasticization begins. This result points out an important difference in the

behavior of rectangular and dissipative T-stubs. In fact, in case of classical T-stubs, that is the case of a rectangular plate subjected to double curvature, the section of minimum resistance, i.e. the section where the plastic hinge arises, is obviously located at the clamped section either considering only bending actions or considering both bending and shear. Conversely, in case of hourglass T-stubs, that is equivalent to the case of ADAS devices, the section of minimum resistance is not known a priori and, in general, accounting both for flexural and shear forces, it is located somewhere between the clamped and the mid-section. Furthermore, from the above reported expressions follows that the position of the section of minimum resistance depends only on the geometrical properties of the device. Therefore, as the shape of the device is defined, the section of minimum resistance is known. In Fig. 5.67. a representation in non-dimensional form of abscissa z^* is provided. From the reported figures, comes out that as the plate slenderness increases range of s/B values which leads to the condition $0 < z^* < m/2$ increases.



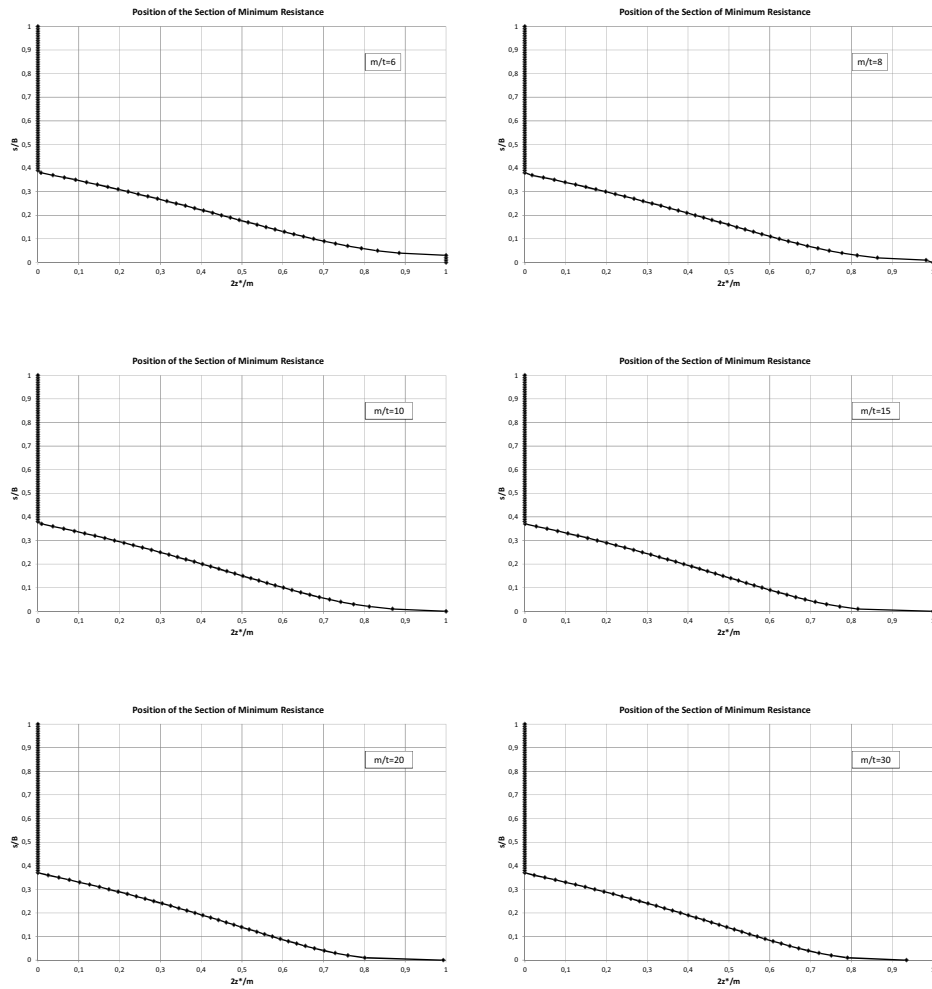


Fig. 5.67 – Influence of hourglass geometry on the position of the section of minimum resistance

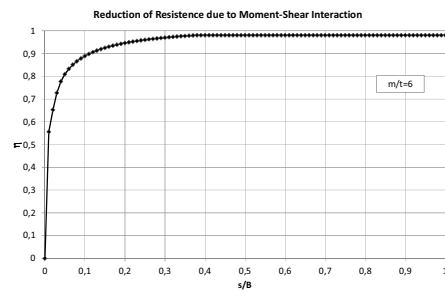
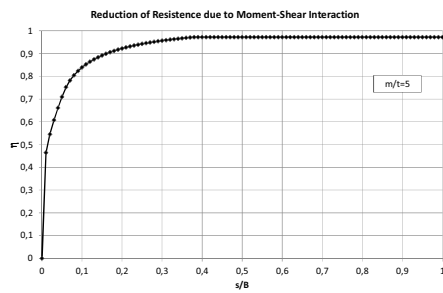
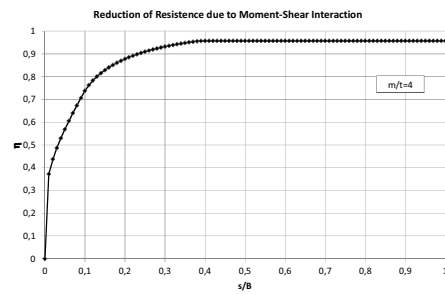
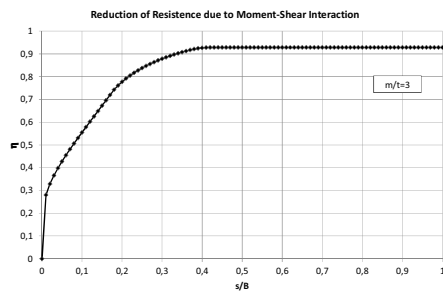
Through the knowledge of the position of the section of minimum resistance, the whole T-stub strength can be expressed by means of the following equation:

$$F(z^*) = \frac{2 \cdot B \cdot e^{-\frac{2}{m} \ln\left(\frac{B}{s}\right) z^*} \cdot f_y \cdot (2z^* - m)}{3} \left[1 - \sqrt{1 + \frac{3t^2}{(2z^* - m)^2}} \right] \quad (5.160)$$

In addition, previously, by adopting an approximate approach, the force-displacement curve of an hourglass T-stub has been characterized. In particular, as already proposed by (Whittaker et al., 1989), the largest X-shape inscribed within the real shape of the device has been adopted (Fig. 5.29) and the effective width (B_{eff}) of the simplified bi-triangular X-shape has been determined. On the base of the obtained results, it is possible to account for moment-shear interaction effect by reducing the resistance evaluated neglecting the effect of shear of a factor equal to the ratio between:

$$\eta = \frac{F(z^*)}{F_{nr}} = \frac{F(z^*)m}{4M_{f,Rd}} = \frac{F(z^*)m}{B_{eff} t^2 f_y} = \frac{2 \cdot m \cdot b(z^*) \cdot (2z^* - m)}{3B_{eff} t^2} \left[1 - \sqrt{1 + \frac{3t^2}{(2z^* - m)^2}} \right] \quad (5.161)$$

By means of Eq.(5.161) the influence of the moment shear interaction on the design resistance is depicted in Fig. 5.68



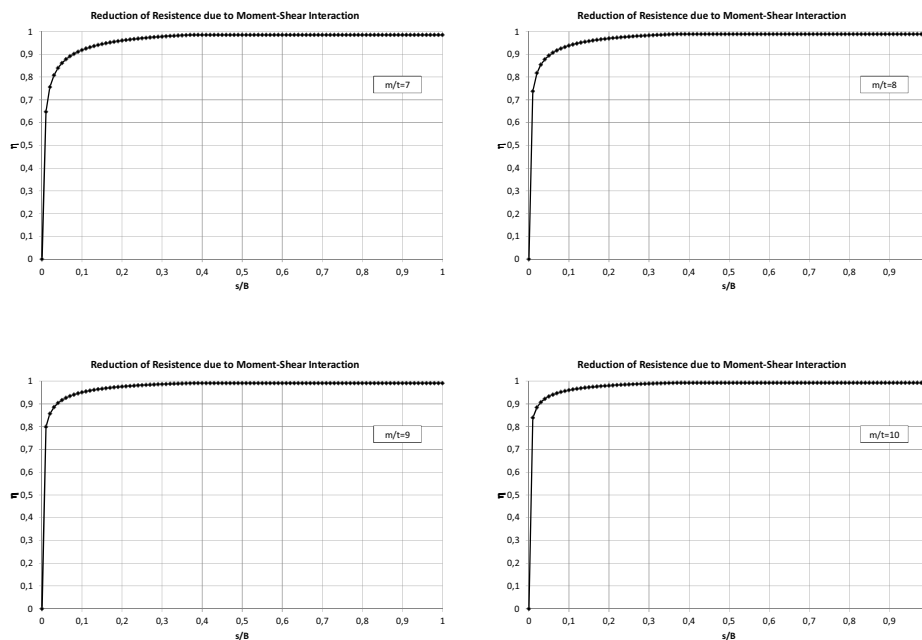


Fig. 5.68 – Reduction of resistance due to moment-shear interaction for different values of m/t

It is possible to observe that for low values of m/t , the influence of the moment-shear interaction can be significant, especially in case of low s/B ratios. In particular, for values of m/t lower than 5, if it is desired to avoid reduction of resistance, a proper dimension of the mid-section is necessary. Conversely, for values of m/t greater than 5, it is possible to neglect shear forces only if the ratio between the breadth at mid-section and the width at the clamped section is greater 0.1. Otherwise, moment-shear interaction has to be properly accounted for. Furthermore it is worth note that the obtained results considering $s/B=1$, i.e. the case of rectangular T-sub, are in perfect agreement with those found by (Faella et al., 2000).

5.3.1.2 Optimum Shape of Dissipative T-stubs

Concerning modeling of ADAS elements, in technical literature geometry of the device is usually optimized only with reference to bending moment actions. This approximation is because ADAS devices are usually sufficiently slender to assume that flexural actions are prevalent compared to shear actions. As an example, in case of (Whittaker et al., 1989) tests, the ratio between ADAS length and thickness is of about 20. Conversely, as before pointed out, in case of application of dissipative T-stubs to beam-to-column joints the more the bolt is closer to the T-stub web the more the shear force plays a major role on the response of the device. Dealing with T-stubs to be applied to beam-to-column joints, ratios between lever arm and thickness of the plates are much lower. In fact, current values adopted for application to beam-to-column joints usually can range largely from 2 to 10.

Classically, optimum shape of ADAS devices is determined neglecting shear and axial forces acting on the element. Considering a metallic damper made of a single steel plate with constant thickness t and variable width $b(z)$ the plastic moment at any section of the plate $M_p(z)$ is given by:

$$M_p(z) = \frac{b(z)t^2}{4} f_y \quad (5.162)$$

to ensure plastic yielding simultaneously at all section, Eq.(5.162) has to be equated to the external bending moment diagram.

$$\frac{b(z)t^2}{4} f_y = M(0) \cdot \left(1 - \frac{2z}{m}\right) \quad (5.163)$$

Therefore, the optimum variation of the plate width is given by:

$$b_f^{opt}(z) = \frac{4M(0)}{f_y t^2} \cdot \left(1 - \frac{2z}{m}\right) \quad (5.164)$$

which results in a linear variation of the width along the extension of the plate. Therefore, classical approach consists on defining the shape of the device to be close, as much as possible, to the optimum bi-triangular shape. It is worth note that in classical design of ADAS devices, no exact relationships are given to determine breadth at the mid-section and, usually, s/B ratios contained in range 0.1 – 0.2 are adopted.

On the base of the expressions accounting for moment-shear interaction above formulated, by following the same approach classically adopted for defining the ADAS optimum shape, it is possible to rewritten classical expression taking into account the effect on the ultimate resistance of shear. In particular, it is possible to define the “optimum” shape as the variation law of the plate breadth, which provides the same resistance in all plate sections accounting both for bending moment and shear forces. Recalling Eq.(5.153):

$$\frac{V_f(z)}{V_{f,Rd}(z)} = \frac{(2z-m)}{\sqrt{3}t} \left[1 - \sqrt{1 + \frac{3t^2}{(2z-m)^2}} \right] \quad (5.165)$$

it is possible to rewrite the equation in the following way:

$$V_f(z) = \frac{b(z)f_y(2z-m)}{3} \left[1 - \sqrt{1 + \frac{3t^2}{(2z-m)^2}} \right] \quad (5.166)$$

therefore, by assuming that $b(z)$ is the unknown and imposing that $V(z)$ is equal to a desired value \bar{V} which is assumed to be constant, results:

$$b_{opt}^{fs}(z) = \frac{3\bar{V}}{f_y \cdot (2z-m) \left[1 - \sqrt{1 + \frac{3t^2}{(2z-m)^2}} \right]} \quad (5.167)$$

As far as the optimum plate shape, i.e. the shape that leads to the contemporary plasticization of all plate sections, is described through Eq.(5.167), it could be of interest to found the exponential law which best fits the optimum shape for a fixed value of the force acting on the damper. Aiming to reach this goal, it is necessary to found the correlation between the parameters describing the exponential shape, namely s/B and m/t , and the optimum shape. Therefore, a numerical analysis aiming to evaluate the mean

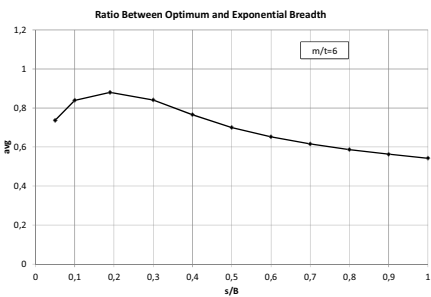
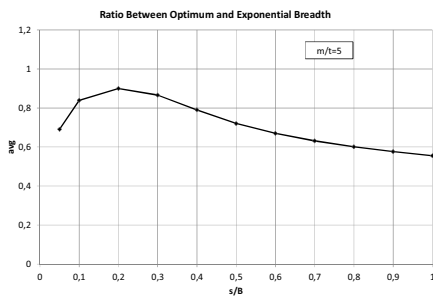
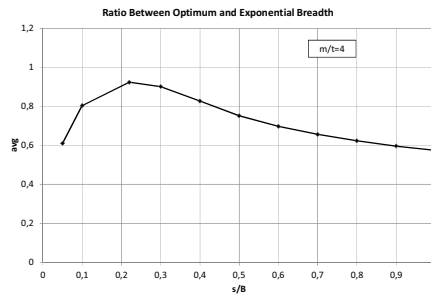
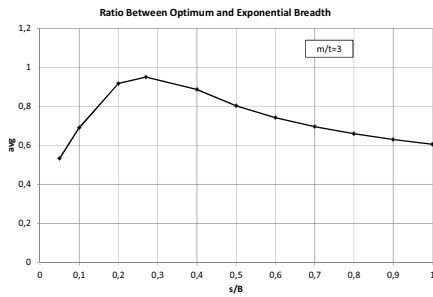
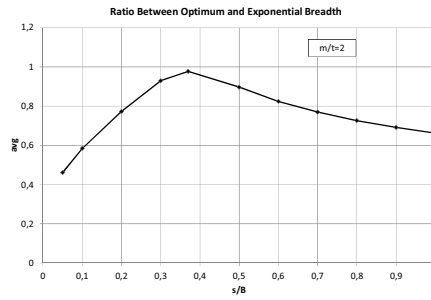
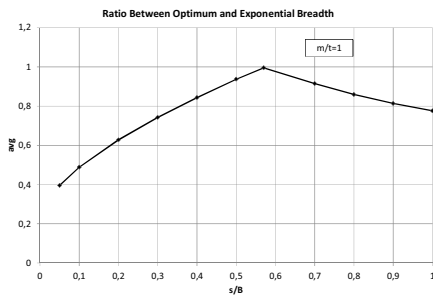
value of the ratio between the plate width described through the exponential law and that defined by means of Eq.(5.167), for different values of m/t and s/B , has been carried out.

If a design value of the force acting on the damper is considered and m/t ratio is fixed, optimum shape accounting for both moment and shear is given by Eq.(5.167) while, dealing with the exponential law, in order to obtain the desired design force, the following relationships for a single damper, have to be written:

$$\left\{ \begin{array}{l} b(z) = B \cdot e^{-\alpha z} \\ B_{eff} = \frac{2\bar{V}m}{\eta t^2 f_y} \\ B_{eff} = B \cdot e \cdot \left(\frac{s}{B}\right) \ln\left(\frac{B}{s}\right) \\ \eta = \frac{m \cdot b(z^*) \cdot (2z^* - m)}{3B_{eff} t^2} \left[1 - \sqrt{1 + \frac{3t^2}{(2z^* - m)^2}} \right] \end{array} \right. \quad (5.168)$$

from last system of equations derives that for a given value of m/t , it is possible to define infinite exponential shapes having the same resistance, but different values of s/B . Therefore, by varying the ratio between the width at the mid-section and the maximum plate width it is possible to analyze the mean value of the ratio between the plate breadth defined by means of Eq.(5.168) and the optimum plate breadth defined through expression (5.167). Obtained results, for $1 < m/t < 16$ and $0 < s/B < 1$, are depicted in Fig. 5.69, where the average

of the ratio between optimum and exponential width is represented versus s/B ratio.



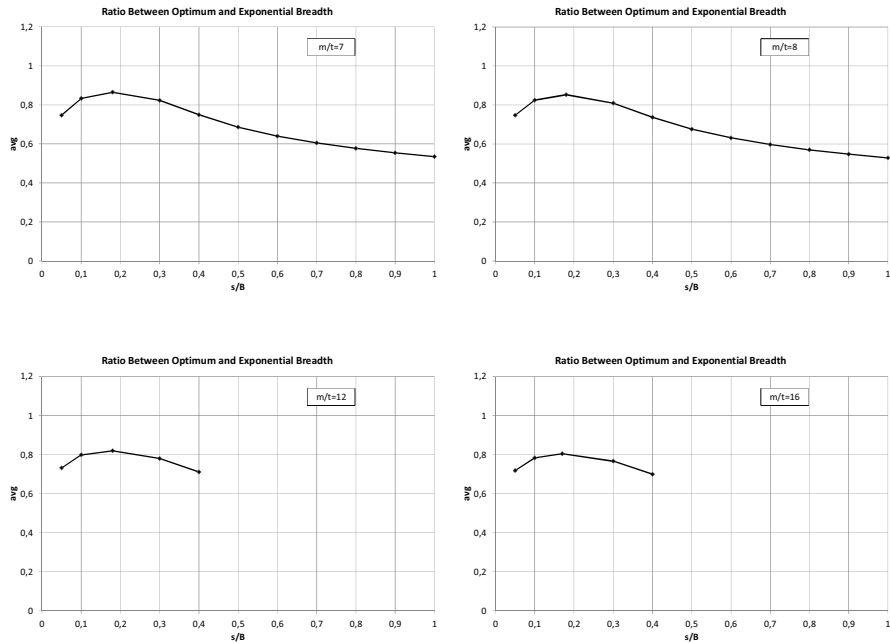


Fig. 5.69 – Average of the ratio between optimum shape and exponential law
(Devices with same resistance and same m/t ratio)

Fig. 5.69 clearly points out that an optimum s/B ratio exists. In particular, for a given ratio between device length and plate thickness, the optimum s/B ratio is given by the s/B value corresponding to the maximum of the mean values of the ratio between width of optimum and exponential shape. This optimum value of s/B is greater as m/t decreases. This is obviously due to the shear actions, which have a greater importance as the slenderness of the plate decreases.

Therefore, aiming to found a relationship between optimum s/B ratio and plate slenderness, s/B values corresponding to the maximum given in Fig. 5.69 have been represented versus the corresponding values of m/t (Fig. 5.70).

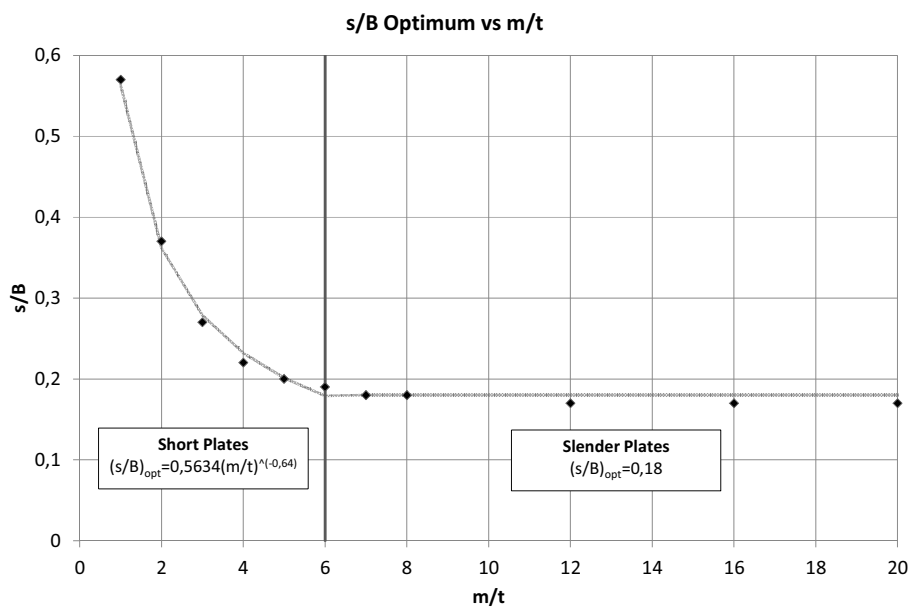


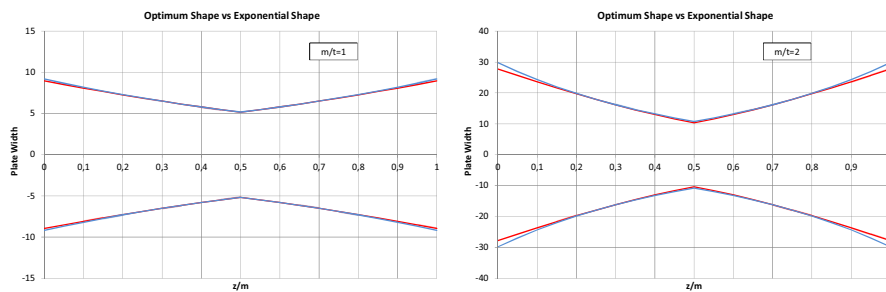
Fig. 5.70 – s/B optimum vs m/t

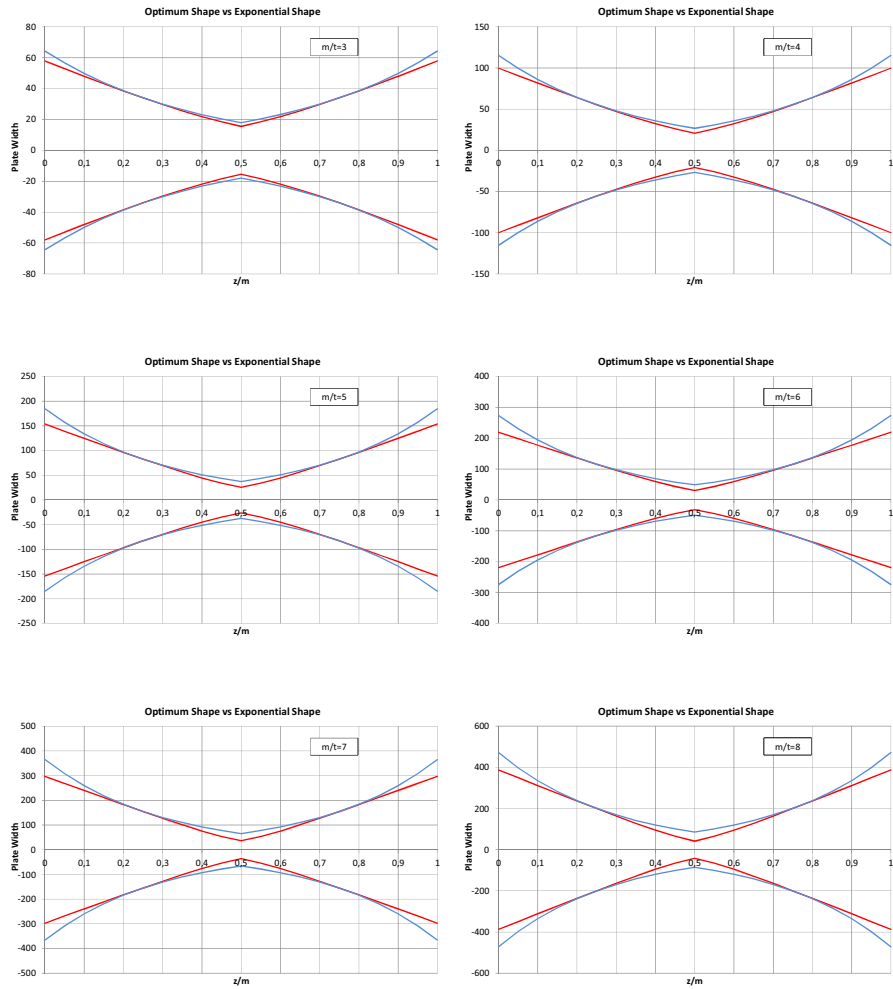
From Fig. 5.70 it is possible to understand that, up to values of m/t equal to 6, the optimum ratio between the width at mid-section and the maximum width strongly depends on m/t while, for higher values of plate slenderness optimum s/B becomes independent on m/t . In fact, for low values of m/t shear forces provide an important influence on the flexural behavior of the plate and, due to the significant difference between the bi-triangular and the optimum shape, proper detailing of the plate mid-section is necessary. Conversely, for high values of plate slenderness, bending moment becomes prevalent compared to

shear forces and, as the slenderness increases, the optimum shape becomes closer to the bi-triangular one, so that the optimum ratio between minimum and maximum width becomes almost constant. Through regression analysis of the obtained numerical data the following relationships, with correlation factor equal to 0,991, have been obtained:

$$\begin{aligned} \text{if } \left(\frac{m}{t}\right) \leq 6 & \quad \left(\frac{s}{B}\right)_{opt} = 0,5634 \left(\frac{m}{t}\right)^{-0,64} \\ \text{if } \left(\frac{m}{t}\right) > 6 & \quad \left(\frac{s}{B}\right)_{opt} = 0,18 \end{aligned} \quad (5.169)$$

Therefore, as the design tool for detailing the damper mid-section has been individuated, in the following figures damper shape for different values of m/t is reported.





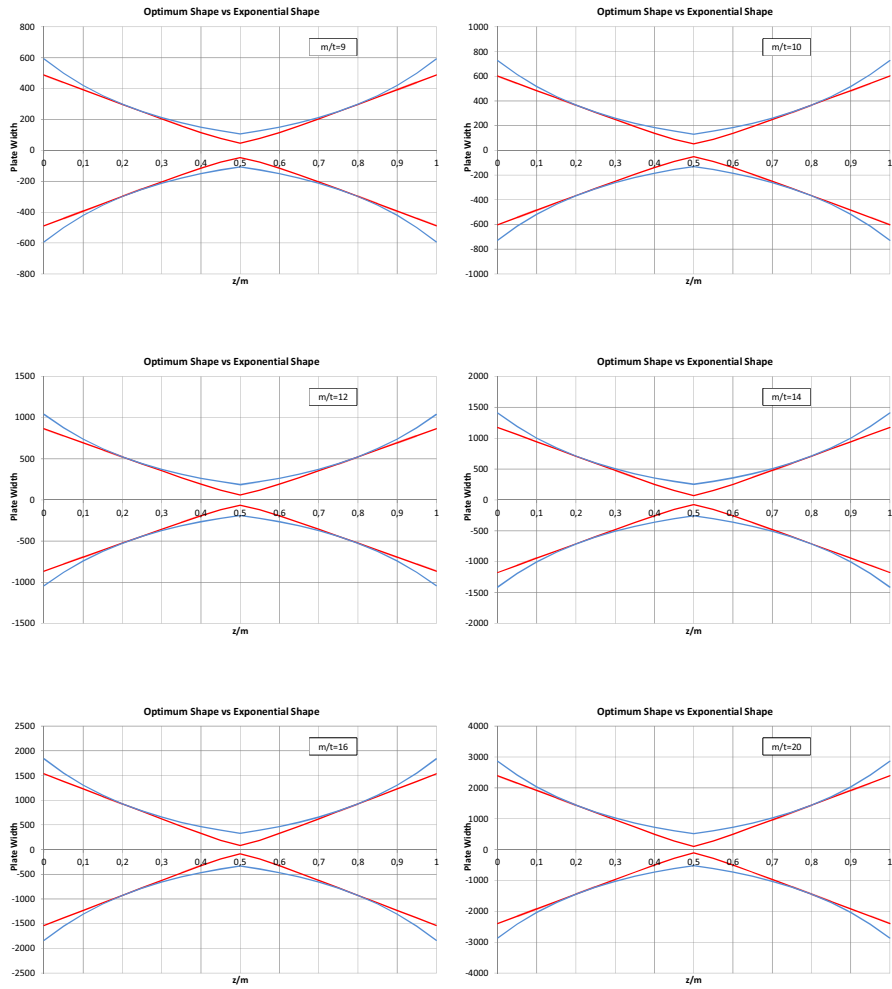


Fig. 5.71 –Optimum shape vs Exponential Shape

5.3.2 Experimental Tests on Dissipative T-stub Joints

As above remarked, the aim of the work herein presented is to show how to improve the energy dissipation capacity of classical bolted details by means of the application of dissipative devices expressly studied to this scope. In previous paragraphs, a theoretical and experimental analysis devoted to the development of a supplemental metallic damping system to be applied to steel beam-to-column joints has been presented. Main idea of the work has been to show how to increase the energy dissipation capacity of classical rectangular T-stubs by applying basic concepts governing plates working under double curvature, such as ADAS devices. In particular, by properly tapering the flange plate section in the region between the T-stub web and the bolt, a T-stub with high dissipative capacities has been developed. Experimental behavior of the device has been analyzed and a mechanical model for the prediction of the whole monotonic force-displacement curve has been pointed out. Moreover, some peculiar aspects of the behavior of dissipative T-stubs have been evidenced, such as the influence of moment-shear interaction on the resistance or the principles governing the optimum design of the shape. In addition, tools for designing dissipative elements possessing certain resistance and stiffness have been pointed out.

In this paragraph, an experimental work dealing with the cyclic behavior of dissipative T-stub joints is carried out. The scope of the study is comparative. In fact, the leading purpose is to show how to design a T-stub connection, implementing dissipative T-stubs as weak component, with same stiffness and resistance of the classical T-stub joint (TS-CYC 04) presented in chapter 3. In this way, a joint having the same behavior under serviceability loads of joint TS-

CYC 04 but an improved hysteretic behavior, will be obtained. The test setup is the same already shown in chapter 3, the same beam-column coupling has been employed, the same loading history has been applied and the same instruments to monitor the joint components and the whole joint behavior have been used. Two joints have been tested:

- **TSJ-XS-CYC 06/ TSJ-XS-CYC 07** are two partial strength joints with a couple of T-stubs bolted to beam flanges and to the column flanges, designed to be the main source of plastic deformation capacity. In first case M24 bolts have been adopted to fasten the T-stub flange to the column. In second case M30 bolts have been employed.

5.3.2.1 Design of Tested Specimens

This specimen is a dissipative double split tee connection. The same design procedure previously applied to detail classical partial strength joints having as weakest component bolted elements, is applied. Therefore, the weakest joint component is first selected, detailed and, successively, other connecting elements are designed to have sufficient overstrength aiming to avoid their plastic engage. As in this case the weakest joint component are the bolted T-stubs, main scope is to design these elements in order to have same resistance and stiffness of the rectangular T-stubs of specimen TS-CYC 04. As far as the design requirements are two, i.e. stiffness and resistance, thickness of the flange plate is fixed equal to 25 mm while damper width and length are assumed as design parameters. The flexural resistance of the joint, provided

that the T-stub in tension is the weakest joint component and fails according to a type-1 mechanism, is given by the following expression:

$$\frac{2\eta B_{eff} t_{ep}^2}{m} f_y (d_b - t_{bf}) = M_{jR,d} = 100 \text{ kNm} \quad (5.170)$$

where B_{eff} is the effective plate width, η is the factor reducing the T-stub resistance due to moment-shear interaction, m is the device length, f_y is the material yield strength, d_b is the beam depth and t_{bf} is the thickness of the beam flange. For sake of clarity, relationships defining effective width and factor η are here recalled:

$$B_{eff} = B \cdot e \cdot \left(\frac{s}{B}\right) \cdot \ln\left(\frac{B}{s}\right) \quad \text{if } \frac{s}{B} < \frac{1}{e} \quad (5.171)$$

$$B_{eff} = B \quad \text{if } \frac{s}{B} > \frac{1}{e} \quad (5.172)$$

$$\eta = \frac{2 \cdot m \cdot b(z^*) \cdot (2z^* - m)}{3B_{eff} t^2} \left[1 - \sqrt{\left(1 + \frac{3t^2}{(2z^* - m)^2}\right)} \right] \quad (5.173)$$

In addition, aiming to control the stiffness of the joint, the following relationship equating stiffness of rectangular T-stub of joint TS-CYC 04 to that of the dissipative T-stub, has to be written:

$$0,25 \frac{EB_{eff} t_{ep}^3}{m^3} = S_{jR,d} = 324737 \text{ N/mm} \quad (5.174)$$

Therefore, aiming to define design parameters providing desired stiffness and resistance, the following system of equations has to be solved:

$$\begin{cases} \frac{2\eta B_{eff} t_{ep}^2}{m} f_y (d_b - t_{bf}) = M_{jR,d} = 100000000 \text{ Nmm} \\ 0,25 \frac{EB_{eff} t_{ep}^3}{m^3} = S_{jR,d} = 324737 \text{ N/mm} \end{cases} \quad (5.175)$$

As before demonstrated, η factor depends on the geometrical design parameters and in particular on m/t and s/B ratio. In addition, also optimum value of s/B depends on m/t by means of the following relationships:

$$\begin{aligned} \text{if } \left(\frac{m}{t}\right) \leq 6 & \quad \left(\frac{s}{B}\right)_{opt} = 0,5634 \left(\frac{m}{t}\right)^{-0,64} \\ \text{if } \left(\frac{m}{t}\right) > 6 & \quad \left(\frac{s}{B}\right)_{opt} = 0,18 \end{aligned} \quad (5.176)$$

therefore, as it is not easy to solve system (5.175) in a closed form, plate geometry has been determined in iterative way:

$$\left\{ \begin{array}{l} \eta = 0.827 \\ \left(\frac{s}{B}\right)_{opt} = 0.325 \\ m = \sqrt{\frac{0.25 \cdot E \cdot t \cdot M_{j,Rd}}{2\eta \cdot f_y (d_b - t_{bf})}} = \sqrt{\frac{0.25 \cdot 210000 \cdot 25 \cdot 100000000}{20.827 \cdot 275(270 - 10)}} = \\ = 58.45 \cong 59mm \\ B_{eff} = \frac{S_{jR,d} m^3}{0.25 \cdot E \cdot t^3} = \frac{324737 \cdot 58.45^3}{0.25 \cdot 210000 \cdot 25^3} = 79.77mm \end{array} \right. \quad (5.177)$$

and therefore:

$$\left\{ \begin{array}{l} B = \frac{B_{eff}}{e \cdot \left(\frac{s}{B}\right) \ln\left(\frac{B}{s}\right)} = 80.34 \cong 81mm \\ s = \left(\frac{s}{B}\right) \cdot B = 26.4mm \end{array} \right. \quad (5.178)$$

In addition, as before demonstrated, in order to assure a type-1 mechanism the following limitation has to be satisfied:

$$t_{ep} \leq \sqrt{\frac{4B_{Rd}nm}{b_{eff} f_y (m + 2n)}} \quad (5.179)$$

In case of tests TSJ-XS-06 and TSJ-XS-07 T-stub elements have been fastened to the column through bolts M24 and M30 class 10.9 respectively. In the two cases, Eq.(5.179) can be rewritten as:

$$t_{ep} \leq \sqrt{\frac{4B_{Rd}nm}{b_{eff}f_y(m+2n)}} = \sqrt{\frac{4 \cdot 220500 \cdot 50 \cdot 59}{(81) \cdot 275(59 + 2 \cdot 50)}} = 27 \text{ mm} \quad (5.180)$$

$$t_{ep} \leq \sqrt{\frac{4B_{Rd}nm}{b_{eff}f_y(m+2n)}} = \sqrt{\frac{4 \cdot 505000 \cdot 50 \cdot 59}{(81) \cdot 275(59 + 2 \cdot 50)}} = 41 \text{ mm} \quad (5.181)$$

therefore, in both cases the adoption of a thickness of the flange plate equal to 25 mm provides a type-1 failure mechanism.

On the base of the above results, after designing the weakest joint component, it is possible to design the components related to the column web zone. The shear panel resistance can be designed as already discussed with reference to EEP-CYC 01 specimen. In order to obtain a sufficient overstrength degree two 10 mm supplementary web plates have been adopted. By means of equations [(3.4)-(3.10)] and considering a full effectiveness of the supplementary web plates, the shear panel resistance can be computed as:

$$k_b = \frac{C_r EI_c}{[(d_b - t_{bf})/2]^3} = \frac{5 \cdot 210000 \cdot 56960000}{[(270 - 10)/2]^3} = 27222576 \text{ N/mm} \quad (5.182)$$

$$k_s = \frac{G(A_{vc} + R_f A_{dp})}{[(d_b - t_{bf})/2]} = \frac{80769 \cdot (2483 + 3700)}{[(270 - 10)/2]} = 3841498 \text{ N/mm} \quad (5.183)$$

$$K_e = \frac{k_b k_s}{k_b + k_s} \frac{(d_b - t_{bf})}{2} \frac{(d_b - t_{bf})}{\beta} = \frac{27222576 \cdot 3841498}{27222576 + 3841498} \frac{(270 - 10)^2}{2 \cdot 1} = 1.138 \cdot 10^{11} \text{ Nmm} \quad (5.184)$$

$$M_{pz} = 1.137 \cdot 10^{11} \cdot 0.85 \cdot 0.00242 = 233.9 \cdot 10^6 \text{ Nmm} \approx 234 \text{ kNm} \quad (5.185)$$

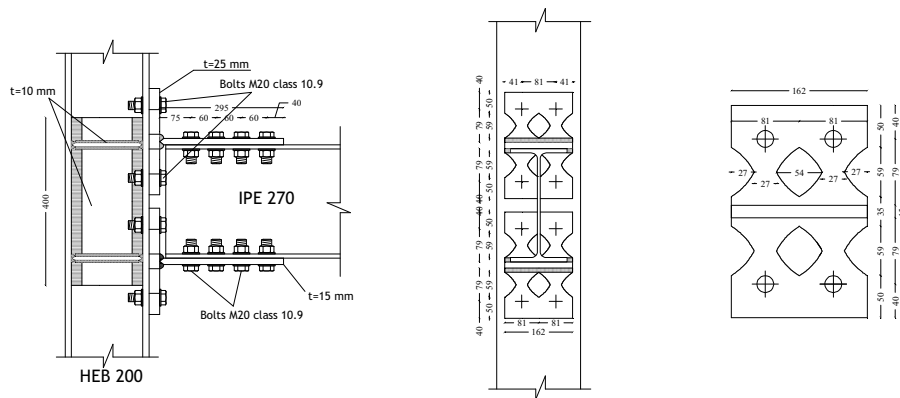


Fig. 5.72 – Specimen TSJ-XS-CYC-06

Therefore, by adopting such supplementary web plates, the shear panel resistance is greater than the joint design resistance of a factor greater than 2, so that it is expected that the panel zone remains in elastic range up to the failure of the end-plate in bending. Moreover, the use of a couple of continuity plates with a thickness equal to the beam flange thickness assures that the column web in tension and the column web in compression also remain in elastic range.

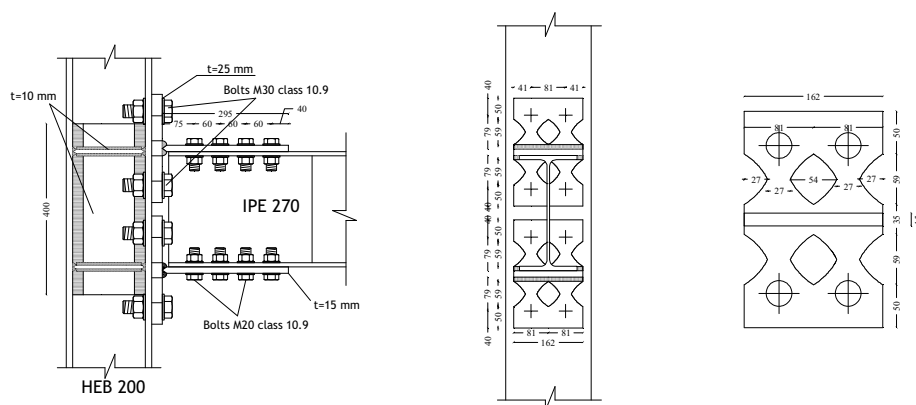


Fig. 5.73 –Specimen TSJ-CYC-07

Furthermore, the elements connecting the T-stubs to the beam flanges have to be designed. The two T-stub elements have been connected through the webs to the beam flanges by means of eight M20 bolts class 10.9. The ultimate strength of such connection according to Eurocode 3, is given by:

$$F = n_b \alpha_v f_{ub} A = 8 \cdot 0.5 \cdot 1000 \cdot 245 = 980000N \geq \frac{M_{j,Rd}}{(d_b - t_{bf})} =$$
$$= 384615N \quad (5.186)$$

The geometry of the specimens is depicted in Fig. 5.72-Fig. 5.73.

5.3.2.2 Description of Test TSJ-XS-CYC 06

Test TSJ-XS-CYC 06 and the measurement devices are depicted in the following pictures:

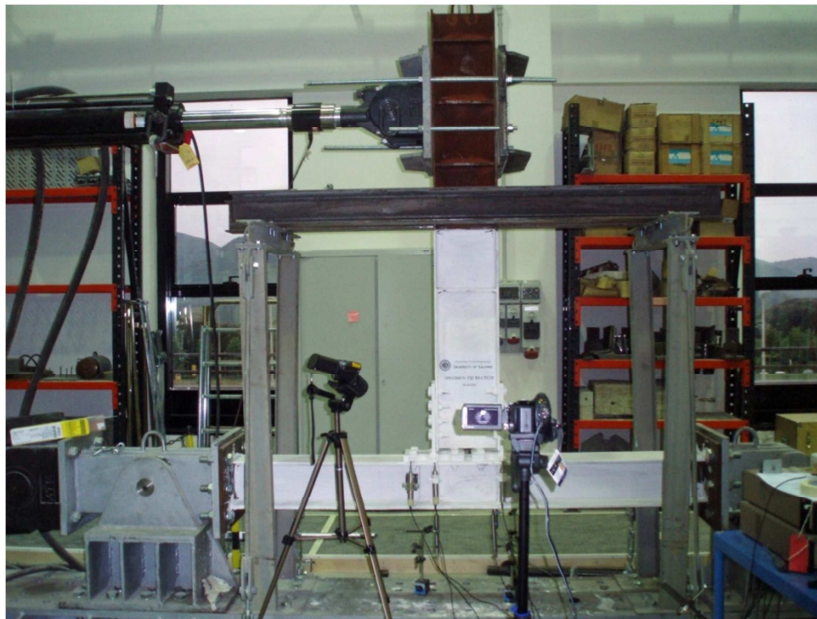


Fig. 5.74 –Test TSJ-XS-CYC 06

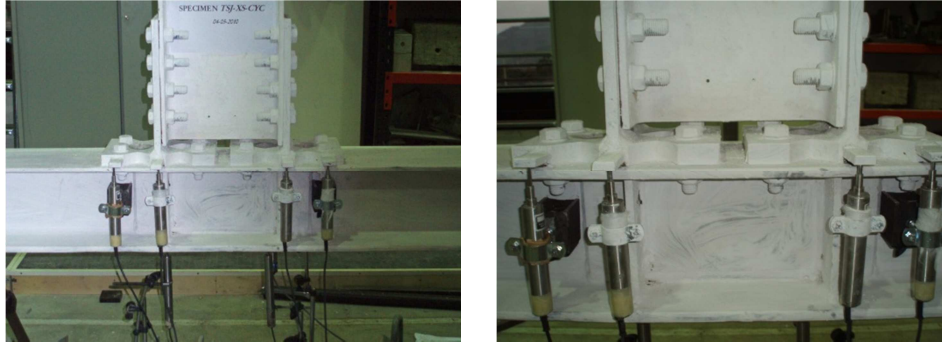


Fig. 5.75 –Measurement devices (TSJ-XS-CYC 06)

As above said, specimen TSJ-XS-CYC 06 is a double split tee connection where the elements involved in the energy dissipation are mainly the T-stubs subjected alternatively to tension and compression.

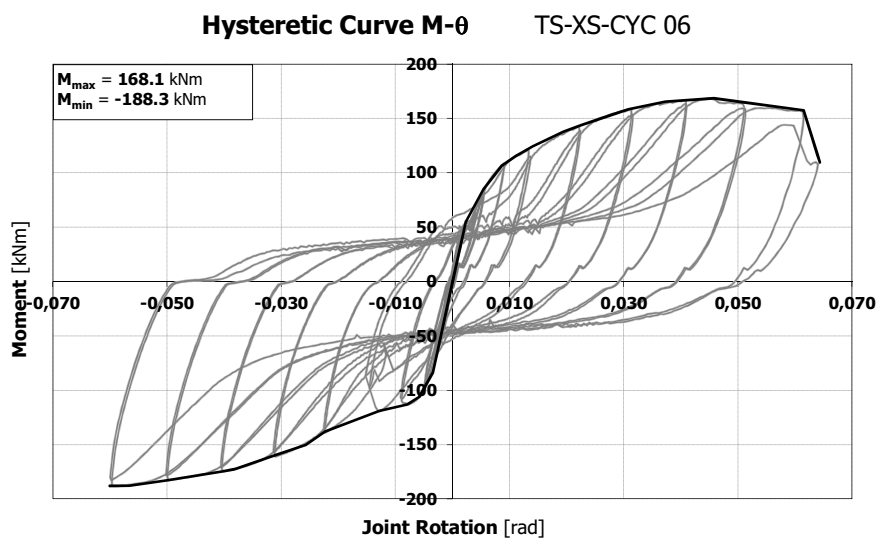


Fig. 5.76 –TSJ-XS-CYC 06 Moment-Rotation Curve

Panel zone is designed to be over-strengthened with respect to the weak elements. Therefore, column panel components do not provide a significant contribution to the dissipative behavior of the whole joint. The scope of the study is comparative. The main purpose is to evaluate the cyclic behavior of an innovative detail, realized by applying hourglass T-stub elements, in order to compare its cyclic response with that of a classical double split tee joint having the same stiffness and resistance, but realized fastening the beam to the column through classical rectangular T-stubs.

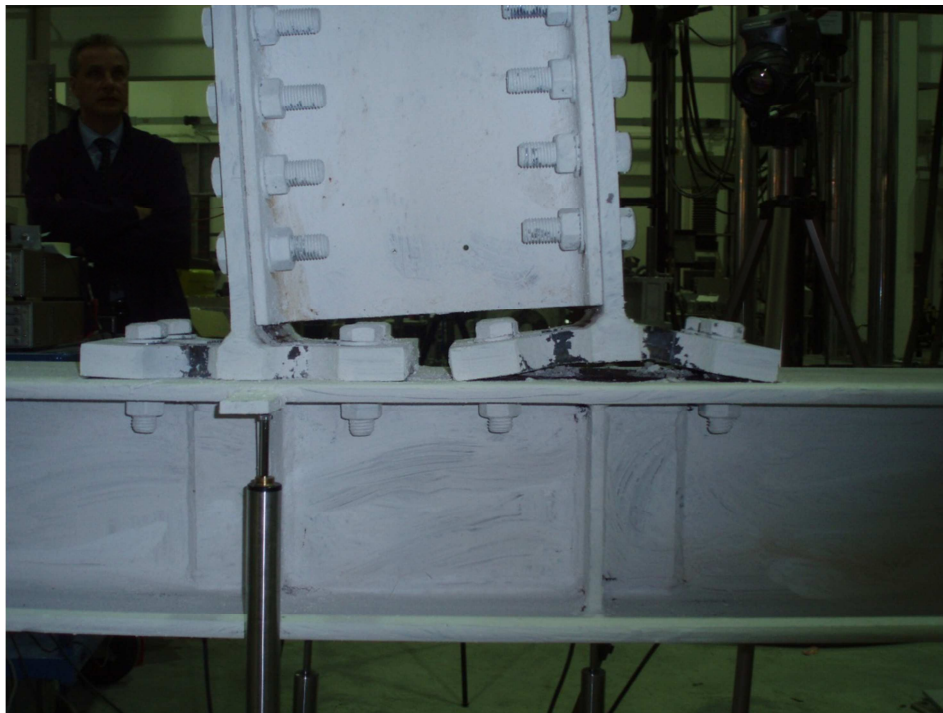
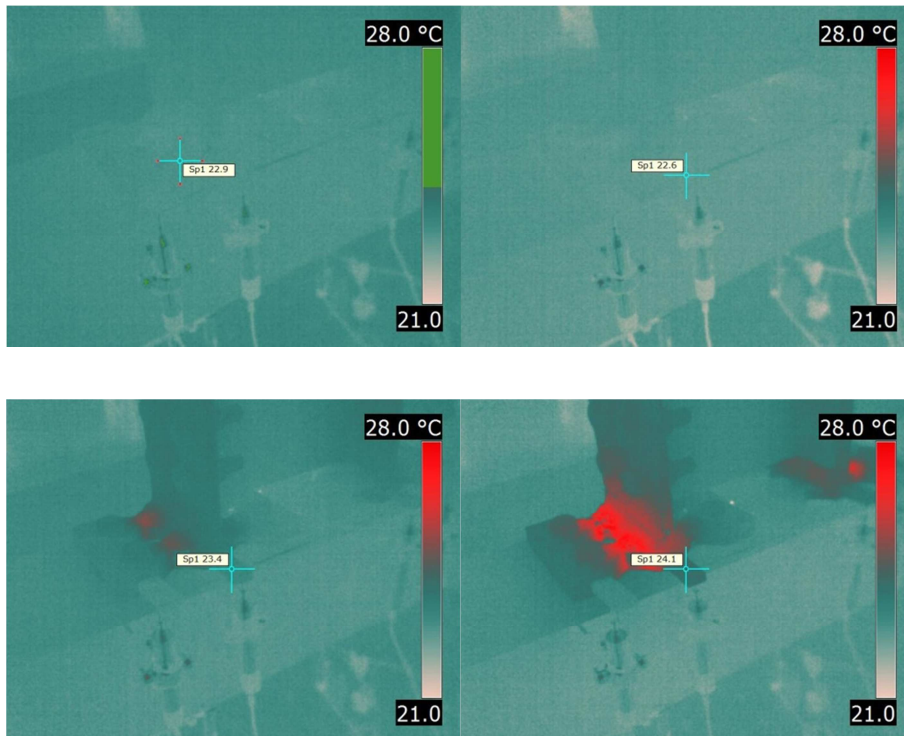


Fig. 5.77 –Plasticization of the tee elements

The behavior of the specimen during the test has been the one expected according to the design criteria. In fact, only the plastic engage of T-stubs has been observed with development of plasticization in the dissipative elements (Fig. 5.77). The shape of the hysteresis loops is similar to that exhibited by joint TS-CYC 04. In fact, significant pinching phenomena, mainly due to the bolt plastic deformation, are evidenced (Fig. 5.76). The diffusion of the plasticization has been visualized through shots took by means of thermal camera during the test. A sequence that shows the specimen thermal state during the first cycles of plasticization is proposed in Fig. 5.78.



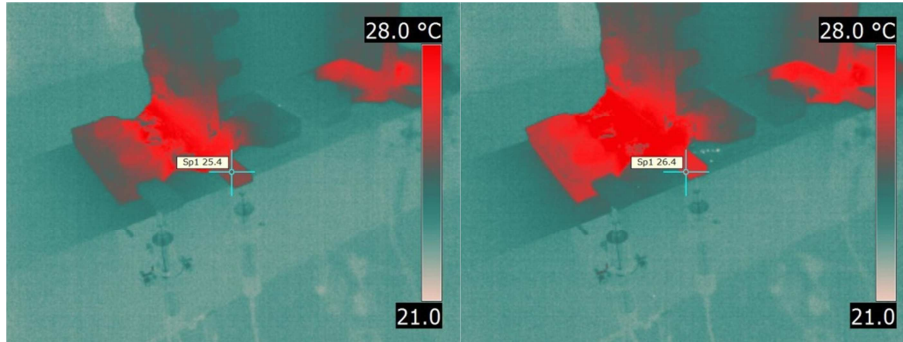


Fig. 5.78 –Thermal state of the specimen during first cycles

From these figures, it is easy to understand that plasticization begins in a zone contained between the damper mid-section and maximum breadth section and then propagates through the whole plate. In addition, a greater plastic engagement of the dampers located externally to the beam flanges is shown. This behavior is obviously due to the beam rotation. In fact, when isolated T-stubs are studied in laboratory, they are usually tested under axial loads and, as a consequence, the behavior of the flange plate is symmetrical. Conversely, when T-stubs are used as connecting elements to fasten the beam to the column, during the loading process, as a result of compatibility requirements, they are subjected to an axial displacement equal to the joint rotation multiplied for the lever arm and to a rigid rotation due to the beam rotation. Such behavior leads to a larger plastic engagement of the dampers located outside the column flange.

The joint has surprisingly exhibited lower plastic rotation supply and less energy dissipated at collapse compared to the case of joint TS-CYC 04. This result can be justified by analyzing the different failure mechanisms of the two joints. In fact, in case of joint TS-CYC 04 failure arose due to the propagation of

a crack through the plate in correspondence of the plastic hinge located at the T-stub web leading to the complete loss of resistance of the joint. Therefore, in case of joint TS-CYC 04 the collapse condition was reached due to the complete exploit of the plate plastic deformation capacity. In fact, the connection failed according to a failure 1 mechanism, after the full development and fracture of the plastic hinges located at the T-stubs web and bolts (Fig. 5.79).



Fig. 5.79 –Joints after failure. On the left: TS-CYC-04- On the right: TS-XS-CYC-06

Conversely, in case of joint TSJ-XS-CYC 06, even though bolts were designed to allow full plasticization of the plate, collapse condition was reached due to the premature fracture of bolts. Such a failure has obviously limited the plastic capacity of dissipative T-stubs leading to an amount of energy dissipated at collapse lower than the actual damper dissipation supply. In fact, it has to be noted that when bolt failure occurred there was no apparent sign of crack formation on the plate. A further observation has to be made with reference to the bolt failure. In fact, as the maximum moment reached in case of joint TS-

CYC 04 and TSJ-XS-CYC 06 are similar there is no apparent reason to expect bolts failure at a lower number of cycles in case of the dissipative joint.

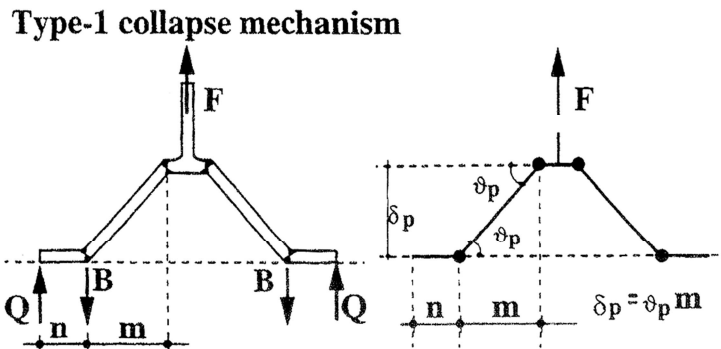


Fig. 5.80 –Rotation of the plate due to the force acting on the T-stub

This experimental result can be justified only if values of m in case of rectangular and dissipative T-stub are considered. In fact, in case of joint TS-CYC 04, the distance between the plastic hinges located on the flange plate is equal to 81 mm whereas, in case of joint TSJ-XS-CYC 06 the length of the plastic zone, i.e. the length of the damper, is equal to 59 mm. Considering that, for a fixed value of displacement at the beam tension flange, the flexural engagement of bolts due to compatibility requirements with plate deformation increases as m decreases, justifies the development of bolt fracture of joint TSJ-XS-CYC 06 at a joint rotation lower than joint TS-CYC 04 (Fig. 5.80). The influence of bending moment on bolts ultimate resistance is an aspect neglected in classical T-stub theory and represents an approximation that, in some cases, can lead to poor prediction of the T-stub ductility. In fact, when the connection is designed to dissipate energy in the flange plate, more

accurate procedures accounting for bending moment arising in bolts due to the plate plastic deformation should be adopted.

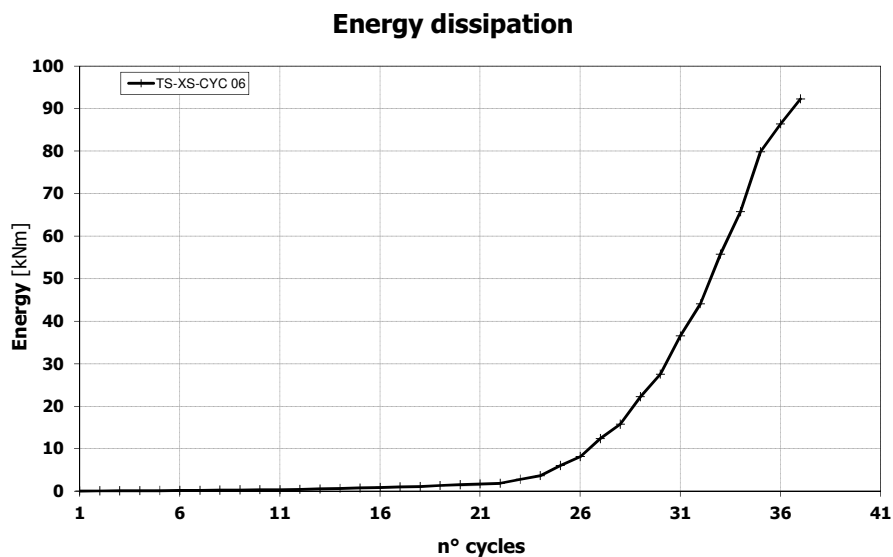


Fig. 5.81 – Dissipated Energy – TSJ-XS-CYC 06

5.3.2.3 Description of Test TSJ-XS-CYC 07

As far as poor results have been obtained during test TSJ-XS-CYC 06 due to the premature failure of bolts a new test has been planned. The joint detail of test TSJ-XS-CYC 07 is equal to the previous one but, aiming to develop the full plasticization of dampers, higher diameter bolts have been used. In fact, in this test, M30 bolts have been adopted to fasten the beam to the column. Scheme of measurement devices and the test setup are shown in Fig. 5.82-Fig. 5.83.

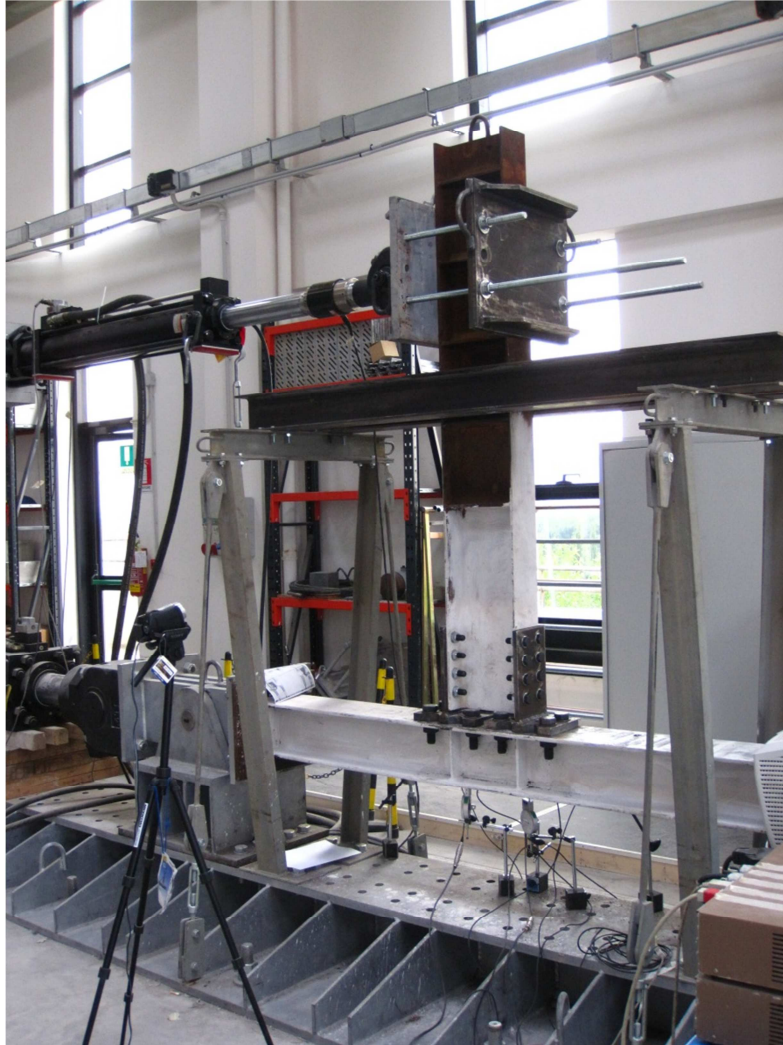


Fig. 5.82 –Test TSJ-XS-CYC 07

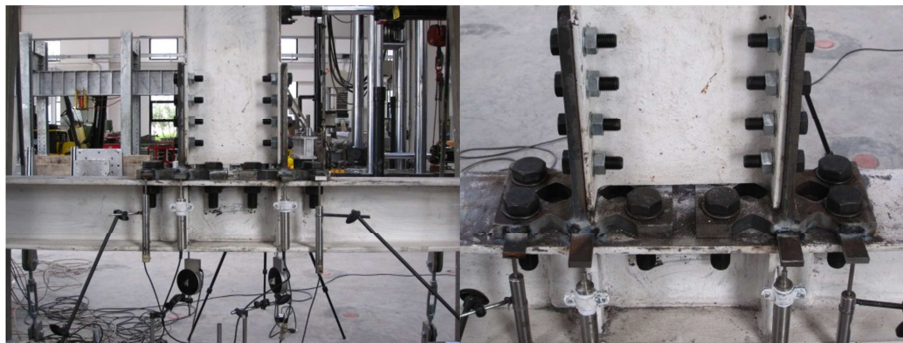


Fig. 5.83 –Measurement devices (TSJ-XS-CYC 07)

Even though only bolts diameter differentiates joint TSJ-XS-CYC 06 and TSJ-XS-CYC 07 some substantial differences can be evidenced in the hysteretic behavior. In fact, although pinching is not completely avoided, joint TSJ-XS-CYC 07 does not show strength degradation phenomena up to the joint failure that has been reached after a high number of cycles (44) at the ultimate rotation of about the 10% (Fig. 5.84). Obviously, a so large rotational capacity is not required in current structural applications. In fact, as already remarked, in case of Ductility Class High MRFs Eurocode 8 requires that the ultimate plastic rotation exhibited by the joint is higher than 35 mrad. Notwithstanding, it is useful to note that as the beam depth increases the local ductility demand of the component localized at the tension flange level linearly increases. In fact, ductility demand on the joint component at tension flange is directly related to the joint lever arm. Therefore, because of their high ductility supply, the adoption of dissipative T-stubs as weakest joint component can be even more useful in case of challenging applications, such as that of joints fastening high beams.

On the base of this consideration, it is in the author opinion that, in order to better point out the strong difference in cyclic behavior of dissipative and classical joints, further experimental efforts should be devoted to the comparison of the response of classical joints and innovative dissipative joints in case of high beam depths. In addition, as already demonstrated by Piluso et al. the adoption of dissipative partial strength joints leads to significant savings on the total structural cost especially in case of frames where beam design is governed by gravity loads rather than seismic loads, which just might be the case of high beam depths.

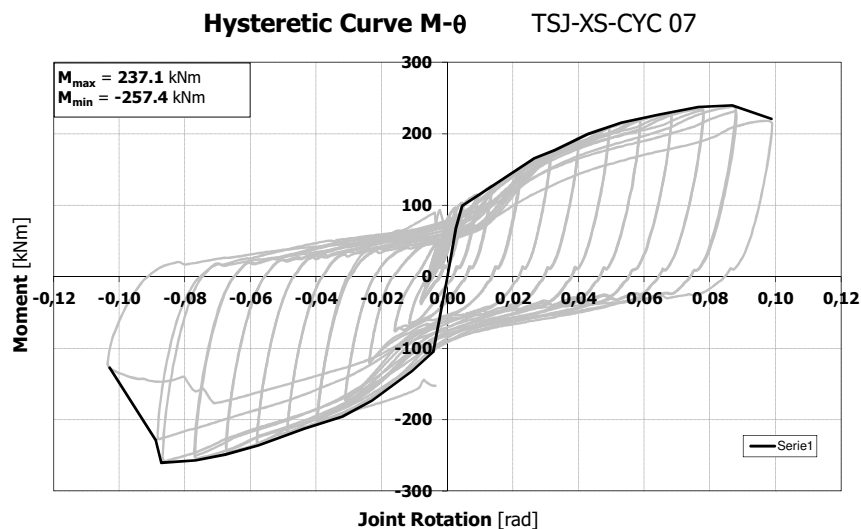


Fig. 5.84 –Cyclic Response of Joint TSJ-XS-CYC 07

As expected, during this test the only components engaged in plastic range have been the hourglass T-stubs in tension and compression. Components on the column panel have not been significantly involved in the dissipation

mechanism. Failure condition has been reached after the full development of the cyclic ductility supply of the steel dampers. Collapse occurred at the 44th cycle due to the formation of a crack, which started in the heat-affected zone and then propagated through the plate following a circular shaped pattern (Fig. 5.85).

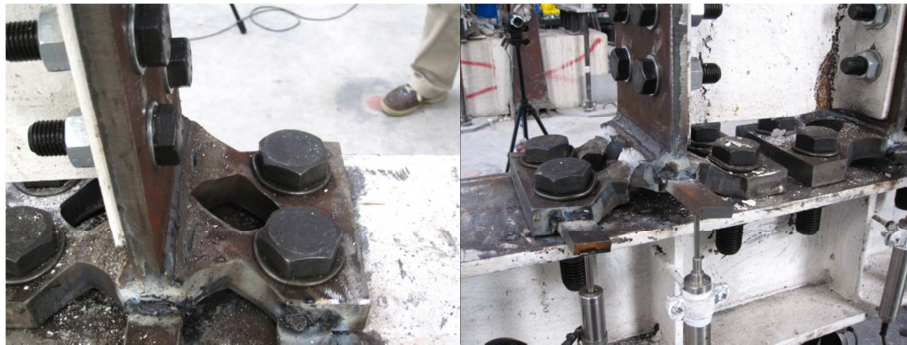


Fig. 5.85 –Crack Formation and propagation (TSJ-XS-CYC 07)

This particular failure mode, which differentiates the behavior at collapse of hourglass T-stubs from those of classical T-stubs, whose failure is usually characterized by the formation of a straight crack in correspondence of welds, may find a theoretical justification in the results obtained in paragraph 5.3.1.1. As previously demonstrated, in case of dissipative T-stubs, the section of minimum resistance where first plasticization occurs, is not necessarily located in correspondence of the section of maximum width. In fact, as bending moment is linear with point of zero at the mid-section and shear is constant along the plate, due to the moment-shear interaction, the section of minimum resistance, depending on the plate geometry, can be in general located somewhere in between T-stub web and damper centerline.

Formulation previously found, predicting the position of the section of minimum resistance, can be specialized in case of specimen TS-XS-CYC 07:

$$\text{if } e^m \sqrt{\frac{1}{m^2+3t^2}} = 2.24 < \frac{B}{s} = 3.07 < e^{\frac{m}{\sqrt{3}t}} = 3.90$$

$$z^* = \frac{\alpha^2 m - \sqrt{4\alpha^2 - 3\alpha^4 t^2}}{2\alpha^2} = 14.36\text{mm} \quad (5.187)$$



Fig. 5.86 – Position of the section of minimum resistance (TSJ-XS-CYC 07)

In Fig. 5.86 the location of the end of the crack line is shown. In particular, the substantial agreement with the prediction provided by (5.187) is evidenced

through measurement by means of ruler. Finally, in Fig. 5.87 the joint energy dissipation capacity is represented.

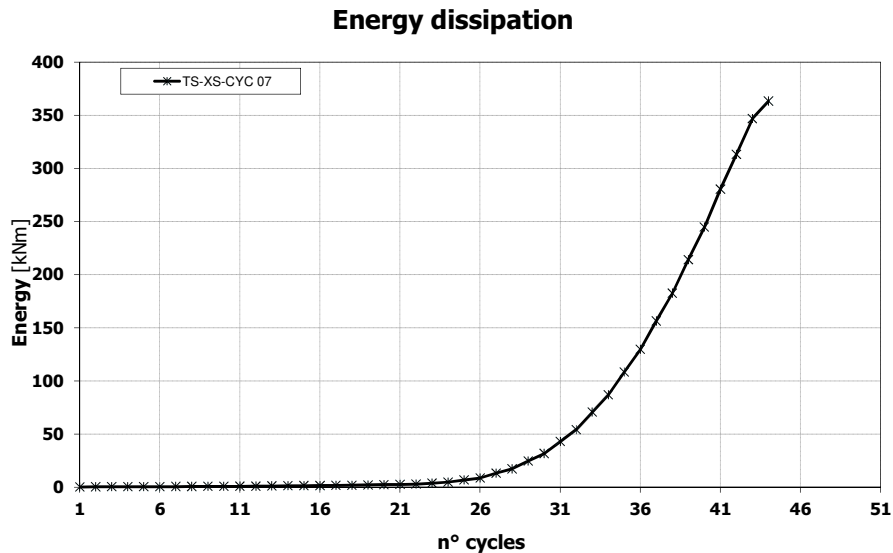


Fig. 5.87 – Energy dissipated by joint TSJ-XS-CYC 07

5.3.2.4 Comparison between Dissipative and Classical Joints

First of all a comparison between test TS-CYC 04 and TSJ-XS-CYC 07 in terms of moment rotation curve is proposed. Fig. 5.88 clearly points out that design of dissipative joint has been properly carried out. In fact, the two design parameters, i.e. initial stiffness and knee resistance are approximately equal in the two considered cases. This aspect confirms that, concerning hourglass T-stubs, mechanical modeling and design tools previously identified provide an

accurate prediction of force-displacement curve of dissipative T-stub. In addition, Fig. 5.88 demonstrates that, by properly tapering the plate in the section contained between the T-stubs web and bolt section, a significant improvement of the behavior under cyclic loads has been obtained. In fact, pinching and strength degradation phenomena have been strongly reduced.

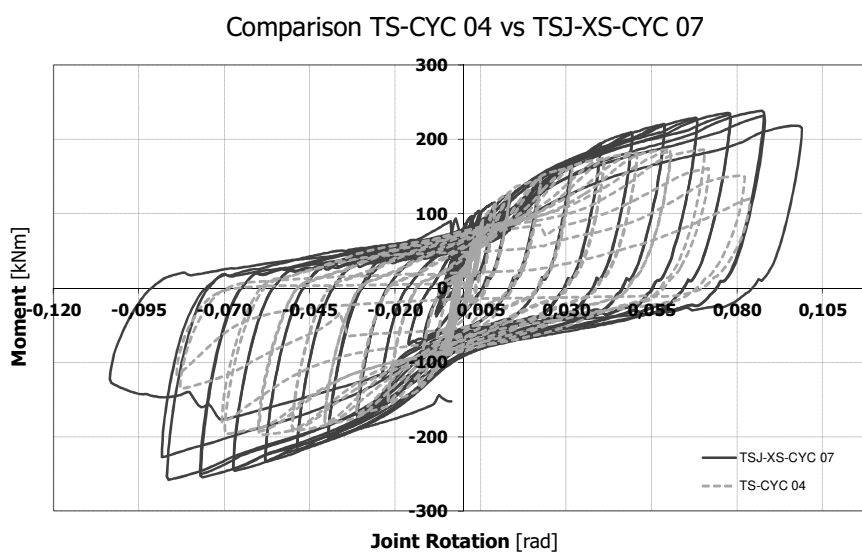


Fig. 5.88 – Comparison between joints TS-CYC 04 and TSJ-XS-CYC 07

Furthermore, concerning the comparison of dissipative T-stub joints with respect to other joint typologies, whose testing has been discussed in chapter 3, cyclic envelopes of all tested joint are given in Fig. 5.89. The assessment of moment-rotation curves shows that all joints have exhibited largely the same initial stiffness, knee resistance and ultimate resistance. Only in case of joint TSJ-XS-CYC 07 a significant increase of the bending moment at failure has been exhibited. In fact, compared to the case of joint TS-CYC 04 ultimate

resistance is higher of about 40%. This behavior can be partially justified by considering that in case of joint TSJ-XS-CYC 07 M30 bolts have been used. In fact, as already demonstrated by Faella et al., the dimension of the bolt head can affect the T-stub resistance by reducing m , which is the distance between the plate sections where maximum moment occurs.

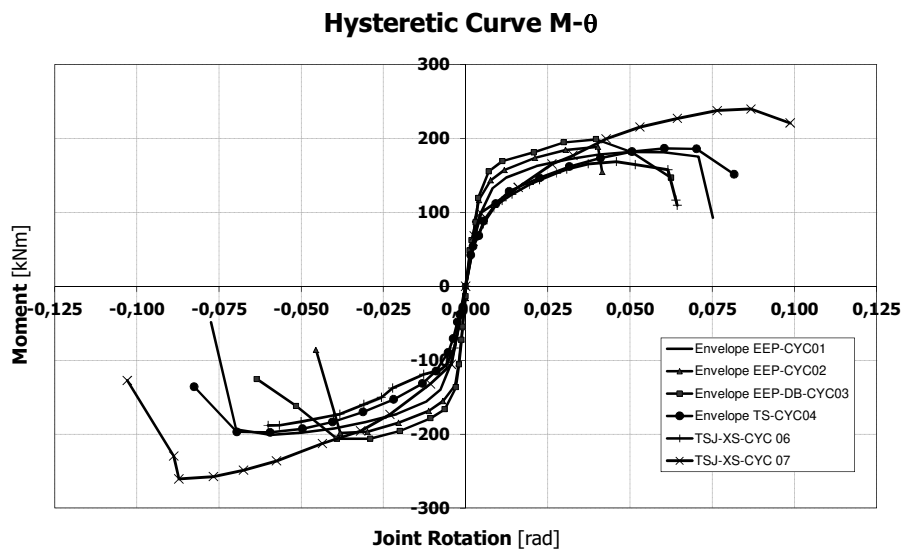


Fig. 5.89 – Cyclic envelopes of all tested joints

Finally, Fig. 5.90 shows the energy dissipated by tested joints versus the number of cycles. As already commented, the best behavior in terms of energy dissipation is shown by dog-bone joint, in fact, for a fixed cycle number, joint EEP-DB-CYC 03 gives the greatest energy dissipation. Notwithstanding, it has to be noted that, even though joint TSJ-XS-CYC 06 provides a dissipation similar to that of simple rectangular T-stub joint, energy dissipated at failure is significantly greater compared to those of other joint typologies. In fact, it is

almost two times greater than the total energy dissipated at collapse by joints adopting RBS strategy, dissipating in the shear panel or in rectangular T-stubs.

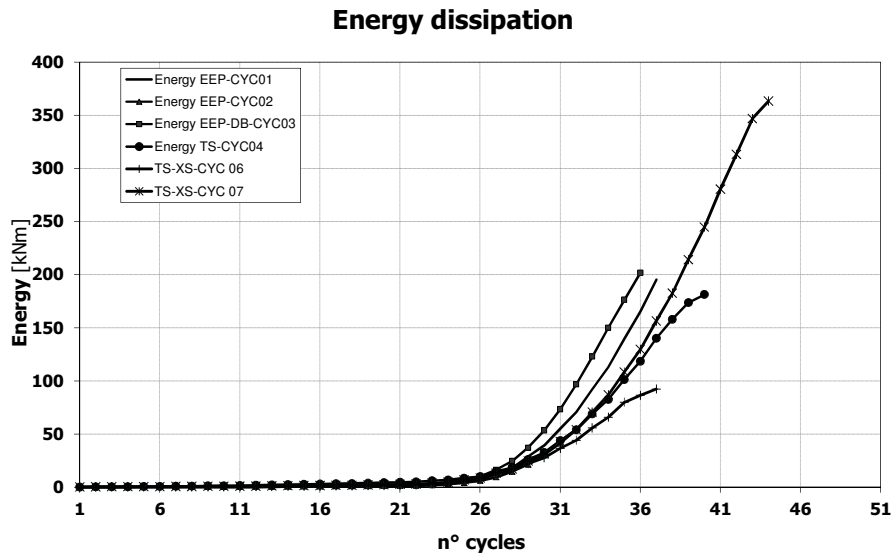


Fig. 5.90 – Energy dissipated by joints

5.4 References

Aiken, I., Clark, P. & Kelly, J., 1993b. Design and Ultimate-Level Earthquake Tests of a 1/2.5 Scale Base-Isolated Reinforced-Concrete Building. In *Proceedings of ATC-17-1 Seminar on Seismic Isolation, Passive Energy Dissipation and Active Control*. San Francisco, California, 1993b.

Aiken, I., Nims, D., Whittaker, A. & Kelly, J., 1993a. Testing of Passive Energy Dissipation Systems. *Earthquake Spectra*, 9(3).

Alonso, J., 1989. *Mechanical Characteristics of X-Plate Energy Dissipators*. Berkeley: University of California.

ASCE, 2000. *Prestandard and Commentary for the Seismic Rehabilitation of Buildings*. Reston, Virginia: FEMA-356 American Society of Civil Engineers.

BSSC, 2003. *NEHRP Recommended Provisions for Seismic Regulations for New Buildings and Other Structures: Parts 1 and 2*. Washington D.C.: FEMA-450 Building Seismic Safety Council.

Cahis, X., Bozzo, L., Foti, D. & Torres, L., 1997. An Energy Dissipating Device for Seismic Protection of Masonry Walls. In *L'ingegneria Sismica in Italia*. Taormina, Italia, 1997.

CEN, 2005a. *Eurocode 3: Design of steel structures - Part 1-1: General rules and rules for buildings*.

CEN, 2005b. *Eurocode 3: Design of steel structures - Part 1-8: Design of joints*.

CEN, 2005c. *Eurocode 8: Design of structures for earthquake resistance - Part 1: General rules, seismic actions and rules for buildings*.

Chopra, A.K., 1995. *Dynamics of Structures*. New Jersey: Prentice-Hall.

Christopoulos, C. & Filiatrault, A., 2006. *Principles of Passive Supplemental Damping and Seismic Isolation*. Pavia: IUSS PRESS.

Constantinou, M., Soong, T. & Dargush, G., 1998. *Passive Energy Dissipation Systems for Structural Design and Retrofit*. State of New York: University at Buffalo.

Drucker, D., 1956. The Effect of Shear on the Plastic Bending of Beams. *Journal of Applied Mechanics*, pp.509-14.

Faella, C., Montuori, R., Piluso, V. & Rizzano, G., 1998. Failure mode control: economy of semi-rigid frames. In *Proceedings of the XI European Conference on Earthquake Engineering*. Paris, 1998.

Faella, C., Piluso, V. & Rizzano, G., 1998b. Experimental Analysis of Bolted connections: snug versus preloaded bolts. *Journal of Structural Engineering*, 124(7), pp.765-74.

Faella, C., Piluso, V. & Rizzano, G., 2000. *Structural Steel Semi-Rigid Connections*. Boca Raton: CRC Press.

Filiatrault, A., 2002. *Elements of Earthquake Engineering and Structural Dynamics*. Montreal, Canada: Polytechnical International Press.

Fleischman, R. & Hoskisson, B., 2000. Modular Connectors for Seismic Resistant Steel Moment Frames. In *Proceedings of Structures Congress 2000*. Philadelphia, PA, 2000.

Huang, Z. & Foutch, D., 2009. Effect of Hysteresis Type on Drift Limit for Global Collapse of Moment Frame Structures Under Seismic Loads. *Journal of Earthquake Engineering*, 13(7), pp.939-64.

Iannone, F., Latour, M., Piluso, V. & Rizzano, G., 2011. Experimental Analysis of Bolted Steel Beam-to-Column Connections: Component Identification. *In Press in Journal of Earthquake Engineering*.

Kasai, K. & Popov, E., 1986. Cyclic Web Buckling Control for Shear Link Beams. *Journal of Structural Engineering ASCE*, 110(3), pp.505-23.

Kelly, J., 1979. Aseismic Base Isolation: A review. In *Proceedings of 2nd U.S. National Conference on Earthquake Engineering*. Stanford, CA, 1979.

Kelly, J., Skinner, R. & Heine, A., 1972. Mechanisms of Energy Absorption in Special Devices for Use in Earthquake Resistant Structures. *Bulletin of the New Zealand Society for Earthquake Engineering*, 5(3), pp.63-88.

Kim, Y., Ryu, H. & Kang, C., 2007. Hysteretic Behaviour of Moment Connections with Energy Absorption Elements at Beam Bottom Flanges. In *ICAS 2007*. Oxford, 2007.

Kobori, T. et al., 1992. Development of Hysteresis Steel Dampers. In *Earthquake Engineering Tenth World Conference*, 1992.

Kosloff, D. & Frazie, G., 1978. Treatment of Hourglass patterns in low order finite element codes. *International Journal for Numerical and Analytical Methods in Geomechanics*, 2, pp.57-72.

Latour, M., Piluso, V. & Rizzano, G., 2008. Cyclic Model of Beam-to-Column Joints. In *5th European Conference on Steel and Composite Structures, Eurosteel 2008*. Graz, Austria, 2008.

Leon, R. & Swanson, A., 2000. Cyclic Modelling of T-stub Connections. In *Proceedings of Steel Structures in Seismic Areas*. Canada, 2000.

Nakashima, M., 1995. Strain-Hardening Behavior of Shear Panels made of Low-yield Steel: Test. *Journal of Structural Engineering ASCE*, 121(12), pp.1742-49.

Piluso, V., Faella, C. & Rizzano, G., 2001. Ultimate behavior of bolted T-stubs. Part I: Theoretical model. *Journal of Structural Engineering ASCE*, 127(6), pp.686-93.

Piluso, V. & Rizzano, G., 2003. Reliability of full-strength end-plate connections: design criteria and Monte Carlo simulation. In *Proceedings of the ASSCCA '03 Advances in Structures*. Sidney, Australia, 2003.

Piluso, V. & Rizzano, G., 2008. Experimental Analysis and modelling of bolted T-stubs under cyclic loads. *Journal of Constructional Steel Research*, 64, pp.655-69.

Popov, E., 1980. Seismic Behavior of Structural Subassemblages. *Journal of the Structural Engineering ASCE*, 106(7), pp.1451-74.

Rai, D. & Wallace, B., 1998. Aluminium Shear-Links for Enhance Seismic Resistance. *Earthquake Engineering and Structural Dynamics*, 27, pp.315-42.

Rizzano, G., 2006. Seismic Design of Steel Frames with Partial Strength Joints. *Journal of Earthquake Engineering*, 10(5), pp.725-47.

SAC, 2000a. *Recommended Seismic Design Criteria for New Steel Moment Resisting Frame Buildings*. California: FEMA.

Scholl, R., 1990. Improve the Earthquake Performance of Structures with Added Damping and Stiffness Elements. In *Proceedings of Fourth U.S. National Conference on Earthquake Engineering*. Palm Springs, California, 1990.

Skinner, R., Kelly, J. & Heine, A., 1975. Hysteresis Dampers for Earthquake Resistant Structures. *Earthquake Engineering and Structural Dynamics*, 3, pp.287-96.

Soong, T. & Spencer Jr, B., 2002. Supplemental Energy Dissipation: State-of-the-Art and State-of-the-Practice. *Engineering Structures*, 24, pp.243-59.

Spencer, B. & Sain, M., 1998. Controlling Buildings: a new Frontier in Feedback. *The Shock and Vibration Digest*, 30(4), pp.267-81.

Su, Y. & Hanson, R., 1990. Comparison of Effective supplemental damping equivalent viscous and hysteretic. In *Proceedings of Fourth U.S. National Conference on Earthquake Engineering*. Palm Springs, California, 1990.

Tena-Colunga, A., 1997. Mathematical Modelling of the ADAS Energy Dissipation Device. *Engineering Structures*, 19(10), pp.811-21.

Tsai, K., Chen, H., Hong, C. & Su, Y., 1993. Design of Steel Triangular Plate Energy Absorbers for seismic-resistant construction. *Earthquake Spectra*, 9, pp.505-28.

Tsai, K. & Wang, T., 1998. Shear Link Energy Absorbers for Seismic Energy Dissipation. In *Proceedings of Sixth U.S. National Conference Earthquake Engineering*. Seattle, Washington, 1998.

Whittaker, A., Bertero, V., Alonso, J. & Thompson, C., 1989. *UCB/EERC-89/02 Earthquake Simulator Testing of Steel Plate Added Damping and Stiffness Elements*. Berkeley: College of Engineering University of California.

Whittaker, A., Uang, C. & Bertero, V., 1990. *UCB/EERC-88/14 An Experimental Study of the Behavior of Dual Steel Systems*. Berkeley: College of Engineering University of California.

Yang, T. & Popov, E., 1995. *UCB/EERC-95/13 Experimental and Analytical Studies of Steel Connections and Energy Dissipators*. Berkeley: College of Engineering University of California.

Yee, Y. & Melchers, R., 1986. Moment-Rotation Curves for Bolted Connections. *Journal of Structural Engineering ASCE*, 112, pp.615-35.